

Experimental Investigation of Vacuum Breakdown Triggering Mechanisms in a DC Electrode System



Ruth Charlotte Peacock

Supervisors: Professor G.C. Burt
and Dr W. Wuensch

Engineering Department
Lancaster University

A thesis submitted for the degree of
Doctor of Philosophy

August, 2023

Declaration

I hereby declare that the contents of this dissertation have not been submitted in whole or in part for consideration for any other degree or qualification in this, or any other university. This dissertation is my own work and contains nothing which is the outcome of work done by or in collaboration with others except where specifically indicated in the text.

Ruth Charlotte Peacock

Abstract

This thesis describes the testing and results of the two pulsed DC large electrode systems at CERN, as part of a collaborations with the Compact Linear Collider (CLIC) and Linear Accelerator 4 (Linac 4) projects. The pulsed DC systems consist of two precision machined electrodes placed parallel to one another, with a gap between $60\ \mu\text{m}$ and $100\ \mu\text{m}$, under high vacuum to observe vacuum breakdown triggering mechanisms and conditioning.

Descriptions of the setup will be given, as well as changes to the electrode drawings to improve reliability of machining with a reduced electric field enhancement. Additionally, a description of a new method of conditioning through pulses rather than breakdowns will be discussed. The new conditioning method was used to condition several different materials, including, TiAl_6V_4 , CuCr_1Zr , Nb, Cu OFE, Ta, and AlMgSi_1 , and observations of the characteristics observed are given. This is followed by the same materials except AlMgSi_1 being irradiated by a H^- beam, to observe the effects of irradiation on the electric field holding capabilities and breakdown locations throughout conditioning.

Measurements of the field emission current for each pair of electrodes tested was conducted, using a constant DC supply. Analysis of the results gives the field enhancement factor, as well as comparisons between materials, polarity, and irradiation effects. During field emission measurements an optical spectrometer was attached to one window. The results are presented for the materials that produced light, showing the correlation between the light intensity at different wavelengths, with the voltage and field emission current. This can also be correlated with possible causes of light that would occur during field emission. Additionally fast fluctuations in the field emission current were measured and possible interpretations with respect to mobile dislocations are given.

Acknowledgements

I would like to thank my CERN supervisor Dr. Walter Wuensch, for being the best CERN supervisor I could have hoped for, with whom I have shared many interesting and insightful conversations, as well as a lot of excitement over new results, and a good amount of laughs mixed in. I am also very grateful to my Lancaster supervisor, Prof. Graeme Burt for both providing this opportunity and his support throughout.

A wish to also express a very very big thank you to Iaroslava Profatilova, who trained me to operate the pulsed DC systems! She has been a great support and friend throughout my PhD, with many wishes for breakdowns because it would have been boring otherwise...

I am grateful also for the friends I have made over the course of my PhD, in order of appearance, Lee (who talked me into this), Dan, Gustavo, Liam, Jan, Alejandro, Amelia, Joel, Pedro, and Victoria. They have all helped me get to the point of finishing by making my time at both the Cockcroft Institute and CERN way more fun!

A thank you also to the MeVArc cluster - I wish we had been able to have more in person gatherings during my time! These led to very interesting conversations and very enthusiastic reactions for each others work which was a great environment. A special thank you to , Eli, Yinon, Inna, Anton, Chris, and Marek.

A special thank you to my friends and family for there support getting me to this point in life. Especially to the people that check I am mostly sane on regular occasions, including my twin Cassie, my auntie Fiona and someone as sane as me, Ian!

“Last but not least, I wanna thank me. I wanna thank me for believing in me, I wanna thank me for doing all this hard work, I wanna thank me for having no

days off, I wanna thank me for... for never quitting, I wanna thank me for always being a giver and tryna give more than I receive, I wanna thank me for tryna do more right than wrong, I wanna thank me for just being me at all times.” - Snoop Dogg

Contents

Contents	vii
List of Figures	xiii
List of Tables	xxxv
1 Introduction	1
1.1 High Field Accelerators	1
1.1.1 CERN Compact Linear Collider	1
1.1.2 Radio Frequency Quadrupole	4
1.2 What is Electrical Breakdown	7
1.3 Gas Breakdown Process	8
1.3.1 Initial Breakdown	8
1.3.2 Discharge	11
1.3.3 Paschen Curve	12
1.4 Theories of Vacuum Breakdown	14
1.4.1 Introduction	14
1.4.2 Electron Emission	15
1.4.2.1 Field Emission	15
1.4.2.2 Space Charge Limit	20
1.4.3 Materials	21

1.4.4	Statistical analysis	26
1.4.4.1	Statistics of vacuum breakdown in the high-gradient and low-rate regime	26
1.5	Breakdown Nucleation	28
1.6	Light Emission	35
1.6.1	Transition radiation	35
1.6.2	Black-body radiation	36
1.6.3	Cathodoluminescence	37
1.6.4	Surface plasmon resonance	38
1.7	Context of this work	39
2	Pulsed DC Large Electrode System	43
2.1	Introduction	43
2.2	Physical Setup	46
2.3	Operation and Control	55
2.4	Conditioning	61
2.4.1	Breakdown Rate Limit Conditioning	62
2.4.2	Step Wise Conditioning	66
2.5	Breakdown Rate Error Calculation	70
2.6	Electrode Edge Electric Field Enhancement	71
3	Conditioning of Different Materials	81
3.1	Introduction	81
3.2	Conditioning Results and Discussion	83
3.2.1	Titanium Alloy (TiAl ₆ V ₄)	83
3.2.2	Copper Chromium Zirconium (CuCr ₁ Zr)	84
3.2.3	Niobium (Buffer Chemical Polished)	86
3.2.4	Oxygen Free Electronic Copper	88

3.2.5	Tantalum	88
3.2.6	Aluminium Alloy (AlMgSi1)	90
3.2.7	Niobium	91
3.2.8	Summary and Comparison of Conditioning	93
3.2.9	Quantitative Analysis of Conditioning	97
3.3	Pulse Length Dependence	100
3.4	Electrode Oxidation	102
3.5	Self Organising Plasma	103
3.6	Conclusions of Different Material Conditioning	105
4	Effects of H⁺ Irradiation	107
4.1	Introduction	107
4.2	Irradiation	110
4.3	Pulsed DC System Tests	117
4.4	Matching Conditioning Parameters	119
4.5	Results and Discussion	122
4.5.1	Titanium Alloy (TiAl ₆ V ₄)	123
4.5.2	Oxygen Free Electronic Copper (Cu OFE)	125
4.5.3	Copper Chromium Zirconium (CuCr ₁ Zr)	127
4.5.4	Tantalum (Ta) and Niobium (Nb)	129
4.5.5	Summary and Comparison	132
4.6	Effects of Irradiation Conclusions	136
5	Field Emission Measurements	139
5.1	Introduction	139
5.2	Electrical Setup	140
5.3	Field Emission Measurements and Analysis	144
5.3.1	Normal Field Emission Measurements	144

5.3.2	Field Enhancement Factor Calculations	148
5.3.3	Normal and Reverse Polarity	149
5.3.4	Irradiation Effects on Field Emission	152
5.4	Field Emission Conclusions	154
6	Optical Emission Spectra	155
6.1	Introduction	155
6.2	Optical Setup	157
6.2.1	Spectrometer	160
6.3	Copper OFE Ridged Electrode Tests	163
6.3.1	Spectra Dependence on Alignment of Electrodes	163
6.3.2	Dependence on Observation Angle	167
6.3.3	Measurements of Spectra Variation with Time	169
6.3.4	Correlation of Light with Measured Field Emission Current, Gap Voltage and Power	172
6.4	Large Electrode Tests	174
6.4.1	Copper Based Large Electrode Tests	175
6.4.2	Tantalum and Niobium	177
6.4.3	Aluminium Alloy	183
6.5	Optical Spectroscopy Conclusions	184
7	Current Fluctuations During Conditioning	189
7.1	Introduction	189
7.2	Setup and Measurement Method	191
7.3	Results and Discussion	197
7.4	Mobile Dislocation Interpretation	205
7.5	Current Fluctuations Conclusions	207

<i>CONTENTS</i>	xi
8 Conclusions	209
8.1 Relevance	209
8.2 Summary of Results	210
8.3 Suggestions for Future Work	214
8.3.1 Proposed Conditioning Algorithm	214
8.3.2 Pulse Length Dependence	217
8.3.3 Self Organising Plasma	218
8.3.4 Linac4 RFQ	219
8.3.5 Field Emission	219
8.3.6 Spectroscopy	220
8.3.7 Fluctuations	221
References	223
A CLIASTND0185	243
B CLIASTND0186	245
C CLIASTND0196	247
D CLIASTND097	249
E CLIASTND0149	251
F CLIASTND0138	253
G Upper feed-through	255
H Copper OFE Tests	257
I Copper Chromium Zirconium	261

J Titanium Alloy Tests	263
K Tantalum Tests	265
L Niobium Tests	267
L.1 No BCP	267
L.2 After BCP	268
M Breakdowns within the irradiated area	271
N Pulse Length Dependence Table	275
O Material Hardness Table	277
P Work Function Values Table	279
Q Irradiation Setup	281
Q.1 Changing disk only	281
Q.2 Remove Plate	284
Q.3 Installation of Electrode	284
R Nominal vs. Metrology Gap	287

List of Figures

1.1	CLIC accelerator complex at 3 TeV [1]	2
1.2	CLIC accelerator footprint showing energy stages of 380 GeV, 1.5 TeV and 3 TeV. Proposed to be built between Switzerland and France, close to Geneva.[1]	3
1.3	The accelerator complex for the Large Hadron Collider (LHC) with colour coded names for each segment [3]	5
1.4	Cross section cut-out view of RFQ vanes showing the minimum and maximum distances of the vane surface from the axis [8]	6
1.5	Voltage vs. current diagram showing the different phases of gas discharge [13]	8
1.6	Paschen curve, giving the dependence of the voltage for a breakdown to occur with respect to a function of the pressure and gap distance [13].	13
1.7	Potential relative to the Fermi level for a metal-vacuum interface subject to an external electric field. The position is defined with the interface at zero, with positive values representing the vacuum. In this example, the field is 3 GV/m and the workfunction is 4.7 eV.	16
1.8	Field enhancement factor as a function of aspect ratio for various protrusion shapes [31].	19

- 1.9 Dynamic atomistic model showing the formation of a sharp tip on a tungsten surface when a high electric field is applied [35], starting from a hemispherical asperity as shown on the top left. 21
- 1.10 Saturated electric fields achieved for different materials tested in the tip to plate pulsed DC system, with annotations indicating the crystal structure for each of the materials. The saturated field indicates the electric field after an initial conditioning phase of 20-100 breakdowns [17], [18]. 23
- 1.11 Plots the logarithm of probability density with respect to the number of pulses between breakdowns. The left plot shows data from a CLIC X-band accelerating structure, while the right plot shows data obtained from the LES. In both figures, two distinct linear regimes can be identified, corresponding to primary and secondary breakdowns. [20] 26
- 1.12 Two plots with an x axis being the (log) number of pulses between breakdowns. The y axis of the upper plot shows is the longitudinal distance between breakdowns (units of signal travel time) and the lower plot shows the (log) probability density. [20] 27
- 1.13 (a) Shows a conceptual image of dislocations protruding from the surface causing a field enhancements, leading to field emission, heating and material melting. (b) Shows FIB TEM images of physical dislocations surface protrusions from fatigued Cu specimens. 28
- 1.14 Equilibrium value of dislocation density, ρ^* , and the critical value of dislocation density at which breakdown is initiated, ρ_c vs. applied surface electric field E , according to the MDDF model. [22] 30

1.15 (a) Shows the measured event rate per slip plane λ_0 in s^{-1} vs. surface electric field in MV/m. A threshold E_{th} has been subtracted from the surface field value. Different colours represent different measurement runs [21]. (b) Shows the probability density vs. time interval between successive events in μs . The points represent measured data, the red dashed lines represent the best-fit exponential distribution, and the blue dashed lines represent the best-fit two-parameter hypoexponential distribution [42]	32
1.16 (a) and (b) show TEM images of dislocation slip planes 1 mm away from and on the high field surface area respectively of an RF accelerating structure [39]. (c) shows the correlation between the probability of distances between dislocation slip planes from the near and far samples images given.	33
1.17 Dispersion relation of surface plasmon-polaritons [49].	38
1.18 Absorption spectra caused by localised surface plasmon resonances in nanoparticles of different materials [52].	39
2.1 Conditioning curves for the T24PSI structure, S-band BTW structure and the Cu OFE electrodes in the pulsed DC system [65]–[67]. Where a similar number of pulses is required for the conditioning but due to the difference in repetition rates this takes different amounts of time from 2 months, 4 months and 3.5 days respectively.	44

2.2	(a) Electrodes assembly with (1) being the copper electrodes, (2) a ceramics for setting the gap between the electrodes and (3) isolating the electrodes from the chamber and (b) Pulsed DC Large Electrode System cut-through, showing (4) the perpendicular cameras, (5) and (7) are the upper and lower high voltage feedthroughs respectively, and (6) is the vacuum pump outlet [60].	47
2.3	2 cameras are placed perpendicular to the chamber to view the gap, these are able to determine the breakdown locations in the x and y axis to give coordinates [69].	48
2.4	Shows a flow diagram of the different hardware components and connections displayed as arrows between each.	53
2.5	Capacitance box with ability to change the capacitance to match the pulsed DC system for calibration of the Marx generator and use as a dummy load for testing electronics.	54
2.6	(a) Normal and (b) breakdown pulses measured by an oscilloscope [60]	56
2.7	Images recorded from the (a) x-axis and (b) y-axis cameras respectively for determining the breakdown location.	58
2.8	Camera light intensity for the x and y axis cameras with respect to the voltage with the indication on the distance from the cameras given as blue being the closest to yellow being the furthest away. This shows correlations of an increase in the light with higher voltages and the closer to the camera the breakdown is.	59
2.9	The same data as Figure 2.8 with the x-axis given as the voltage squared giving a linear relationship to the light intensity measured.	60
2.10	Filtered breakdown pressure spike recorded in LabVIEW to observe breakdown timing and pressure within the chamber.	60

- 2.11 Flow diagram showing the relevant steps of the breakdown rate limiting conditioning algorithm, which was designed to replicate the conditioning of the CLIC X-box cavities. 63
- 2.12 Example of conditioning of the pulsed DC system using the breakdown rate limiting algorithm for the CLIC X-band structures. 64
- 2.13 (a) shows the exponential ramp increase from the voltage after a breakdown and (b) is the ramp of the final 10 V over 2000 pulses with a step of 10 V after 100000 pulses. 65
- 2.14 Conditioning plots of various electrodes in the LES [60]. The black plot labelled ‘Hard Cu’ shows an example of a cycle of repeated breakdown clusters, resulting in damage to the surface and a gradual decrease in maximum field. 66
- 2.15 Flow diagram showing the general format of the step-wise conditioning method whilst controlled by the operator, utilising the breakdown rate limiting conditioning algorithm for pulsing during ramps and flat sections using different parameters. 67
- 2.16 Theoretical plot of the electric field vs. the number of pulses for the step-wise conditioning method. Showing the initial ramp in voltage, a series of flat pulses and small ramp increases, then smaller changes in voltage, a cluster in breakdowns leading to a reduction in field, and finally reconditioning. 68
- 2.17 (a) Shows a cut out from the drawing of the CLIASTND0185 electrodes given in Appendix A, showing the cross section of the electrode design, and (b) shows the zoomed view of the details of the edge, where ”NOTE 1” says ”Dimensions which are not visible on the drawing should be extracted from the 3D-model.”. 71

2.18	Physical shape of edges for Euler spiral, Euler spiral approximation, ellipse and a 1 mm radius.	72
2.19	Normalised electric field on the anode for electrodes the same size and with an offset of 0.5 mm to replicate a small anode to large cathode for the different edge shapes, Euler spiral approximation, ellipse and a 1 mm radius.	73
2.20	Physical shape of edge using the Euler equation and approximation equation and the difference in height for each value of x	74
2.21	Breakdown clusters on the edge of half of the electrode [81]	75
2.22	Misalignment of electrodes causing electric field enhancements on the Anode and Cathode on different sides	76
2.23	Edge electric field on the inner and outer edges of electrodes for different steps in the misalignment	78
3.1	Shows the conditioning of the TiAl_6V_4 where, (a) gives the electric field in red and the breakdown count in green and (b) shows the breakdown locations detected by the camera with the first to the last breakdown indicated with colours dark blue through to dark red.	83
3.2	(a) Conditioning of CuCr_1Zr with boxes to highlight the initial ramp, small ramps where breakdowns occurred after a number of steps, ramps with breakdowns throughout, small clusters in breakdowns, additional ramps without issues after clusters, and a large cluster with a recovery process used. (b) Shows the breakdown locations with dark blue to dark red indication the first to last breakdown respectively.	84

- 3.3 Shows the conditioning of the Nb BCP pair where, (a) gives the electric field in red and the breakdown count in green and (b) shows the breakdown locations detected by the camera with the first to the last breakdown indicated with colours dark blue through to dark red. 86
- 3.4 Nb pair electric field reductions to find a stable electric field with reduced clustering. 87
- 3.5 Shows the conditioning of the Cu OFE pair, where, (a) gives the electric field in red and the breakdown count in green and (b) shows the breakdown locations detected by the camera with the first to the last breakdown indicated with colours dark blue through to dark red. 88
- 3.6 Shows the conditioning of the Ta pair, where the electric field is given in red and the breakdown count in green. No breakdown locations are given due to the ceramic used not having holes to allow for camera observations. 89
- 3.7 Shows the conditioning of the AlMgSi1 pair, where, (a) gives the electric field in red and the breakdown count in green and (b) shows the breakdown locations detected by the camera with the first to the last breakdown indicated with colours dark blue through to dark red. 90
- 3.8 Shows the conditioning of the Nb pair, where the electric field is given in red and the breakdown count in green. 91
- 3.9 Image taken with a camera, of what appears to be damage from a number of breakdowns in the centre of the electrodes. 92
- 3.10 Summary bar chart of the final stable electric field of all materials tested. 94

3.11 (a) and (b) show the breakdown cluster events from TiAl_6V_4 and AlMgSi_1 electrode pair conditioning, leading to a decrease in the electric field. This shows a brief increase in the number of breakdowns for TiAl_6V_4 , that was recoverable. Where as for AlMgSi_1 , there is a continuous increase in breakdowns causing a large unrecoverable decrease in the electric field holding capabilities.	95
3.12 Relevant materials from the previous study of conditioning capabilities of different materials [17]	96
3.13 (a) Final stable electric field for each material shown in blue, and the breakdown rate at that field shown in red. (b) Electric field normalised to a reference breakdown rate of 1×10^{-6} , using the electric fields and breakdown rates given in (a) and Equation [3.1].	99
3.14 Puled DC system results of pulse length dependence studies for different materials, giving the breakdown rate at $100 \mu\text{s}$, $250 \mu\text{s}$, $500 \mu\text{s}$, and 1 ms with standard error bars as described in Equation [2.5]	101
3.15 Puled DC system, pulse length dependence test between $1 \mu\text{s}$ and $200 \mu\text{s}$. Blue is the electric field applied for eah pulse, red is the number of breakdowns with the slope indicating the breakdown rate and green shows the pulse length. Showing a decrease in the achievable field with the longer pulse length due to the higher breakdown rates.	102
3.16 Possible contamination transfer, creating mirror image from one electrode to the other during high-field testing.	103
3.17 Cathode and Anode images of CuCr_1Zr after conditioning with a flower pattern that is central to the cathode and mirrored on the anode with the image flipped [89].	104

4.1	(a) Image of the Linac4 RFQ and (b) endoscopy image of the vane damage after operation [10].	108
4.2	Flow diagram for the procedure for each material tested with the blue lines showing the steps for a non-irradiated pair and orange for the irradiated pair. Additionally the dotted lines indicate the extra step of heat treatment for the Cu OFE electrode pairs.	109
4.3	Cathode irradiation setup with a chamber attached to the output of the source and LEBT holding the electrode a set distance of 15 mm from the beam pipe outlet [9].	111
4.4	Images of each of the irradiated and tested cathodes.	113
4.5	Carbon layer observed using FIB analysis of a Cu sample [94].	114
4.6	Images of the melted CuCr_1Zr electrodes after irradiation, taken with a (a) camera and (b) microscope respectively [95].	115
4.7	Blister on the Cu OFE electrodes after irradiation, taken with (a) an optical microscope, (b) and (c) with a scanning electron microscope [96].	116
4.8	Cross section of a blister in Cu OFE with an irradiation dosage of $1.2 \times 10^{19} \text{ p/cm}^2$	117
4.9	(a) As shown previously in Figure 2.3, and (b) Showing the placement of the irradiated Cu samples with the cameras in order to determine breakdown locations with respect to the irradiated and blistered areas during testing.	118
4.10	(a) Electric field calculated using Eq[1.8] and (b) Normalised electric field using Eq[4.1] [60]	120

- 4.11 TiAl₆V₄ (a) conditioning of the irradiated and non-irradiated pairs and (b) the breakdown locations of the irradiated cathode with the breakdown number given from dark blue being the first to dark red being the last. The green circle indicates the diameter of the high field area, determined the the anode. 123
- 4.12 Cu OFE (a) conditioning of the irradiated and non-irradiated pairs and (b) the breakdown locations of the irradiated cathode with the breakdown number given from dark blue being the first to dark red being the last. 125
- 4.13 SEM images of the breakdowns over the blistered area from irradiation and the the splash and melting of blisters surrounding a crater [104] 126
- 4.14 CuCr₁Zr (a) conditioning of the irradiated and non-irradiated pairs and (b) the breakdown locations of the irradiated cathode with the breakdown number given from dark blue being the first to dark red being the last. 128
- 4.15 Large cluster of breakdowns around 2mm in length, and located within the irradiation halo area. This image was taken with a digital camera meaning an accurate scale cannot be provided. 128
- 4.16 Ta, Nb and Nb BCP (a) conditioning of the irradiated and non-irradiated pairs and (b) the breakdown locations of the irradiated cathode with the breakdown number given from dark blue being the first to dark red being the last. 130
- 4.17 Summary bar chart of the maximum and stable fields of both the irradiated and non-irradiated materials tested using the same conditioning parameters. 132

4.18	Bar chart of the calculated normalised field holding values for the L4 RFQ and all pairs of electrodes tested and the L4 RFQ, using the stable electric field values and Equation [4.1].	135
5.1	(a) Upper and Lower feedthrough to LES 3. (b) Schematic representation of connecting to only one feedthrough with possible oxide contamination. (c) Schematic representation of connecting to two feedthroughs with possible oxide contamination.	141
5.2	Field emission current measurements with the increase given using different symbols for each materials and the decrease given as a dash of the same colour. Voltages achieved during pulsed conditioning are given as dashed vertical lines with corresponding colours.	145
5.3	Gap voltage during field emission measurements as described in Equation 5.1, compared to the final stable and maximum electric fields achieved during pulsed conditioning.	145
5.4	Maximum field emission currents verses the gap voltage during the field emission measurements and the maximum and stable fields during pulsed conditioning.	147
5.5	FN plots for each of the materials, with γ determined as the gradient of the slope and the calculated β indicating the field enhancement factor, with E denoting electric field in MV/m and I denoting current in A.	148
5.6	Maximum gap voltage and field emission current with respect to β during the field emission measurements for the different materials.	149
5.7	Measurements of field emission current with respect to the gap voltage made in the normal and reverse polarity from a previous study using Cu OFE electrodes [60].	150

5.8	Normal (N) and reverse (R) polarity field emission current measurements of different materials tested.	151
5.9	Field emission current measurements for the non-irradiated and irradiated pairs of the different materials tested.	152
6.1	Images of the (a) crossed and (b) parallel alignments of the ridged electrodes	158
6.2	Plots of the electric field on the surface of the electrodes for the (a) crossed and (b) parallel alignments. Where the x and y labelled axis give the surface dimensions and the electric field is given from the other axis and the colour representation.	159
6.3	Microscopy images of the anode and cathode high-electric-field surfaces respectively after testing in both alignments.	159
6.4	Diagram of the collimator aligned with one of the chamber windows, to view the electrode high electric field gap, without the light shielding applied.	161
6.5	Plots of wavelength attenuation for the a) UV-VIS [112] and b)VIS-NIR [113] optical fibres	161
6.6	Layout inside of the spectrograph with white light entering at the input and diffracted by the one of the three grating represented by the triangle, with mirrors to change the direction of the light. . . .	162
6.7	Diffracted light is captured by the different pixels of the CCD camera corresponding to a wavelength and is used to generate a corresponding graph of the light intensity are different wavelengths.	163

- 6.8 Field emission spectroscopy measurements at different supply voltages during 2 individual tests with the parallel electrode alignment. From this a broad band light between 550 nm and 750 nm can be seen with an increase with supply voltage. 164
- 6.9 Field emission spectrum measurement at different supply voltages during 2 individual tests with the crossed electrode alignment with observations of a variation in the spectrum between 700 nm and 850 nm. 165
- 6.10 Counts at a single wavelength (WL) around the peak of each measurement from Figures 6.9 and 6.8 and the current (Cur) for different supply voltages for each of the crossed and parallel examples given 166
- 6.11 Spectra measurements from each perpendicular angle and both polarities. (a) Conditioning polarity transverse anode, (b) Reverse polarity longitudinal anode, (c) Conditioning polarity longitudinal anode, (d) Reverse polarity transverse anode with noise removed in post processing. 168
- 6.12 Spectra measurements from each perpendicular angle and both polarities at their maximum supplied voltages. This shows the correlation in the light intensity at the 700 nm wavelength for the different polarities, with the change in wavelengths being below 700 nm. 169
- 6.13 Spectrum taken every 30 s with a 7 kV supply voltage applied with the colours indicating the order of the measurements. It is observed that there are variations of the spectra with time between 700 nm and 850 nm. 170

- 6.14 Value of total light intensity, current measured with respect to time where a measurement is taken every 30 s and the ratio (current/total light intensity). Total light intensity is the number of counts at each wavelength summed together for each spectrum. 171
- 6.15 Normalised light intensity at different wavelengths and current with respect to time with measurement taken every 30 s. The values are normalised to the minimum and maximum values ranging between 0 and 1. 172
- 6.16 Field emission current, total light intensity counts, and counts of light intensity at different wavelengths with respect to the gap voltage. 173
- 6.17 Total light intensity counts, counts of light intensity at different wavelengths and gap power with respect to the field emission current. 173
- 6.18 (a) Cu OFE and (b) CuCr₁Zr optical spectra during field emission current measurement, using large high-field area electrode tested and discussed in Chapter 3.6. Showing a similar broad band light measurement with a increase in light intensity with supply voltage. 175
- 6.19 Plots of field emission current, light intensity at a specific wavelength and the total light intensity with respect to voltage for (a) Cu OFE and (b) CuCr₁Zr. Showing an exponential increase in the field emission current and light measured. 176
- 6.20 Light intensity at specific wavelengths and total light intensity at different supply voltages with respect to the field emission current. Showing a linear relationship between the light intensity detected and the field emission current measured. The spikes that can be seen are the result of cosmic-rays hitting the CCD. 177

- 6.21 Optical spectra during field emission measurements for irradiated samples of (a) Ta and (b) Nb BCP as discussed in Chapter 4.6. Colours from dark blue to dark red show the measurements from the first to the last respectively with only increases in the supply voltage applied. The sharp peaks in (a) are believed to be caused by cosmic rays striking the sensor. Details of the measured field emission current can be found in Figure 6.23 178
- 6.22 Normalised comparison of the black body radiation curve for a temperature of 3450K and a measured spectrum from the Nb electrodes. This shows a narrower spectrum from the Nb electrodes, suggesting the light detected is not the result of black body radiation. 179
- 6.23 Correlation between field emission current, light intensity measured from the perpendicular cameras and spectrometer, and pressure from breakdowns with respect to time. This shows the gradual increase and decrease of the field emission current with time due to step increases in the supply voltage, and a period in which light is detected and stops after a pressure spike as the result of a breakdown. 181
- 6.24 Light emission locations during the field emission measurements with the majority of locations being breakdowns, and one location being the source of the field emission light with no breakdown. . . . 182
- 7.1 Block diagram of the setup for field emission current fluctuation during tests in the pulsed DC system [42]. 192
- 7.2 Oscilloscope measurement of a single current fluctuation from the output of the bias-tee using a sample rate of 500 MHz. This shows an oscillation after the initial spike in the voltage measured, which is proportional to the change in current [21]. 193

- 7.3 Hypothetical example of (a) the random walk of current that occurs
(b) and how this would be seen after filtering. 194
- 7.4 Oscilloscope measurement of a single pulse, showing the voltage,
supply current and bias-tee output measuring current fluctuations
with an amount of transients at the beginning of the pulse. 195
- 7.5 Three different fluctuation measurements for different pulses, count-
ing between 0 and 2 fluctuations per pulse. Blue vertical lines
indicate the window in which the results are analysed and a
horizontal purple line indicating the threshold over the noise to
count the fluctuations. 196
- 7.6 Plot showing the breakdown number, electric field, (a) positive and
(b) negative fluctuation counts per pulse, and the average number
positive and negative fluctuations per pulse. This shows a gradual
increase in the number of fluctuations per pulse when the electric
field stops increasing. 198
- 7.7 Plot showing the breakdown number, electric field, (a) positive and
(b) negative fluctuation counts per pulse, and the average number
positive and negative fluctuations per pulse. Showing an increase
during a higher breakdown rate and decrease after (green box), and
an increase before a breakdown and decrease after (blue box). . . . 199
- 7.8 Plot showing the breakdown number, electric field, (a) positive and
(b) negative fluctuation counts per pulse, and the average number
positive and negative fluctuations per pulse. A relatively large
increase and decrease in the fluctuations per pulse can be seen
between consecutive breakdowns (orange box). Also seen are breakdowns
that lead to an increase or decrease in the number of fluctuations
per pulse, indicated by blue arrows. 200

7.9	Plot showing the breakdown number, electric field, (a) positive and (b) negative fluctuation counts per pulse, and the average number positive and negative fluctuations per pulse. Showing 3 time intervals with a relatively large amount of time between consecutive breakdowns where the number of fluctuations per pulse increases compared to the surrounding pulses (3 blue boxes).	201
7.10	Plot showing the breakdown number, electric field, (a) positive and (b) negative fluctuation counts per pulse, and the average number positive and negative fluctuations per pulse. Showing relatively stable running and low fluctuation rate before the red line in the direction of the blue arrow and a deconditioning of the electrodes with an increased fluctuation rate in the direction of the red arrow.	202
7.11	Oscilloscope measurement of many current fluctuation during a singular high voltage pulse.	203
8.1	Flow diagram integrating the breakdown rate limiting conditioning algorithm with a higher level of control that more qualitatively makes the decisions of the user during the conditioning of the various materials shown.	215
8.2	Small clusters in breakdowns taken from the CuCr ₁ Zr conditioning shown in Chapter 3.6.	216
8.3	Large cluster in breakdown leading to a significant decrease in the electric field and the following reconditioning, taken from the TiAl ₆ V ₄ conditioning shown in Chapter 3.6.	217
H.1	Conditioning plots of both Irradiated and non-irradiated Copper OFE, showing the electric field and number of breakdowns on the respective axes.	257

H.2	Breakdown locations measured during testing of electrode pair 40. a) shows the breakdown locations over time relative to the scale to the right of the image, b) shows the number of breakdowns per square mm	258
H.3	Breakdown locations measured during testing of electrode pair 42. a) shows the breakdown locations over time relative to the scale to the right of the image, b) shows the number of breakdowns per square mm	258
H.4	Breakdown locations measured during testing of electrode pair 45. a) shows the breakdown locations over time relative to the scale to the right of the image, b) shows the number of breakdowns per square mm	259
I.1	Conditioning plots of both Irradiated and non-irradiated Copper Chromium Zirconium, showing the electric field and number of breakdowns on the respective axes.	261
I.2	Breakdown locations measured during testing of electrode pair 50. a) shows the breakdown locations over time relative to the scale to the right of the image, b) shows the number of breakdowns per square mm	262
J.1	Conditioning plots of both Irradiated and non-irradiated Titanium Alloy (TiAl6V4), showing the electric field and number of break- downs on the respective axes.	263
J.2	Breakdown locations measured during testing of electrode pair 46. a) shows the breakdown locations over time relative to the scale to the right of the image, b) shows the number of breakdowns per square mm	264

J.3	Breakdown locations measured during testing of electrode pair 47. a) shows the breakdown locations over time relative to the scale to the right of the image, b) shows the number of breakdowns per square mm	264
K.1	Conditioning plots of both Irradiated and non-irradiated Tantalum, showing the electric field and number of breakdowns on the respective axes.	265
K.2	Breakdown locations measured during testing of electrode pair 55. a) shows the breakdown locations over time relative to the scale to the right of the image, b) shows the number of breakdowns per square mm	266
L.1	Conditioning plots of both Irradiated and non-irradiated Niobium, showing the electric field and number of breakdowns on the respective axes.	267
L.2	Breakdown locations measured during testing of electrode pair 43. a) shows the breakdown locations over time relative to the scale to the right of the image, b) shows the number of breakdowns per square mm	268
L.3	Breakdown locations measured during testing of electrode pair 44. a) shows the breakdown locations over time relative to the scale to the right of the image, b) shows the number of breakdowns per square mm	268
L.4	Conditioning plots of both Irradiated and non-irradiated BCP Niobium, showing the electric field and number of breakdowns on the respective axes.	269

L.5	Breakdown locations measured during testing of electrode pair 54. a) shows the breakdown locations over time relative to the scale to the right of the image, b) shows the number of breakdowns per square mm	269
L.6	Breakdown locations measured during testing of electrode pair 56. a) shows the breakdown locations over time relative to the scale to the right of the image, b) shows the number of breakdowns per square mm	270
M.1	Shows the normalised number breakdown per square mm, inside and outside the irradiated, over all the surface, and not detected by the cameras, for the TiAl_6V_4 electrodes.	271
M.2	Shows the normalised number breakdown per square mm, inside and outside the irradiated, over all the surface, and not detected by the cameras, for the Cu OFE electrodes.	272
M.3	Shows the normalised number breakdown per square mm, inside and outside the irradiated, over all the surface, and not detected by the cameras, for the CuCr_1Zr electrodes.	272
M.4	Shows the normalised number breakdown per square mm, inside and outside the irradiated, over all the surface, and not detected by the cameras, for the Ta electrodes.	273
M.5	Shows the normalised number breakdown per square mm, inside and outside the irradiated, over all the surface, and not detected by the cameras, for the Nb electrodes.	273
M.6	Shows the normalised number breakdown per square mm, inside and outside the irradiated, over all the surface, and not detected by the cameras, for the Nb BCP electrodes.	274

Q.1 Sample disk irradiation setup assembly drawing. 282

Q.2 Images of disk attached with the irradiated chaber from (a) above
and (b) the side to highlight the wire to ground. 283

Q.3 (a) Image of an electrode upside down on a ceramic to avoid dam-
aging the surface during assembly, and (b) showing the electrode
installed in the irradiation assembly. 285

List of Tables

2.1	Normalised electric field enhancement for the range of misalignments as shown in Figure 2.23	79
4.1	Table of the irradiation parameters for each of the materials tested.	111
4.2	Summary table of Irradiated and non irradiated conditioning	133
4.3	Absolute and normalised number of breakdowns inside and outside of the irradiated beam pipe halo area, compared with the total number and breakdowns not detected by the cameras.	134
5.1	Maximum gap voltage and field emission current for both normal and reverse polarity of the different materials as seen in Figure 5.8, and the difference between them.	151
5.2	Maximum gap voltage and field emission current for both irradiated and non-irradiated pairs of the different materials as seen in Figure 5.9, and the difference between them.	153
6.1	Table of the properties seen in the spectra throughout tests versus the possible causes. Squares are coloured based on whether the properties, align with (green), may align with (orange), rule out (red), or unknown (white) with respect to each of the possible causes.	185

- N.1 Table showing the number of pulses and breakdowns used for each pulse length for each material used to determine the breakdown rate and standard error for the value given in Figure 3.14. 275
- O.1 Table of the hardness values using different methods for the materials tested, where hardness is given for individual materials and not the alloys as tested. [84] 277
- P.1 Table of the work function values for different elements, given for individual materials and not the alloys as tested. [24]–[26] 279
- R.1 Electric fields for the calculated gap using the metrology reports for each electrode and the given results using the 60 μm nominal gap . 288

Chapter 1

Introduction

1.1 High Field Accelerators

There are two different high field linear accelerators (LINACs) that have had have been linked to the following studies, these include the CERN Compact Linear Collider (CLIC) and Large Hadron Collider (LHC) Linac 4 (L4). For this reason, details of the background to each of these accelerators is given.

1.1.1 CERN Compact Linear Collider

The Compact Linear Collider (CLIC) is a linear electron-positron collider project proposed by the European Council for Nuclear Research (CERN) [1], [2]. The particle physics community is interested in an electron - positron collider for precision measurements of Higgs and search for new particles. Use of lighter particles allows for more accurate calculations of the energy and momentum, as well as cleaner collisions. Figure 1.1 shows the setup of the accelerator with the positrons and electrons being accelerated in opposite direction towards each other, with the collision occurring in the centre.

A TeV circular e^-/e^+ collider machine is less practical as a result of synchrotron

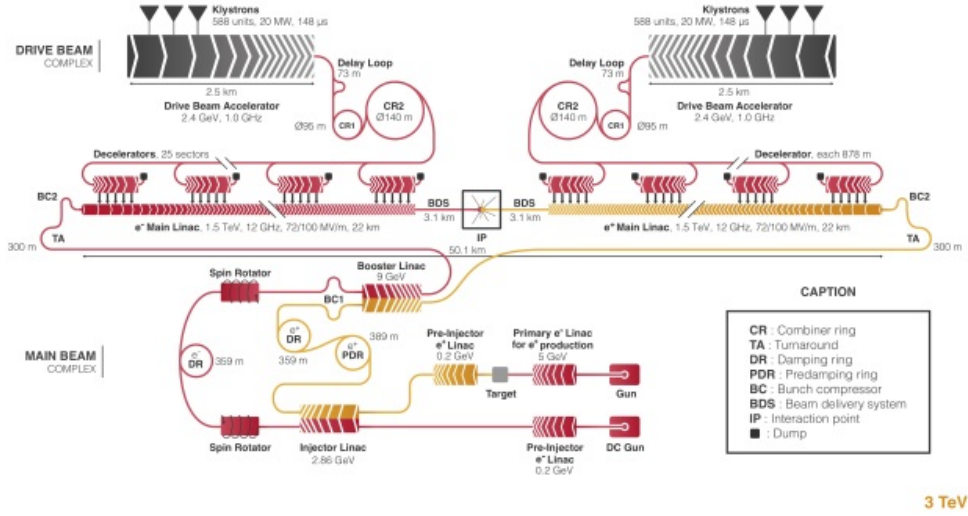


Figure 1.1: CLIC accelerator complex at 3 TeV [1]

losses that would occur [1]. Synchrotron losses are radiated energy particles lost when the beam turns, and is given as:

$$P_{loss} \propto \frac{E^4}{m_0^4 \rho^2} \quad (1.1)$$

Where, P_{loss} = power lost, E = particle energy, m_0 = particle rest mass, and ρ = bending radius. The rest masses of electrons and protons are 511 keV and 938 MeV, respectively [3]. From Equation [1.1] it can be seen that the heavier the particles accelerated, the lower the synchrotron radiation power emitted, which increases efficiency. For this reason a linear collider is used to avoid bending high-energy beams.

One advantage of linear accelerators is the ability to extend them to reach higher energies over time [1]. For CLIC the plan is to first achieve 380 GeV, then 1.5 TeV, and a final stage planned with energies of 3 TeV, with lengths of 11 km, 29 km and 50.1 km respectively, as seen in Figure 1.2. The final parameters for CLIC include a length of 50 km with an energy of 3 TeV. To achieve this high

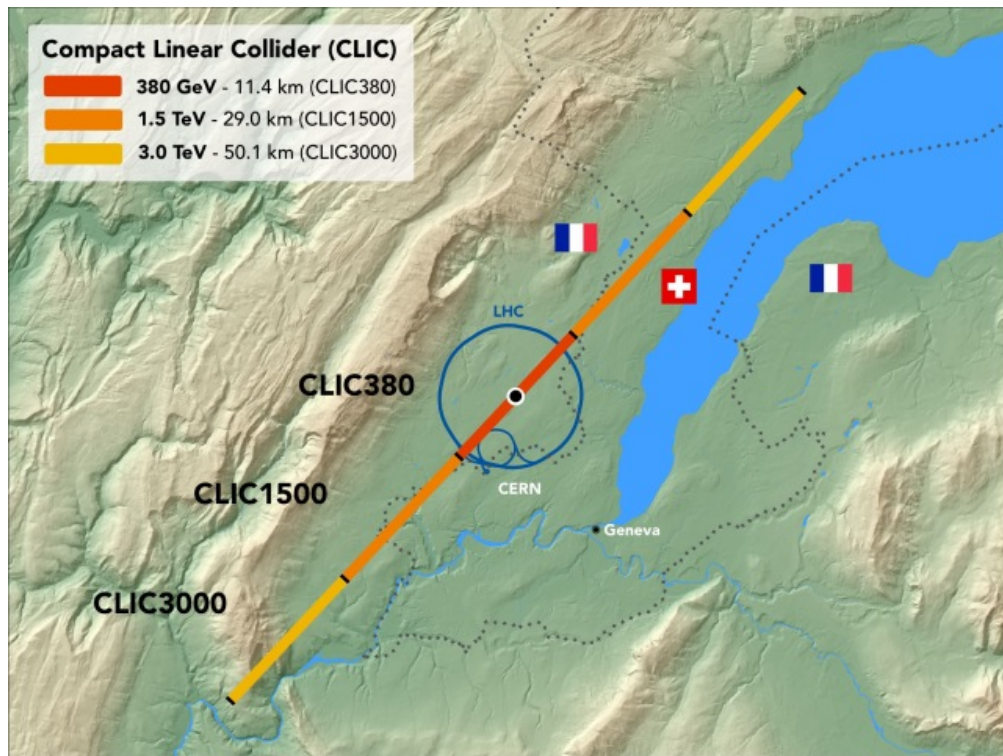


Figure 1.2: CLIC accelerator footprint showing energy stages of 380 GeV, 1.5 TeV and 3 TeV. Proposed to be built between Switzerland and France, close to Geneva.[1]

energy a high accelerating gradient would be required in order to contain it within a reasonable length. The accelerating gradient required to meet the parameters given is 100 MV/m, this accelerating gradient would require peak surface field within the cavities up to 230 MV/m [4].

High electric fields in vacuum machines, lead to a phenomenon called vacuum breakdown which is one of the main limiting factors of the CLIC accelerator [5]. Breakdowns decrease the luminosity of the accelerator, as when a breakdown happens the magnetic field from the arc kicks on of the beams transversely, causing the beams not to collide. To have a level of control over the number of breakdowns, the structures are conditioned to a specified breakdown rate. For CLIC this was decided as a maximum of 1 breakdown anywhere along the linac per 100 pulses, therefore the $BDR \leq 3 \times 10^{-7}$ BD/pulse/m. Additionally to reduce the likelihood

of breakdowns, a total pulse length of 242 ns would be used [4], this is in accordance with a study of the effect of pulse length on the breakdown rate [6], giving a dependence of:

$$BDR \propto \tau^5, \quad (1.2)$$

where BDR = Breakdown rate and τ = pulse length. This shows that the smaller the pulse length used, the lower the breakdown rate which means higher fields can be achieved.

1.1.2 Radio Frequency Quadrupole

The Large Hadron Collider (LHC) is the largest and most powerful particle accelerator at the time of this report [3]. It is a circular collider and has a circumference of 27 km, that consists of many superconducting magnets to control the beam. As mentioned in the section on the CLIC project as this is a circular collider the particles that are used are protons and ions. For the context of this thesis only the initial stage of the proton acceleration will be covered. There are several accelerating stage machines that are used to get the beam to the energy required for the LHC. In the case of the LHC the protons used are H^+ , these consist of Hydrogen atoms that have been stripped of their electrons.

Figure 1.3 shows the whole LHC accelerator complex with the different injection points and storage rings for increasing the beam energy to different level [3]. The first stage is Linac4 (L4) that accelerates the beam from a H^- source, from 45 keV to an energy of 160 MeV. A charge-exchange injection scheme is used to combine the H^- ions with the H^+ beams already in the Proton Synchrotron Booster (PSB) [7]. This is done by passing the H^- ions through a stripping foil to convert them into protons, which can then be merged with minimal losses with the beam that is already circulating within the PSB. The PSB accelerates the beam to energies

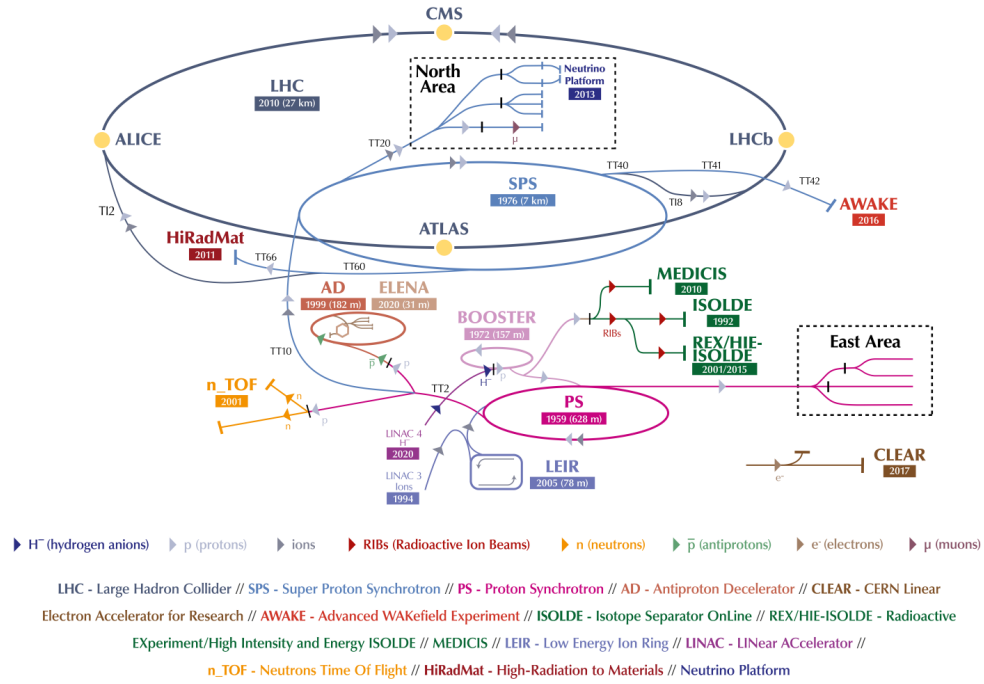


Figure 1.3: The accelerator complex for the Large Hadron Collider (LHC) with colour coded names for each segment [3]

of 2 GeV, with a radius of 157 m in circumference [3]. The PSB feeds the beam into the Proton Synchrotron (PS) that accelerates the beam to an energy of 26 GeV with a circumference of 628 m that then feeds into the Super Proton Synchrotron (SPS) to accelerate to 450 GeV with a circumference of 70 km. After the SPS the beam is injected in opposite directions around the two beam pipes of the LHC where there are 4 different collision points for different experiments.

The initial stages of L4 are the H^- source feeding into a Low-Energy Beam-Transport (LEBT) used for steering the beam. Then several accelerating stages with the first being a Radio Frequency Quadrupole (RFQ) that accelerates to 3 MeV, then drift tube linacs (DTLs) accelerating to 50 MeV, then coupled cavity drift tubes (CCDTLs) to reach 100 MeV, and finally Pi mode structures (PIMS) to achieve an energy of 160 MeV.

An RFQ is a form of linear accelerator that focuses, bunches and accelerates a

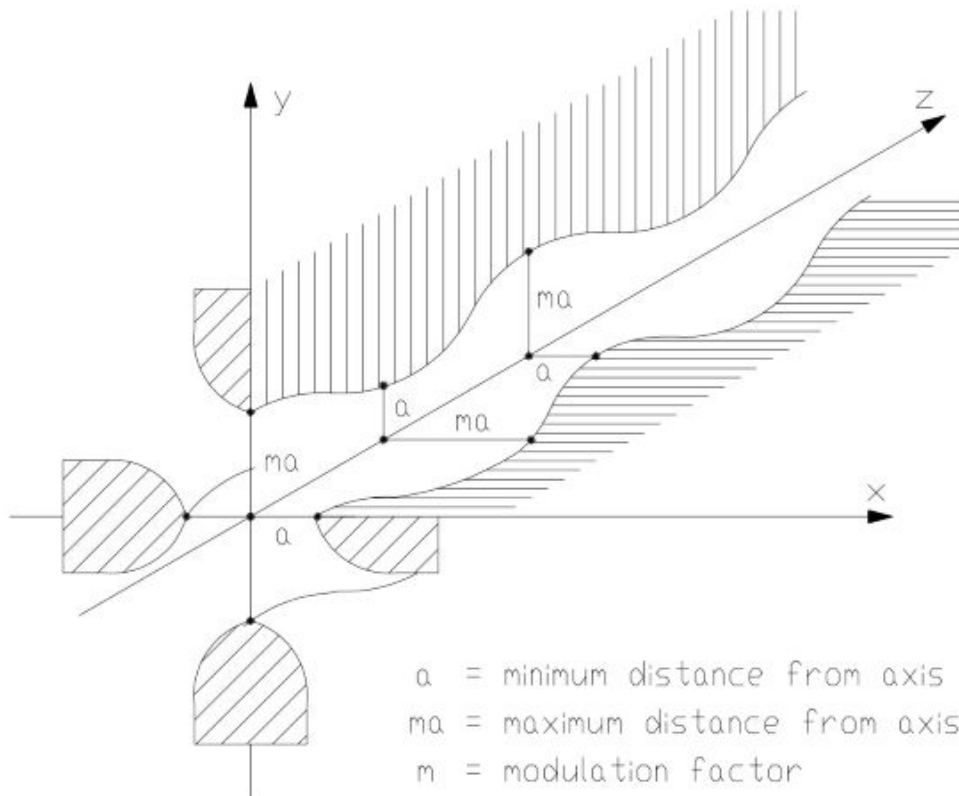


Figure 1.4: Cross section cut-out view of RFQ vanes showing the minimum and maximum distances of the vane surface from the axis [8]

continuous beam of charged particles, providing low emittance increase, low beam loss, and high power efficiency [8]. Figure 1.4 shows a cross section diagram of an RFQ, from this the 4 electrode vanes can be seen where the beam dynamics for the RFQ are determined by the geometrical parameter of the vanes. Where focusing strength and acceptance of the beam are determined by the aperture, the electric field for acceleration is determined by the depth of modulation, and the synchronicity of between the particles and the field is determined by the distance between the vane peaks and troughs.

The RFQ of L4 has an inter-vane peak surface electric field of 34 MV/m to accelerate the beam to the energy of 3 MeV, which is sufficient to have caused breakdowns to occur [9]. Originally when a breakdown occurred there was

no implementation to detect the breakdown itself, therefore it did not respond appropriately, and instead supplied additional power to the RFQ maintaining the arc [10]. This led to interventions to fix this, and to also investigate the cause of breakdowns within the RFQ. An endoscopy was done of the RFQ and damage was found in the form of blisters on the surface and breakdown craters. The blisters were most likely the result of irradiation from the beam loss which contained H^- , H neutral and electrons as a result of H^- being a relatively unstable ion. The increased breakdown rate influences the beam and the damage to vanes has caused degradation over time. This in turn reduces the achievable electric field holding capacities of the structure.

1.2 What is Electrical Breakdown

Electrical breakdown is when current flows through an insulator or gas between two electrodes with an applied electrical potential difference. The higher the potential between the two electrodes the higher the probability that the insulator will become conductive. Breakdown can occur with different types of insulator whether they are solid, liquid or a gas but breakdown should not be possible in a vacuum. For breakdown to occur there must be a path of free electrons, making the insulator conductive allowing current to flow between the two potentials [11]. The type of breakdown to be explained is 'gas breakdown', as a gas becomes conductive when ionised, which requires energy input. A voltage potential between plates gives an electric field, where the greater the potential difference, the higher the amount of ionisation that occurs. The breakdown voltage is the voltage potential at which the insulator begins to conduct. For a gas, this depends on the species, pressure and temperature, gap distance, and voltage potential.

Particle accelerators operate with a vacuum in order to avoid the beam colliding

with gas, despite the ultra high vacuum breakdowns occurred, commonly known as ‘vacuum breakdowns’ [12]. In principle, breakdowns should not occur in a vacuum as there should be no gas to ionise to generate an electrical connection. Therefore, for there to be a breakdown in a vacuum there must be a source of gas, this then becomes a gas breakdown. The process that leads to gas being introduced into the system is not completely understood but the most prominent theories will be discussed in more detail.

1.3 Gas Breakdown Process

1.3.1 Initial Breakdown

The first stage that leads to a fully-developed breakdown is background ionisation, which is when the first few gas particles become ionised [13]. This can occur naturally and on its own is not enough to cause a breakdown as there are insufficient free electrons. Background ionisation is relatively low and occurs at a steady rate. Causes of this type of ionisation could be the result of a small amount of energy transferred to particles causing the electrons to become excited, increasing

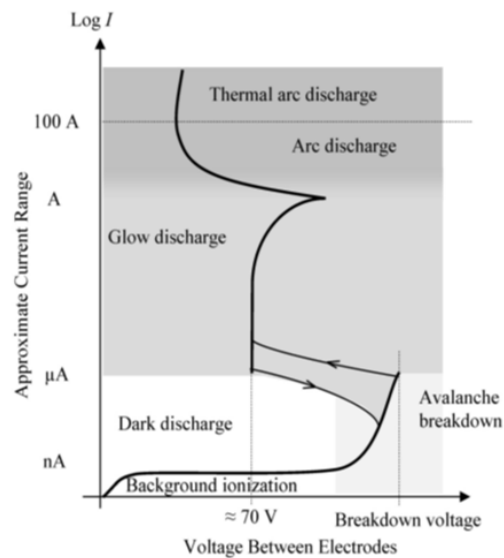


Figure 1.5: Voltage vs. current diagram showing the different phases of gas discharge [13]

the likelihood of emitting electrons. Figure 1.5 displays the voltage vs current curve for an electrical breakdown. From this it can be seen that for a small voltage the

current increases to the nA range and saturates. As the voltage increases the current remains constant until the critical point at which avalanche breakdown occurs.

When an electrical potential is applied, an electric field is developed that leads to increase in ionisation within the gas. Electrons that escape are then accelerated towards the anode and will collide with other particles. Depending on several factors including the ionisation energy of the gas species the energy of the free electron, the collisions may cause more ionisation and thus a larger population of free electrons.

At high voltages when the electrons start to escape and collide with other particles, the increased voltage causes an increase in energy and speed of the electron [13]. As the energy of the electrons increases, the probability that a collision results in the emission of more electrons also increases. This generates an avalanche effect and the number of free electrons increases rapidly, which is called an avalanche or Townsend breakdown, named after John Townsend who mathematically described the process of an avalanche breakdown. Townsend's description begins from the differential equation [13]:

$$dn_x = n_x \alpha dx, \quad (1.3)$$

where x is the position along an axis perpendicular to two electrodes, n_x is the number of free electrons at position x , and α is the primary ionisation coefficient (number of secondary electrons produced per primary electron per unit length). This differential equation has the solution:

$$n_x = n_0 e^{\alpha x}, \quad (1.4)$$

where $n_0 = n_x$, when $x = 0$. The solution shown in Equation [1.4] of the

primary ionisation equation shows that the number of free electrons increases exponentially with distance.

Townsend primary ionisation only considers the impact of electrons on the ionisation of the gas. For this reason, he also introduced a secondary ionisation coefficient to determine ionisation caused by ion impact (positive ions within the gas colliding with neutral atoms and the electrode causing further ionisation), as well as other ionisation mechanisms such as photoionisation. The Townsend secondary ionisation coefficient γ is the number of electrons generated through secondary mechanisms per electron produced in the primary avalanche. It can be expressed as:

$$\gamma = \gamma_p + \gamma_m + \gamma_{ion}, \quad (1.5)$$

where γ is the the total number of electrons produced by secondary emission processes, and γ_p , γ_m , γ_{ion} are the respective contributions from photons, metastable particles, and ions respectively.

The current is given by Equation [1.6], assuming all the free electrons reach the anode:

$$I = \frac{I_0 e^{\alpha d}}{1 - \gamma(e^{\alpha d} - 1)}, \quad (1.6)$$

where I_0 is the initial seed current produced by an external process, and I is the total current. Under this model, the condition:

$$\gamma(e^{\alpha d} - 1) = 1 \quad (1.7)$$

implies infinite current. Practically, this represents the breakdown becoming self-sustaining, due to secondary ionisation processes producing sufficient seed

current for the primary ionisation process. The gas quickly becomes a plasma with the majority of the gas particles becoming ionised.

1.3.2 Discharge

Glow discharge is the phase in which the plasma emits a large number of photons [13]. The reason for this is excited electrons return to their lowest energy state. Also, the free electrons may recombine with positive ions causing the release of more energy as light. When a glow discharge is occurring the flow of ions accelerated between the plates, hit the cathode which causes further electrons to be emitted. This continues repeatedly with each impact, causing further electrons to be emitted, and this glow discharge phase is therefore considered as self-sustaining. As the glow discharge is self-sustaining with a high current, the voltage across the electrodes decreases.

This continues until a plasma sheath is generated that covers the surface of the cathode. A cathode plasma sheath is a positively-charged plasma that screens the negative charge of the cathode, creating a barrier. This causes a drop in the voltage across the sheath, at which point the current stops increasing; to further increase the current density, the external applied voltage needs to be increased. The current density is constant and therefore the total current is dependent on the spot size of the field emission area [14]. For there to be an increase in current emitter the surface area of field emitters must increase, this can be the singular spot increase or several field emitters emerging on the surface.

The next stage that occurs is arc discharge. This is when an arc occurs between a voltage potential gap and in general it is destructive causing damages the surfaces leaving craters of melted material. This can occur if the power supplied is high enough and the supply is capable of supplying enough current for an arc. An arc

occurs straight after a high voltage breakdown when there is very little resistance leading to a high current flow that is determined by the current capabilities of the supply. The main difference between glow and arc discharge is that for arc discharge there is an increase in electrons emitted due to thermal emission as well as field emission.

As the arcs are powered by the supply to the system, the systems can be powered down to extinguish the arc. Arcs that can be initiated and driven by the power from the external supply will most likely have a very fast increase from virtually no current to an arc with no time for the glow discharge to occur. This is likely to be the case within high gradient accelerators due to the high powers used, therefore the glow discharge cannot be used to predict breakdowns.

1.3.3 Paschen Curve

The Paschen curve describes the relationship between the breakdown voltage of a gas and the product of pressure and distance between the electrodes [13]. From Figure 1.6 it can be seen that, except for very low pressures, the breakdown voltage increases with an increase in pressure and/or distance between the electrodes. A Paschen curve can be used to determine the pressures and voltage for initiating or reducing the likelihood of breakdowns.

At pressures approaching absolute vacuum the breakdown voltage tends towards infinity as breakdown cannot occur without gas molecules [13]. The reason the voltage tends towards infinity is that the particles in the gap have a relatively large mean free path to accelerate due to the low pressure, it is possible that it would not collide with another particle. If the particles were to hit with this high velocity due to the field applied, there is a large chance that they would excite more electrons to escape, that will then go on to collide with another particle. The

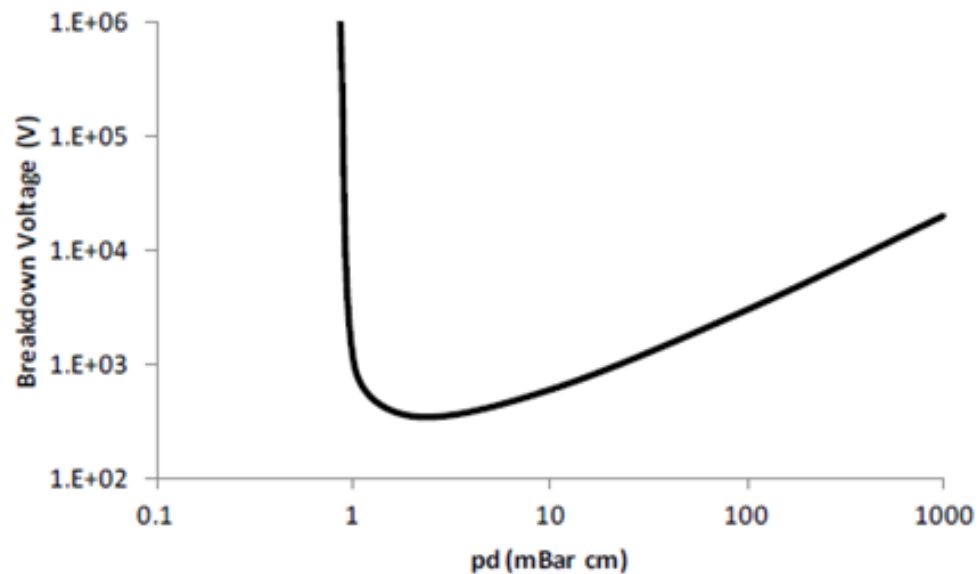


Figure 1.6: Paschen curve, giving the dependence of the voltage for a breakdown to occur with respect to a function of the pressure and gap distance [13].

lower the pressure of particles within the volume the less likely they are to collide, this reduces the chance of breakdown.

If the product of pressure and distance between the electrodes coincides with the minimum voltage of the Paschen curve, it has the optimal conditions for initiating a breakdown [13]. Meaning free electrons reach the ideal velocity before hitting particles in the gas causing an avalanche. This principle is a main contributor to the theory of breakdown in a vacuum system, were a relatively high voltage is required dependent on the amount of gas present. If the material experiencing a high field is able to introduce electrons or gas particles either from the material itself or contaminants on the surface, then a small amount of gas can be present to cause breakdown.

The Paschen curve shows the relationship between the voltage that would cause an electrical breakdown with respect to the function of the pressure and distance [13]. As the product of the pressure and gap distance increases, the voltage required for breakdown also increases. This is because with an increased pressure the

particles within the area have a reduced mean free path to accelerate to a sufficient velocity to cause further emission. Therefore, a higher voltage needs to be applied to deliver more energy to electrons to cause a greater acceleration.

1.4 Theories of Vacuum Breakdown

1.4.1 Introduction

For there to be a breakdown in a vacuum there must be a source of gas present, allowing a plasma to be produced. There are several theories of the process leading to a gas being introduced in a vacuum system. There are also several factors that can impact the likelihood and affect the number of breakdowns [15]–[22]. Some of these theories relate to the material aspects of the system and some to the high electric field present.

In most electron emission mechanisms, an electron must gain energy from an external source to escape the material. The energy can be provided by a number of different mechanisms [23]. One of these is an increase in temperature causing the electrons to become excited, allowing some of them to have enough energy to escape, which is called thermal emission. The energy required to remove an electron from the bulk of a material is called the work function, which is a material property [24]–[26]. Another mechanism is field emission, which is the emission of electrons that occurs when an electric field is applied. It is unique among emission mechanisms in that it does not need an external source of energy to occur as it involves quantum tunnelling of the electron through the potential barrier posed by the workfunction. Field emission requires electric fields of tens of Mv/m to be measurable in practice. In the flat-plate DC system at CERN the electric field is produced by applying a voltage between two electrodes that are a set distance

apart, with the field given as:

$$E = V/d, \quad (1.8)$$

where E is the electric field (V/m), V is the voltage (V) and d is the distance between the cathode and anode.

1.4.2 Electron Emission

1.4.2.1 Field Emission

The Fowler-Nordheim equation was the original equation used to determine the tunnelling probability of electrons, but this was later improved upon with the Murphy-Good equation that included temperature effects. This is an equation of the current density of emitted electrons from the surface via quantum tunnelling when a material is subject to a high electric field [27]. For an electron to tunnel out of a material it must pass the potential barrier between the material and the vacuum [28] [29]. When the electron is just about the metal surface, a positive image charge is induced in the metal, attracting the electron back. This modifies the shape of the potential barrier. For strong electric fields, image charge effects can significantly decrease the height of the potential barrier and increase the probability of tunnelling.

Figure 1.7 displays the electric potential, relative to the Fermi energy of the metal, as a function of position for different circumstances. Φ is the work function of the metal and $\Delta\phi$ is the reduction in effective work function due to image charge effects. With a higher electric field, the potential in the vacuum has a steeper slope and the width of the potential barrier for electrons to tunnel through decreases.

The current density depends on the work function and local surface electric

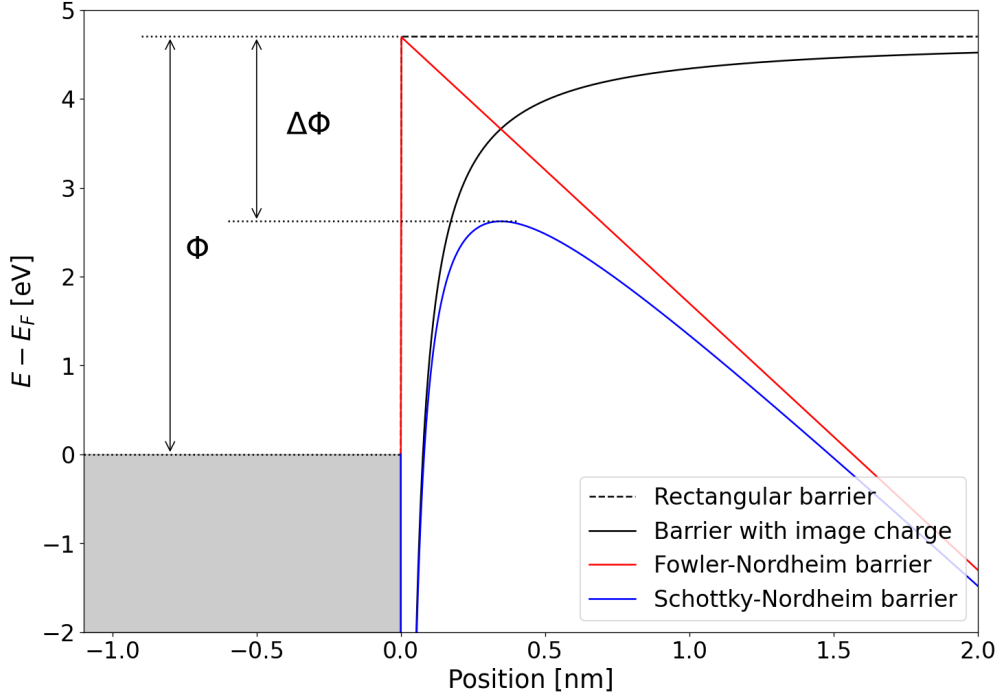


Figure 1.7: Potential relative to the Fermi level for a metal-vacuum interface subject to an external electric field. The position is defined with the interface at zero, with positive values representing the vacuum. In this example, the field is 3 GV/m and the workfunction is 4.7 eV.

field, and is can be modelled by the Murphy-Good equation [23] [1.9]:

$$J = \frac{e^3 \beta^2 E^2}{8\pi h \phi t^2(y)} \exp\left(-\frac{8\pi \sqrt{2m_e} \phi^{3/2} v(y)}{3heE\beta}\right), \quad (1.9)$$

where J is the current density, e is the electron charge, E is the macroscopic electric field (V/m), β is the field enhancement factor, h is Planck's constant, m_e is the electron mass, and ϕ is the work function. $v(y)$ and $t(y)$ are elliptical integral functions, with

$$y = \sqrt{\frac{e^3 E}{4\pi \epsilon_0 \phi}}, \quad (1.10)$$

where ϵ_0 is the permittivity of free space. The Murphy-Good formulation reduces to the Fowler-Nordheim formulation [30] when $v(y) = t(y) = 1$ is assumed. These values correspond to an exactly triangular potential barrier, meaning that include

temperature or image charge effects are not included [29].

A field enhancement is an area on the surface of a material with a higher field than the surrounding area as the result of an imperfection [31]. The field enhancement factor is the peak field from the enhancement divided by the normal idealised field for a perfect surface, given as:

$$\beta = \frac{E_{\text{local}}}{E_{\text{macroscopic}}} \quad (1.11)$$

where, β is the field enhancement factor, E_{local} is the peak electric field, and $E_{\text{macroscopic}}$ is the normal electric field.

To simplify Equation [1.9], the constants can be grouped together inside and outside of the exponential to form two constants. These constants are referred to as the Fowler-Nordheim constants and are denoted as A_{FN} and B_{FN} . Numerical values for these constants are given in Equation [1.12] and Equation [1.13] respectively.

$$A_{FN} = \frac{e}{8\pi h} = 1.54124146 \times 10^{-6} \frac{\text{A}}{\text{eV}} \quad (1.12)$$

$$B_{FN} = \frac{8\pi\sqrt{2m_e^3}}{3he} = 6.830676478 \times 10^9 \frac{1}{\sqrt{\text{eVm}}} \quad (1.13)$$

With the above simplifications of $t(y) = 1$ and $v(y) = 1$, Equation [1.14] can be obtained in terms of the two Fowler-Nordheim constants:

$$J = \frac{A_{FN} (E\beta)^2}{\phi} \exp\left(-\frac{B_{FN}\phi^{\frac{3}{2}}}{E\beta}\right) \quad (1.14)$$

Using Equation [1.14], it can be seen that as the field is increased the current density increases exponentially. This current has a sudden onset with respect to the electric field, which means that once a few electrons are able to tunnel, other

are also able to escape before reaching a limit. The other factors that the emitted current depend on include the field enhancement factor and the work function of the material. In terms of the field enhancement, the larger this is the higher current density from the emission site. The work function is a material constant, with a larger material work function implying a higher field required for emission. In practice, the field enhancement factor and work function most likely change during the process as the temperature increases and forces act on the enhancement area [23]. Temperature increase is caused by collisions between the electrons in the material, these collisions cause a release of energy in the form of heat; this process is called Joule heating [32]. The higher the electron density the higher the number of collisions and therefore the temperature increases with an increase in current density.

Field enhancement on the electrode can be caused by protrusions from the surface, with the highest field found at the tip of the protrusion [31]. Figure 1.8 displays the relationship between the dimensions of a surface protrusion and the field enhancement factor for various types of protrusion geometry, with more slender features resulting in higher field enhancement factors.

If the field-enhancing feature reaches the melting temperature of the material, then it will start to melt and evaporate. Evaporation of the material leads to gas emission that can form a plasma due to high fields and free electrons. Then as a result of the presence of the plasma there is a breakdown within the system that causes damage at the location of the field emitter, leaving no trace of the field-emitting tip.

Measurements of the field emission current as a function of the macroscopic electric field can be used to calculate the field enhancement factor β . This can be

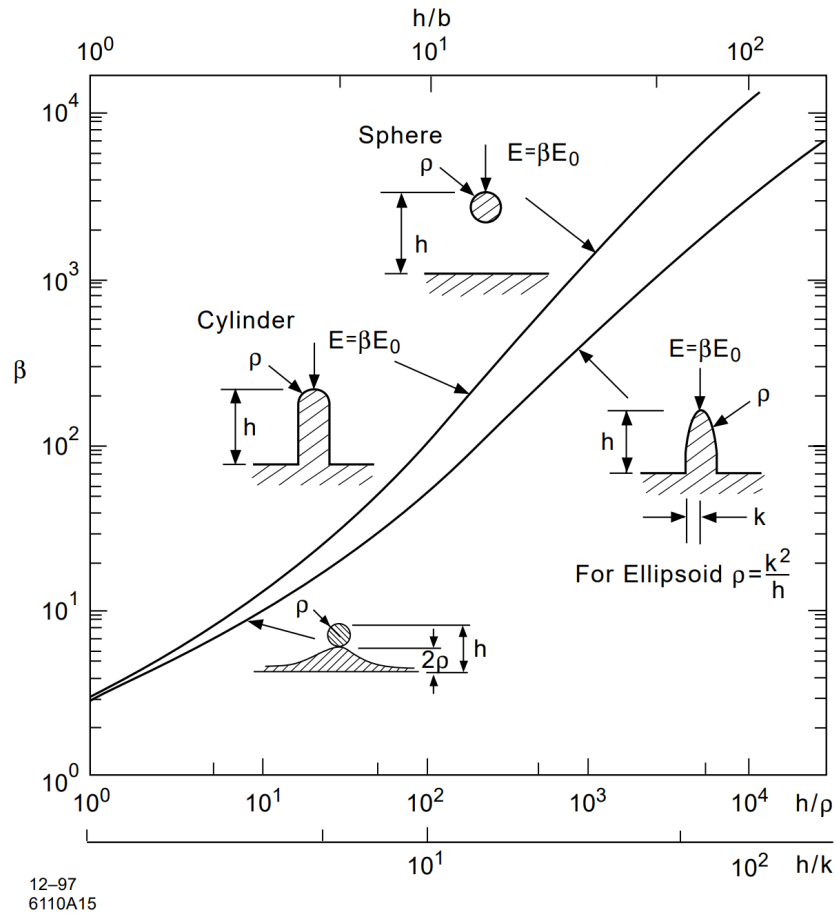


Figure 1.8: Field enhancement factor as a function of aspect ratio for various protrusion shapes [31].

done by expressing Equation [1.14] as:

$$I = \xi E^2 e^{-\gamma/E}, \tag{1.15}$$

where:

$$\gamma = \frac{6.53 \times 10^{-9} \times \phi^{3/2}}{\beta} \tag{1.16}$$

$$\xi = A_e \frac{1.54 \times 10^{-6} \beta^2}{\phi} e^{10.41 \phi^{-1/2}} \tag{1.17}$$

Equation [1.15] can also be expressed in the form:

$$\ln\left(\frac{I}{E^2}\right) = \ln(\xi) - \frac{\gamma}{E}, \quad (1.18)$$

By plotting $\ln(I/E^2)$ against $1/E$ in what is commonly known as a ‘‘Fowler-Nordheim plot’’ and taking the gradient, γ can be obtained, which is related to β by Equation [1.16] [31].

1.4.2.2 Space Charge Limit

The Child-Langmuir Law, also known as Child’s Law describes the space-charge-limited current between two flat parallel electrodes in a vacuum [33]. Though it was first applied to thermal emission, it describes the space-charge limit for any emission mechanism. This is the maximum current density for a given electrodes electrode spacing and potential difference. The equation for Child’s Law is:

$$J_{SCL} = \frac{4\epsilon_0}{9D^2} \left(\frac{2e}{m}\right)^{\frac{1}{2}} V^{\frac{3}{2}} \quad (1.19)$$

where J_{SCL} is the space-charge-limited current density, V is the potential difference between anode and cathode, D is the distance between anode and cathode, ϵ_0 is the permittivity of free space, m is electron mass, and e is electron charge [34].

In terms of the physical meaning of these results, this is related to the space charge between electrons [28]. As electrons have their own electric field that has a negative charge, this repels other electrons. Therefore, as an electron escapes the surface of a material cancels out some of the surface electric field. When the space charge of the electrons becomes large enough, there is a point at which the surface field becomes zero and no more electrons can escape the material.

Increasing the voltage across the two electrodes causes the electron velocity to increase [28]. This reduces the build-up of space charge near the surface of the

material as each electrons spends less time close to the surface.

1.4.3 Materials

Several studies have been done to investigate possible causes to breakdown related to the material condition or composition [15]–[22]. It is likely that breakdown is influenced by a multitude of different characteristics relating to each sample rather than one singular property.

This section summarises the different material properties and characteristics that could influence breakdown behaviour. These include surface defects that could occur as a result of stress on the materials, voids beneath the surface, crystal structure. The effect of surface coatings has been studied to observe whether the number of breakdowns is decreased.

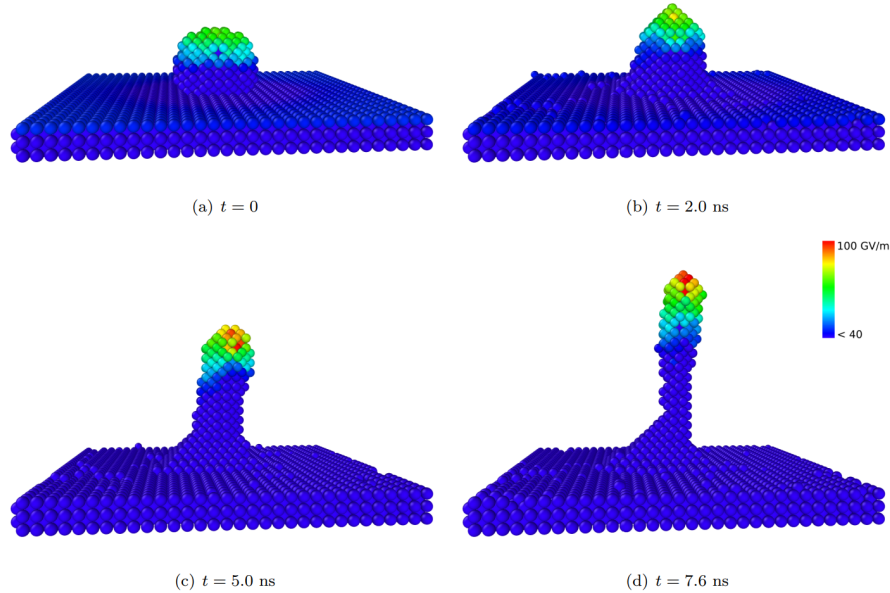


Figure 1.9: Dynamic atomistic model showing the formation of a sharp tip on a tungsten surface when a high electric field is applied [35], starting from a hemispherical asperity as shown on the top left.

Atomistic molecular dynamics simulations [15] have shown that the surface

atoms of a metal can migrate due to thermal effects, as demonstrated in Figure 1.9. These simulations have shown that if the applied electric field is sufficiently large, it becomes energetically favourable for the surface atoms to move to regions of higher electric field. This causes them to clump into field-enhancing tips, whose growth causes a further increase in field enhancement factor and thus local electric field. The simulations also show field evaporation (i.e. detachment) of atoms when the field on the tip becomes sufficiently high.

Although sharp protrusions can cause local electric field enhancement, features irregularities of a sufficient aspect ratio to explain the β calculated from measurements [36] have not been seen on the surface before or after being inserted into a cavity or DC system where breakdowns occurred. This led to investigations as to whether the irregularities could be caused by the stress of the electric field and then evaporate or be destroyed by a breakdown, if this is a fast process then this would explain not having seen any in an SEM. An important point to note is that field emission is measured whenever a high field is applied suggesting a field enhancement is present the whole time but breakdowns are only on some occasions.

For a tip to develop there are most likely dislocations in the material moving, causing a protrusion to emerge at the surface of the material [16]. Although a dislocation can be formed at any point in the material (known as homogenous nucleation), this has higher activation energy, and is therefore much less likely, than nucleation at defects such as grain boundaries or other dislocations. Sub-surface voids have also been proposed as possible dislocation nucleation mechanism [16]. Ways in which a sub-surface void could form include oxidation on the surface diffusing into the material by the Kirkendall effect or mass transport of material above the void [37]. Other possible causes proposed include technological imperfection of the metal production or electromigration [38]. As a result of the

dislocations that occur as a result of a void, this can lead to deformation of crystals within the material.

Deformation of the material under the surface could cause several defects at the surface due to movement of dislocations [16]. One of these includes the growth of whiskers on the surface that then provide a field enhancement. Voids are more likely to cause dislocations if they are located close to the surface as they will be subjected to the most stress.

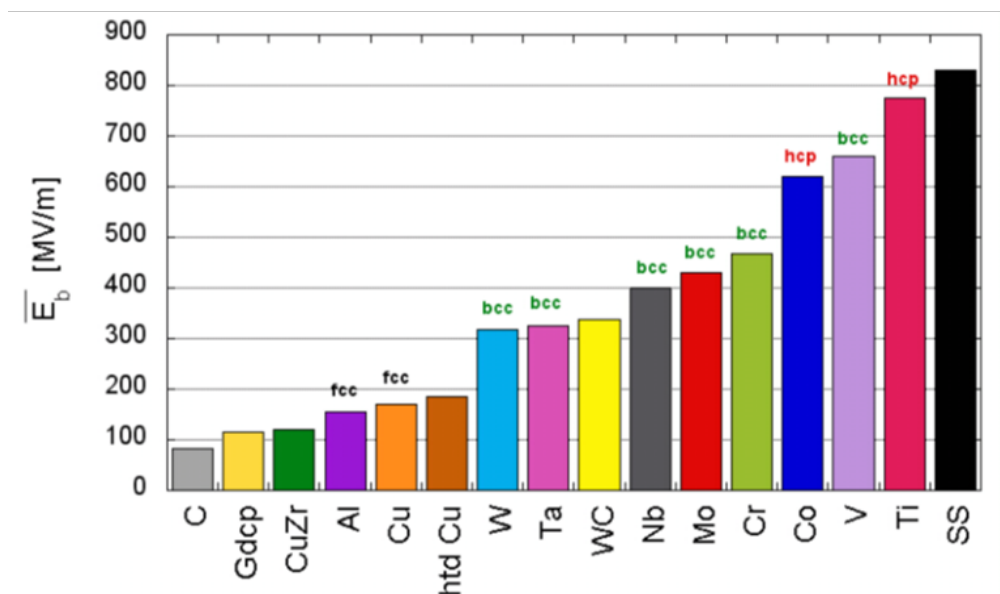


Figure 1.10: Saturated electric fields achieved for different materials tested in the tip to plate pulsed DC system, with annotations indicating the crystal structure for each of the materials. The saturated field indicates the electric field after an initial conditioning phase of 20-100 breakdowns [17], [18].

Studies have also been done, looking at how different materials can impact breakdowns and conditioning [17]. These tests were done using the previous pulsed DC system at CERN, with a 2 mm tip anode a variable distance from a flat plate. Each of the different materials was conditioned with pulses using the same setup in order to determine the electric field each materials could achieve. Figure 1.10 displays the breakdown field for different material after conditioning and above the different bars on the chart are terms to describe the crystal structures of each

material. FCC is face centred cubic, BCC is body centred cubic, and HCP is hexagonal closest packing. From Figure 1.10, there is a clear correlation between the crystal structure of each and the average breakdown field.

The different crystal structures have different values of ductility and dislocation mobility [17]. FCC has the highest ductility and dislocation mobility meaning it is the most likely to deform when subject to a force. HCP has the lowest and therefore most likely to avoid voids collapsing and BCC is in the middle of these two.

Other material characteristics that could influence the breakdown field include the melting point, latent heat of fusion, thermal conductivity, electrical conductivity, vapour pressure, surface tension, and work function. A issue found that could influence the result given was gap instabilities that varied for different materials [17], [18]. From the experiments it was found that the gap distance changed due to a significantly large amounts of damage to the 2 mm anode tip after several sparks, causing erosion of the surface and displacement of material. This led to the distance changing by $\pm 50\%$ for titanium and $< \pm 10\%$ after 50 breakdowns with copper or molybdenum.

Conditioning of the samples is done by increasing the voltage in steps until there is a discharge and then kept at that voltage until it stabilises before increasing the voltage further [19]. When a breakdown occurs, the field is measured in order to determine whether the sample is being conditioned or de-conditioned, depending on whether it is increasing or decreasing respectively. From tests it has been determined that breakdown performance depends on the cathode material and processing used for preparation [18], [19]. It has also been found that the amount damage caused during tests is dependent of the stored energy in the system available to the breakdown. With higher energies there has been more significant damage and the spot size tends to scale with the energy.

Experiments have been performed in which different materials were subject to a ramping field until a breakdown occurred, at which point the field was reduced to zero and the ramping was restarted [18]. The maximum field just before breakdown eventually saturated, and it was observed that copper reached saturation immediately but at a relatively low electric field. The material with the largest breakdown field after conditioning was titanium but as mentioned previously this had a larger gap instability. To improve the mechanical properties of metals, they can be alloyed with other materials. Tests were done on copper alloys to improve tensile and fatigue strengths, to observe their conditioning performance and resistance to gap instabilities. The alloys performed worse than the pure copper, which is thought to have occurred due to tensile and fatigue strength properties arising from the micro structure of the material, affected by thermal processes [17].

Tests have been done on the effect of oxide layers of copper and molybdenum to observe the difference in breakdown field and conditioning [18]. Use of a copper oxide layer improved the breakdown field and was found to increase the work function. Although initially less prone to breakdowns, after around 12-15 sparks the oxide layer was completely eroded and the sample behaved like pure copper. When a molybdenum oxide sample was tested this had a decreased performance with a lower breakdown field and a longer conditioning time. Other surface treatments were tested with a copper sample and it was found that after 2-3 sparks the sample performed the same as Cu, due to the surface layer being removed by the spark. It can be determined that with the current treatments available, it is not possible to use them for extended use.

1.4.4 Statistical analysis

In more recent studies, work has been done on the statistics of vacuum breakdown using data analysis and simulations. Looking at the probability of breakdown and the possible factors that influence them, with possible ways to predict when a breakdown will occur.

1.4.4.1 Statistics of vacuum breakdown in the high-gradient and low-rate regime

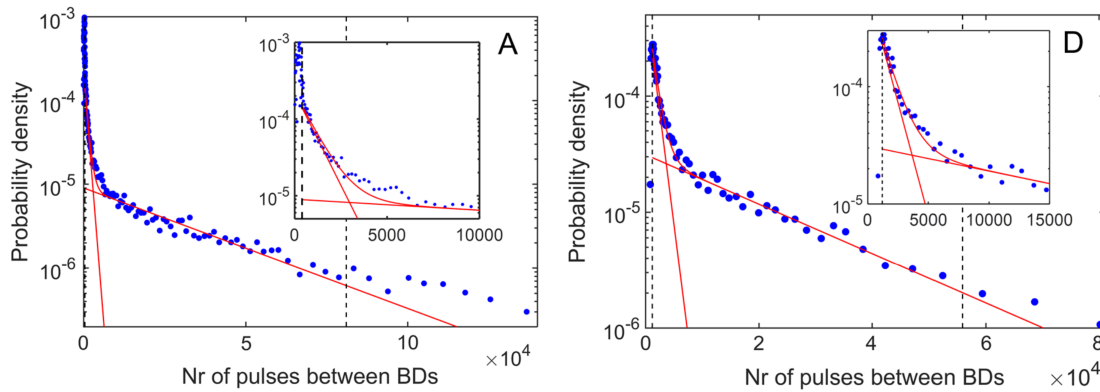


Figure 1.11: Plots the logarithm of probability density with respect to the number of pulses between breakdowns. The left plot shows data from a CLIC X-band accelerating structure, while the right plot shows data obtained from the LES. In both figures, two distinct linear regimes can be identified, corresponding to primary and secondary breakdowns. [20]

Figure 1.11 shows probability density functions (PDF) with respect to the number of pulses between consecutive breakdowns [20]. This analysis was done for both a CLIC x-band structure (TD26CC) and the pulsed DC system, producing very similar results. Two regimes are visible, one for small intervals between consecutive breakdowns and one for large intervals. Each regime corresponds to a straight line on semi-logarithmic axes, which implies an exponential probability distribution. The complete PDF is thus represented by the sum of two exponential distributions, each with its own rate parameter, as shown in Equation [1.20]:

$$f(n) = A \exp(-\alpha n) + B \exp(-\beta n), \quad (1.20)$$

where n is the number of pulses between consecutive breakdowns, α and β are the two rate parameters, and A and B are scaling factors. The two regimes imply two different types of events, which are named primary breakdowns and secondary or follow-up breakdowns. Follow-up breakdowns occur shortly after a primary breakdown, and there can be multiple follow-up breakdowns for each primary. Here, α is the rate of primary breakdowns and β is the rate of follow-up breakdowns.

Follow-up breakdowns could be a result of surface modifications caused by primary breakdowns and a follow up breakdown could lead to further follow-up breakdowns. This means that follow-up breakdowns are not independent events, and are a result of other variables. Follow-up breakdowns generally occur in close vicinity to the previous breakdown. Figure 1.12 shows the relationship between distance between breakdowns and the number of pulses between breakdowns in an RF accelerating structure. This shows that when breakdowns happen closer together in time they are also closer together in space.

It is possible also to identify whether a breakdown is primary or follow-up from the exponential PDFs fitted to experimental

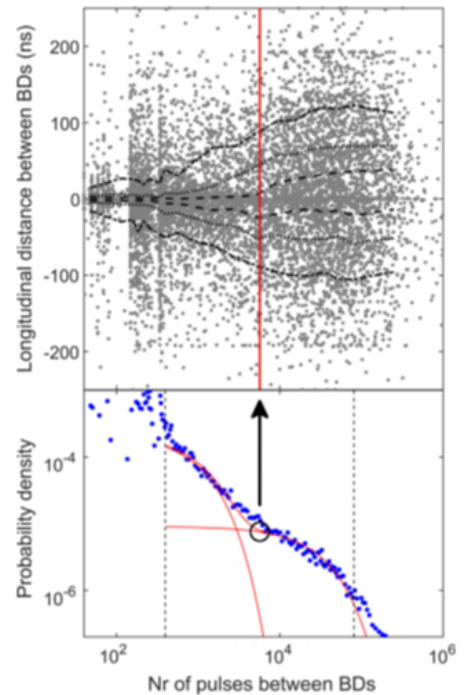


Figure 1.12: Two plots with an x axis being the (log) number of pulses between breakdowns. The y axis of the upper plot shows is the longitudinal distance between breakdowns (units of signal travel time) and the lower plot shows the (log) probability density. [20]

data. The number of pulses at which the two distributions cross becomes the threshold, with breakdowns above the threshold designated primary breakdowns. From Figure 1.11 the threshold of pulses would be approximately 3000 pulses, meaning if a given breakdown occurred more than 3000 pulses after the previous breakdown, it would be a primary.

1.5 Breakdown Nucleation

A possible source of protrusions on the surface could be the material deforming under tensile electric field stress, corresponding to dislocation motion [22].

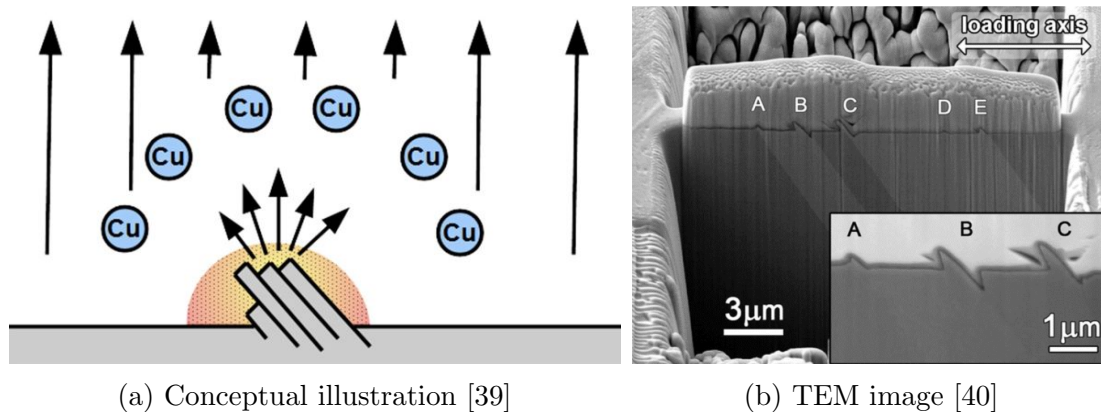


Figure 1.13: (a) Shows a conceptual image of dislocations protruding from the surface causing a field enhancements, leading to field emission, heating and material melting. (b) Shows FIB TEM images of physical dislocations surface protrusions from fatigued Cu specimens.

A metal surface subjected to a high electric field experiences a tensile stress normal to the surface, which can cause the movement, creation, and trapping of mobile dislocations. The applied stress is given by the Maxwell stress tensor, which for a DC electric field reduces to [41]:

$$\sigma = \frac{1}{2}\epsilon_0 E^2, \quad (1.21)$$

where σ is the stress perpendicular to the surface, ε is the permittivity of free space and E is the electric field magnitude. For a 100 MV/m field, this corresponds to 44 kPa. With a field enhancement factor of 50, the stress becomes comparable to the yield strength of copper alloy (c. 30 to 300 MPa). This stress can cause plastic deformation of the metal, and can result in ridge-like features appearing on the surface, as seen in Figure 1.13a.

The dislocations within the material are organised into slip planes, and their motion along these planes can result in features appearing on the surface. The creation of mobile dislocations and their eventual trapping behaves stochastically, and means that plastic deformation on small scales occurs in discrete random steps. Therefore, when a metal surface is subject to a strong electric field, a field enhancing feature can appear suddenly, and possibly trigger a breakdown. This ties in with the random nature of breakdowns. Monte Carlo simulations and theoretical analysis were used by Ashkenazy et. al. to determine the possible relationship between dislocations and breakdown. The effect of protrusions on the surface has already been discussed but this looks at the probability distributions and their correlation with other variables.

This model considers the dislocation density ρ as well as the rate of formation ($\dot{\rho}_+$) and the rate of trapping ($\dot{\rho}_-$) dislocation densities with respect to time. Dislocation density will increase with stress and decrease when they interact with another dislocation or defect and become trapped. The deterministic dynamics of the mobile dislocation density can be given as $\dot{\rho} = \dot{\rho}_+ - \dot{\rho}_-$, where $\dot{\rho}_+$ and $\dot{\rho}_-$ depend on material properties, applied stress and current value of ρ . In theory, the mobile dislocation density fluctuates around a stable value until it reaches a critical point causing a runaway condition.

When $\dot{\rho} = 0$ it outputs two variables given as ρ_* and ρ_c , where the former is the value that ρ tends towards a stable fixed point when decreasing (ρ_*) and the

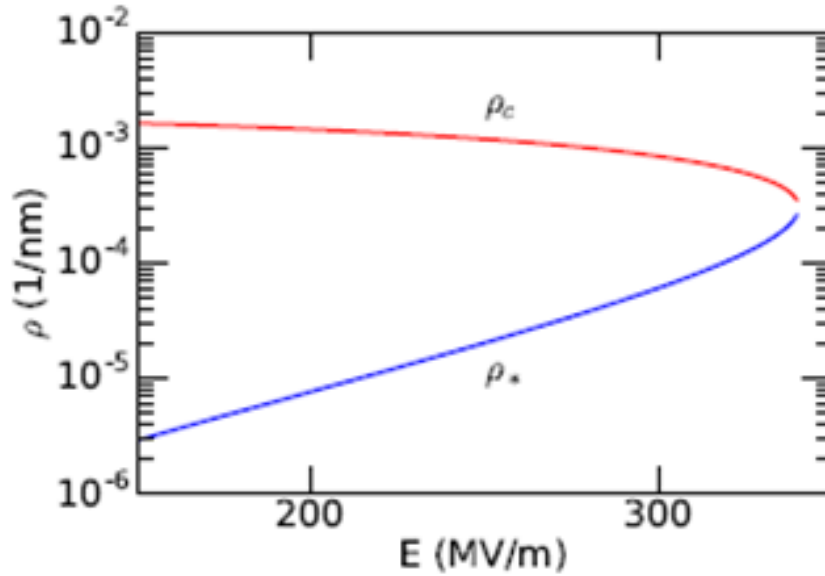


Figure 1.14: Equilibrium value of dislocation density, ρ^* , and the critical value of dislocation density at which breakdown is initiated, ρ_c vs. applied surface electric field E , according to the MDDF model. [22]

other is the critical limit (ρ_c), which is an unstable fixed point of unstable growth leading to a breakdown when $\rho < \rho_c$. Figure 1.14 shows ρ_* and ρ_c with respect to the electric field, this shows that for low fields the values are further apart making the system less likely to experience a breakdown. At the point where $\rho_* = \rho_c$ this is the critical electric field E_c , a breakdown would occur during a pulse if $E \leq E_c$ [20]. There is also a finite probability that the dislocation density will reach the critical value at any time and will lead to a breakdown.

A birth-death Markov process was used to model the behaviour of the dislocation density as the dislocations were created and trapped [20]. This is used because there can only be a whole number of dislocations, so ρ can only take discrete values. Each state corresponds to a certain number of dislocations. The birth (λ_n) and death (μ_n) rates are given with respect to n , which is $\rho/\Delta\rho$, the equations are given as:

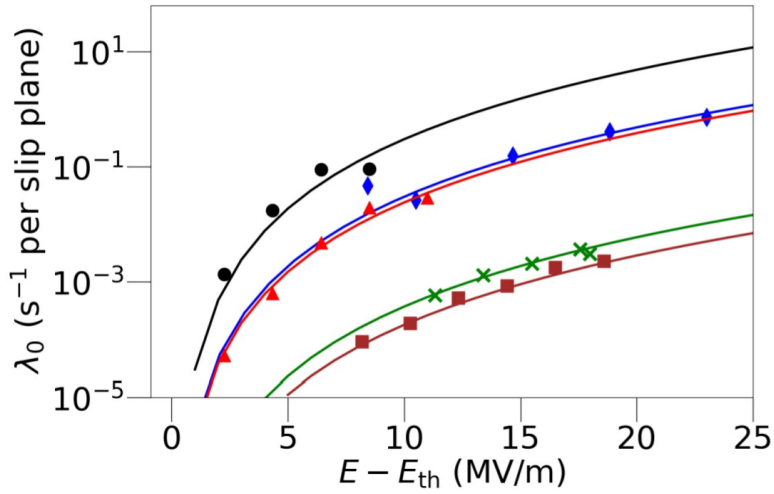
$$\lambda_n = B_1 (n + n_c C) \sigma^2 e^{\alpha \sigma} ; \mu_n = \left(\frac{B_2 n}{n_c} \right) (n + n_c C) \sigma \quad (1.22)$$

Where $\Delta\rho = 0.1\mu \text{ m}^{-1}$, $A_2 = a_2 n_c \Delta\rho$, $B_2 = b_2 n_c \Delta\rho$, $C = c/(n_c \Delta\rho)$, $n_C = \rho_c/\Delta\rho$ and $\sigma(n) = A_1 + A_2 n/n_c$, a_2, b_2 , and c are material dependent. These can then be used in Equation [1.23], giving the probability ($P_n(t)$) of n mobile dislocation per cell at a given time t .

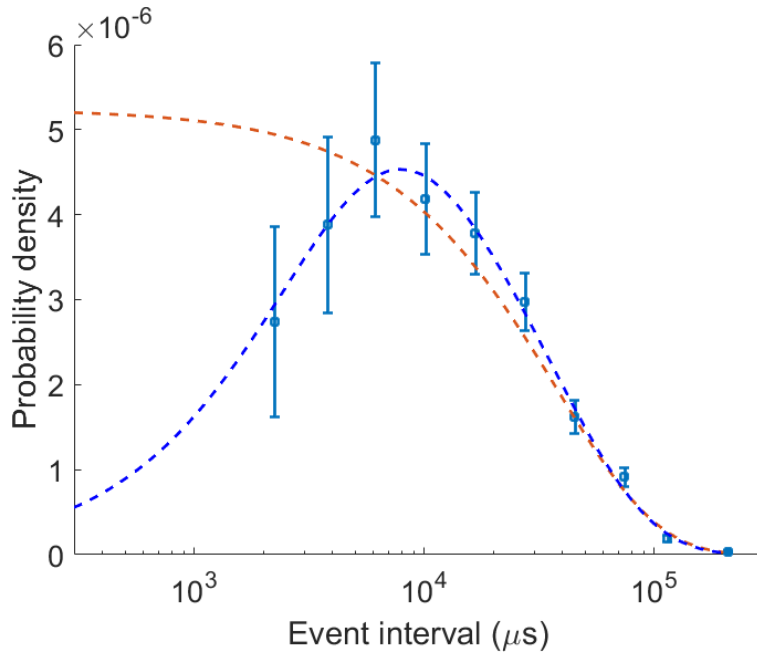
$$\frac{\partial P_n(t)}{\partial t} = \lambda_{n-1} P_{n-1}(t) + \mu_{n+1} P_{n+1}(t) - (\lambda_n + \mu_n) P_n(t) \quad (1.23)$$

Measurements consistent with the mobile dislocation density fluctuation (MDDF) model were first made in the CERN Pulsed DC System in 2019 [21]. In these experiments, a constant DC electric field was applied to copper electrodes while the field-emitted current was monitored for high-frequency signals using sensitive purpose-built electronics. Small impulses, occurring at random time intervals, could be seen on the current signal, with an example shown in Figure 7.2.

The measured distribution of the time intervals between consecutive events was found to be consistent with a hypo-exponential distribution as predicted by the MDDF model, rather than an exponential distribution which would have resulted from independent random events. It was also found that, as the applied electric field was varied, the mean rate of events was proportional to the mean birth rate of mobile dislocations as predicted by the MDDF model. Both of these results are represented in Figure 1.15. These two pieces of evidence suggest that the measured impulses were related to dislocation motion in the copper material. The relatively low event rate measured, however, suggested that only a very small proportion of all of the subsurface dislocation activity in the sample was observable in these measurements.



(a) Measured event rate.



(b) Probability density function of time intervals between events

Figure 1.15: (a) Shows the measured event rate per slip plane λ_0 in s^{-1} vs. surface electric field in MV/m . A threshold E_{th} has been subtracted from the surface field value. Different colours represent different measurement runs [21]. (b) Shows the probability density vs. time interval between successive events in μs . The points represent measured data, the red dashed lines represent the best-fit exponential distribution, and the blue dashed lines represent the best-fit two-parameter hypoexponential distribution [42]

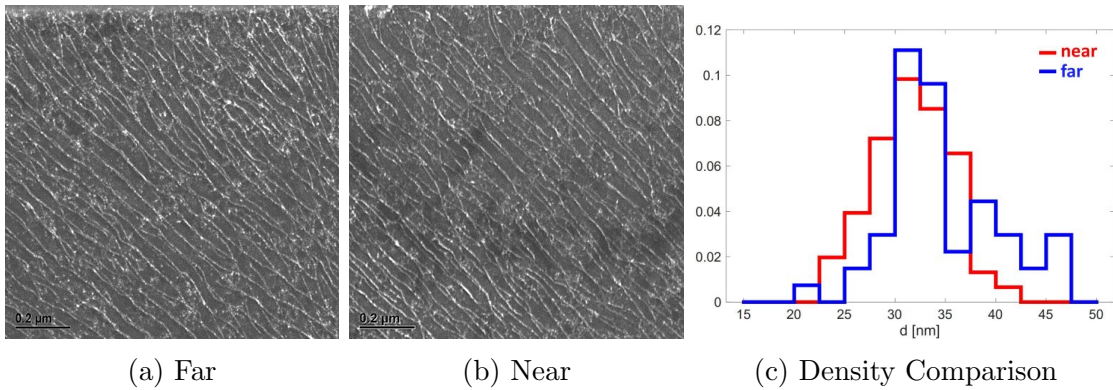


Figure 1.16: (a) and (b) show TEM images of dislocation slip planes 1 mm away from and on the high field surface area respectively of an RF accelerating structure [39]. (c) shows the correlation between the probability of distances between dislocation slip planes from the near and far samples images given.

Figures 1.16 (a) and (b) show TEM images of the cross-sections of samples taken from a high-gradient copper accelerating cavity [39]. The samples were taken from two locations, one on the iris, labelled ‘near’ and exposed to a high peak electric field, and the other from 1 mm away, labelled ‘far’ and exposed to a lower peak electric field. Dislocations appear as diagonal lines that are visible in both images. Figure 6.10 (c) shows a histogram of the spacing between lines for each case, demonstrating a greater density of lines in the sample exposed to higher electric field.

This change in surface geometry can result in a change in the field-enhancement factor and thus a change in the field-emitted current from the site. Since dislocation motion events are believed to be very short in duration (on the order of a few nanoseconds for stresses on the order of 100 MPa [43]) and occur at random intervals, this implies that the total field-emitted current in an experiment undergoes a random walk of step-like changes.

Compounding of the field enhancement factor would most likely occur due to dislocations being proportional to the field applied and a ‘field enhancement area’

would be the most prone to experiencing dislocations. The use of the term ‘field enhancement area’, is due to this possibly being an area of the surface with several ridges forming a grating structure. Where, the grating structure is a series of period ridges that are smaller than the wavelength that reflect specific polarisation, depending on the structure. If fluctuations occur on a ‘field enhancement area’ that provides some additional field enhancement, the field enhancement changes due to the more recent dislocation movement will be compounded with the field enhancement of the ‘field enhancement area’ that was already present. This would imply that measuring fluctuations in field-emitted current only provides information about dislocation motion in this region, and not the entire surface as the rest of the surface appears as noise in the data.

The mobile dislocation density fluctuation (MDDF) model gives a quantitative description of the statistics of the sub-critical fluctuation events not causing a breakdown imminently, and critical breakdown events given the applied field and material properties. Under the MDDF model, the process of conditioning alters the mobility of dislocations in a material, and should therefore correspond to a measurable change in dislocation properties.

SEM studies of samples that have undergone conditioning have shown no difference in the number of dislocations lines for a given area compared to those that have not been conditioned. There are preliminary results suggesting that the configuration of the dislocations is modified such that they become less mobile [39]. This can be seen in Figure 1.16c [39], where the distance between dislocations lines is smaller for the sample taken from the high field compared to the lower field. Another observation they made was a reduced amount of dissociation (bifurcation) of dislocation lines for the low field sample.

1.6 Light Emission

Light emission has been observed during field emission experiments in the first pulsed DC system at CERN [44]. This system consisted of a tip to plate setup as opposed to the two large surface area electrodes in the current system, which allowed for optical fibres to be placed close to the high field area. A high voltage was applied across the gap with no breakdowns occurring, with light emission persisting as long as the voltage was applied. Measurements of the spectrum of the emitted light were conducted by Jan Kovermann, who concluded that it was caused by Optical Transition Radiation (OTR) on the basis that the spectrum was broad. A key feature of the emission spectrum noted by Kovermann was a sharp drop in intensity above 2.1 eV, which was attributed to the presence of an inter-band transition of this energy in copper.

There are a number of light emission mechanisms that could produce light during field emission experiments other than OTR, including blackbody radiation, cathodoluminescence, and surface plasmons, all of which considered when conducting measurements in the LES. Characteristics that could be experimentally observed to evaluate possible emission mechanisms include the dependence of the spectrum on the emitted current, electrode material and conditioning, measurement angle, and voltage polarity.

1.6.1 Transition radiation

Transition radiation occurs whenever a charged particle traverses a sharp boundary between media of different optical properties. For the case of a boundary between vacuum and a perfect conductor, Frank and Ginsburg describe the energy dW radiated over the solid angle $d\Omega$ and bandwidth $d\omega$ at angle Ω to the trajectory of the particle by a non-relativistic particle of charge e moving with constant velocity

v normal to the surface as:

$$dW = \frac{e^2 v^2 \sin^2 \theta}{\pi^2 c^3} d\omega d\Omega, \quad (1.24)$$

where c is the speed of light [45]. Since there is no ω term in Equation [1.24], the spectrum should be flat over all frequencies. In a real metal, variation in the permittivity with frequency and various energy loss mechanisms such as interband transitions result in a non-flat spectrum. Equation [1.24] shows a dependence of emitted power on electron energy. Since electrons are emitted with relatively low energy at the cathode, gain energy when crossing the gap, and arrive at the anode with high energy, there should be much more light emitted by OTR from the anode than the cathode. The emitted light intensity should therefore depend on the applied voltage.

1.6.2 Black-body radiation

Field emission from copper surfaces into vacuum is known to occur on a number of microscopic field-emitting sites where there is a local enhancement of the surface electric field. Due to their extremely small size, the current density can be very large, resulting in very high temperatures due to Ohmic heating [14]. Black-body radiation could therefore be a possible cause of light emission. The spectral intensity of black-body radiation is given by Planck's law [46]:

$$B(\lambda, T) = \frac{2hc^2}{\lambda^5} \frac{1}{\exp\left(\frac{hc}{k\lambda T}\right) - 1}, \quad (1.25)$$

where B is the light intensity, h is Planck's constant, c is speed of light in vacuum, λ is the wavelength, k is Boltzmann's constant and T is the temperature. The black-body emission spectrum has a strong dependence on temperature, and the frequency of the peak can be used to deduce the temperature of the emitter. An

experiment performed on a continuous-wave (CW) accelerating cavity at the High Energy Accelerator Research Organization (KEK) showed light emission from a number of small points on the surface of the cavity. The Planck formula showed a good fit to the measured emission spectra, and implied temperatures between 1000 °C and 1500 °C, above the melting point of copper [47].

The blackbody emission spectrum is broad and has a specific shape described by Equation [1.25]. Unlike the other mechanisms, the light should be emitted by the cathode where the emitting tips are located. A lower current density is expected on the anode, as the emitted electrons will likely spread out as they cross the gap, leading to less heating.

1.6.3 Cathodoluminescence

Cathodoluminescence is a light emission mechanism that occurs when a high-energy electron beam strikes a material that has an electronic structure that has a filled valence band and an empty conduction band separated by an energy gap [48]. Incident electrons can collide with the valence electrons and promote them to the conduction band, leaving a hole in the valence band. After a short time, the electrons and the hole recombine, producing a photon of energy equal to the band gap. Since a band gap is required, this cannot happen with pure copper. However, if there are any non-metallic impurities or oxides on the anode surface, cathodoluminescence can occur in principle. Since the band gap plays a significant role in this process, it is expected that the emitted spectrum would have a peak or shoulder at the wavelength corresponding to photons of this energy.

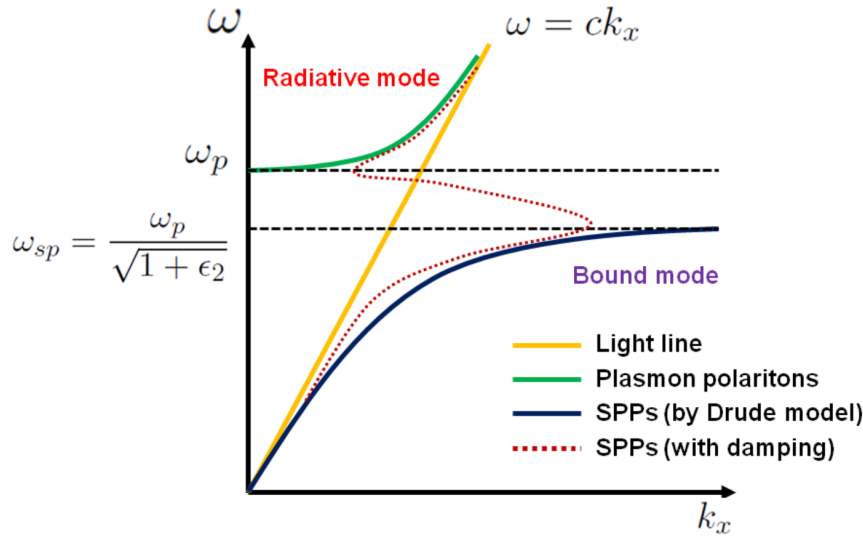


Figure 1.17: Dispersion relation of surface plasmon-polaritons [49].

1.6.4 Surface plasmon resonance

Surface plasmon-polaritons (SPPs) are electromagnetic waves that can occur on a metal-vacuum interface, which can be excited by an electron beam striking the metal [50]. For a given frequency, SPPs have much shorter wavelengths than light in free space (as can be deduced from the dispersion diagram in Figure 1.17), and thus do not normally couple to light and remain confined to the surface. In the presence of surface features, such as a grating whose size is on the order of the SPP wavelength, coupling between SPPs and light can occur. Since dislocation motion is known to form periodic surface features on copper surfaces conditioned at high fields [22], they are a potential light emission mechanism. Diffraction gratings are resonant structures, as their operation depends on their physical dimensions being related to the wavelength. There should therefore be a peak in the light spectrum that corresponds to the spacing of the surface features. Since ridges or other features caused by from dislocation motion likely will not have as regular a structure as specifically engineered plasmon resonators, they will likely not have as strong a resonance. Such a peak will therefore probably be broader and less

prominent than normally seen for plasmons (with typical quality factors of 1 to a few tens [51]).

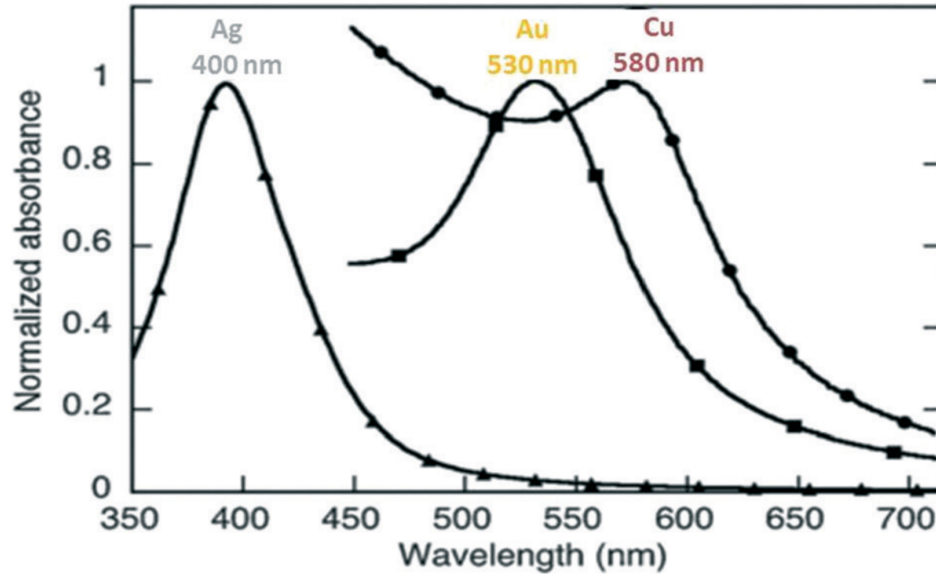


Figure 1.18: Absorption spectra caused by localised surface plasmon resonances in nanoparticles of different materials [52].

Localised surface plasmon resonances, which are generally observed with individual nanometer-scale particles, could have a sharp resonant peak whose wavelength is related to the plasma frequency of the material. On Figure 1.17, this corresponds to the large values of wavenumber k_x and thus small wavelength. In vacuum, the resonant frequency is $\omega_p/\sqrt{2}$, where ω_p is the plasma frequency of the material [49]. Such resonances are often observed in the absorption spectra of metal nanoparticles [52].

1.7 Context of this work

The study of vacuum breakdowns is an active field of research with frequent advances in understanding of the problem. In addition to various high-gradient RF cavity test stand at CERN [53], SLAC [54], and KEK [55], there are also the

two DC LES setups at CERN which are the focus of this thesis, one LES at the University of Helsinki [56], as well as a cryogenic setup in Uppsala [57].

Dislocations in the metal have been recognised to play an important role in the early stages of breakdowns, as described by the MDDF model described in Section 1.5. More recently, measurements of fluctuations in field-emitted current indicative of dislocation motion consistent with the MDDF model have been made in the LES [21].

Motivated by the need to experimentally investigate this and other models relating material defects to breakdown [58], the cryogenic DC system in Uppsala, allowing measurements of breakdown and field-emission phenomena to be made on a set of electrodes over a wide temperature range [57], has been recently commissioned. In this system, significantly lower breakdown rates and much more stable field emission has been measured at cryogenic temperatures than at room temperature, consistent with theoretical predictions.

Much effort has also been put into attempting to understand the subsequent stages of breakdown, and to explain how high field enhancements come about from small initial perturbations. This includes atomic-scale simulations of electrostatics and molecular dynamics which demonstrate how sharp field-enhancing tips can spontaneously form when a metal surface is subject to high electric fields [59], explaining why such sharp tips are not seen in electron microscope studies of experimental samples (see Section 1.4.3).

There has been a significant amount of work done to understand and improve the conditioning process itself, and to understand how pulsing brings about the ability to withstand higher electric fields without breakdown. For example, recent studies have revealed dependencies on voltage polarity, repetition rate, and gap size in the LES [60]. The effect of different voltage ramping profiles has also been studied [61]. The addition of cameras and specially-machined electrodes in the

LES have allowed the exact location of each breakdown in sequence to be recorded and correlated to post-mortem microscope images, which was not possible in this or similar systems before.

Key contributions of this work to the state of the art in breakdown science, briefly outlined above, include:

- A systematic comparison of the breakdown behaviour of different materials, using more refined conditioning and analytical procedures than with previous studies [18].
- A detailed study of the effect of irradiation on breakdown, which showed a significant reduction in maximum stable field, but not much correlation between the locations of breakdowns and irradiation-induced blisters. This is particularly relevant to relevant to accelerator applications where accelerator components are subject to irradiation by beam loss. To the author's knowledge, this is the first systematic study of this type. These results also provide experimental data on the effect of sub-surface voids on breakdown. Up to this point, only simulations have been performed on this specific case [62].
- Novel measurements of field-emitted current fluctuations during pulsed conditioning have been made, correlation between the stable electric fields during pulsed conditioning and gap electric field during field emission measurements, with the potential to be developed into a new method of quantifying conditioning progress (see Chapter 7.5).
- New measurements showing a weak or no dependence of breakdown rate on pulse length for pulses between 100 μ s and 1 ms. This is in contrast to typical fifth-power dependence often seen for pulses below 200 ns in accelerating

structure tests [63], [64].

- A new algorithm to determine how the applied electric field should be changed during conditioning that has shown an improvement in the stability of the field over the previous iterations.
- Optical spectroscopy measurements conducted in parallel with field emission current measurements which show a clear correlation between the current and light intensity measured for Cu based materials, and not for other materials, suggesting that a mechanism other than transition radiation may be responsible for the light.

Chapter 2

Pulsed DC Large Electrode System

2.1 Introduction

This section covers description of the pulsed DC large electrode systems (LES) used throughout the experiments to be discussed in the following chapters. There are two very similar systems at CERN and they are designed for studies of conditioning, field electron emission, and vacuum breakdown phenomenon. The main focus of the systems are the precision machined electrodes that are tested in pairs and changed. The electrodes are placed in the system, parallel to one another and under high vacuum, then tested by applying a pulsed high field. There are several automated data-acquisition instruments to record breakdown properties. Additionally, a Marx generator is used to supply pulses from 1 μ s to 1 ms with repetition rates from 1 Hz to 6 kHz, allowing the electrodes to be conditioned in fast time scales of 3.5 days at 2000 Hz in the pulsed DC systems compared to 2 months for the T24PSI CLIC accelerating structure in Xbox 3. This time does not include the time take to install new samples and achieve a suitable vacuum

for conditioning. Conditioning plots comparing these can be seen in Figure 2.1 [65], [66]. Use of the pulsed DC systems allows for easier observations of light, breakdown locations, pressure and changes in the voltage and current when a breakdown occurs, and correlate the data with relatively high precision.

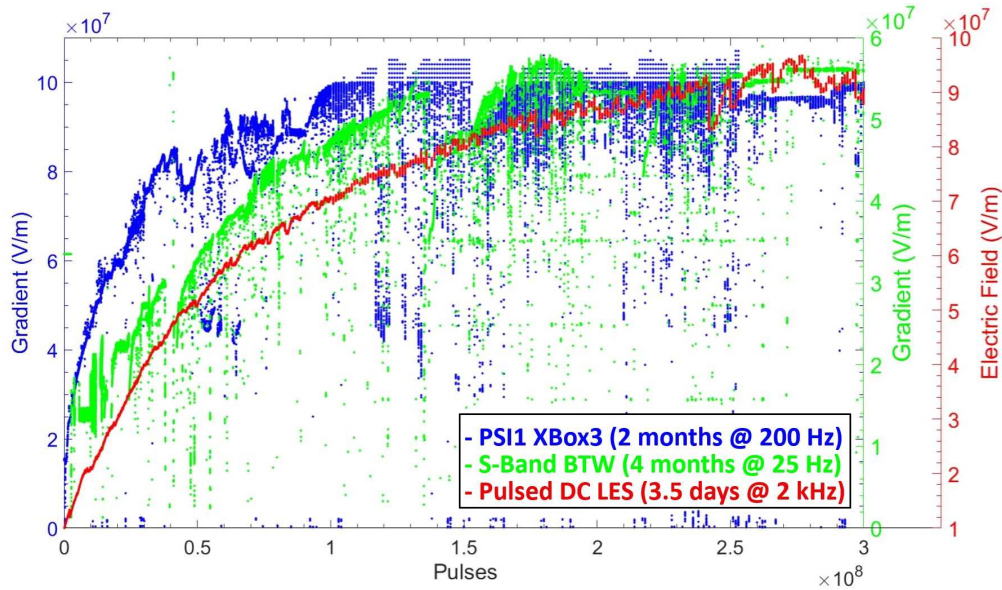


Figure 2.1: Conditioning curves for the T24PSI structure, S-band BTW structure and the Cu OFE electrodes in the pulsed DC system [65]–[67]. Where a similar number of pulses is required for the conditioning but due to the difference in repetition rates this takes different amounts of time from 2 months, 4 months and 3.5 days respectively.

The pulsed DC systems were designed and in use prior to this work [68], with some adjustments made throughout studies described in this report, which will be discussed where appropriate. The design of the system was done as part of the PhD of Nicholas Shipman and the decisions behind certain aspects can be found in the relevant thesis [68]. Additions to the control and analysis from the original implementation include the cameras used to determine breakdown locations for the system, found in reference [69]. Also the high-voltage supply system used was a high performance Marx generator, developed for providing high voltage pulses to the system, designed in collaboration with Energy Pulse Systems [70]. The

LabVIEW code to control and record data for the different hardware was also generated previously with only a few changes made throughout these tests [68].

The physical setup of the previously designed chamber will be discussed including the precision machined electrodes to be conditioned and operated at high field, ceramics for setting the space between the electrodes, ceramics for isolating from the chamber, high voltage feedthroughs to apply the voltage, vacuum pump, cameras for breakdown locations, and power generation. Additionally the procedure is described for calibration with use of the dummy load for both calibrating the Marx and testing electronics.

One issue experienced during earlier work was an electric field enhancement causing a number of breakdowns around the edges of the electrodes during testing. This section talks about the previous and more recent theories as to the cause of this electric field enhancement and the methods used to reduce this effect. This includes testing with a small anode to large cathode configuration to remove the cathode electric field enhancements caused by the machined edge of the electrodes. Simulations of the electric field for different edge designs and misalignment will be shown.

Descriptions will be given of the data acquisition methods used throughout the pulsed conditioning. This includes LabVIEW codes for control of the Marx generator, and acquisition and display of pressure, oscilloscope and camera data for each breakdown. Also, details will be given of the analysis of the breakdown light intensity detected by the cameras with respect to voltage and the distance from the cameras.

Two different conditioning methods will be described within the chapter, with the inherited method of using the breakdown rate limit algorithm, and the second method using this in a different way and controlled by the operator. The breakdown rate limiting algorithm was used previously with a target electric

field set above the electric field holding capabilities of the material, which led to an asymptotic approach towards each materials electric field limit. Whereas, a different conditioning method was developed over the course of this thesis that used the breakdown rate limiting algorithm, but with small steps in the target electric field to gradually increase the electric field holding capabilities whilst limiting the breakdown rate during the ramps between steps. This will be referred to as the 'step-wise' conditioning method, and was the method used throughout the experiments in this thesis, unless specified otherwise.

After the conditioning of the electrodes, a test of the pulse length dependence on the breakdown rate can be performed. The method for conducting these tests and analysing the data to be shown in Chapter 3.6, will be described.

2.2 Physical Setup

Figure 2.2 displays the electrode assembly inside the system (a) and a cross section of the system containing the electrodes (b). The assembly consists of 2 high precision machined electrodes (1), a ceramic spacer (2), and ceramics to isolate the electrodes from the chamber (3). See Appendices A and B, for the drawings of the electrodes used for tests, with a small anode to large cathode setup to avoid cathode edge electric field enhancements, to be discussed. The majority of electrodes tested have an outer diameter of 80 mm, a cathode precision machined surface of 60 mm diameter, and an anode diameter and therefore high-field area of 40 mm. There are a few due to material availability, that use a different sizes of 60 mm outer, 40 mm cathode and 30 mm anode diameters. The drawing specifies the tolerances that allow us to achieve small gaps between the electrodes, as small as 20 μm . This includes a surface flatness and parallelism tolerance of 1 μm . Another important requirement to achieve a good surface roughness

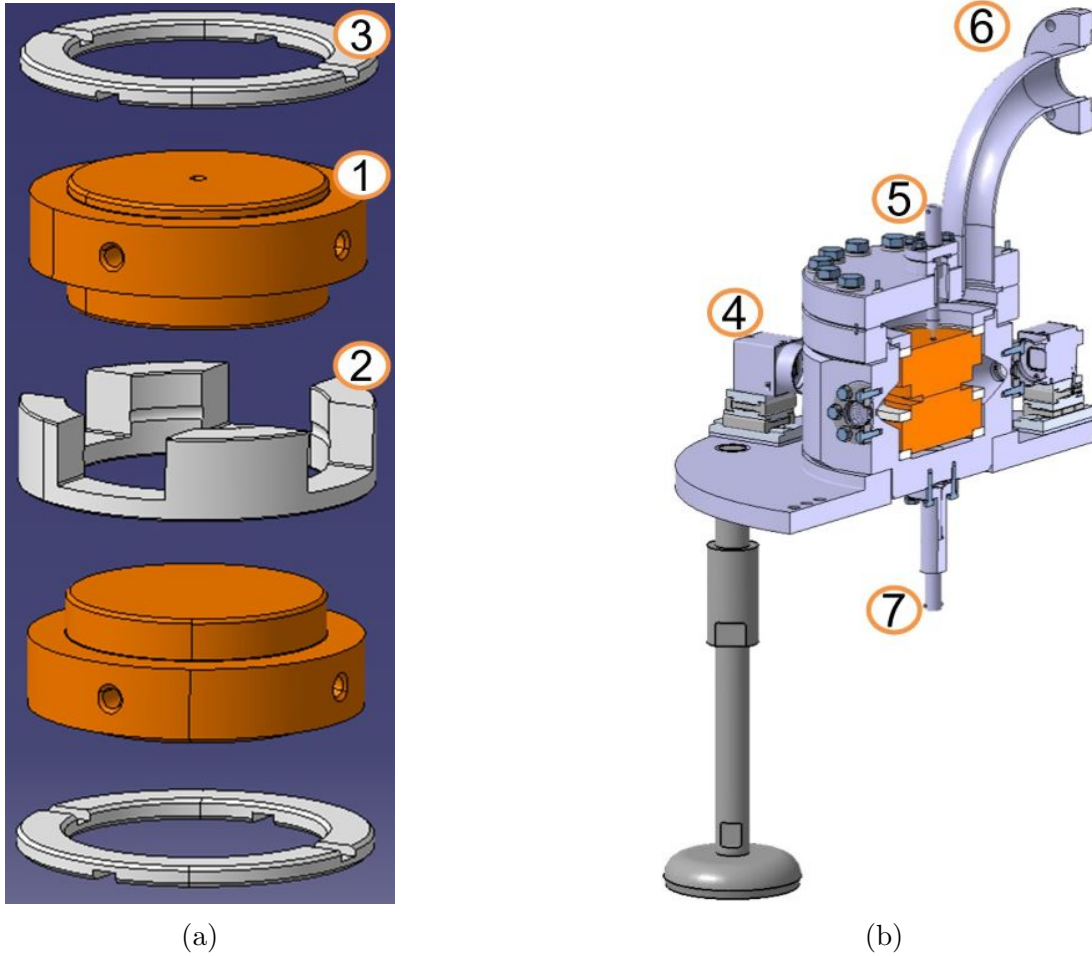


Figure 2.2: (a) Electrodes assembly with (1) being the copper electrodes, (2) a ceramics for setting the gap between the electrodes and (3) isolating the electrodes from the chamber and (b) Pulsed DC Large Electrode System cut-through, showing (4) the perpendicular cameras, (5) and (7) are the upper and lower high voltage feedthroughs respectively, and (6) is the vacuum pump outlet [60].

average, specified as Ra 0.025 (μm) for copper, and is achieved using diamond machining. We will later see tests of a variety of materials. Diamond tools could not be used for all of them, and in these cases the surface finish was somewhat worse. To achieve a mirror finish surface without polishing electrodes, diamond machining was done using machining fluids that required cleaned off afterwards, this may influence the surface due to contamination. The electrodes also have tight tolerances for the shape of the edge and the distance of the critical surface to the

shoulder of the electrode. The most important part of the edge is the initial drop off from the high field surface and this generates an electric field enhancement, therefore specific edge designs are used to reduce this effect, to be discussed. The distance to the shoulder is important, as it in part determines the distance between the electrodes and therefore to get the correct distance between the electrodes, the height must be precise.

In order to obtain different gap spacing, a selection of ceramic spacers of different thicknesses are used. The ceramic is placed between the 2 electrodes, and makes contact with the shoulders of each. Each electrode has a shoulder height of 10 mm, and the ceramic height is equal to 20 mm being the height of both shoulders, plus the distance of the gap between $20\ \mu\text{m}$ and $100\ \mu\text{m}$. Due to the small distances of the gap on the micrometer scale, the ceramic is also required to be tight tolerance of $1\ \mu\text{m}$. As it can be seen from figure 2.2, the ceramic in the centre has 4 slits, that enable visual observation of the electrode gap from the windows.

There are 4 windows 90 degrees to one another around the chamber. An optical system based on two cameras installed at 90 degrees from each other is used to determine breakdown position through triangulation. Figure 2.3 shows a cut of the setup showing two perpendicular windows and the cameras with respect to electrodes in the centre [69]. The light emitted during breakdown is imaged on the charge-coupled device (CCD) cameras through narrow slits. Each camera contains an array of 1920 pixels along the vertical axis and

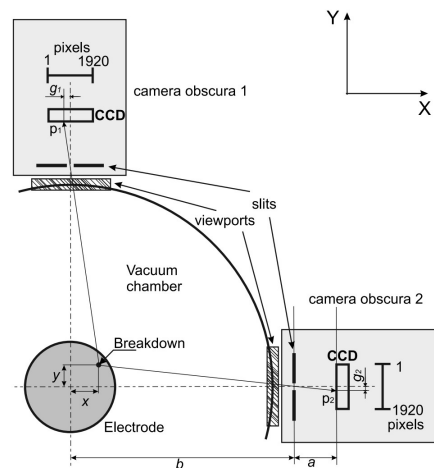


Figure 2.3: 2 cameras are placed perpendicular to the chamber to view the gap, these are able to determine the breakdown locations in the x and y axis to give coordinates [69].

from knowing the distance between the centre of the electrode and the distance to the CCD camera it is possible to determine the coordinates of the breakdown in the transverse planes of the electrodes. Measurements from the CCD camera also give a value for the intensity that can be used in post testing analysis.

There are 2 pulsed DC large electrode systems (LES) at CERN with the main difference being that one system (LES 3) has a 10 kV rated high voltage feedthrough at the top and bottom of the chamber making connection with the electrodes as seen in Figure 2.2b, labelled as (5) and (7). For the other system (LES 2), there is only a feedthrough to the top electrode, with the bottom electrode in contact with the chamber connecting it directly to ground. With respect to the components seen in Figure 2.2a, LES 3 used all as seen whereas LES 2 does not use the bottom ceramic to make contact with the chamber.

A metallic plate is placed on top of the assembly and secured with 4 screws using a torque screw to maintain equal force on each screw to improve the reliability of the gap. Once the force is applied to the electrodes, the capacitance is measured to determine that the gap is as expected. Equation (2.1) gives the equation for capacitance for a given area, this case determined by the anode area and the gap distance determined by the ceramic spacer used. Depending on the system used, stray capacitance of the system also need to be taken into consideration.

$$C = \frac{\varepsilon A}{d} + C_{stray} \quad (2.1)$$

Where, C = Capacitance (F), $\varepsilon = \varepsilon_0 \times \varepsilon_r$, with ε_0 being the permittivity free space and ε_r being the relative permittivity of the material between the surfaces, A is the surface area (m^2), d = gap (m). C_{stray} is the stray capacitance of the chamber measured to be around 65 pF, this was determined by measuring the

capacitance of the isolated electrodes and then grounding the bottom electrode to the chamber and measuring the difference. This value also agrees relatively well with the difference between the expected value for the electrodes to the measured value for the system where the electrodes are not isolated and therefore grounded to the chamber. Whilst it is an option to add the grounding of the chamber for LES 3, it is permanently grounded in LES 2 due to not having a ceramic at the bottom to isolate the cathode. Whilst the accuracy of these measurement is not fully known, there is a measurable difference in capacitance between a 60 μm and 100 μm gap, it also highlights if there is a short between the electrodes.

After comparing the measured capacitance to the value calculated from the expected gap, it is possible to draw a conclusion as to whether the gap is correct or if something is wrong. In the case that the capacitance does not correspond to the expected value, it can be determined whether the gap is larger or smaller than it should be with a smaller capacitance meaning a larger gap. A smaller gap could suggest an issue with machining causing the electrodes to not be within tolerance. This has been seen in the case that the radius on the shoulder of the electrodes was not within tolerance and did not fit with a specific ceramic spacer due to interference between the corresponding edges. Or an issue with the spacer, which could be a result of the wrong spacer or damage to the spacer.

The first possible cause to check is evidence of dust on the surface as this can easily be fixed by blowing this away. Determining whether the issue is with the spacer can be tested using a pair of electrodes that have been proven to be correct or use of a micrometer. If the gap is too large then this could be the same as with a small gap or due to an issue with the assembly and may be fixed by re-installing the same electrodes.

For all of the results shown a nominal gap was used for the calculations of the electric field throughout of 60 μm . The drawing for the 60 μm cathode and 40 μm

high field area anode electrodes can be found in Appendices A and B respectively. These electrodes are machined to tight tolerances for the roughness and flatness in order to be able to obtain gaps as small as $20 \mu\text{m}$. This includes a surface roughness Ra value of $0.025 \mu\text{m}$, and flatness of $0.001 \mu\text{m}$, full details can be found in the drawing in Appendix A. As mentioned, during the assembly of the system for each pair of electrodes a capacitance measurement is done to verify that the gap is correct. Despite this there is still some level of difference in the gap because machining can never be to ideal tolerances. Metrology measurements of each electrode was done to determine the shoulder height, to calculate the gap. With these measurement the height does vary over the whole surface. Approximate values from the metrology can be used to calculate the electric fields alongside the nominal electric field values to be given. From these values an error of around $\pm 5\%$ of the nominal electric field is possible. A table can be found in Appendix R. of all the electric field values for the nominal and metrology gaps for each of the electrode pairs tested. This difference in the electric field has not affected the order of performance for each of the materials.

Once the capacitance measurement is correct the rest of the system can be assembled. The lid to the chamber can be placed on top with a copper gasket and secured using several bolts. It is important to tighten the bolts by going back and forth between the different sides and tightening a small amount each time, this is to achieve an even surface contact for good vacuum. Once this is secured the high voltage feedthroughs are inserted to make contact with the electrodes. The drawing for the upper feed through can be found in Appendix G, this shows the external high voltage female Kings connector and the internal connection. Design of the internal connection was increased in diameter compared to the off the shelf component, in order to make 2 perpendicular cuts allowing the tip to be splayed for a better contact with the whole in the electrode. As mentioned one of the systems

has a feed-through at the bottom, the other system has three ports that are covered with end plates but could be used to attach other equipment if required.

Figure 2.2b, label (6), indicated the vacuum pump outlet to which a Pfeiffer vacuum Hi cube turbo pump is attached [71]. Between the outlet as shown and the pump is a vacuum gauge to determine the pressure throughout pumping down and testing of the systems. Tests are normally conducted once a minimum pressure of 1×10^{-7} mbar is achieved and continues to decrease during conditioning reaching pressures as low as 3×10^{-9} mbar. Starting measurements at a higher pressure allows to start earlier, reducing the time taken for individual tests. Where as a decreased pressure should decrease the likelihood of breakdowns as a higher voltage potential would be required.

The system consists of hardware external to the chamber, including a FuG power supply and Marx generator, as seen in Figure 2.4. The FuG power supply can provide a voltage up to 1 kV with the Marx generator multiplying the voltage supplied by 10 [70]. The generator supplies pulses to the chamber to replicate pulses similar to that of the CLIC X-band structures. The RF structures are powered by klystrons [1], using short pulses to reduce heating and the breakdown rate for the given power level of the pulses [72]. Whilst the pulse lengths for the X-band structures are in the 100s of ns range, for the pulsed DC systems generators, the pulse length can range from 1 μ s to 1 ms. Other parameters of the Marx generator include repetition rates in the range of 1 Hz to 6 kHz and voltages up to 10 kV. Control of these settings and running of the Marx generator and FuG is done from a computer, to be discussed later in this chapter.

The data acquisition setup consists of a LeCroy oscilloscope that records various outputs from the Marx generator. There are four inputs to the oscilloscope and these can record the synchronous signal indicating pulse timing and length, short circuit signal from the Marx generator indicating when a breakdown has occurred,

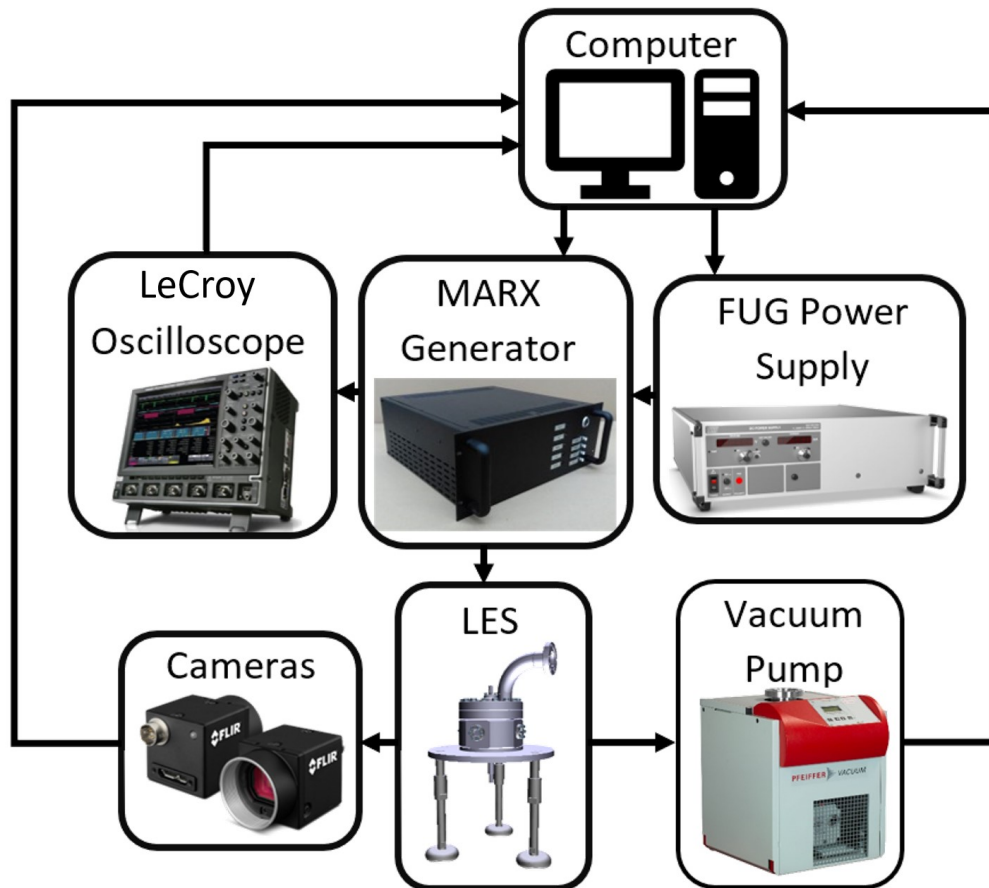


Figure 2.4: Shows a flow diagram of the different hardware components and connections displayed as arrows between each.

charging and discharging current, output voltage and for the most recent Marx generator also the electric field emission current during the pulse. For all pulsed conditioning tests this was set to record the waveform when a breakdown occurred, triggered by the short circuit output of the Marx generator.

As well as the physical setup and components of the system the Marx generator also requires calibrating for the different gap capacitance. This is required because the charging current during pulses changes for different load capacitance values. The value for the peak charging current of a normal pulse is used to determine whether a breakdown has occurred, as a breakdown causes the current to exceed the charging current by a significant amount. This will be described in more detail

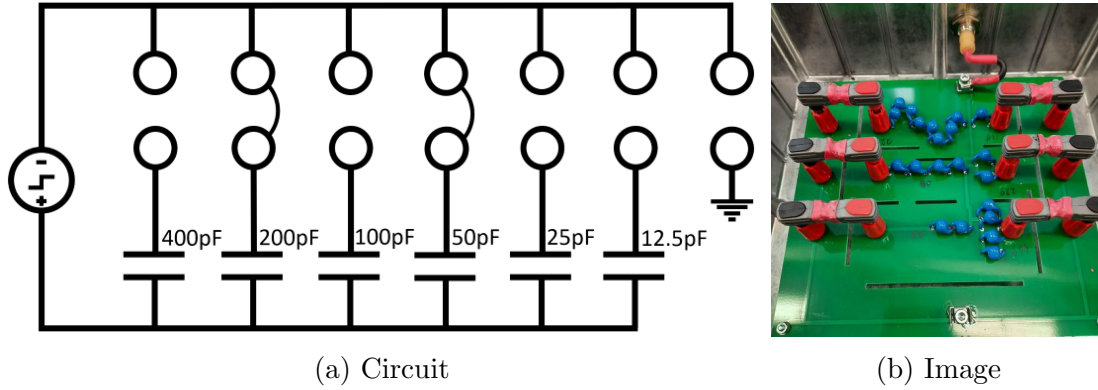


Figure 2.5: Capacitance box with ability to change the capacitance to match the pulsed DC system for calibration of the Marx generator and use as a dummy load for testing electronics.

in Section 2.3, on the operation and control of the systems.

For calibration, a capacitance load equal to that of the LES is attached to the Marx high voltage output. Figure 2.5 shows a circuit diagram and image of the capacitance load used. The circuit diagram from Figure 2.5a shows the overall capacitance for the array of capacitors seen in Figure 2.5b. Each of the individual capacitors has a capacitance of 100 pF and rated for 10 kV, these are arranged in parallel to sum the values and in series to halve the values in accordance with the parallel and series capacitance equations shown in Equation 2.2 and Equation 2.3 respectively:

$$C = C_1 + C_2 + C_3 + \dots + C_n \quad (2.2)$$

$$\frac{1}{C} = \frac{1}{C_1} + \frac{1}{C_2} + \frac{1}{C_3} + \dots + \frac{1}{C_n} \quad (2.3)$$

Where, the total capacitance is calculated as a function of the each of the capacitance values in parallel or series. Different configurations of the capacitors were implemented to create capacitance values of 12.5 pF, 25 pF, 50 pF, 100 pF, 200 pF and 400 pF. These can be used in a similar manner as binary to produce any capacitance between 12.5 pF and 787.2 pF with a resolution of the smallest

value, by changing the capacitors connected to the negative terminal. Figure 2.5a shows capacitance lines 200 pF and 50 pF connected to the negative terminals, these are changed using the banana jacks, as shown in Figure 2.5b. Additionally there are two high voltage outputs that allow it to be used in similar ways to LES's but if only one connector is used then a connection to the ground, which is the containment box of the electrics that is made of steel.

Once the capacitance is set this can be used in place of the LES as mentioned and high voltage pulses applied. During the pulses, waveform measurements of the supplied current and voltage are measured on the oscilloscope are recorded at different steps in the voltage. The average charging current and flat voltage at the output are determined for the supplied voltages from the FuG power supply. The relationship between the FuG voltage and the voltage at the output of the Marx generator can be described by a linear line equations and for the current a quadratic equation can be used. These values for the different relationships are used in the code to correct for the error in the supplied voltage from the FuG to applied voltage from the Marx generator for conditioning. The charging current measured is used to determine when a breakdown occurs, to be discussed in more detail in the next section.

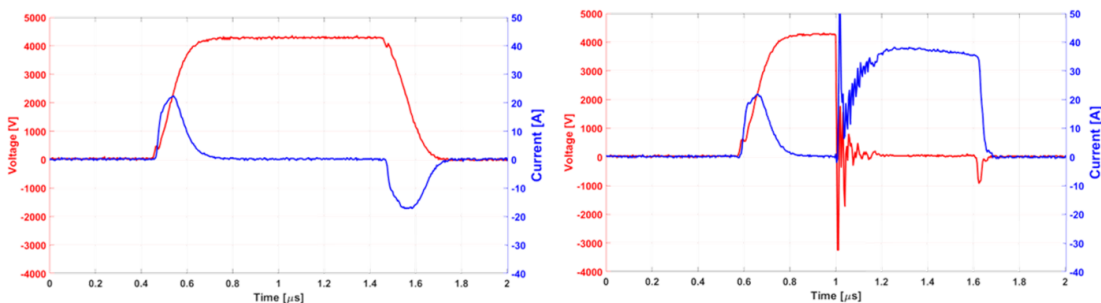
2.3 Operation and Control

The system is controlled and monitored using multiple LabVIEW (Laboratory Virtual Instrumentation Engineering Workbench) codes [73]. LabVIEW is a system-design platform using visual programming language named 'G' which was developed by National Instruments. LabVIEW is most commonly used for data acquisition and instrument control, it is also the program used for the running of the CLIC X-band structures [72]. LabVIEW has a front panel

and block diagram setup, the front panels is essentially a GUI (Graphical User Interface) for the operator and the block diagram contains the actual code. Along with hardware, LabVIEW was used to communicate with different hardware to send, receive, and record information. There are 4 codes used for the general running of the pulsed DC system, these include the main control of the generator, recording breakdowns from the cameras, recording pressure throughout running, and recording breakdown waveforms from the oscilloscopes.

Operation of the system is through the main code that controls the fug power supply and Marx generator. This code sets the FuG power supply to the specific voltage required and communicates with the generator to set all the parameters specified. The parameters to be set are contained within the front panel and can be changed whilst the code is running.

For conditioning of electrodes the user must specify the start voltage, a target voltage, step size, pulses per step, breakdown rate, repetition rate and pulse length. The program will then start from the start voltage and increase by the step size every given number of pulses until it reaches the target or until it reaches the specified maximum breakdown rate. If it is able to reach the target voltage it can be set to stop pulsing or to continue pulsing at the target voltage. In the case that it reaches the specified breakdown rate then code will change the electric field applied to maintain the breakdown rate close to the specified value.



(a) Normal Pulse

(b) Breakdown Pulse

Figure 2.6: (a) Normal and (b) breakdown pulses measured by an oscilloscope [60]

The code is designed to protect the electrodes from accumulating damage that compromises the voltage holding capability of the electrodes. Whilst the pulsed DC system can detect and shut off the power when an arc is detected, the RF structures do not as they receive the full pulse from the klystron [74], therefore a delay of 600 ns before stopping applying power from the Marx generator is implemented to replicate the impact of maintaining an arc for an amount of time. As discussed previously in this Chapter, the calibration of the Marx generator as part of the setup is to measure the charging current at different voltages for a given capacitance, if the current exceeds this by a specific amount, the Marx triggers as a breakdown and follows the procedure for a breakdown. Figure 2.6 a and b show the waveforms for a normal and breakdown pulse respectively. From the figure it can be seen that for a normal pulse, there is a positive charging current and a negative discharge current. The charging current is the value used for the calibration and a threshold above this is set so that if the supply current exceeds this value as seen in Figure 2.6b then the Marx generator registers as a breakdown. When the Marx generator detects a breakdown it reacts by maintaining the power supplied for 600 ns, after which the power is stopped. After a short period on the second scale with no pulsing, the voltage is ramped up exponentially starting from 20 % of the target voltage, with 100 pulses at each voltage. When the system reaches the target voltage minus a given amount specified in the code, normally set as 10 V, the voltage will ramp linearly to the target voltage for a given number of pulses specified in the front panel. After the linear ramp it remains at the target voltage for specified number of pulses before either stepping up or moving onto the next period of pulses at the same voltage.

There are several outputs from the Marx generator that are measured on an oscilloscope and saved through LabVIEW. These outputs include, a breakdown trigger, synchronous signal, supply current and a electric field emission

measurement for the more recent Marx. A probe is also attached to the ground and high voltage within the Marx with a 100:1 ratio. The breakdown trigger and Synchronous signal can be used to trigger the oscilloscope to save specific waveforms, the breakdown trigger is used to save every breakdown waveform during conditioning. These waveforms along with the pressure breakdown counter can be used to determine whether the generator is triggering on breakdowns correctly. The oscilloscope data can determine the current during the breakdown and when in the pulse the breakdown occurred to analyse the distribution in time of the breakdowns during the pulse.

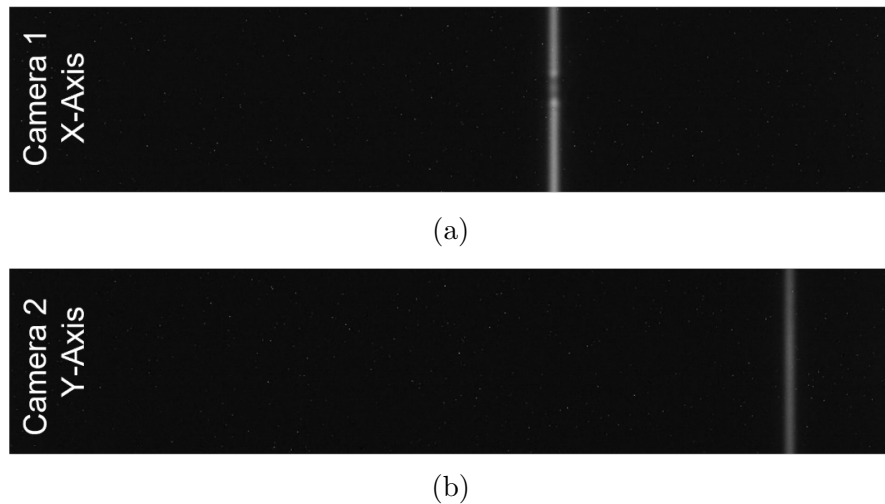


Figure 2.7: Images recorded from the (a) x-axis and (b) y-axis cameras respectively for determining the breakdown location.

For the breakdown location detection the LabVIEW code records images taken by the cameras. An exposure time of 3 seconds, with the resulting image being analysed in LabVIEW to determine if there is a breakdown. The breakdowns look like a thin vertical line of white light as seen in Figure 2.7. Its location from left to right indicates the x or y coordinate depending on the camera. The LabVIEW programme saves the image and a plot of the intensity over the length of the image, where the position of the peak is used to determine the location.

Using triangulation of the x and y positions given by the camera, it is possible to determine the location of breakdowns and correlate this to other data. Depending on the intensity or number of breakdowns this can vary the images detected on the camera. At low voltage intensities it is possible the breakdown will not be detected in one or both of the camera, and therefore it is not possible to determine the location. If there is more than one breakdown then there are multiple lines and it is not possible to uniquely determine the location of each breakdown. If there is one breakdown and both cameras detect it, then the coordinate can be determined.

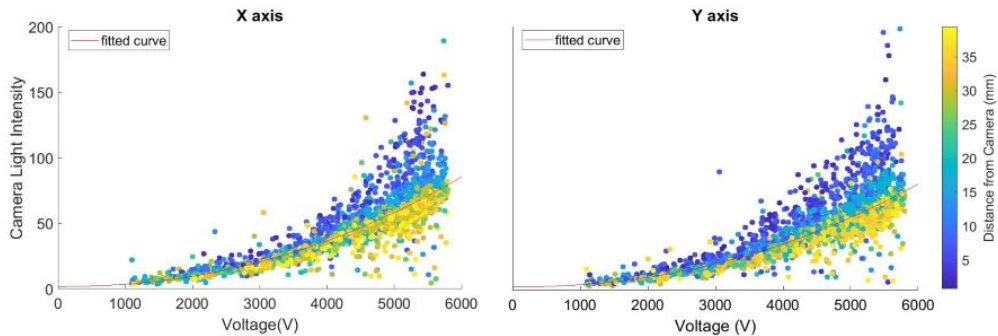


Figure 2.8: Camera light intensity for the x and y axis cameras with respect to the voltage with the indication on the distance from the cameras given as blue being the closest to yellow being the furthest away. This shows correlations of an increase in the light with higher voltages and the closer to the camera the breakdown is.

It was noticed throughout testing of different samples that the light from a breakdown showed a dependence of the voltage and distance from the windows. To quantify the observation and show the relationship between these variables Figure 2.8 is given. This is taken from a Cu OFE set of electrodes with a $60 \mu\text{m}$ gap, but was seen in most cases. Figure 2.8 shows the breakdown light intensity with respect to the gap voltage on the x-axis and distance from the camera displayed using a colour gradient. There is a clear dependence on the light intensity to the voltage supplied as shown in Figures 2.8. This can be seen as the increase in intensity with the increase in voltage with a fitted curve of V^2 to the data. The dependence

on the light from the breakdown detected by the camera has a dependence on the distance from the breakdowns seen in Figure 2.8, this is seen as the variation from dark blue as the closest breakdowns to yellow as the furthest away. It can be seen the the yellow colours are clustered lower on the y-axis compared to the blue being the highest with the highest intensity and closest to the camera.

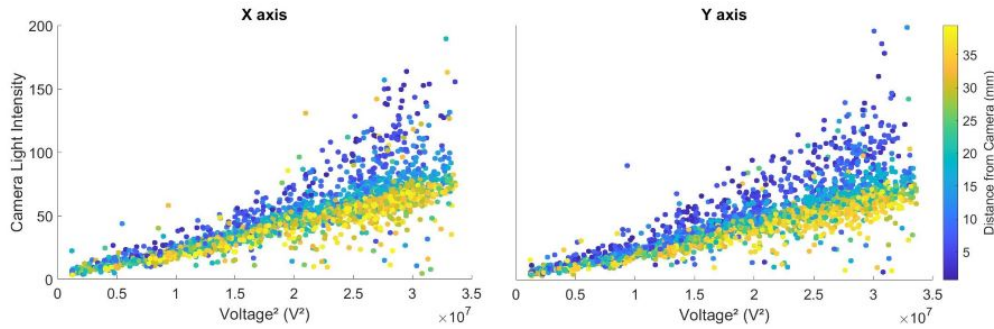


Figure 2.9: The same data as Figure 2.8 with the x-axis given as the voltage squared giving a linear relationship to the light intensity measured.

Figure 2.9 shows the same data as Figure 2.8 with the x-axis given a V^2 to match the fit shown in Figure 2.8. From this it can be seen that the data has a linear relationship between V^2 and the light intensity giving $V^2 \propto \text{Light Intensity}$.

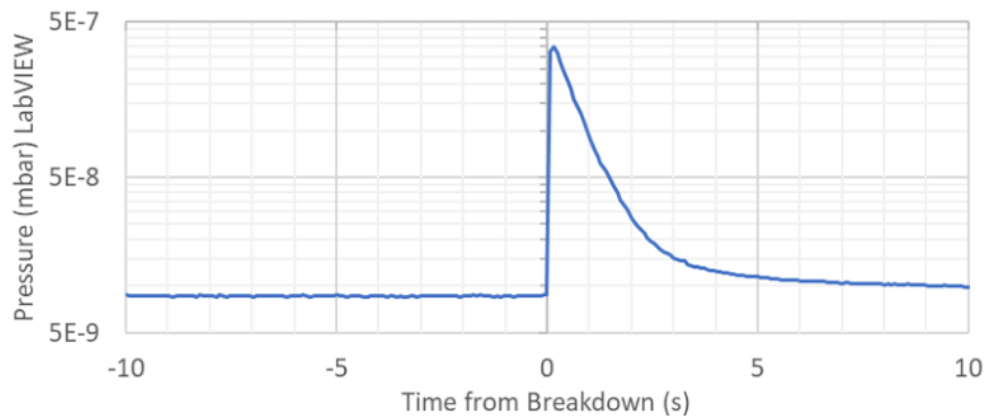


Figure 2.10: Filtered breakdown pressure spike recorded in LabVIEW to observe breakdown timing and pressure within the chamber.

The pressure gauge connected to the outlet of the vacuum pump is connected to the computer and the data is recorded via LabVIEW to a text file. On the

front panel of LabVIEW it is possible to see the pressure and in a digital format as well as a live plot of the pressure that can be used to determine if a breakdown happens. A threshold can be set in the code to count the number of times the pressure rises above that pressure value, indicating a breakdown occurred. This is not ideal as the pressure can change over time from the initial pump down making the threshold less accurate. For this reason a moving threshold was implemented into the code that uses the average pressure over an amount of time and if the pressure rises a certain amount above this then it would count as a breakdown. Figure 2.10 shows an example of the pressure recorded to the text file, from this it can be seen that a Gaussian filter has been used on the data making the pressure appear to last on the order of several second when in fact this would happen faster.

2.4 Conditioning

Previously the breakdown rate limiting conditioning algorithm was used for the pulsed DC systems, and was designed to replicate the X-box test stand conditioning, to make comparisons of the conditioning done in the pulsed DC system with the RF structures. This conditioned the electrodes whilst limiting the breakdown rate, which lead to the samples being conditioned with a constant breakdown rate and observing the point at which the field saturated. This resulted in the electric field exceeding the capabilities of the materials and causing clusters that reduced the field, and the code repeatedly pushing the field beyond its limit and causing further cluster. After a number of pulses with electric field essentially hitting a 'brick wall' of its field holding capabilities for the given breakdown rate, a deconditioning of the electrodes is seen with the field holding capabilities reduced. Deconditioning can be described as the reduction in the electric field holding capabilities with continued pulsing, observable as an increase in the breakdown

rate for a given electric field, and is most likely the result of damage to the surface. This can be seen as a gradual decrease in the electric field for a given breakdown rate or a cluster of breakdowns temporally causing a sharp reduction in the electric field. In some cases the surface can be reconditioned after deconditioning to recover the electric field holding capabilities.

A step-wise conditioning method was developed and tested during this thesis work. The objective of the step-wise method is to condition in a more safe way for the electrodes, to reduce the occurrence of deconditioning. This utilised the breakdown rate limiting algorithm but with target fields set at intermediate field with a number of pulses at each step. Details of these are given in the following sections.

2.4.1 Breakdown Rate Limit Conditioning

Figure 2.11 shows a flow diagram of the most important aspects of the breakdown rate limiting conditioning algorithm, that play a role in the conditioning process. An example conditioning flow using this method can be seen in Figure 2.12. On the left of the flow chart in Figure 2.11 is the general conditioning process that is looped if no breakdowns occur, determining whether to increase the voltage after each series of pulses depending on the breakdown rate and target voltage. The right side of the flow diagram shows what happens in the event of a breakdown. There are several parameters that need to be set before and can be changed if necessary during the tests, these include the voltage to condition to (Target V), the step size for the voltage (V step) that occurs every specified number of pulses (LoopPulses), repetition rate (Rep Rate) of pulses of a specific pulse length (Pulse Length), breakdown rate limit (breakdown ratelim), and the voltage reduction after a breakdown (Voltage reduction).

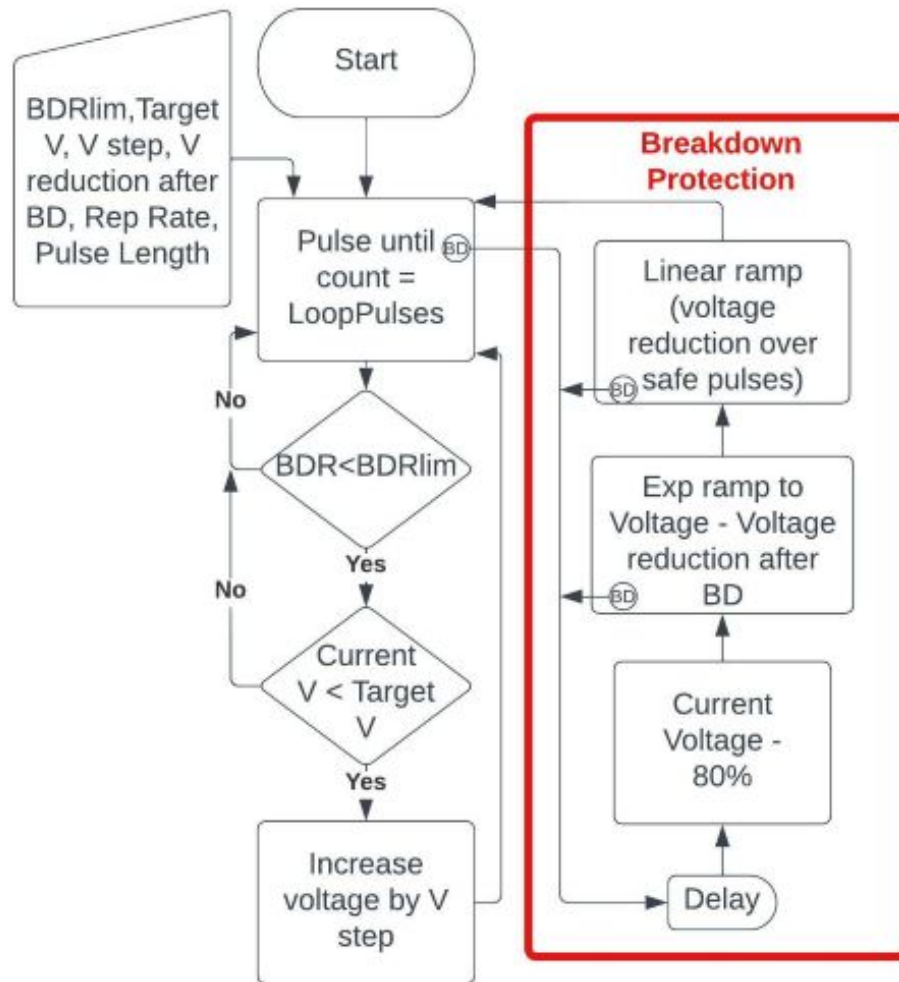


Figure 2.11: Flow diagram showing the relevant steps of the breakdown rate limiting conditioning algorithm, which was designed to replicate the conditioning of the CLIC X-box cavities.

To condition to a specified breakdown rate the system will pulse at a single value of voltage step for a set number of pulses, if no breakdowns occur during set number pulses it is below the breakdown rate. If breakdown occurred previously then the code will take into account the breakdown rate additionally before increasing the applied voltage. For the materials tested, a breakdown rate limit of 1×10^{-5} was used, meaning there were 1×10^5 pulses per step to maintain this breakdown rate. If no breakdowns happen throughout conditioning, after each set of pulses in the

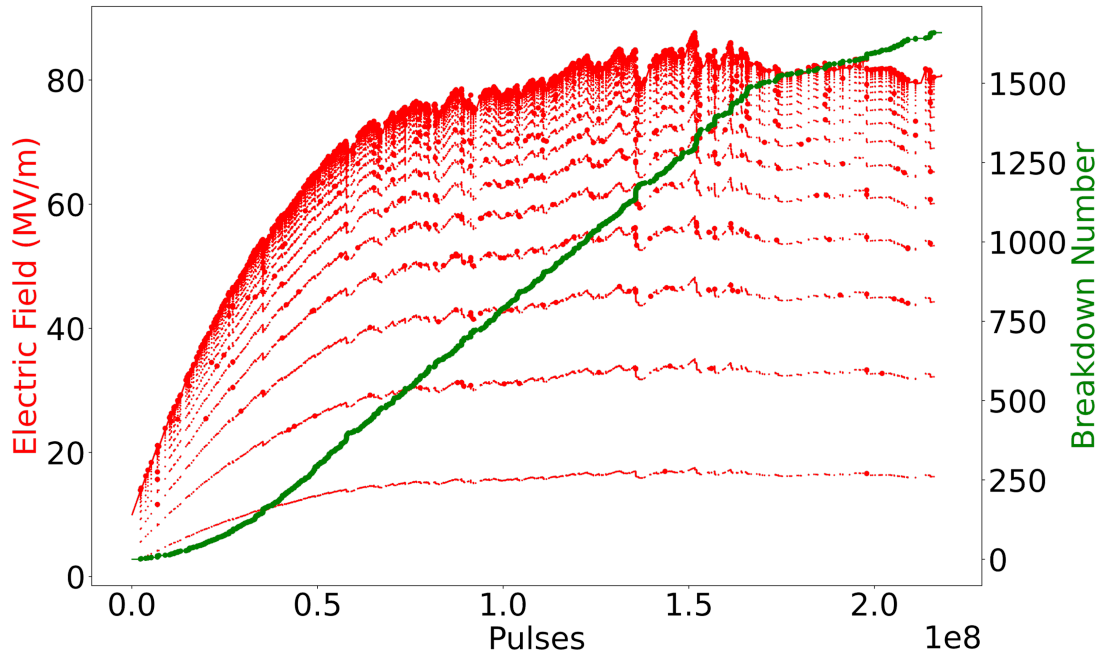


Figure 2.12: Example of conditioning of the pulsed DC system using the breakdown rate limiting algorithm for the CLIC X-band structures.

loop it compares the current voltage to the target voltage and if below then it would increase periodically to bring the measured breakdown rate closer to the target value. When the applied voltage reaches the target voltage it maintains the same voltage and continues the loop until stopped.

When a breakdown happens, the supplied power is held high for 600 ns to replicate an RF accelerator reaction time, then the pulsing is inhibited for a few seconds to allow the vacuum to recover. After this the voltage ramps up asymptotically from 20 % of the current voltage to the current voltage minus the breakdown reduction, normally set to 10 V for the following tests. It pulses at 20 different intervals with 100 pulses for each, as seen in Figure 2.13a. The values for each step are calculated using the equations:

$$V_{out} = V_{prev} + (V_{target} - V_{prev})/Factor \quad (2.4)$$

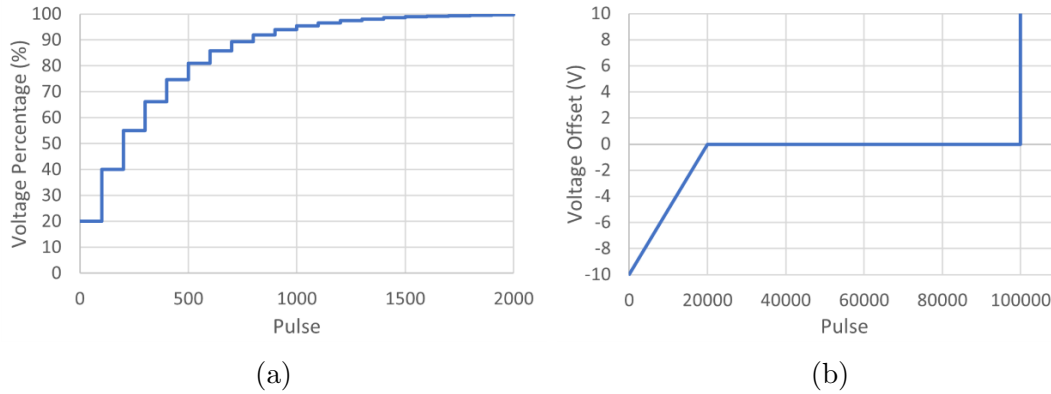


Figure 2.13: (a) shows the exponential ramp increase from the voltage after a breakdown and (b) is the ramp of the final 10 V over 2000 pulses with a step of 10 V after 100000 pulses.

Where V_{out} is the voltage to apply for the current step (up to 8 kV), V_{prev} is the voltage applied in the previous step, V_{target} is the voltage achieved before the breakdown minus 10 V and Factor is the amount the difference between the current and target voltage is divided to make the asymptotic increase to the target voltage. The Factor value for the measurements shown was set to 4 throughout all tests to be discussed in this thesis.

After completing the final step of the ramp seen in Figure 2.13a, the voltage is ramped linearly for a number of pulses given as 20000 pulses in Figure 2.13b and then continues pulsing at the target voltage until the final pulse when a step in voltage is made. After the breakdown recovery algorithm, the code proceeds into the main loop as described. If a breakdown occurs during the ramp after a breakdown then a further reduction of the target voltage is made and the breakdown protection loop starts again. When a large temporal cluster of breakdowns occurs this can lead to the breakdown rate exceeding the specified limit in the parameter. As a result of this, a number of cycles of pulses will occur without an increase in the electric field, until the breakdown rate as calculated by the code no longer exceeds the threshold.

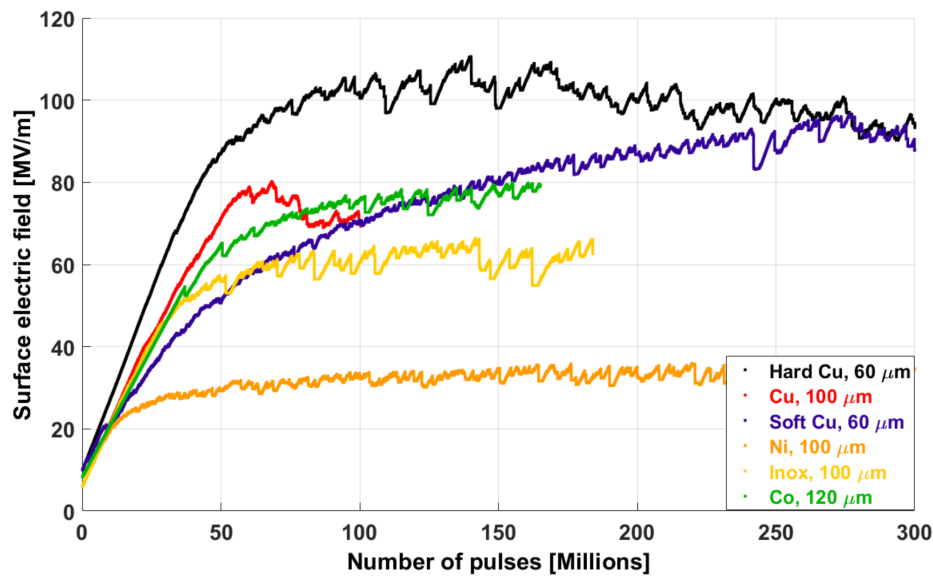


Figure 2.14: Conditioning plots of various electrodes in the LES [60]. The black plot labelled ‘Hard Cu’ shows an example of a cycle of repeated breakdown clusters, resulting in damage to the surface and a gradual decrease in maximum field.

One of the issues of this code for conditioning is that the voltage will eventually be ramped beyond what the material is capable of withstanding. When the system reaches a voltage which exceeds the limiting value, a cluster of breakdowns will occur. This then results in the code reducing the operating voltage to try to maintain the breakdown rate below the specified value. Once the breakdown rate goes below the limit, the code ramps up again until the and the cycle repeats indefinitely. Over time this causes more significant damage to the surface through breakdowns and a degradation of its performance can be observed. An example is shown in Figure 2.14.

2.4.2 Step Wise Conditioning

As mentioned, during the conditioning of more recent materials a more careful step-wise approach was taken whilst conditioning. The step-wise approach may

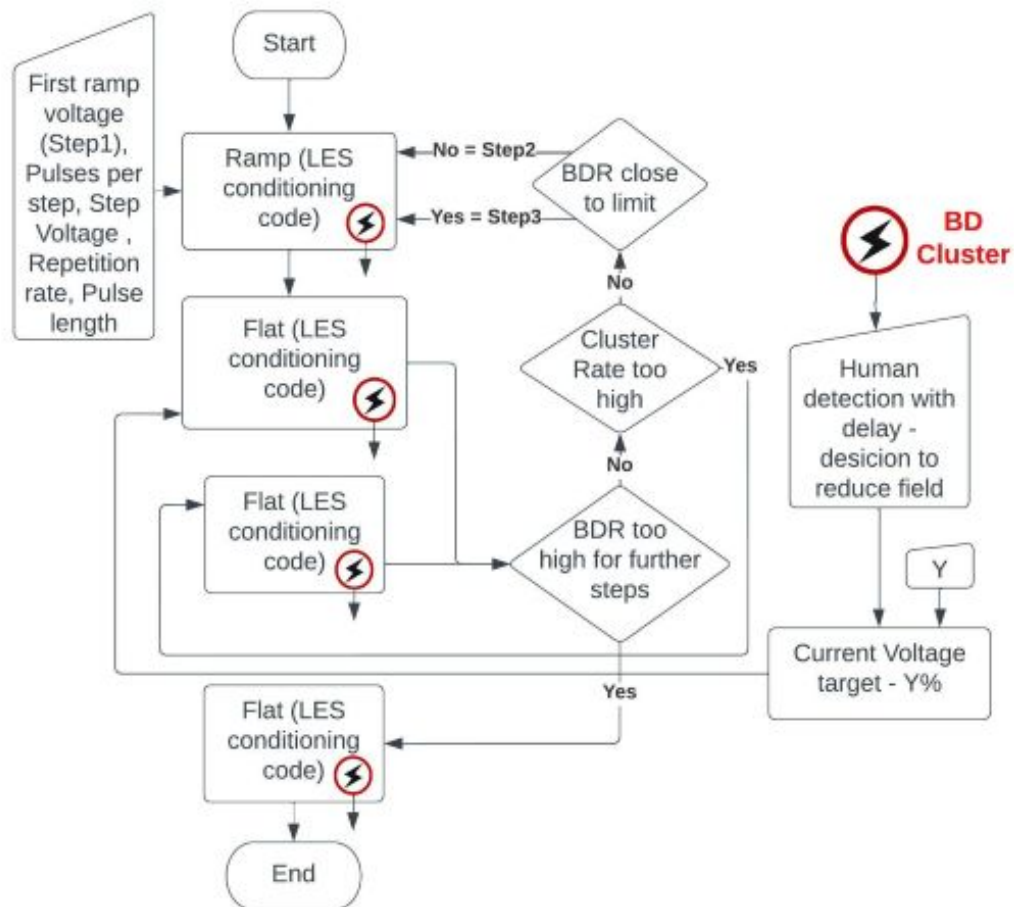


Figure 2.15: Flow diagram showing the general format of the step-wise conditioning method whilst controlled by the operator, utilising the breakdown rate limiting conditioning algorithm for pulsing during ramps and flat sections using different parameters.

also provide insight into the conditioning process. The implementation of this new approach has been 'manual' for the data shown in this thesis. At a later stage this could be programmed into the LabVIEW code to make the results more comparable, details of this are given in Chapter 8.3.7.

Figure 2.15 displays a flow diagram of how the previously explained breakdown rate limiting code was utilised to condition the following pairs of electrodes, in a step wise manner. The first stage of the step-wise conditioning process shown in Figure 2.15, was an initial ramp to a set voltage as specified by the user.

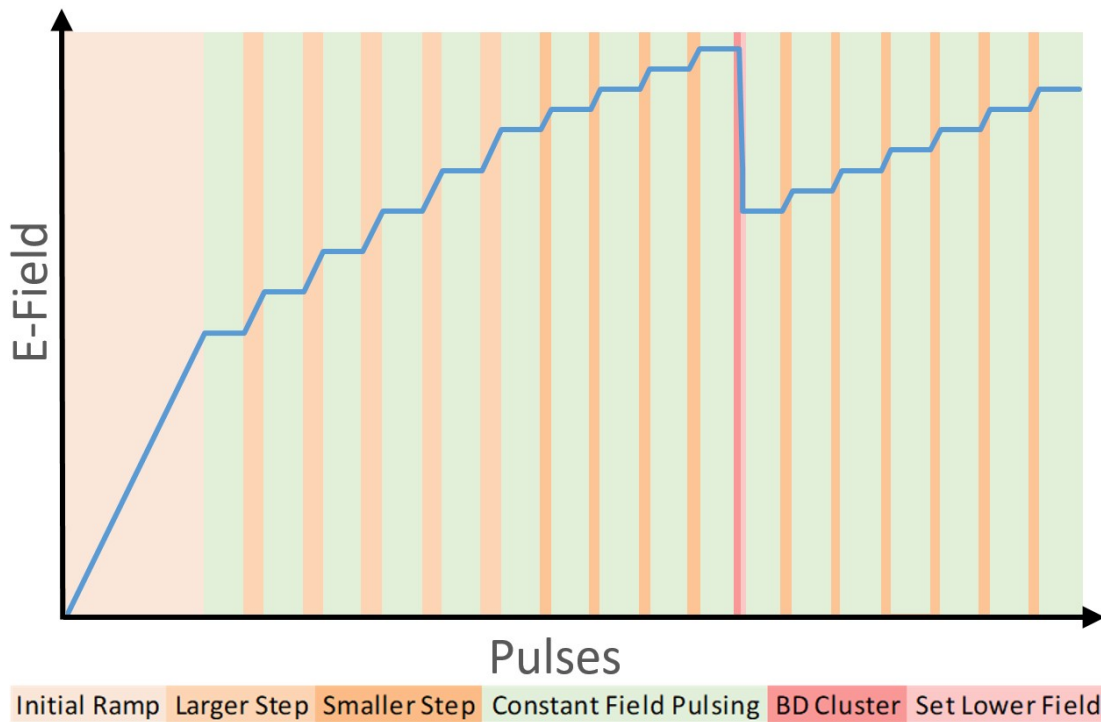


Figure 2.16: Theoretical plot of the electric field vs. the number of pulses for the step-wise conditioning method. Showing the initial ramp in voltage, a series of flat pulses and small ramp increases, then smaller changes in voltage, a cluster in breakdowns leading to a reduction in field, and finally reconditioning.

Once electric field reaches the specified target electric field it stops increasing. It then pulses at a constant electric field for an amount time before setting the parameters to increasing the electric field further. Figure 2.16 shows an example of conditioning using steps and several pulses at each step. When the system was stable larger steps were used and as it became more unstable a smaller step was applied. If a temporal cluster in breakdowns occurred then the user would set a lower field as the target and recondition from this point.

Previous studies have shown that conditioning appears to be more correlated to the number of pulses than to the number of breakdowns [75]. Prior to that study, it was thought that the way to condition electrodes was through breakdowns, and that the breakdowns would remove the surface defects. When comparing the

conditioning field for different structures against the number of pulses and the number of breakdowns, it was seen that the closer correlation was through the number of pulses. There is also evidence that the breakdowns themselves can lead to degradation of the structures and therefore the achievable field, with each breakdown either making the surface worse or better and if worse this can lead to follow up breakdowns [76], [77]. This suggests that it would be possible to condition a structure with the minimal number of breakdowns, but currently it is unknown how to predict when a breakdown would happen or how to stop them from happening.

When the system is set to run with a fixed target breakdown rate, is it possible that the conditioning algorithm can increase the field setting beyond the limit of the material and cause a deconditioning affect. The aim of the proposed new method is to ensure the sample is conditioned effectively without bringing it to the point of deconditioning. For this reason, at the different steps the breakdown rate was observed for signs of reducing and the surface improving before initiating a different step. This ability to ‘settle’ at different field suggest it is conditioning over these pulses and that another step may be possible. With the aim to avoid setting the field above the field holding capabilities of the material certain characteristics were observed at each step to try to determine whether another step was possible, as increasing the field beyond the material capabilities could degrade the surface. These characteristics include the breakdown rate, clusters in breakdowns, and multiple breakdowns during a single pulse determined by the cameras. Generally, clusters in the breakdowns and multiple breakdowns during a single pulse are signs of instability, suggesting a proximity to the limit of the material.

Two phrases will be used throughout this thesis; these are ‘maximum field’ and ‘stable field’. The ‘maximum field’ is the maximum field achieved throughout the whole conditioning, this means that it would have conditioned up to that field

using the breakdown rate limiting algorithm. In the cases that the maximum field is not the same final stable field it will be explained. For example with the example given in Figure 2.16, the maximum would be the electric field before the drop due to a large cluster. It should be emphasised that the maximum field has to be reached by the conditioning algorithm and not set manually. This means that the electrodes must have undergone at least 10^5 pulses at this field level with at most one breakdown. The other term, ‘stable field’, is the final electric field that is deemed to be stable, but that another step in the electric field could lead to a breakdown cluster, degrading the material. This decision varies due to it being made by human judgement and not programmed but is based on the breakdown rate and its ability to stabilise at the different electric field steps, the existence, regularity and size of breakdown clusters, and the existence of multiple breakdowns during a single pulse. Each target field was set manually, and for most cases was not increased unless the pair showed signs of the breakdown rate settling and being able to reach around 1×10^7 pulses without a breakdown. In some cases the stable field is the same as the maximum as the field did not exceed the field holding capabilities of the material. It is possible that these could have been conditioned to higher electric field, but doing so could have caused a deconditioning effect and to condition like this would most likely require several tests of each material to know how much it can be pushed before degrading.

2.5 Breakdown Rate Error Calculation

After conditioning of the different materials, a measurement of the pulse length dependence on the breakdown rate was conducted. Pulse length dependence measurements were done once the electrodes were considered fully conditioned. For each pulse length tested the electrodes started at a reduced field between 5 MV/m

and 10 MV/m to recondition to the target electric-field. The field was maintained for an amount of time at each pulse length in order to determine the breakdown rate before changing to the next pulse length step. The breakdown rate was calculated for each by dividing the number of breakdowns by the number of pulses. An error term was also considered, given by equation (2.5), which gives an indication of the errors as a results of the amount of breakdowns with respect to the number of pulses for each pulse length.

$$SE = \frac{\sigma}{\sqrt{n}} = \frac{\text{breakdownrate}}{\sqrt{\text{No.BD}}} \quad (2.5)$$

where, SE = standard error of the sample, *sigma* = sample standard deviation, n = number of samples, breakdown rate = Calculated Breakdown Rate and No.BD = Number of Breakdowns in sample.

2.6 Electrode Edge Electric Field Enhancement

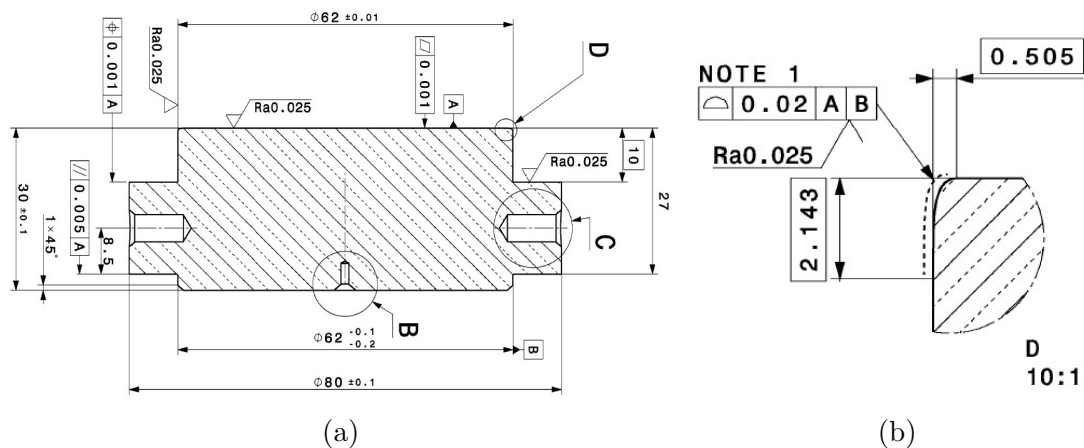


Figure 2.17: (a) Shows a cut out from the drawing of the CLIASTND0185 electrodes given in Appendix A, showing the cross section of the electrode design, and (b) shows the zoomed view of the details of the edge, where "NOTE 1" says "Dimensions which are not visible on the drawing should be extracted from the 3D-model."

Electrode designs to avoid the electric field enhancement on the edge had been a consideration when designing the system. Initial electrode designs used a simple 1 mm radius [68], but it was seen that there were many breakdowns around the edge of the electrodes. For this reason, studies were done to try and reduce the electric field enhancement by changing the shape of the edge. Simulations were done using COMSOL to create an edge, using an iterative code to optimise the location of consecutive points along the edge [78]. The drawing used for this could only be described by the individual points, which was often misinterpreted from the drawings. There was no equation for this edge and only a set of points which made this difficult to convey to machining companies, this detail can be seen in Figure 2.17. The drawing specifies dimensions that can be read as an ellipse and the note specifies to refer to the 3D model, which lead to the electrodes being machined incorrectly on some occasions. This edge when machined as desired, also did not solve the problem of the breakdowns around the edge of the electrodes [60].

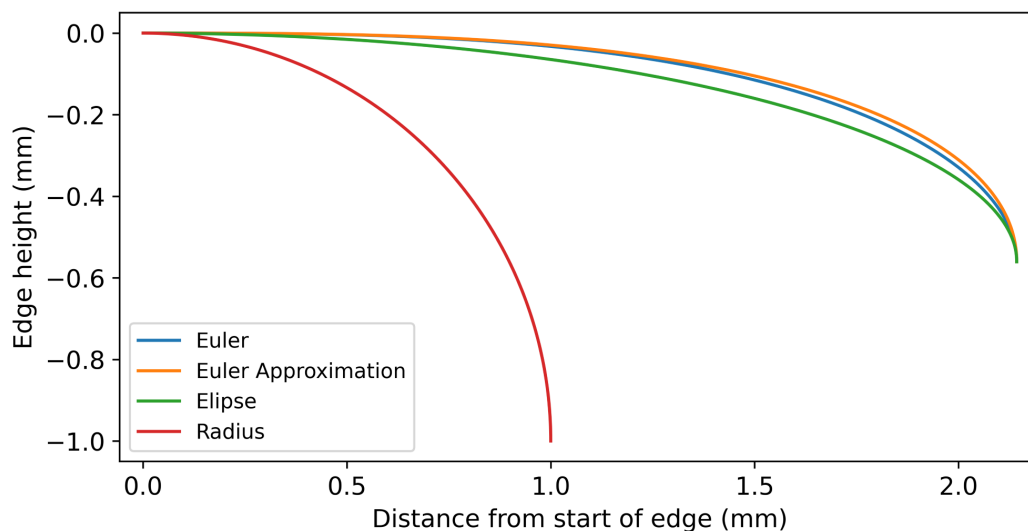


Figure 2.18: Physical shape of edges for Euler spiral, Euler spiral approximation, ellipse and a 1 mm radius.

Whilst an ellipse was never intended to be the shape of the edge, from the drawing seen in Appendix A, it looks like an ellipse, which caused confusion with

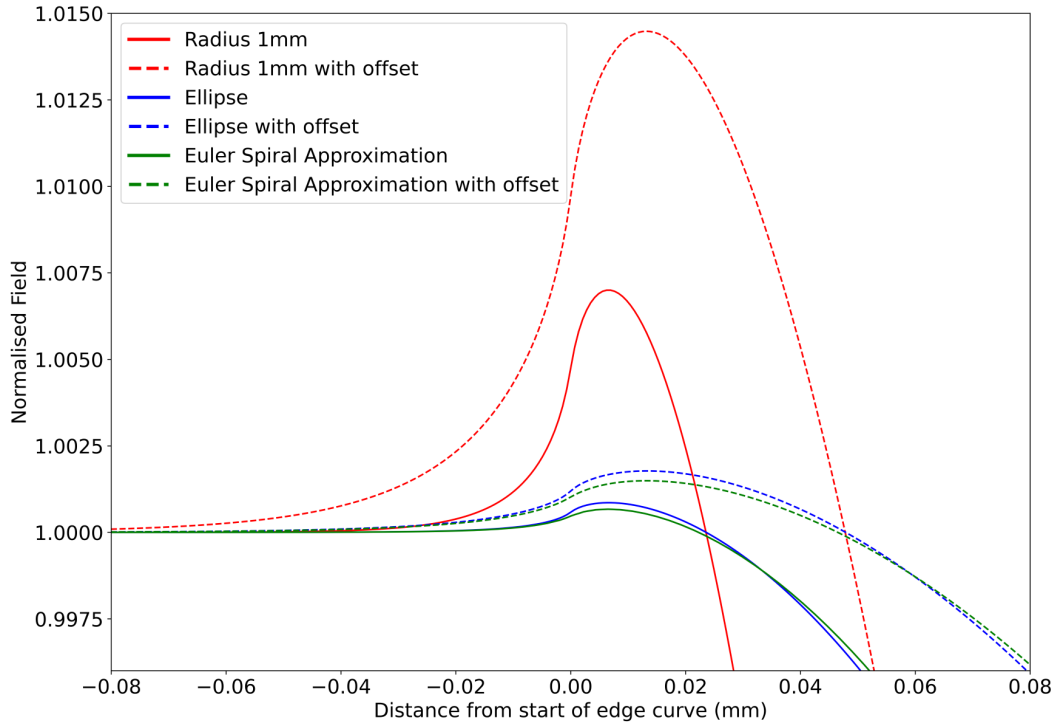


Figure 2.19: Normalised electric field on the anode for electrodes the same size and with an offset of 0.5 mm to replicate a small anode to large cathode for the different edge shapes, Euler spiral approximation, ellipse and a 1 mm radius.

machining and metrology companies. Due to still having issues with the edge of the electrodes during tests and with machining due to the ambiguity of the drawing, it was decided to generate an equation for the edge. Figure 2.19 displays the different edges including the 1 mm radius, an ellipse, Euler spiral and Euler spiral approximation. To limit the field enhancement, use of a Euler spiral equation was chosen, with the normalised expression given as [79]:

$$\begin{aligned}
 x &= \int_0^L \cos(s^2) ds, \\
 y &= \int_0^L \sin(s^2) ds,
 \end{aligned} \tag{2.6}$$

where x = x-axis position, y = y-axis position, L = length of the curve, s = distance along the curve.

The Euler's spiral was decided due its curvature beginning at zero and varying linearly as a function of curve length [79][80]. The most important part of the curve is the initial decrease in height from the critical surface, as this is when the electric field enhancement occurs. Due the the Euler equation giving a tangential transition from the critical surface and gradually changing the curvature this should maintain a low electric field enhancement at the edge. Due to the equations for Euler spiral shown in equation (2.6) not being of the form x as a function of y , an approximate equation was produced, which is useful for inputting into a CNC machine, given as [80]:

$$y = 2.252551272 \left((3x)^{\frac{1}{3}} - \frac{(3x)^{\frac{1}{3}}}{10} \right) \quad (2.7)$$

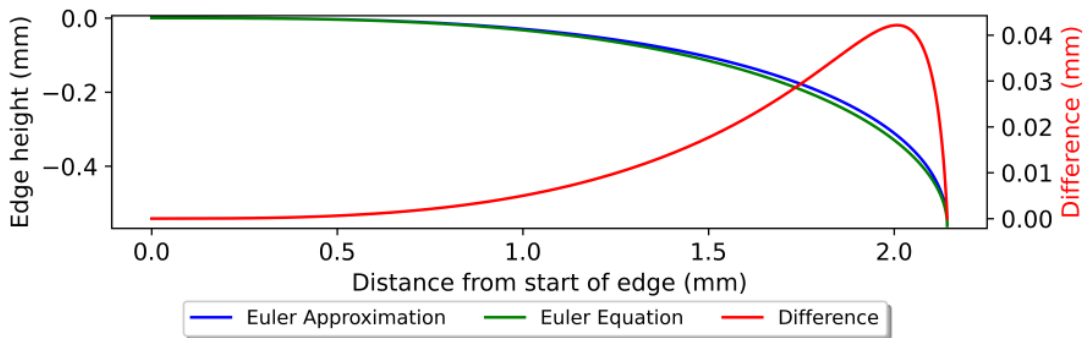


Figure 2.20: Physical shape of edge using the Euler equation and approximation equation and the difference in height for each value of x

The Euler equations and the approximation were compared, both for shape and for resulting field enhancement. Figure 2.20 shows the results curve from the Euler equation (2.6), the approximation equation (2.7) and the difference between the 2 curves. It can be seen that the different is minimal at the critical point of the curve where the field enhancement is the highest. Both curves shown are scaled to achieve a longer range on the x -axis, to closely match the previous drawing and to decrease change in height per machining step. For the approximate equation

the x values range from 0 to $2^{\frac{3}{4}}3^{-1}$, which is the point at 90 degrees to the critical surface that is connected to the edge, the y value this gives is 2.143. It is also worth noting that even with the perfect edge in simulations to remove the electric field enhancement completely, machining will never achieve the same. Simulations given of the electric field enhancement for the different edge shapes give an indication of the difference in field enhancement, but when machined will most likely have an increased enhancement due to machining tolerances and roughness.

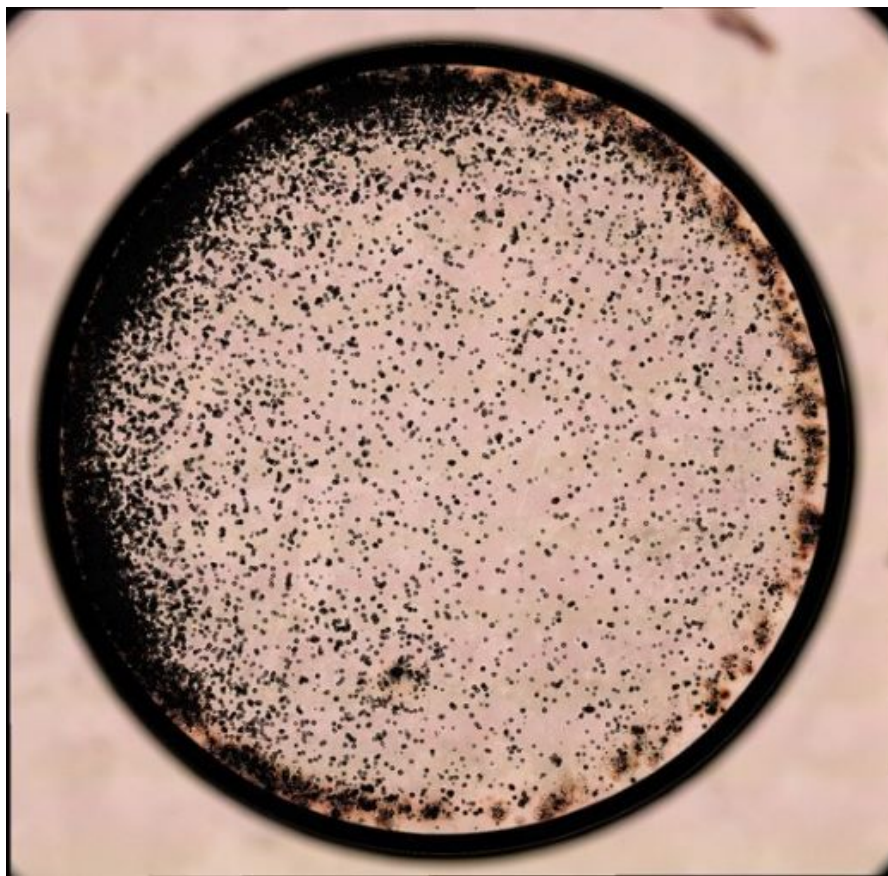


Figure 2.21: Breakdown clusters on the edge of half of the electrode [81]

Figure 2.21 shows a microscope image of a copper electrode tested as a pair of the same size, using a previous edge design [81]. There is a visible difference between the number of breakdowns on one side compared to the other. Previous explanations for this characteristic was that the electrodes were placed at an angle

leading to a higher field on one side compared to the other [60]. Whilst this would explain such a result, the design of the system should reduce this possibility with the use of the high precision ceramic between electrodes and securing the sandwich of electrodes and ceramic through compression. To secure this setup four screws are tightened using a torque screw driver, with curved washers and alternating between screws to avoid over tightening one side compared to another.

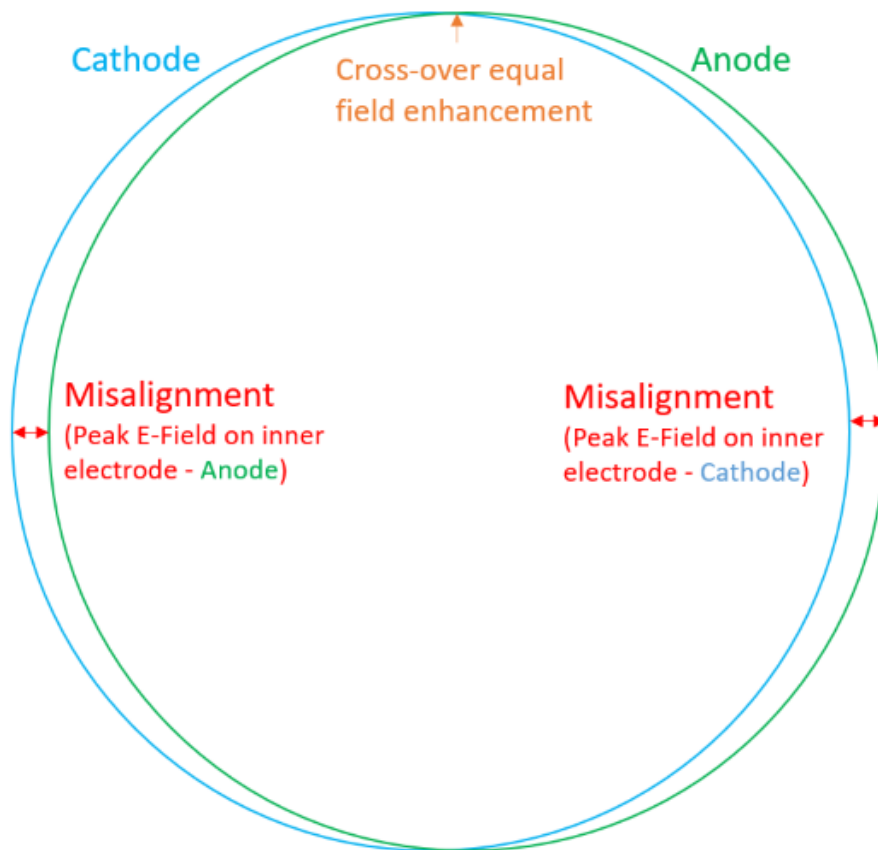


Figure 2.22: Misalignment of electrodes causing electric field enhancements on the Anode and Cathode on different sides

A more recent theory as to the cause of the breakdown locations clustering on one side would be misalignment of the electrodes. Observations of the electric field during between the transition from the high-field area are dependent of there being a surface of a sufficient distance to cause a significant field enhancement. If the electrodes are misaligned this could lead to a field enhancement on the cathode

on one side and the anode of the opposite side of the misalignment. Figure 2.22 shows an exaggerated example of a misalignment between the cathode and anode if they have the same area. Labels show the points at which the electrodes most misaligned and whether this is a peak electric field enhancement on the anode or cathode, where the peak is on the inner edge, being the edge of the electrode that is parallel to the opposing electrode rather than on the over hang with a reduced electric field. There is also a point where the two electrode edges are aligned and the electric field are also equal. There is evidence that breakdowns are initiated on the cathode [82], [83], therefore having a electric field enhancement on the cathode is more likely to lead to breakdowns. In this case the electric field enhancement around the edge of the electrodes would increase between the maximum misalignment on one side to the other, like the peaks seen in Figure 2.23. This increase appears to also correlate with the breakdown density shown in Figure 2.21.

Figure 2.23 shows a plot of the electric field enhancement for different misalignments between electrodes. Starting from 0 μm if the electrodes were perfectly aligned, or different values of misalignment between the electrodes, up to a misalignment of 140 μm . The purpose of these simulations was to determine the point at which the electric field enhancement saturates to determine the likely field enhancement in the experiment. From Figure 2.23 it can be seen that the enhancement saturates at around a 80 μm misalignment. The reason for saturation is that mechanical drop off of the electrode edge becomes far enough from the flat surface of the opposing electrode that it is essentially a flat surface to the smaller electrode. There is evidence that the electrodes were misaligned more that 100 μm using central breakdowns, to be shown in Chapter 3.6, Figure 3.17, suggesting this is a plausible reason for such breakdown characteristics. The electric field enhancement present around the edges of the electrodes, corresponds to the peaks

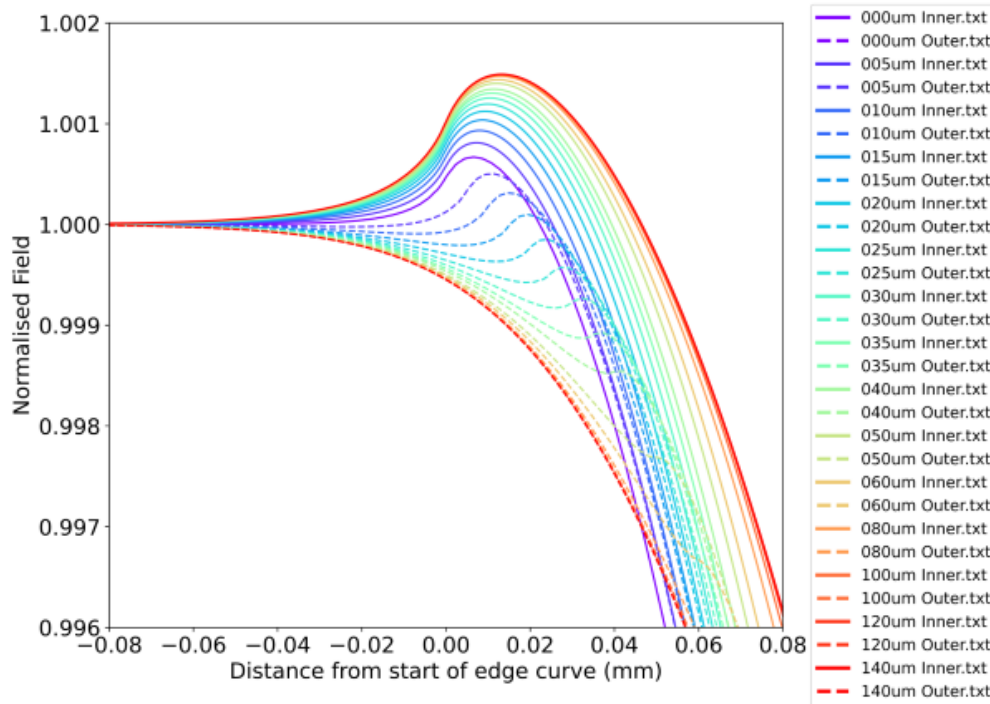


Figure 2.23: Edge electric field on the inner and outer edges of electrodes for different steps in the misalignment

from the lowest misalignment value line to the highest depending on the physical misalignment of electrodes and it will saturate either side if misalignment is large enough.

Table 2.1 displays the maximum normalised electric field as seen in Figure 2.23, highlighting the enhancement for different values of misalignment for electrodes with the Euler approximation edge. This highlights that the electric field enhancement saturates at around a $80 \mu\text{m}$ misalignment and that the electric field does not exceed the chosen surface electric field value for a misalignment more than $20 \mu\text{m}$ from the opposing electrode. As the Euler approximation edge was used for these simulations, the electric field enhancements given are relatively small. Earlier versions of electrodes had the 1 mm circular radius edge which would increase this electric field enhancement and effect as seen in Figure 2.19, machining will also play a role in this result.

Misalignment (μm)	Normalised Inner E-Field	Normalised Outer E-Field
0	1.000669	1.000669
5	1.000811	1.000502
10	1.000933	1.000313
15	1.001036	1.000098
20	1.001123	1
25	1.001195	1
30	1.001255	1
35	1.001303	1
40	1.001343	1
50	1.0014	1
60	1.001436	1
80	1.001471	1
100	1.001484	1
120	1.001489	1
140	1.001491	1

Table 2.1: Normalised electric field enhancement for the range of misalignments as shown in Figure 2.23

After simulating different edge shaped with the purpose of being able to provide exact edge details on the drawing it was decided to use the Euler approximation equation (2.7). This produced a lower electric field enhancement compared to the radius and ellipse, whilst providing a specific equation to define the edge in drawing to avoid confusion during machining.

Another issue that is also considered is if the electrodes are parallel as this would also make an uneven electric field. This non-parallelism could arise from a ceramic that is not parallel, but also from an uneven amount of pressure when securing the assembly in the system. Appendix F displays the drawing for the ceramic which specifies a flatness and distance from the reference surface defining the parallelism both as 0.001 mm. These become important values when talking about 20 μm to 100 μm gaps where this difference in machining can vary the gap from 5 % to 1 % respectively which directly influences the electric field as given

in Equation [2.8]

$$E = \frac{V}{\text{Nominal Gap}} \times (\text{Gap Error})^{-1} \quad (2.8)$$

Where E = electric field (V/m), V = gap voltage, Nominal Gap = intended gap of the spacer (m), and Gap Error = the percentage difference of the real gap from the nominal gap. In one case of having ceramics machined the flatness was within tolerance but they had an angle of 0.02 degrees which for a 40 mm diameter would equate to a height difference of approximately 13.96 μm from one side to the other. For a gap voltage of 6000 V and a central gap at 60 μm the electric field would range from around 90 MV/m to 113 MV/m. This was considered unusable due to the large difference in electric field and therefore was re-machined but is an example of the importance of tolerances of the ceramic.

Chapter 3

Conditioning of Different Materials

3.1 Introduction

Both theoretical simulations and physical experiments have been conducted to study the effects of different materials, limiting the field holding capabilities. The main observation from this was that the conditioning field appeared to depend on the crystal structure of the material [17]. These prior physical tests used different parameters for the different materials making them difficult to compare and potentially introducing errors of interpretation. The results shown here attempted to keep the conditioning parameters for each material as similar as possible for a better comparison.

The most common material tested in the pulsed DC system is Cu OFE as this is the most common materials used in RF structures. A more recent collaboration with the Linac 4 RFQ project led to the testing of multiple materials in the pulsed DC system. Cu OFE was tested either hard as machined or with different methods of heat treating. Each of the materials have different material properties that could

determine their performance.

The motivation for choosing these materials will be discussed in the Chapter 4.6. The materials tested for the RFQ project include Titanium Alloy (TiAl4V6), Niobium (Nb), Copper OFE (Cu), Tantalum (Ta) and Copper Chromium Zirconium (CuCr₁Zr). In addition to the RFQ motivated program, an Aluminium Alloy (AlMgSi1) was also tested with this choice of material being related to the spectroscopy measurement to be discussed in Chapter 6.5. This chapter will focus on the materials and their electric field holding performance isolated from the other tests conducted which will be covered in detail in the following chapters. The results for the individual pairs of electrodes of different materials will be discussed in the order of performance with respect to the stable field achieved. There are two pairs of Nb electrodes shown, one as-machined and the other having undergone Buffer Chemical Polishing (BCP), due to issues during conditioning of the non-polished pair, to be discussed in more detail.

Measurements of the pulse length dependence on the breakdown rate are given for pulse lengths between 100 μ s and 1 ms for each material tested. As this did not appear to display a pulse length dependence an additional test with pulse lengths of 1 μ s and 100 μ s is also shown with a clear increase in the electric field holding capabilities for the 1 μ s.

Additional observations made during tests are also presented in isolation to the results. There include oxidation of heat treated Cu OFE and the transfer of contamination on the surface during high field testing. Another observation made from the CuCr₁Zr electrodes, was a melted flower type shape, that is possible evidence of self organising plasma as the result of a central tip from machining and influenced by machining lines.

3.2 Conditioning Results and Discussion

3.2.1 Titanium Alloy (TiAl_6V_4)

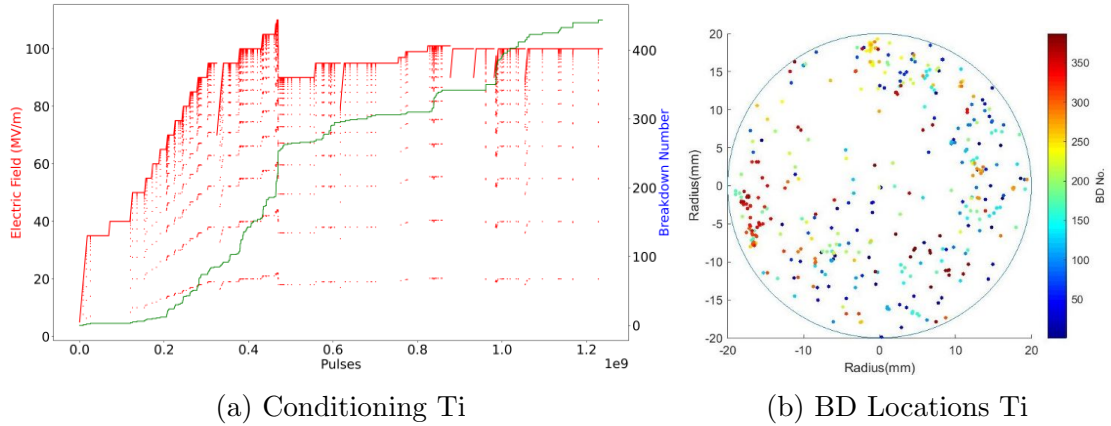


Figure 3.1: Shows the conditioning of the TiAl_6V_4 where, (a) gives the electric field in red and the breakdown count in green and (b) shows the breakdown locations detected by the camera with the first to the last breakdown indicated with colours dark blue through to dark red.

The Ti alloy achieved the highest stable electric field. One issue with the program used for conditioning is its ability to detect large clusters in breakdowns that may lead to deconditioning of the electrode pairs, as seen in Figure 3.1a. The conditioning of the Ti alloy is a good example of a cluster in breakdowns. Where 66 breakdowns occurred in 7×10^6 pulses reducing the electric field and a process of reconditioning was used to recover the electrodes. It is not always possible to recondition the electrodes. Reconditioning consists of lowering the target voltage to see if the algorithm can correct whatever effect caused the deconditioning. The cause of a cluster like this is not completely understood and while we cannot predict the cluster, detecting it earlier may allow for the user to reduce the amount of damage caused. After a large event like this there can be a significant change to the surface and reconditioning can help to improve this in a more controlled and less destructive manner.

3.2.2 Copper Chromium Zirconium (CuCr_1Zr)

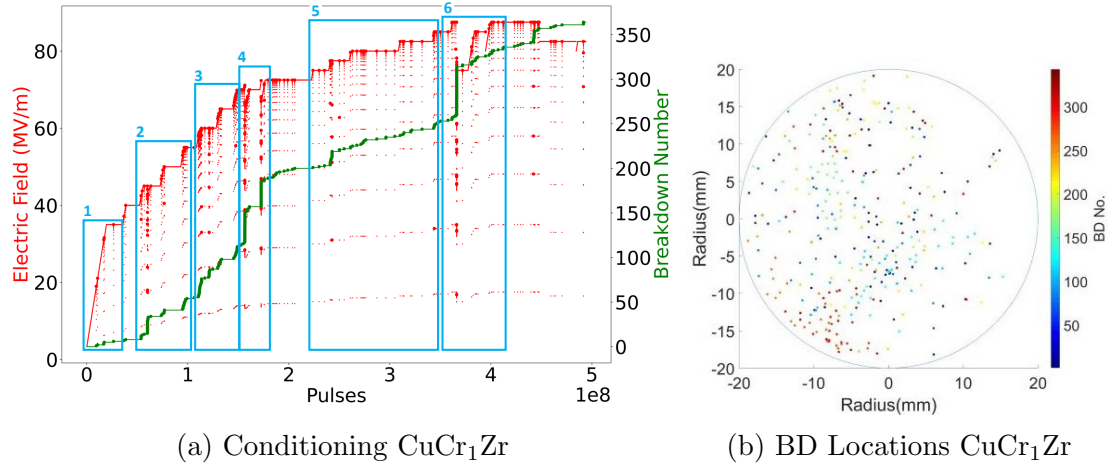


Figure 3.2: (a) Conditioning of CuCr_1Zr with boxes to highlight the initial ramp, small ramps where breakdowns occurred after a number of steps, ramps with breakdowns throughout, small clusters in breakdowns, additional ramps without issues after clusters, and a large cluster with a recovery process used. (b) Shows the breakdown locations with dark blue to dark red indication the first to last breakdown respectively.

A good example of the conditioning method used can be seen in figure 3.2a showing the conditioning of CuCr_1Zr . Also included in this image are numbered boxes to highlight different phases of conditioning and breakdown behaviour seen in the conditioning in order of the initial ramp, smaller ramps where breakdowns occurred after a number of steps, ramps with breakdowns throughout, small clusters in breakdowns, additional ramps without issues after clusters, and a large cluster with a recovery process used. Box one from this plot shows the initial step with very few breakdowns observed. The second box highlights the following steps of 5 MV/m where a trend develops of the breakdown rate starting low and increasing on each ramp to the point of flat running. This suggests that some form of conditioning was occurring whilst running flat at a fixed voltage, that allows the next step to occur with a reduced number of breakdowns.

Box three shown in Figure 3.2a displays a larger number of breakdowns

throughout the step. This increased number of breakdowns appears to be related to the larger cluster in the breakdowns further on in the conditioning, this could mean breakdowns during a ramp in the electric field could be used as an indicator of a possible cluster that could occur. Visible in the following step highlighted as box four, are two relatively large clusters in breakdowns with respect to time. This caused a reduction in the electric field, after the cluster the electrode pair were able to recover to the previous stable electric field. The electric field was then held constant to determine the stability of the electrode pair before increasing the electric field further. Once it was determined that the electrodes were able to maintain the electric field stably, conditioning was continued as highlighted by box five. After a large cluster reducing the electric field significantly from 85 MV/m highlighted by box six, the target electric field was reduced manually to 75 MV/m to obtain a stable electric field before reconditioning. It was able to recover to the previous maximum electric field, but the breakdown rate did not appear to settle and consisted of a number of cluster in breakdowns and therefore was not conditioned higher than this.

The conditioning of CuCr₁Zr may be further evidence of conditioning being a function of the number of pulses rather than breakdowns and could be a good method of conditioning for this reason [75]. This result is for CuCr₁Zr but where this conditioning method appears to be beneficial but there is evidence that this method is less effective for other materials, for example Nb to be discussed.

With regard to the breakdown locations, there are a few small clusters on the surface that did not seem to dominate the breakdowns. An observation was also made using the breakdown locations over time and pulses, this showed that breakdowns clustered spatially during a temporal cluster. It can also be seen that the breakdown locations are asymmetric over the surface, which was most likely the result of non-parallelism between the electrodes.

3.2.3 Niobium (Buffer Chemical Polished)

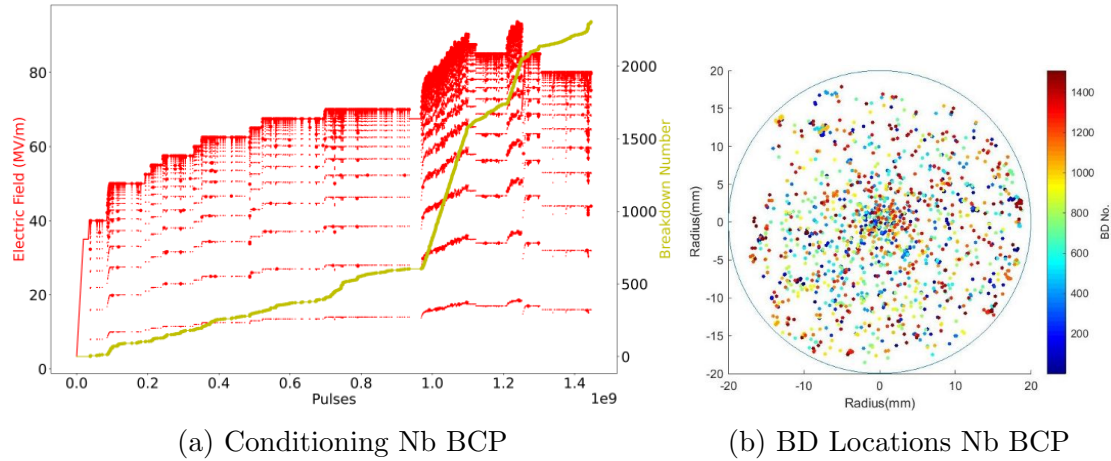


Figure 3.3: Shows the conditioning of the Nb BCP pair where, (a) gives the electric field in red and the breakdown count in green and (b) shows the breakdown locations detected by the camera with the first to the last breakdown indicated with colours dark blue through to dark red.

During each step with Nb BCP the breakdown rate was relatively high without settling over time, for other materials this would have indicated being close to the limit of the material. When the field was increased the breakdown rate did not significantly change and was relatively regular without large clusters. The method used to try to determine whether a pairs of electrodes was close to their electric-field limit was to pulse at at a constant electric-field for each step, to determine if the breakdown rate would decrease. For some materials this seemed to work, with the breakdown rate decreasing at each electric field and then increasing to the next electric field. As mentioned this was not the case for Nb, but it appeared to have stable but relatively high breakdown rates at each step. This suggests that the pulsing was not aiding in the conditioning of the Nb. At around 9.8×10^8 in pulses it can be seen that the conditioning changes in appearance. At this point the breakdown rate limiting conditioning algorithm with a target field beyond the capabilities of the material was used to condition more efficiently. This increases

the electric field whilst maintaining the set breakdown rate, to observe the field at which it saturates. Using this method showed a saturation of the electric field at around 90 MV/m, from this point a more stable electric field was found. From Figure 3.3a, it can be seen there there are several reductions in the electric field to observe whether that electrodes are conditioned at lower electric field and in this case a reductions in the breakdown rate can be seen with a decrease in the electric field.

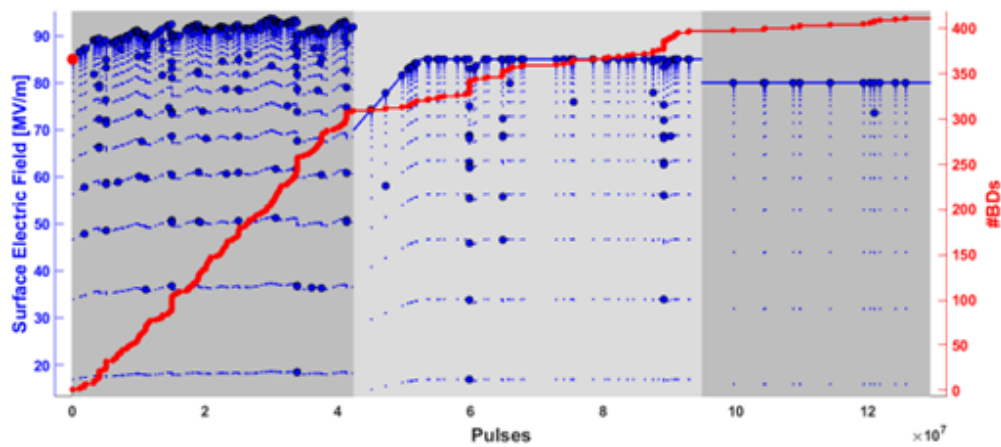


Figure 3.4: Nb pair electric field reductions to find a stable electric field with reduced clustering.

Figure 3.4 shows the transition from the breakdown rate controlled conditioning to a set lower electric field to establish a stable breakdown rate. The first block in the figure shows the saturation of the electric field at around 90 MV/m for a breakdown rate of 1×10^{-5} . The second block was with a set electric field of 85 MV/m but at this electric field the electrodes experienced a number of cluster in breakdowns reducing the electric field temporarily. Due to the number of cluster the electric field was reduced further to 80 MV/m, at this electric field it can be seen that the breakdown rate is more stable with much less clustering.

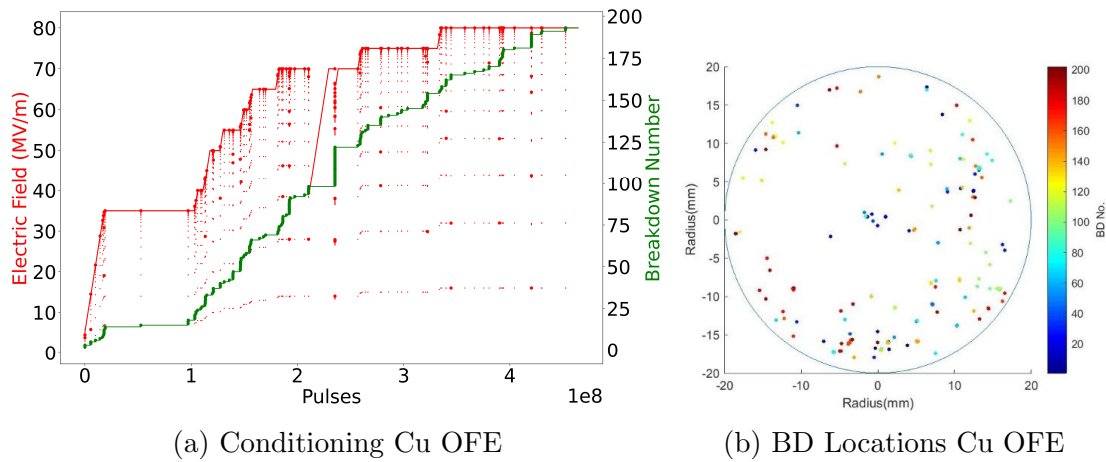


Figure 3.5: Shows the conditioning of the Cu OFE pair, where, (a) gives the electric field in red and the breakdown count in green and (b) shows the breakdown locations detected by the camera with the first to the last breakdown indicated with colours dark blue through to dark red.

3.2.4 Oxygen Free Electronic Copper

The Cu OFE electrodes conditioned stably to 80 MV/m without any detrimental clusters in the breakdowns deconditioning the electrode pair, the conditioning plot is shown in Figure 3.5a. This pair of electrodes were left in vacuum, not pulsing for several weeks just after 2×10^8 pulses and then reconditioned before continuing. Conditioning was stopped at this electric field as it was estimated that it would not reach the next step due to the number of small temporal clusters in breakdowns. As this pair of electrodes was not conditioned to an electric-field beyond what it is capable of maintaining stably, the electric field did not need to be reduced.

3.2.5 Tantalum

Figure 3.6 shows the conditioning of the Ta electrodes conditioned to 60 MV/m. This pair of electrodes were conditioned in advance of the Nb BCP electrodes and at this point it was not considered that they should be conditioned using the breakdown rate limiting algorithm to push the electrodes to a higher electric-

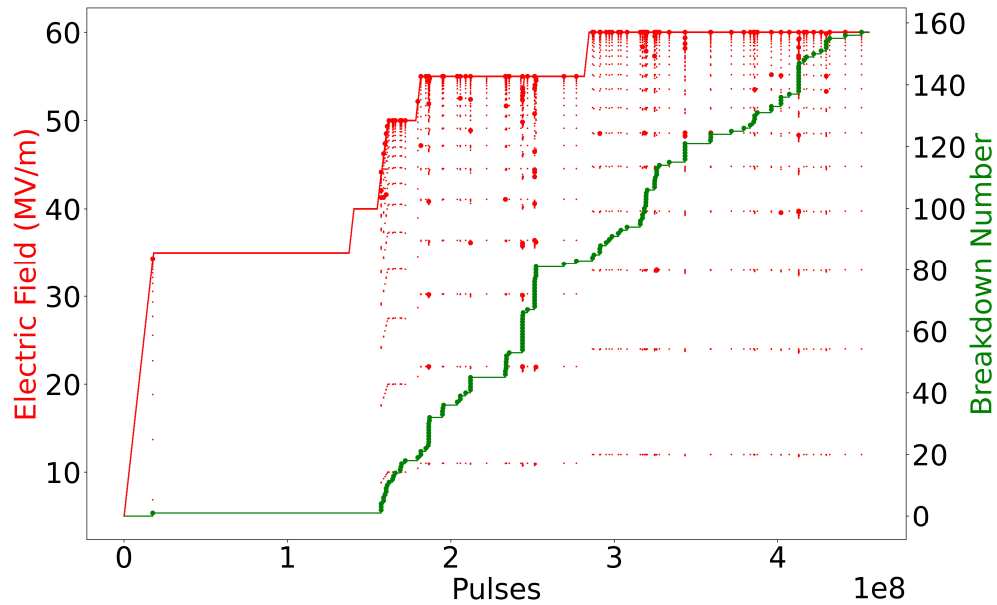


Figure 3.6: Shows the conditioning of the Ta pair, where the electric field is given in red and the breakdown count in green. No breakdown locations are given due to the ceramic used not having holes to allow for camera observations.

field. Due to the hardness of Ta, it is possible that it would have performed in a similar way to Nb [84]. As seen with the Nb BCP each step has a similar breakdown rate, this may be the result of breakdowns not being able to remove the defects leading to the breakdown, making it beneficial to have a higher energy to remove surface defects. This material most likely could have reached higher electric fields without becoming unstable and further tests would be required for this. This results possibly suggests a different physical mechanism is responsible for conditioning for the two cases. One being pulses and the other requiring breakdowns or that they need breakdowns at higher electric field to condition and reduce the electric field enhancements causing breakdowns at lower electric fields. To summarise, these results suggest that the Ta electrodes would condition more efficiently using the breakdown rate limiting algorithm as opposed to the step-wise conditioning method, as seen with the Nb electrode pair. Whilst this is not completely understood and is not explained in the scope of this thesis, it

could be useful for the argument that there are two different behaviours when conditioning that are material dependent. This includes that softer materials seem to require more pulses at steps to allow them to condition, where as harder materials may condition better from having the breakdowns occur to change the physical properties of the surface.

3.2.6 Aluminium Alloy (AlMgSi1)

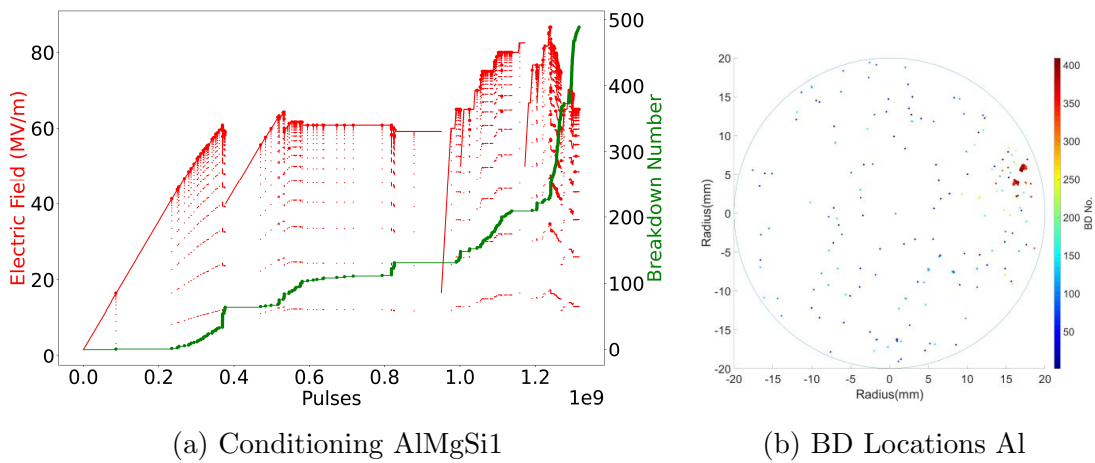


Figure 3.7: Shows the conditioning of the AlMgSi1 pair, where, (a) gives the electric field in red and the breakdown count in green and (b) shows the breakdown locations detected by the camera with the first to the last breakdown indicated with colours dark blue through to dark red.

The conditioning plot from the Aluminium alloy electrodes can be seen in figure 3.7a. The conditioning of Al was more unpredictable than other materials, possible as a result of several characteristics of Al. The characteristics observed include a reduced number of breakdowns during the initial conditioning and then a number of clusters after a single breakdown. There were a number of temporal clusters in the same area of the electrodes, this was possibly due to one relatively large breakdown causing a electric field enhancement that attracted several breakdowns until the surface state improved, allowing further conditioning. At 85 MV/m a number of breakdowns occurred in the same area as previously that greatly

reduced the achievable surface electric field. Many of the breakdowns with the Al alloy occurred in a spatially concentrated area. The aluminium alloy showed similar behaviour to an insulator coated material [82], this is able to increase the achievable electric field until a breakdown occurs when the material underneath is exposed decreasing stable electric field, therefore leading to more breakdowns. A possible reason for this effect, is the characteristic of Al to form surface oxide layers that form a protective coating over the material [85]. If the layer is removed it is able to reform in the presence of oxygen which may be possible if transferred from somewhere else on the electrode pair, evidence of this will be shown in Section 3.4.

3.2.7 Niobium

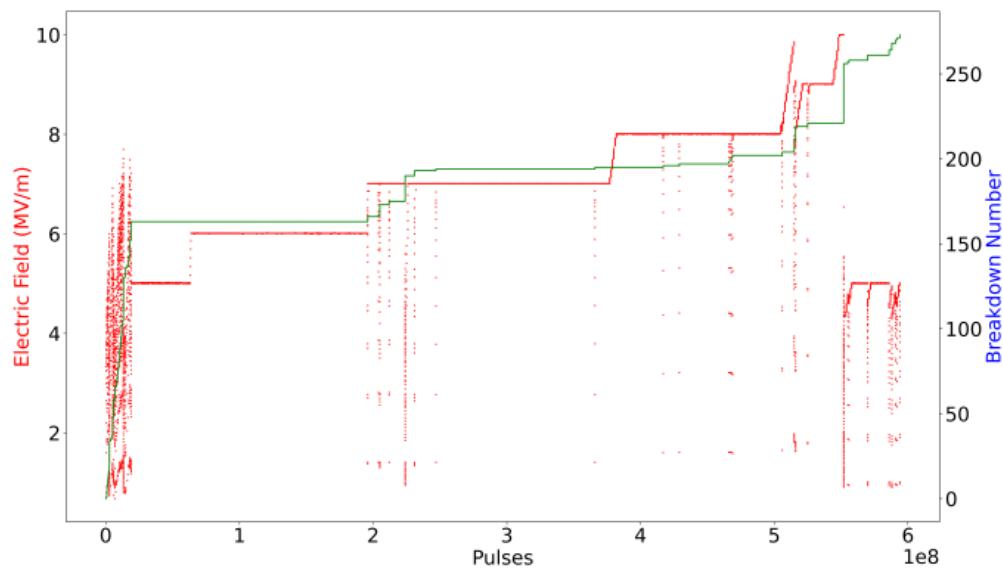


Figure 3.8: Shows the conditioning of the Nb pair, where the electric field is given in red and the breakdown count in green.

Figure 3.8 displays the conditioning of the first set of Nb electrodes that were not polished. The very low level of achieved field, combined with the observation of a poor surface finish, motivated BCP polishing the second pair previously shown. From the plot shown it can be seen that the electrode pair reached around

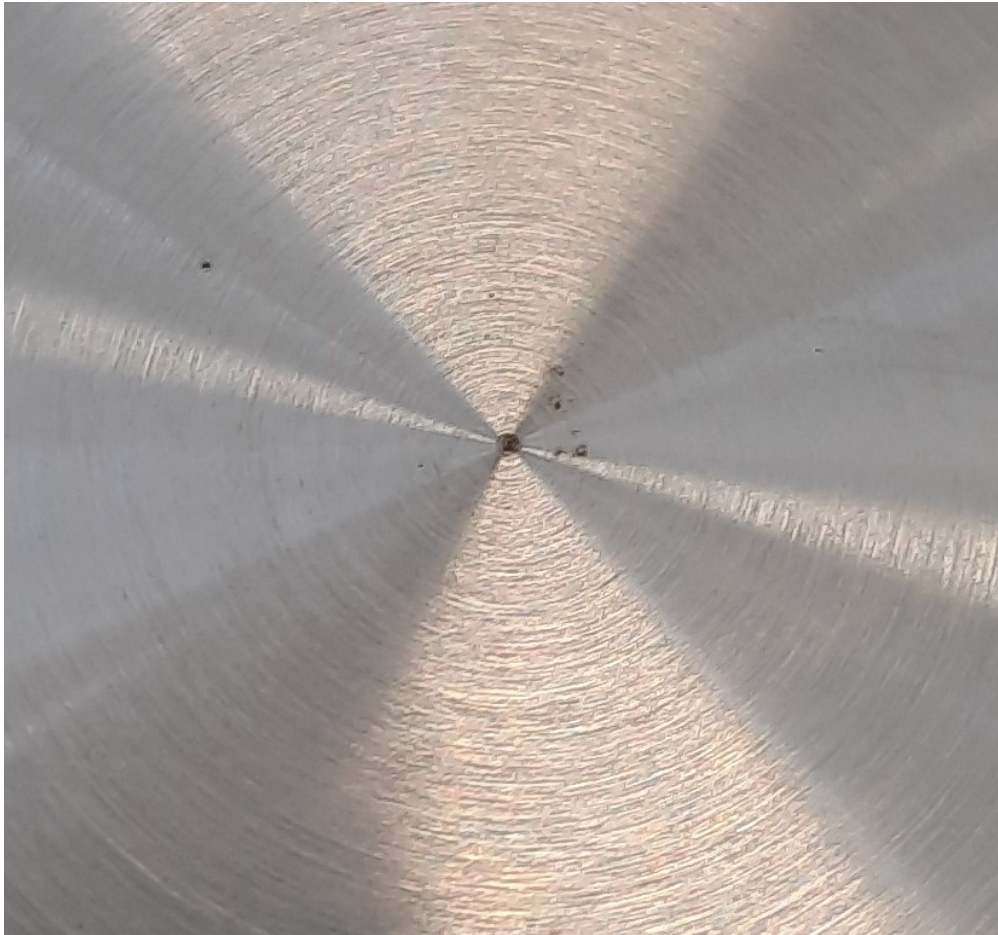


Figure 3.9: Image taken with a camera, of what appears to be damage from a number of breakdowns in the centre of the electrodes.

10 MV/m maximum but had a large cluster in breakdowns and could not maintain a electric field of 5 MV/m.

Figure 3.9 shows an image of the electrode after testing where there was a visible discolouration in the centre due to multiple breakdowns. This suggests the most likely reason these electrodes were unable to reach high electric fields was due to the peak in the centre due to machining. All electrodes were machined by turning, this is done by keeping the tool moving at a relatively constant speed over the surface. To do this the speed is gradually reduced as it approaches the centre of the electrode, to the point of almost having zero speed. Due to this reduction in speed the material experiences more of a smearing effect that produces a protrusion

in the centre. It is possible that this could have been removed using high voltage pulses but this was not tried and polishing was used to improve the surface state after machining. It is important to note that it is possible that the machining may have played a role in the conditioning performance of other pairs of electrodes but in a less obvious way.

3.2.8 Summary and Comparison of Conditioning

A summary of the different materials tested using the step-wise conditioning method as chosen for the RFQ program, can be seen in Figure 3.10. This plot shows the maximum electric field and final stable electric fields reached for each of the materials tested. Instead of conditioning using only the breakdown rate limiting algorithm to determine the saturation field for a given breakdown rate, the following conditioning increases the electric field using a step-wise method, to a stable point at which a further step increase in the electric field may result in a deconditioning effect. Different materials tested were considered conditioned using several factors in relation to the breakdowns occurring. These include the breakdown rate, clusters in breakdowns with respect to pulses, cluster rate, occurrence of multiple breakdowns within a single pulse determined by the cameras, and proximity to a previous limit causing a large cluster. Any of these individually are a sign of instabilities and have a dependence on the electric field applied and depend on the proximity to the limit of the materials.

In figure 3.10 the materials are ordered for the highest stable electric field to the lowest. The Ti alloy achieved the highest electric field even after a large cluster in breakdowns that required reconditioning. CuCr₁Zr had the second highest stable electric field with no unpredictable clusters causing a reduction from the maximum electric field achieved. The BCP Nb and Cu OFE had the same final stable electric

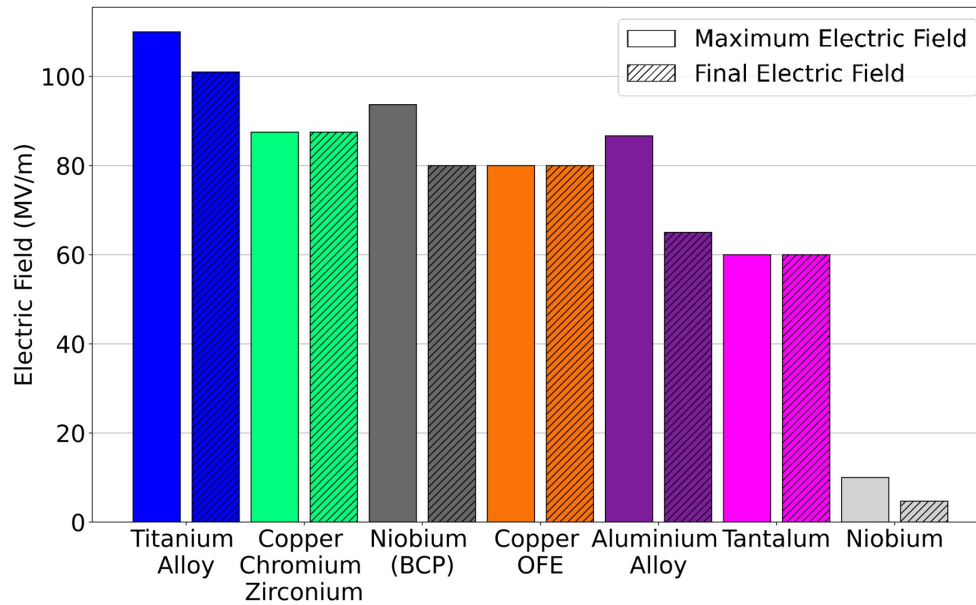


Figure 3.10: Summary bar chart of the final stable electric field of all materials tested.

field. For the Nb (BCP) the electric field was reduced from a higher electric field due to the higher breakdown rate it was experiencing during pulsing. The Cu did not exceed the stable electric field as it was showing signs of being close to its limit having a number of small clusters and multiple breakdowns. The Aluminium alloy had an increased breakdown rate shortly after reaching the maximum value given and this gradually reduced the electric field to a stable point. The Ta electrodes achieved a stable electric field of 60 MV/m but after testing other materials it has become clear that these electrodes should have been tested similar to Nb (BCP) and could have reached a higher electric field than recorded, this will be discussed in more detail in the results.

Differences can be seen between the degradation of TiAl_6V_4 and AlMgSi_1 , Figure 3.11 shows the degradation of the two materials respectively. The TiAl_6V_4 electrode pair experienced a cluster of around 100 breakdown in around 1×10^7 of pulses. When a lower electric field was set the breakdown rate decreased and was able to recover much of the field without any additional large clusters. At this

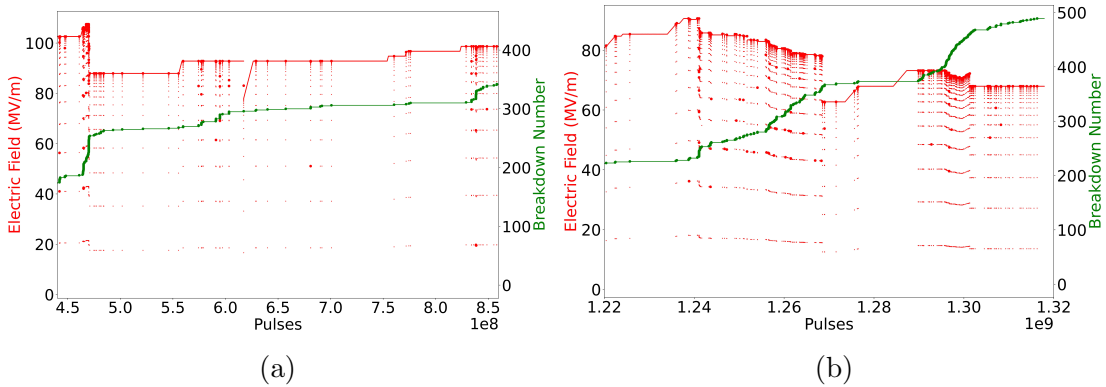


Figure 3.11: (a) and (b) show the breakdown cluster events from TiAl_6V_4 and AlMgSi_1 electrode pair conditioning, leading to a decrease in the electric field. This shows a brief increase in the number of breakdowns for TiAl_6V_4 , that was recoverable. Whereas for AlMgSi_1 , there is a continuous increase in breakdowns causing a large unrecoverable decrease in the electric field holding capabilities.

point due to an increase in the breakdown rate during the last step to 101 MV/m, it was decided not to increase further in case of incurring an additional large cluster short period with cluster of breakdowns.

A more gradual deconditioning effect can be seen in Figure 3.11b of the AlMgSi_1 electrode pair. This has a breakdown rate higher than the threshold set, leading to a decrease in the electric field over time, from 86.7 MV/m to 65 MV/m. After a decrease in the field manually the breakdown rate settles. Similar to the TiAl_6V_4 , steps to recondition the surface can be seen, but a following cluster in breakdowns was observed. Due to the additional cluster the electric field was reduced again to the previous stable step, but it can be seen to have a higher breakdown rate than previously.

It can be seen in both the Figures 3.11 (a) and (b), that the materials had previously been stable at a higher electric field. The materials may have been able to operate at higher fields, if this electric field had not exceeded the electric field holding limits of the material. Therefore avoiding exceeding the limits may lead to better performance of materials and reduced degradation over time.

Machining capabilities of each material varied due to their respective hardness, leading to different roughness's and in some cases a physical tip in the centre. The electrodes were machined using turning where the material of the tool varied depending on the electrode material. For the Cu and Al electrodes a diamond tool was used by an external company and they were able to produced a mirror finish surface. For CuCr₁Zr, TiAl₆V₄ and Nb an aunsteel korloy CCGT09304-AK carbide tool with a radius 0.4 mm was used [86]. Due to the

hardness of Ta, these electrodes were machined using kennametal CCGT09T302HP tool of radius 0.4 mm, that experienced a significant amount a wear during machining. As the tool moved from the outer diameter of the electrode to the centre it reduces in speed to almost zero and this causes worse surface finish from smudging and possible tip formation in the centre of the electrodes seen with microscope observations [87]. Also due to damage of the machining tool whilst machining the different materials there is a large difference in the overall surface roughness. It is believed that the Nb as-machined that achieved very low electric field was a result of the central tip left from machining, this is the reason for the BCP (Buffer Chemical Polishing) process used on the subsequent Nb electrodes.

Relevant materials from the study conducted in the previous pulsed DC system at CERN can be seen in Figure 3.12 [17]. This aligns well in terms of the order of the material from the best performing to the worst. There is a large difference in the field recorded for each materials but the tests shown were performed in a different system using a different method. During the study shown in Figure 3.12,

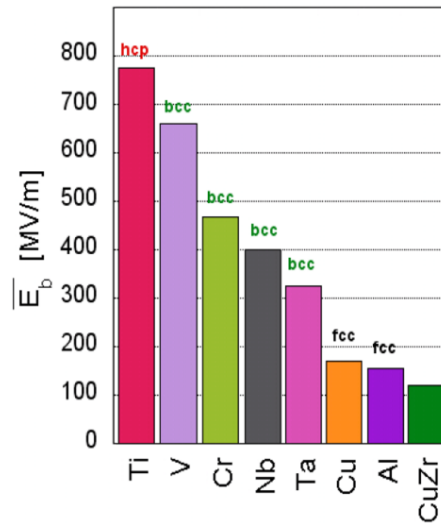


Figure 3.12: Relevant materials from the previous study of conditioning capabilities of different materials [17]

the power was ramped linearly from zero for each pulse and stopped when an arc occurred, meaning a breakdown occurred every pulse. This means that this was not conditioned to a breakdown rate as done during the experiments within this thesis, and therefore this did not limit the field achieved in the previous studies. Additionally the previous studies used a small anode with a diameter of 2 mm that was often destroyed and would have changed the gap throughout testing.

The Titanium alloy used in this study consisted of Ti, Al and V elements and for the previous study Ti and V were the best performing materials. CuCr₁Zr aligns with Cr from the previous study but not the CuZr alloy tested. It was realised after, that the Ta electrodes may have reached a higher electric field holding if they had been conditioned in the same way as the Nb pair. One difference in results from the two studies, is the electric fields achieved for the different materials and the proportional difference in performance. This may be a result of the differences between the way the materials were tested, with differences including the shapes of samples used and difference in the conditioning algorithm and parameters used. It was noted previously that this order of material performance also correlated with the their primary metallic crystalline structures of hexagonal close packed (hcp), body center cubic (bcc), face centered cubic (fcc) [17]. See Appendix O, for values of the hardness of different materials.

3.2.9 Quantitative Analysis of Conditioning

As all of the conditioning was controlled partially by human judgement, with variations between the different materials, this makes the results less comparable than if it was a more quantitative process, further details as to how this could be done will be covered in Chapter 8.3.7. However, they do appear to reflect the likelihood that the optimum conditioning process is material dependent. To

summarise the materials, the majority were conditioning without exceeding the stable electric field, TiAl_6V_4 and AlMgSi1 had a reduction in electric field due to a cluster of breakdowns and Nb BCP was conditioned past a stable electric field using a different algorithm before being reduced to find a stable electric field. The stable electric fields for each materials were determined by the breakdown rate as well as the occurrence of clusters in breakdowns and multiple breakdowns during an individual pulse.

In order to compare the conditioning results of the different electrode pairs, despite differences in their testing histories, the electric field was normalised using the scaling law:

$$E_{norm} = E \left(\frac{\text{BDR}_{ref}}{\text{BDR}} \right)^{1/n}, \quad (3.1)$$

where E_{norm} is the normalised electric field, E is the original electric field, BDR is the measured breakdown rate, BDR_{ref} is the reference breakdown rate, and n is a constant. The measured breakdown rate is the breakdown rate averaged between the final voltage step and the end of the experiment. A value of 30 was used for n , in accordance with the empirical relation:

$$\text{BDR} \propto E^{30}, \quad (3.2)$$

observed in high-gradient RF accelerating structures [75], [88]. Measurements with DC electrodes in the LES have been conducted previously and gave a dependence with an exponent around 30 [68]. These were all done using Cu OFE, which could make an impact on the correlation. The final values for the breakdown rate were within the range of 3.17×10^{-7} to 2.38×10^{-6} . Due to the differences in the materials and no data of the dependence for each, Equation [3.1] was used to normalised fields, shown in Figure 3.13b (b), for the final stable electric fields and the corresponding breakdown rates given in Figure 3.13a.

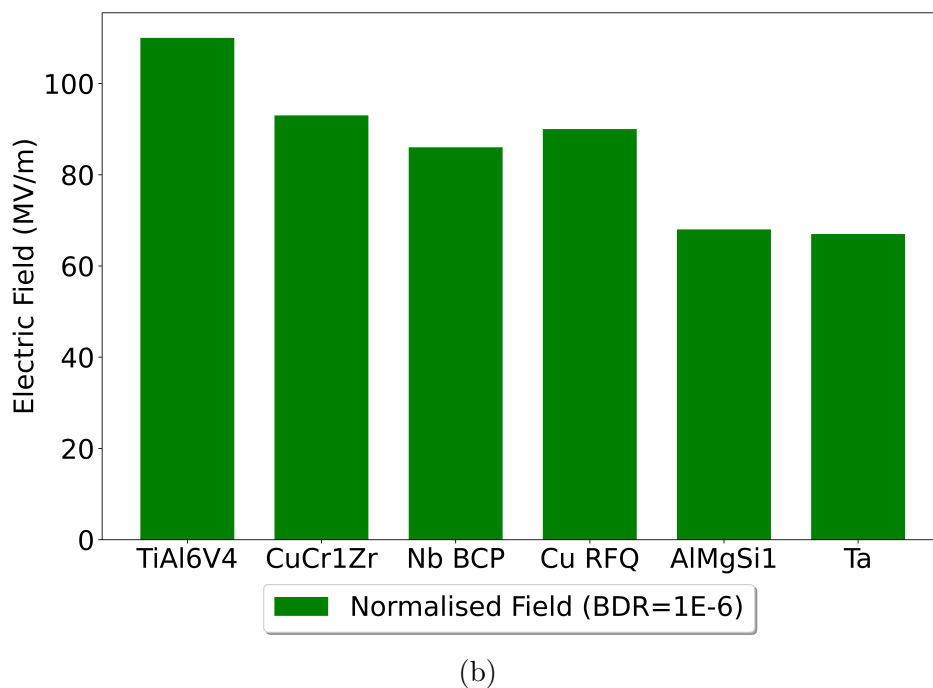
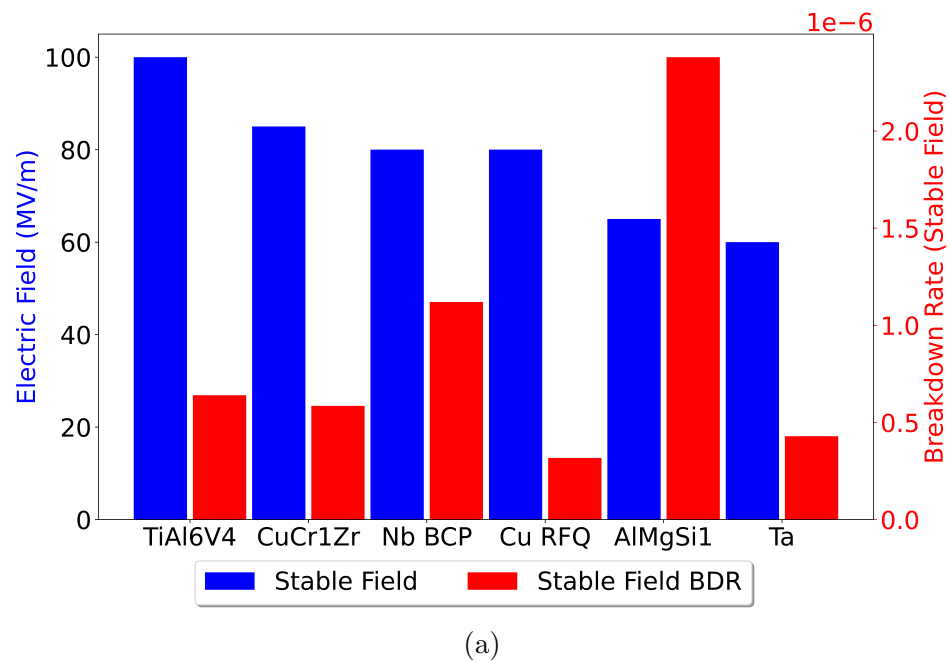


Figure 3.13: (a) Final stable electric field for each material shown in blue, and the breakdown rate at that field shown in red. (b) Electric field normalised to a reference breakdown rate of 1×10^{-6} , using the electric fields and breakdown rates given in (a) and Equation [3.1].

The results of normalising the pulsed conditioned electric field to a reference breakdown rate of 1×10^{-6} for each material shown in Figure 3.13 allow their

breakdown performance to be compared more easily. As the Nb BCP and Cu RFQ achieved the same electric fields during conditioning but with Nb BCP having the higher breakdown rate this would change the order from what is shown in previous plots. Whilst this plot still gives Ta as having the lowest electric field, it is believed that this could achieve a higher electric field and that breakdowns for this material may require a higher electric field to condition and improve the surface with respect to defects.

3.3 Pulse Length Dependence

After conditioning every set of electrodes a study of pulse length dependence was done over the range from 100 μs being the pulse length of conditioning to 1ms being the pulse length used for the RFQ, to be discussed in Chapter 4.6. Previous studies of pulse length dependence focused on the 100s of ns range which gave a relatively large dependence of $\text{BDR} \propto \tau^5$, with τ being the pulse length [6].

For this the electrodes were kept at a constant field chosen to be low enough to give a stable breakdown rate, and pulsed for a period of time before increasing the pulse length in the order of 100 μs , 250 μs , 500 μs and 1 ms. For the majority of materials only one scan of the pulse lengths was done, this allows for the possibility that the materials condition throughout causing the breakdown rate to decrease as the pulse length increases. For a more thorough study more time would need to be taken to increase and decrease the pulse length. Previous measurements, all below 100 μs showed a distinct pulse length dependence [6]. It appears from these results that above for pulses longer than 100 μs , a pulse length dependence on the breakdown rate is no longer observed.

Figure 3.14 shows the breakdown rate as a function of pulse length for the different materials. The pulse lengths within this range, did not appear to make

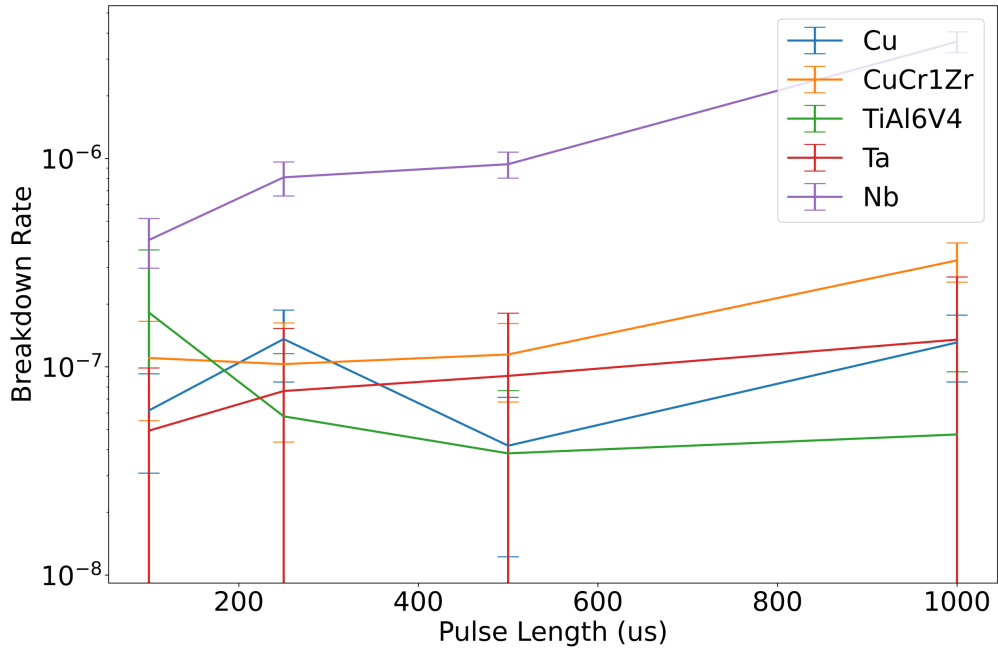


Figure 3.14: Pulsed DC system results of pulse length dependence studies for different materials, giving the breakdown rate at 100 μs , 250 μs , 500 μs , and 1 ms with standard error bars as described in Equation [2.5]

much or any difference to the number of breakdowns. For less stable materials the results seemed to suggest a random breakdown cluster characteristic that most likely was not a result of the pulse length change. Therefore it is possible that some points have a higher breakdown rate that was due to a cluster that may have occurred randomly had the electrodes remained at the same pulse length throughout.

Appendix N, shows a table of the number of pulses and breakdowns for each part material and pulse length, used to calculate the breakdown rate. This is given to show the statistical accuracy of these measurements, as this was only done once for each it is not very reliable. To improve the pulse length could be increased and decreased several times and tested on more than one pair.

A short test changing between a 1 μs and 200 μs pulse lengths shows a significant change in the field reached suggesting that there is a dependence in

this range and that $100 \mu\text{s}$ is more likely beyond the range in which the pulse length has an effect on the breakdown rate. Figure 3.15 shows the data from the conditioning for the different pulse lengths where the electrodes were conditioned to a breakdown rate and the observed stable field that they reached. It can be seen that when the pulse length was shortened the electrodes were able to achieve higher fields and stable running fields beyond the achievable field for the longer pulse lengths.

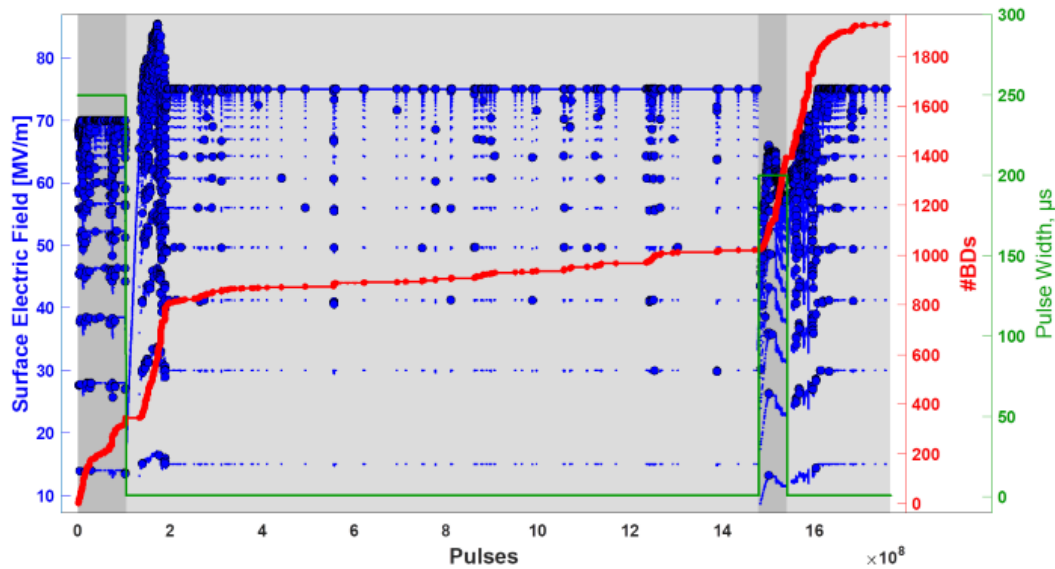


Figure 3.15: Pulsed DC system, pulse length dependence test between $1 \mu\text{s}$ and $200 \mu\text{s}$. Blue is the electric field applied for each pulse, red is the number of breakdowns with the slope indicating the breakdown rate and green shows the pulse length. Showing a decrease in the achievable field with the longer pulse length due to the higher breakdown rates.

3.4 Electrode Oxidation

Evidence of a form of transfer of contamination has been seen with Cu and shown in Figure 3.16. Seen often with heat treated copper electrodes is discolouration of Cu if not kept in vacuum. In one case as seen in Figure 3.16, one of the electrodes most likely had a non-visible contamination but after high-field testing and then

being stored in nitrogen for an amount of time developed a discoloured region that is seen on both electrodes. As the electrodes are tested facing each other this produces a mirror image that can be seen as a flipped version of the same contamination between Figures 3.16a and 3.16b. This discolouration looks very similar to other samples and due to this not being visible previously it is not known on which electrode the contamination originated.

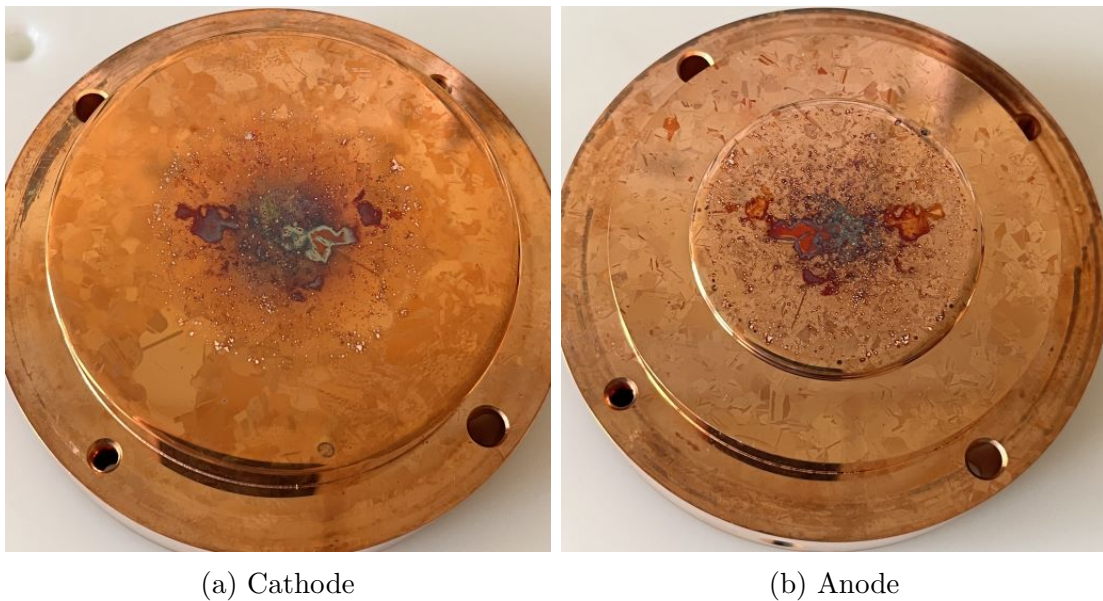


Figure 3.16: Possible contamination transfer, creating mirror image from one electrode to the other during high-field testing.

3.5 Self Organising Plasma

After testing CuCr_1Zr electrodes a feature was observed that only occurred for this one pair, this is shown in Figure 3.17 where a flower like pattern with a diameter of around $50 \mu\text{m}$ can be seen [89]. The flower matches the location of the centre suggesting it was cathode related and most likely previously looked similar to the centre of the anode as seen. This centre deformation is an effect of the machining as discussed previously and if it had melted then may have generated a relatively

large density of plasma in the gap. From the appearance there are suggestions that the plasma was influenced by the machining lines of both the anode and cathode. The cathode machining line would generate the radial lines seen on the anode central to the cathode centre and in the area of the anode centre machining this generates more interference that can be seen more clearly on the cathode. The large machining line from the anode seen going through the flower appears to remove one of the segments but also has additional circles around the diameter of the line coming from the flower area as though the plasma was following this line. There is research into self organising plasma that forms flower shapes like seen in this result and may be good evidence of that phenomenon and explain the results [90].

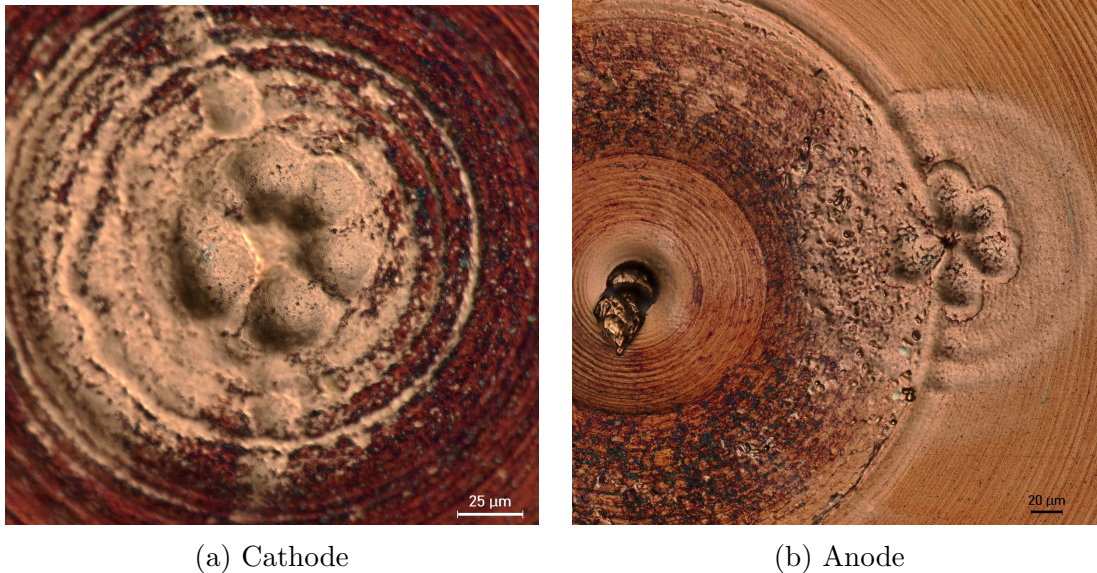


Figure 3.17: Cathode and Anode images of CuCr_1Zr after conditioning with a flower pattern that is central to the cathode and mirrored on the anode with the image flipped [89].

3.6 Conclusions of Different Material Conditioning

The majority of materials performed well reaching stable fields between 60 MV/m and 100 MV/m. There was a variability between electrodes in terms of the machining quality that in some cases appeared to have generated a field enhancement limiting the achievable electric field, and in other cases may have been compensated for during conditioning by the hardness of the material allowing for higher electric fields to be achieved. Values for the different elements of the materials used can be found in Appendix O . In general they follow the same order in terms of field reached as previous tests of the same materials, but with less difference in the field achieved, most likely because of the difference in the testing method used.

The experience gained in testing electrodes of different materials resulted in new insights into optimising the step-wise conditioning process. Conditioning using steps appears to be a good conditioning method for the majority of electrodes tested, giving a good indication of the electrodes proximity to their field limit based on their stability. Where the number of breakdowns occurring on each step tends to increase the closer to the limit and the breakdown rate at each step increasing and becoming less stable, as discussed with respect to the conditioning of CuCr₁Zr. The Ti alloy and CuCr₁Zr achieved the highest stable electric fields of all materials tested. They displayed a possible characteristic of sudden large breakdown clusters causing deconditioning, however, the electrodes were able to recondition and recover their electric field from before the breakdown cluster. The effect of improving over a number of pulses allowing for a step with fewer breakdowns, appears to have had more of an impact on softer materials than the harder materials tested. For harder materials specifically seen for the Nb and Ta

is that increasing in steps and pulsing at intermediate fields does not show the settling of breakdown rates at each field and as seen by Nb was able reach higher fields compared to Ta, whilst maintaining a breakdown rate of around 1×10^{-5} . Therefore for conditioning these harder material it may be more effective to use the previous method of using the breakdown rate liming algorithm of conditioning to a breakdown rate to an electric field saturation point.

Aluminium was a very different material to condition acting different to the other materials, this was most likely due to the softness of the material and ability to form an oxide layer. Aluminium performed in a way similar to coated materials with breakdowns occurring at higher field than expected and a sudden change in the breakdown rate. Due to the softness there appears to have been a significant crater that dominated the breakdowns causing a significant reduction in the achievable feed for a given breakdown rate of 1×10^5 .

No clear dependence of BDR (evident from the slope of plots of cumulative number of breakdowns as a function of the number of pulses) on pulse length was observed during measurements between $100 \mu\text{s}$ and 1 ms for each of the materials tested. Only one sweep of the different pulse lengths was done for each material reducing the reliability but it was the case for the different materials suggesting that the dependence is very low if there is one. There is also the effect of conditioning on breakdown rate over the number of pulses that would naturally lead to a reduced breakdown rate whilst applying longer pulses with the expectations of an increased breakdown rate. Also, during tests there were a number of random clusters that could skew the results depending on which pulse length they occurred on whilst not being an effect of pulse length. There is evidence of pulse length dependence between $1 \mu\text{s}$ and $200 \mu\text{s}$ but further studies are required.

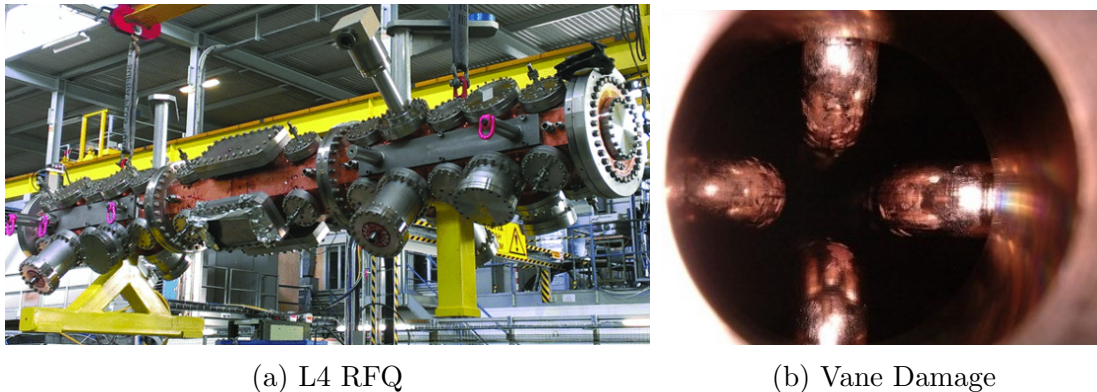
Chapter 4

Effects of H^- Irradiation

4.1 Introduction

After beam generation in an H^- ion source, there are several stages of acceleration before the beam is injected into the Large Hadron Collider (LHC), in order these include LINear ACcelerator 4 (Linac4) [91], Booster, Proton Synchrotron (PS), Super Proton Synchrotron (SPS) and then the LHC [3]. The first stage of the acceleration in Linac4 after the H^- source consists of the Low Energy Beam Transport (LEBT) and the Radio Frequency Quadrupole (RFQ). The main focus in this chapter is the effect of beam loss and material choice related to the RFQ and investigating a range of materials to compare their voltage holding capabilities, both without and following irradiation with 45 keV protons. Breakdowns in the RFQ were first noticed when the fields in the RFQ suddenly collapsed on certain pulses, to which the cavity feedback system responded by increasing the RF power in an attempt to keep the fields at the set level. This was followed up by endoscopic imaging of the RFQ vanes that showed a large amount of damage from breakdowns and evidence of blisters caused by irradiation, as seen in Figure 4.1b. The concern emerged that accumulated H^- beam loss on the vanes degraded

the voltage holding capability of the RFQ. Therefore, calculations were done to determine an approximate amount of irradiation the vanes of the RFQ would have received over a year of operation, giving a value of $1.2 \times 10^{20} H^- p/cm^2$ [92].



(a) L4 RFQ

(b) Vane Damage

Figure 4.1: (a) Image of the Linac4 RFQ and (b) endoscopy image of the vane damage after operation [10].

In order to determine the effects of irradiation from beam loss on the voltage holding capabilities, tests were done in the pulsed DC system at CERN. The pulsed dc system is particularly well adapted for an investigation of the effect of irradiation because it allows for measurements of the conditioning and breakdown locations throughout conditioning to make observations of the effects of irradiation on the process of conditioning. Due to conditioning being cathode dependent, the cathode of different materials was irradiated with the equivalent of 10 days of irradiation of the RFQ at around $1.2 \times 10^{19} H^- p/cm^2$, with an energy of 45 keV from the source. The material used for the RFQ is heat treated Oxygen-Free Electronic Copper (Cu OFE) which is known to form blisters when irradiated. A pair of Cu OFE electrodes was tested to compare to the performance of the RFQ. The expectation at the beginning of the tests was that the blisters would be the main cause of breakdowns and therefore materials that should not form blisters were considered. Two criteria for material choice were adopted. One was for increased solubility of hydrogen in order to decrease bubble formation and

the other was increased mechanical strength in order to resist the formation of blisters. For the first criteria, CuCr_1Zr was chosen, which was the material used for previous RFQ used as part of the accelerator chain for the LHC [3]. For the second criteria the materials chosen were Niobium (Nb), Tantalum (Ta) and a Titanium Alloy (TiAl_6V_4).

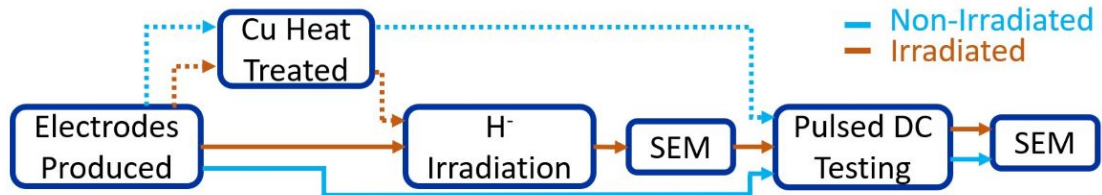


Figure 4.2: Flow diagram for the procedure for each material tested with the blue lines showing the steps for a non-irradiated pair and orange for the irradiated pair. Additionally the dotted lines indicate the extra step of heat treatment for the Cu OFE electrode pairs.

Figure 4.2 shows the sequence for the irradiation experiments, with the blue and orange line indicating the sequences of the non-irradiated and irradiated pairs respectively. Only Cu OFE electrodes were heat treated. The irradiation took place in a H^- test stand at CERN with the same initial stages and energies as L4, with the electrode placed of the output of the LEBT receiving a 45 keV beam directly on the surface of the electrode. Following irradiation of the electrodes, scanning electron microscope (SEM) observations were done to study the physical surface changes to determine if blisters had formed. Optical microscope observations were also performed to record physical deformities and discolouration on the surface. Observations were also made after conditioning with the system to observe the breakdown craters.

For each material irradiated and tested, another electrode of the same material was tested without being irradiated for comparison. The high-gradient testing protocol for each of the different materials was aimed to be as close as possible for comparison. The testing protocol also followed the RFQ operation as closely

as possible, however, parameters for conditioning and flat running were chosen to compromise between the parameters used for the RFQ and the amount of time spent conditioning each material. This led to a decreased pulse length and increased repetition rate but with a test of pulse length dependence when at the end of conditioning each material. Additionally, a ceramic spacer for a 60 μm gap was used for all pairs of electrodes tested to reduce the effects of gap dependence.

4.2 Irradiation

Irradiation was carried out in the linac4 ion source test stand. The test stand consists of a H^- ion source followed by a LEBT, producing 45 keV energy beam. Electrodes to be irradiated were placed directly in the path of the beam coming out of the test stand. The LEBT is used to steer and focus the beam and in this case is directed perpendicular to the electrode. As seen in Figure 4.3, electrodes were placed on the output of the beam from the LEBT in a position roughly the equivalent position as the front end of the RFQ in Linac4. [9]. To do this a chamber and end plate were designed to fix the electrode a set distance from the output of the beam pipe of the H^- source test stand. Only the cathodes of each material were irradiated, as there is significant evidence that breakdowns are cathode dependent. Evidence of this was seen when testing pairs of different materials, the field holding capabilities lined up with that of the cathode [66]. Another test with a scratch on the anode and cathode showed a mirror image of the scratch from the cathode and not from the anode [83]. For the purpose of steering the beam and determining the instantaneous and accumulated dose, the current to the electrode was measured by a current measurement through a wire connected to the end cap. To isolate the electrode from ground it was mounted onto a ceramic the same diameter as the electrode to avoid the beam damaging

the ceramic. A description of the assembly process can be found in Appendix Q.3.

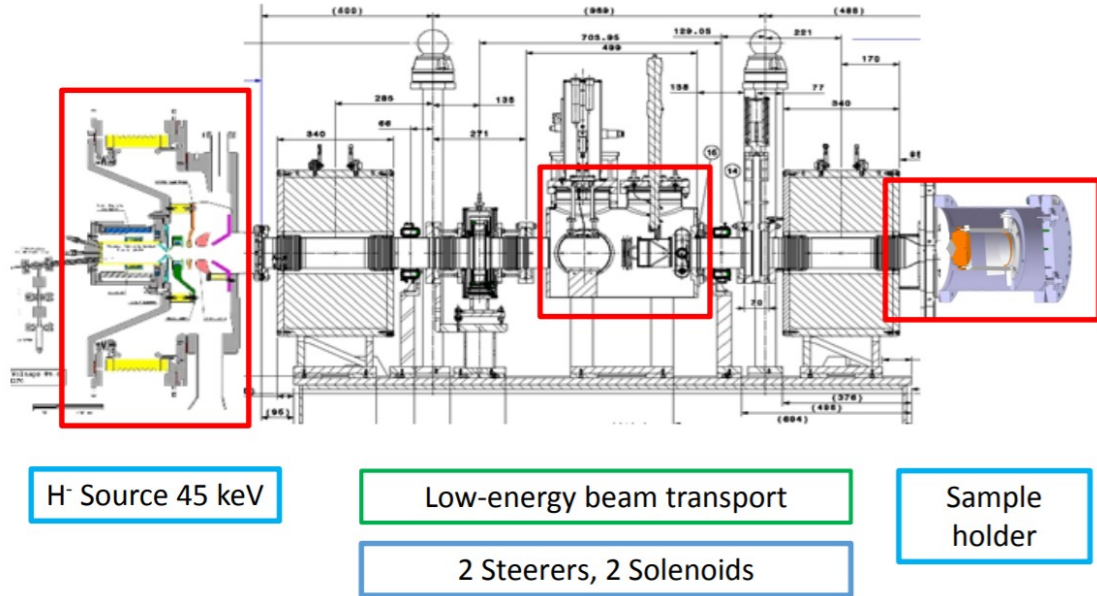


Figure 4.3: Cathode irradiation setup with a chamber attached to the output of the source and LEBT holding the electrode a set distance of 15 mm from the beam pipe outlet [9].

Material	Irradiation Duration (hr)	Total H- (p/cm^2)	Pulse Length (μs)	Beam Current (mA)	Spot size (cm)	Notes
TiAl6V4	55	1.20E+19	600	20	2	'C' shape
Cu OFE	40	1.20E+19	600	22-31	1	
CuCr1Zr	64	1.31E+19	600	20	2	
Ta	54	1.20E+19	600	17	2	2 Irradiations
Nb	140	4.88E+18	600	16	1	
Nb BCP	52	1.20E+19	600	21	2	Melted
CuCr1Zr Melt	50	9.80E+18	600	16	1	

Table 4.1: Table of the irradiation parameters for each of the materials tested.

Table 4.1 shows the irradiation parameters for each of the materials tested [93]. As mentioned the energy in all cases as supplied from the source is 45 keV, this would be the energy at the input of the RFQ, at the end of the RFQ the energy would reach around 3 MeV which could impact the results [91]. Simulations were done to calculate the amount of H^- irradiation from beam losses on the vanes,

over a year of running of the RFQ [92]. One calendar year of running corresponds to 100 days of operation, with an estimated integrated H^- flux of 1.2×10^{20} ions per cm^2 over the course of a year. It was predicted that the blisters were the source of breakdowns, but the smallest amount of irradiation required for blister to form was not known. Irradiation on the same scale as a year of operation of the RFQ would have taken a significant amount of time for each samples, therefore, the first irradiation of Cu was the equivalent of 10 days of irradiation at 1.2×10^{19} ions per cm^2 . From this amount of irradiation, blister were formed, therefore a similar amount was used for each of the materials tested. As it can be seen from Table 4.1, irradiation times were between 40 and 64 hours, excluding the Nb that experienced some issues during irradiation due to the current not being measured. This reduced time of irradiation introduced some differences compared to RFQ operation, while maintaining accumulated dose, this resulted in a higher intensity and related effects like melting. Other parameters include the pulse kept at $600 \mu\text{s}$, beam current from 16 mA to 31 mA and a spot sizes from approximately 1 cm to 2 cm. The beam spot size was chosen to be smaller than the high field area, in order to compare to other areas of the electrode not affected by irradiation.

Initial observations were made after irradiation and after pulse DC system testing with images taken with a normal camera. Observations after irradiation were to check for signs of the beam, these include the beam halo, and beam spot and to determine if any anomalies had occurred such as melting or evidence of blistering. Observations after conditioning focus on the correlation between the breakdown appearances and locations, specifically determining for the irradiated electrodes whether breakdowns were in the irradiated area. Figure 4.4 shows images of cathodes after high-field testing of the sets of electrode that were irradiated. The order from a-f is the order of irradiation to show the evolution of the appearance, including the shaped and sizes of the different areas.

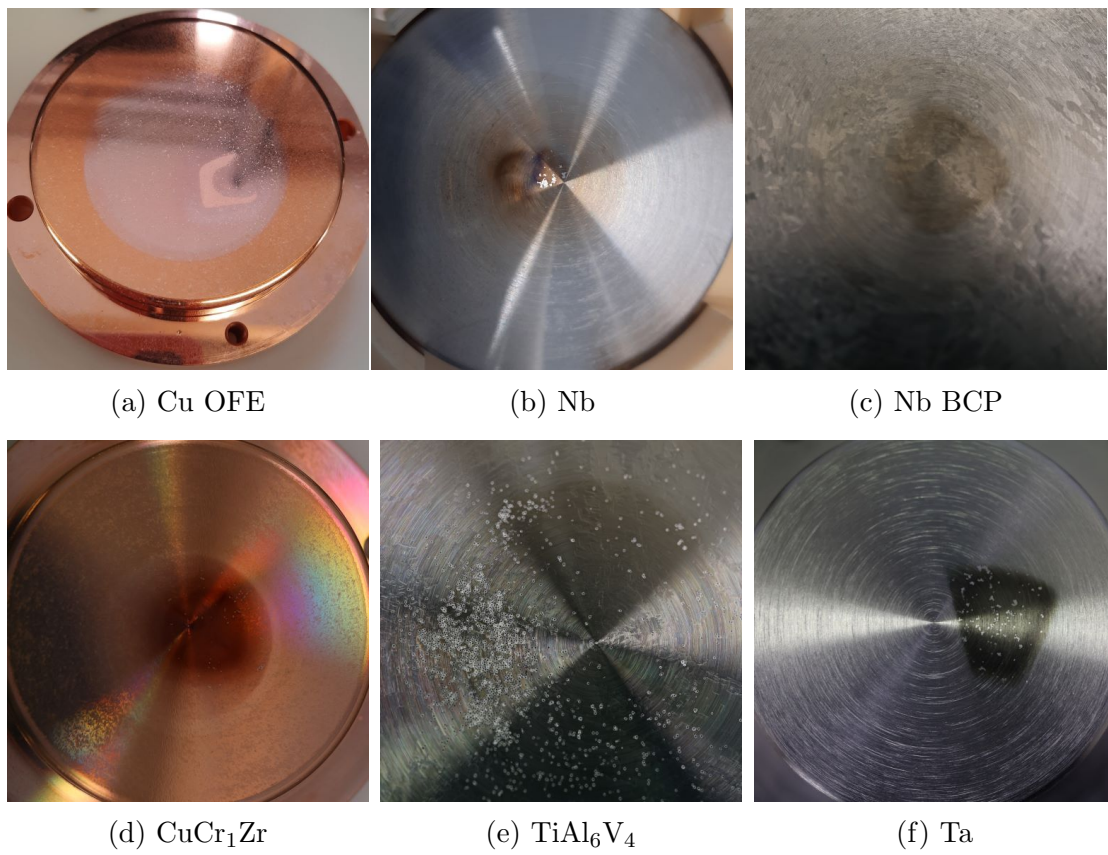


Figure 4.4: Images of each of the irradiated and tested cathodes.

The expectation was that the beam would have an approximately circular, Gaussian cross section. However, from all of the beam spots shown it can be seen that there is a trapezoidal shape with what appears to be an inner circle, this suggests that the beam was hollow when it reached the surface. Simulations of the beam dynamics do not predict this [93], but the evidence would strongly suggest this as the case, especially in the formation of blisters that also appeared to form a hollow shape. Where the blisters indicate the areas in which the H^- was implanted under the surface of the material.

Irradiation of the first Cu electrode is shown in Figure 4.4a, it can be observed from this that there was a circle of discolouration around the beam, this was found to be the same diameter as the beam pipe at 40 mm. Because the outlet beam pipe diameter was coincidentally the same as the anode diameter (as described in

Chapter 2.6), this meant that it was not possible to distinguish whether this also was a source of breakdowns. Following tests after the first irradiated electrodes a 30 mm diameter collimator was used to reduce the diameter of the beam pipe output, to eliminate the ambiguity. For the Ta electrodes seen in Figure 4.4f, the commercially available bulk material was not of a large enough diameter to produce large electrodes, therefore a smaller electrode design was developed and machined. These had a 30 mm diameter and therefore a half circle collimator was used for irradiation. Use of the collimators allowed for areas of all the different levels of irradiation on one sample, with a direct comparison to an non-irradiated surface, to make a clear correlations during tests.

The halo area around the central beam spot, was the unfocused head of the beam, consisting of the same components. These include H^- , H neutrals and electrons due to H^- being relatively unstable. The irradiated regions were consistently darkened. FIB followed by SEM imaging showed that this darkening was associated with the presence of a C layer. It is likely that the C layer formed through cracking

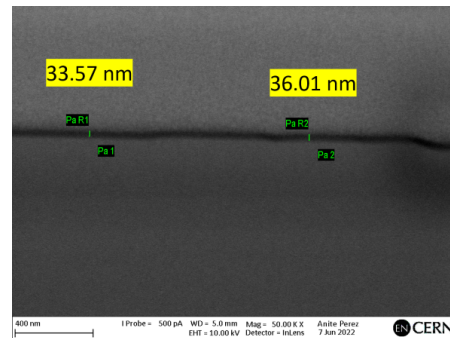


Figure 4.5: Carbon layer observed using FIB analysis of a Cu sample [94].

of residual hydrocarbons in the residual gas in the system. There is strong evidence of a layer of carbon as seen from the FIB analysis shown in Figure 4.5 [94]. This shows the Cu from the bottom of the image and the Pt from the top and the darker line through the centre is a layer of carbon of around 35 nm in depth. The presence of this C layer and whether is a surface layer or bonded with the material, may be important to the conditioning of the materials.

During the irradiation of $CuCr_1Zr$ the beam spot caused melting of the surface, most likely due to a high current intensity and an excessive local average deposited

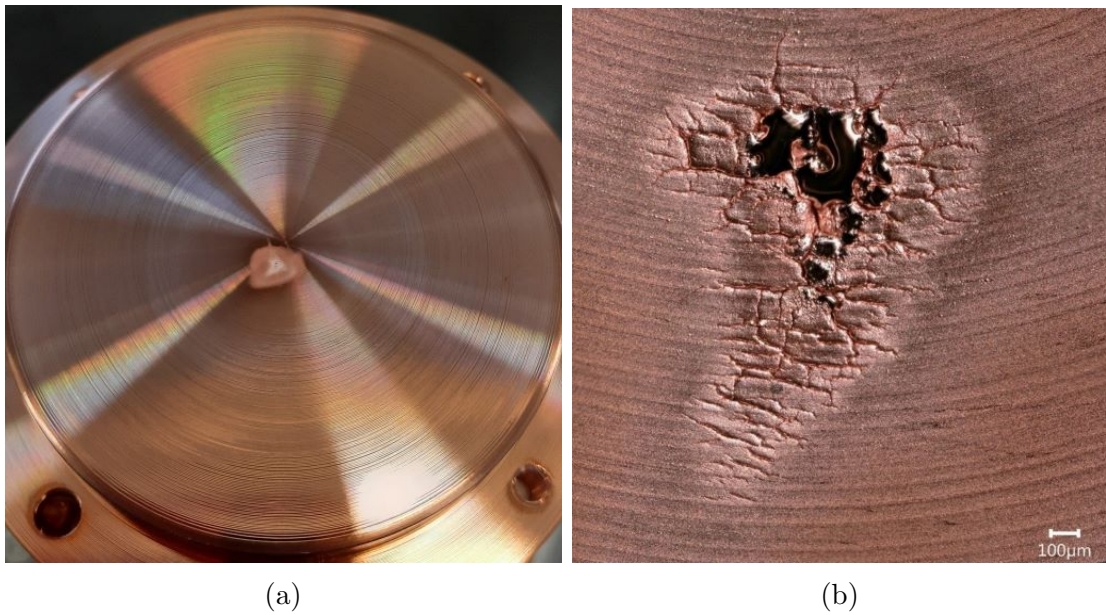


Figure 4.6: Images of the melted CuCr_1Zr electrodes after irradiation, taken with a (a) camera and (b) microscope respectively [95].

power density in the centre, with insufficient time between pulses to cool down completely [93]. To decrease the current intensity, the focusing was adjusted for a spot size on the electrodes of 2 cm instead of 1 cm. Changes in the focusing were determined by simulating the beam dynamics from the source, with the electrode at a fixed distance and followed by a test to validate the changes [93]. Using a lower current intensity per square cm meant also that the irradiation time needed to be increased to achieve the $1.2 \times 10^{19} \text{ p/cm}^2$ required.

As a result of the melting the electrode it was determined that it could not be used for testing and was therefore re-machined and re-irradiated. Following this, an additional irradiation check step was added to the irradiation process to avoid further damage to electrodes. Consecutive irradiations with the test stand are relatively repeatable with the parameters unchanged, as opposed to if different tests are conducted between using different parameters. This irradiation check was carried out by using a test sample being installed before electrodes during each irradiation slot, and providing that the test sample had no signs of melting then

the electrodes would be mounted for irradiation. If the test sample was melted then another sample would be installed and the beam parameters changed to try and avoid melting the surface whilst maintaining the same dose of H^-/cm^2 .

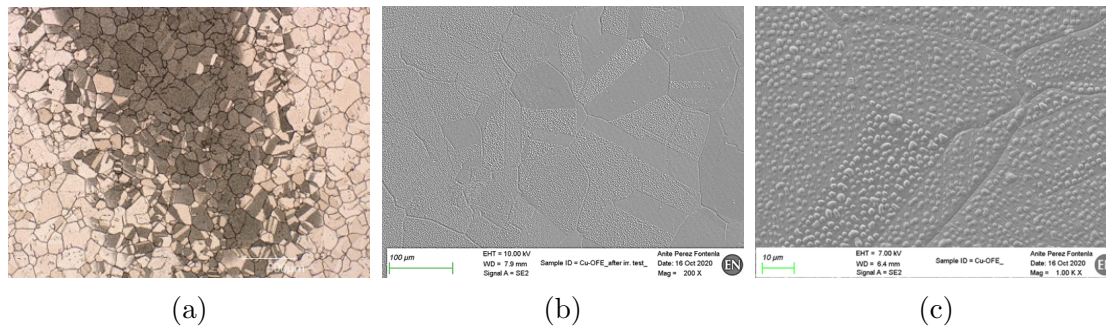


Figure 4.7: Blister on the Cu OFE electrodes after irradiation, taken with (a) an optical microscope, (b) and (c) with a scanning electron microscope [96].

One of the objectives of the tests was to replicate the blisters as seen in the RFQ on the electrodes and to observe how these affected the conditioning and breakdown locations. Figure 4.7 shows SEM images of the irradiated Cu cathode, as seen in Figure 4.4a [96]. Figure 4.7a shows a microscope image of one part of the 'C' shape, where the darker areas are blistered. Figures 4.7b and 4.7c show SEM images of the transition between the beam central beam spot area and the surrounding non blister area and a higher magnification image of the blisters. It was observed that the areas within the central beam spot had a higher density of grains with dense blistering. In transition areas some grains contained blisters whilst other did not, it was observed that this had some dependence on the grain orientation [96].

Also, there is no known reason for the 'C' shape of the first irradiation as seen in Figure 4.4a. The most likely reason suggested is that there was something blocking the path of the beam [93]. This may have resulted in some differences in the intensity on the target electrode. As blisters were the main interest at the time this was not a concern, but it is possible that this could affected the results.

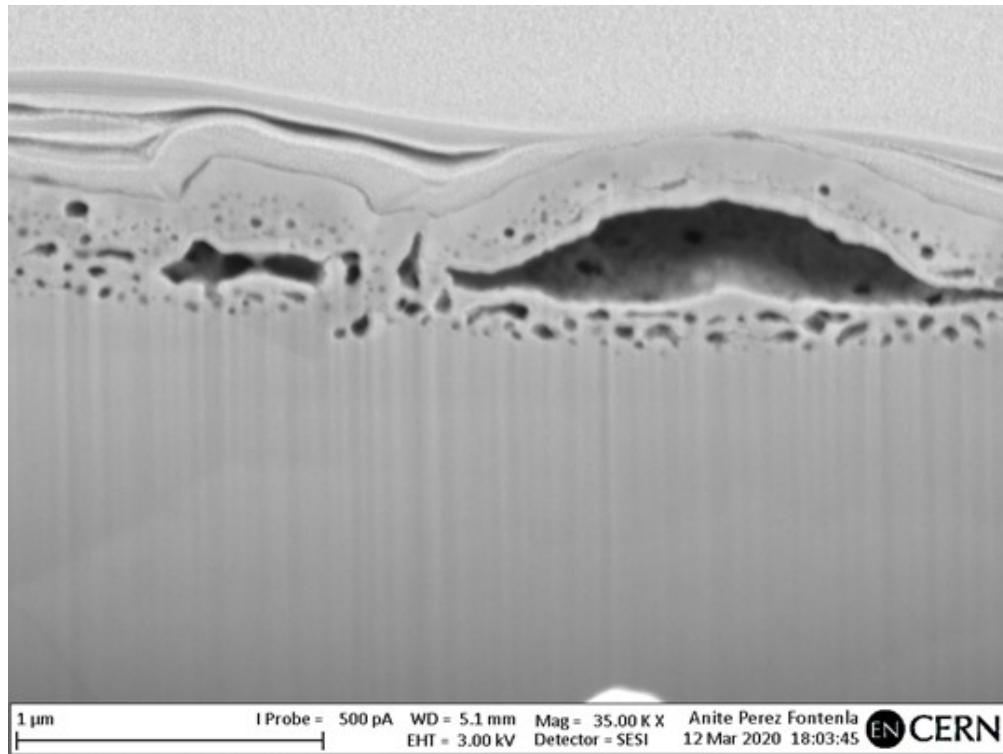


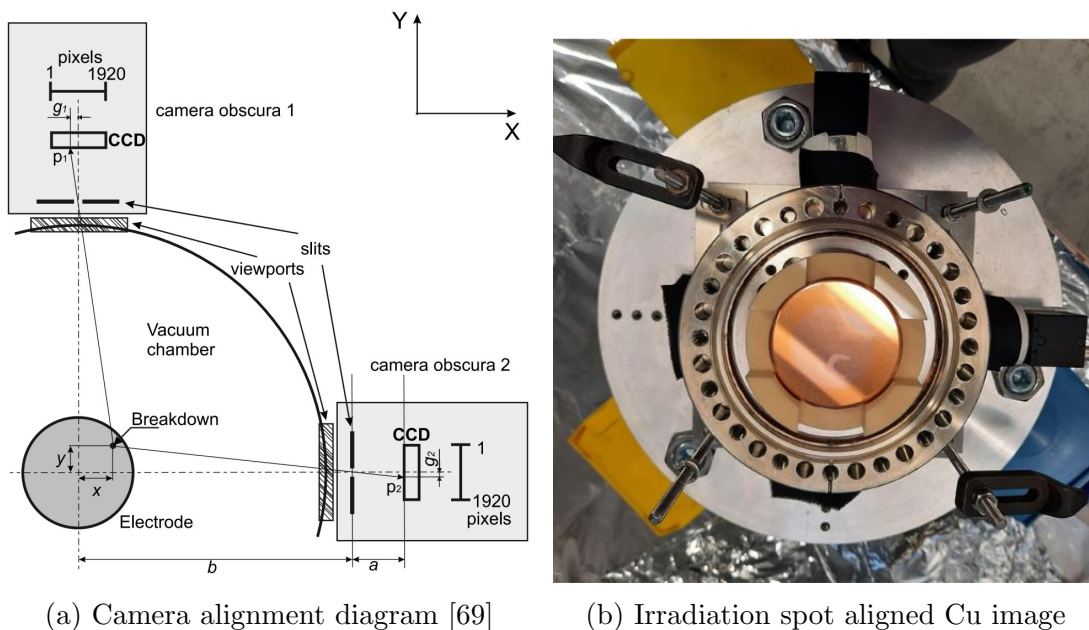
Figure 4.8: Cross section of a blister in Cu OFE with an irradiation dosage of $1.2 \times 10^{19} p/cm^2$.

Figure 4.8 shows the cross section of a blister on a Cu OFE sample, irradiated with a 45 keV H^- beam, with a dosage of $1.2 \times 10^{19} p/cm^2$ [96]. The thickness of material above the blister was around 300 nm thick, which is consistent with the Bragg peak depth of 45 keV electrons in copper [97], [98]. This suggests that the H^- ions penetrated the surface to this depth at which point they stopped and displaced the material forming blisters. Additionally, nanopores were also observed in the layer of the irradiation and not at lower depths of the material [96].

4.3 Pulsed DC System Tests

After irradiation the cathode was placed in the system and an image taken from above as seen in figure 4.9(b). Figure 4.9(a) shows how the cameras were used to determine the locations of breakdowns [69], the perpendicular cameras give

locations in the x and y planes. An image of the cathode with respect to the cameras matching the alignment used for the breakdown locations was taken. This was then used to map the breakdowns recorded from the cameras with the physical image. This could be then used to determine for example, if the breakdowns are in the irradiated regions. This allowed a real-time determination of the location of the breakdowns in order to for example determine if the irradiated area had a higher breakdown rate and slower conditioning speed.



(a) Camera alignment diagram [69]

(b) Irradiation spot aligned Cu image

Figure 4.9: (a) As shown previously in Figure 2.3, and (b) Showing the placement of the irradiated Cu samples with the cameras in order to determine breakdown locations with respect to the irradiated and blistered areas during testing.

Due to machining tolerances, the physical gap can vary slightly from the nominal value for each electrode and this is more of an issue with electrodes that are harder to machine. To have an indication of whether the gap between the electrodes is correct an independent determination of the gap was made using a capacitance measurement. Using the value for the capacitance, the gap can be calculated using Equation [2.1] [99].

For all of the materials tested they had approximately the same capacitance

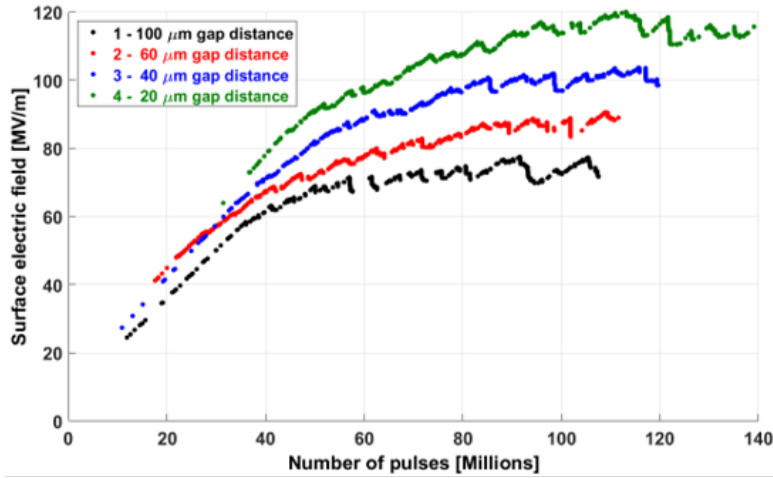
of around 160 pF including stray capacitance of the chamber, suggesting that the machining had not influenced the gap significantly. Use of this capacitance measurement can also determine if the electrodes are touching either due to machining errors or dust before assembling the entire system. Also, if a large breakdown creates a large enough crater to cause a short circuit between the electrodes during testing, this causes a change to the ability to measure the capacitance and can be proven this way.

4.4 Matching Conditioning Parameters

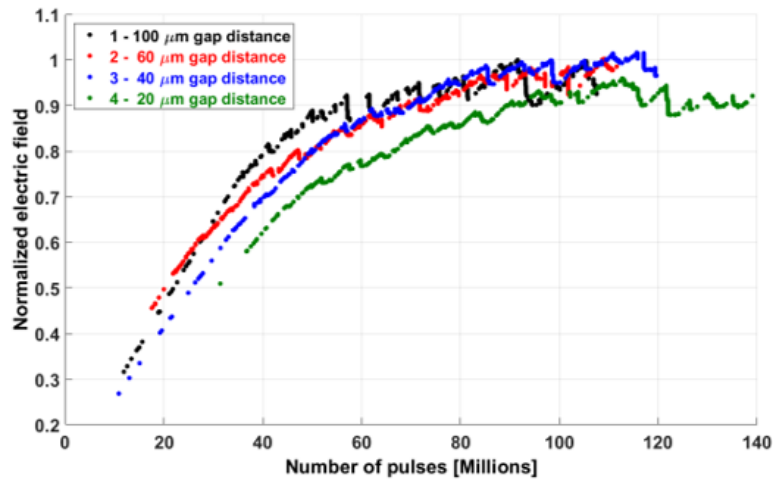
During the initial running of the RFQ for Linac4 conditioning was done manually with very little record of what was done [10]. A best effort was made to match the operational parameters of the conditioning of the LINAC4 RFQ using the recorded data available, in order that the results from the pulsed dc test are as applicable to the RFQ as possible. The Linac4 RFQ conditioning and operating parameters taken into account include, the pulse length of up to 900 μ s, a maximum repetition rate of 2Hz, and surface electric field of 34 MV/m, with a vane voltage of 78.27 kV.

Two possible operating conditions for the pulsed DC system voltage were considered. One was to simply match the surface electric field, using the gap distance and voltage. The other was to consider the previously observed gap dependence on limiting voltage [60].

Tests conducted previously within the same systems with the same electrodes show a dependence on the surface electric field reached for the different gaps [60]. This dependence is also been seen in other experiments [100], [101]. Figure 4.10a taken from reference [60], shows the electric field using equation 1.8, it can be seen from this that there is a difference in the field achieved for each gap with the same electrodes. There is a clear inverse correlation between the gap distance and the



(a) Electric Field Eq[1.8] [60]



(b) Normalised Electric Field Eq[4.1] [69]

Figure 4.10: (a) Electric field calculated using Eq[1.8] and (b) Normalised electric field using Eq[4.1] [60]

maximum electric field reached. Figure 4.10b shows the same data that has been normalised using Equation [4.1]. It can be seen that use of the normalised plot gives a better correlation of the field with the gap.

$$\text{Normalised electric field holding} = (V/V_{max}) \times (d_{max}/d)^{0.72}, \quad (4.1)$$

where V_{max} and d_{max} are the reference voltage and gap size respectively. The specific values used by Profatilova were $d_{max} = 100 \mu\text{m}$, the largest gap size used

in this series of measurements, and $V_{max} = 7747$ V, the voltage reached with this gap size. With these values, the normalised field reached in each run was approximately 1.

The normalised electric field holding equation was applied to the RFQ parameters, using the inter-vane distance values from the RFQ. From electromagnetic solver calculations of the surface electric field on the geometry of the RFQ structure for a given peak inter-vane voltage of 78.27 kV, a peak inter vane surface field of 34 MV/m was given [102]. The inter-vane distance change over the length of the RFQ, but the electric field and voltage values can be used to calculate an approximate inter vane gap distance by rearranging Equation 1.8 for the gap and using the electric field of 34 MV/m and voltage of 78.27 kV. Using this as the gap in Equation 4.1 gives a normalised electric field holding of the RFQ as 1.0563. This being so close to one suggests a relatively good comparison between the two very different setups.

To achieve the same scaled field in the pulsed DC system with a 60 μm gap, the required voltage would be 5664.9 V giving a surface electric field of 94 MV/m from Equation 1.8. The surface electric field in the RFQ is 34 MV/m, the target surface electric field for the electrode test was 35 MV/m. An electric field of 35 MV/m with a gap of 60 μm gives a voltage of 2100 V and a normalised electric field holding of 0.3915. Assuming the gap size scaling holds, when used with the RFQ parameters to compare to the LES with a gap distance of 60 μm , an equivalent electric-field of 94 MV/m using a voltage potential of 5640 V. In order to investigate which limit, between the surface electric field or scaled electric field applies, the system was initially conditioned to a electric field of 35 MV/m then increased in steps as discussed in the previous chapter, with the aim of reaching 94 MV/m.

Pulse lengths used for the RFQ are restricted by the RF power source, which lead to pulse lengths between 750 μs and 900 μs being used. The pulse lengths

available for the Marx generator used to supply the pulsed DC system range from 1 μs to 1000 μs . Previously the system had mostly been operated using 1 μs , in order to test with a pulse length as close to the few-hundred ns of the CLIC X-band structures [103]. Previous studies of the pulse length dependence of the field limit (for constant BDR) showed a pulse length dependence of τ^5 , which is used for determining the conditioning limit for the structures [75]. Therefore if the pulse length had an impact on the breakdown rate, then this would affect the maximum electric field reached during conditioning. As shown in the previous chapter, the pulse lengths used suggest that this dependence saturates and should not influence the results. Therefore, it is justified that conditioning with 100 μs pulse length allowing for faster turn around of samples.

The maximum repetition rate of the RFQ is 2 Hz, therefore the first test in the pulsed DC system operated with a 20 Hz repetition rate, to try to stay as close as possible to RFQ conditions. Running at 20 Hz meant conditioning took a large amount of time. As the objective was to compare the different materials, a higher repetition rate of 200 Hz was used in order to test materials within a smaller time frame.

4.5 Results and Discussion

The following tested materials, TiAl_6V_4 , Cu OFE, CuCr_1Zr , Ta and Nb are discussed in detail in the order of performance of the irradiated samples, from the highest stable electric field to the lowest. Two pairs of Nb electrodes and the Ta pair are grouped together due to performing in a very similar way after irradiated. Full figures for each of the materials for conditioning and analysis of the breakdown locations can be found in Appendices K to L.2.

4.5.1 Titanium Alloy (TiAl_6V_4)

After irradiation there was no evidence of modification to the surface structure due to irradiation [104]. Discolouration was seen, with a visible difference between the beam centre, halo and non-affected areas. This was difficult to see by eye and to take an image of, but was as expected with the 2 cm diameter beam spot and 3 cm diameter halo.

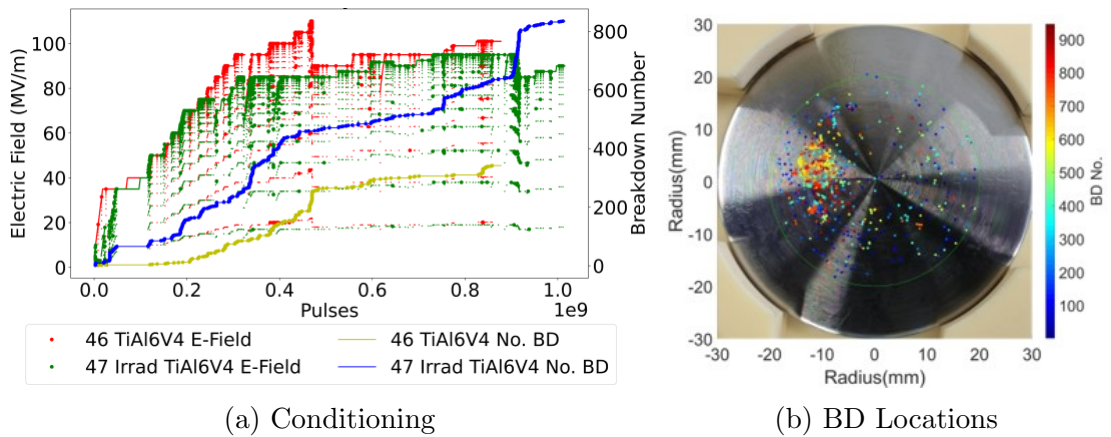


Figure 4.11: TiAl_6V_4 (a) conditioning of the irradiated and non-irradiated pairs and (b) the breakdown locations of the irradiated cathode with the breakdown number given from dark blue being the first to dark red being the last. The green circle indicates the diameter of the high field area, determined the the anode.

After conditioning as shown in Figure 4.11a, TiAl_6V_4 achieved the highest stable electric field out of all the materials, at 90 MV/m and 100 MV/m, for both the irradiated and non-irradiated pairs respectively. A small reduction in electric field is observed for the irradiated electrodes, suggesting the irradiation had some impact on the ability to reach the same electric field. Both pairs of TiAl_6V_4 electrodes exhibited a de-conditioning causing a decrease in the operating electric field. This was caused by a temporal cluster of breakdowns that had reduced the electric field between 15 MV/m and 30 MV/m. After reconditioning, a de-conditioning reduction in the electric field between 5 MV/m and 10 MV/m compared to previously achieved fields, it was not increased further to avoid the risk

of another cluster as this can damage the surface significantly. As this was a feature during the conditioning of both pairs it would suggest that this is a property of TiAl_6V_4 rather than a spurious event. This may mean that TiAl_6V_4 has a tendency to accrue surface damage if conditioned too far. Overall, TiAl_6V_4 performed very well, re-gaining most of the previously achieved electric field without any further issues and maintaining a stable electric field.

The irradiated TiAl_6V_4 had a larger breakdown rate at the start of conditioning that reduced suggesting a strong conditioning effect of the irradiated area that improved the performance. Excluding the clusters, it can be seen that the breakdown rates of both pairs is very similar after around 4×10^8 pulses, where breakdown rate is represented by the gradient of the number of breakdowns. In terms of the breakdown locations the clusters in breakdowns were mostly dominated by the irradiated area, with a similar number of breakdowns per area at the start of the conditioning, see Appendix M for breakdown location counts inside and outside of the irradiated area. Having a similar electric field and breakdown rate after conditioning suggests that it was able to condition any extrinsic breakdown-inducing features caused by the irradiation. The reduction in electric field may be a result of residual impurities or from damage due to the increased number of breakdowns.

Figure 4.11 shows the breakdown locations for the irradiated TiAl_6V_4 electrode. It can be seen that there was a higher concentration on one side within the halo area and not the external high electric field area. It can also be seen that the first breakdowns are more distributed over the surface, with later breakdowns being more concentrated on one side. This suggests it is an effect of the halo from the beam pipe outlet. The reason for the concentration could not be determined but could be explained by the addition of non-parallelism between the electrodes causing a electric field enhancement as well as the halo from irradiation.

4.5.2 Oxygen Free Electronic Copper (Cu OFE)

After irradiation of Cu OFE, blisters were observed in the beam spot area of the electrode, along with dis-colouration of the halo [104]. As mentioned for this irradiation a 'C' shape of blisters was produced. No collimator was used during irradiation, therefore for this cathode the halo is the same diameter as the anode of 4 cm. Therefore it was not possible to determine whether the breakdown locations were a result of the halo as there was no non-irradiated reference area of the electrode for comparison. This deficiency was corrected in later tests.

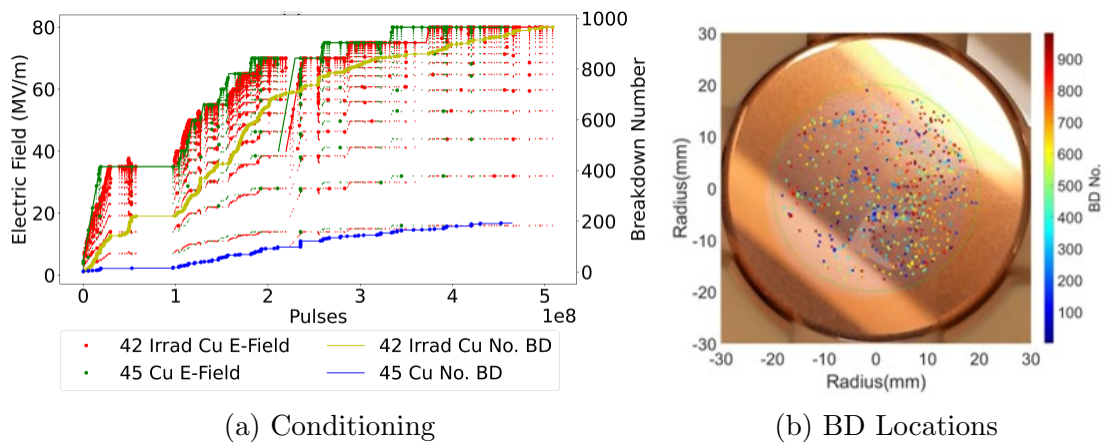


Figure 4.12: Cu OFE (a) conditioning of the irradiated and non-irradiated pairs and (b) the breakdown locations of the irradiated cathode with the breakdown number given from dark blue being the first to dark red being the last.

Two tests of non-irradiated Cu OFE were conducted, the first one with an larger pulse length and lower repetition rate compared to all other samples. This change in repetition rate did not seem to influence the electric field achieved. For comparison purposes, tests from second pair are included in Figure 4.12, due to having been conditioned with the same parameters as the irradiated. For conditioning and breakdowns location details of all Cu samples, refer to Appendix H.

Cu-OFE achieved the second highest stable electric field after irradiation, and also with the same stable electric field for the irradiated and non-irradiated pairs.

Cluster in breakdowns with respect to pulses occurred multiple times during steps. From Figure 4.12a, this can be seen initially as a small peak in the electric field for the irradiated pair around pulse 0.5×10^8 . To try to reduce the damage to the electrodes when clusters occurred, the target electric field was reduced to the previous stable point and pulsed before continuing to increase further. It can be seen that the irradiated pair also had a higher breakdown rate at the start of conditioning, that decreased to a similar level as the non-irradiated pair. As both the irradiated and non-irradiated pairs reached the same stable electric field with a similar breakdown rate this suggests that it conditioned away any breakdown inducing features caused by the irradiation.

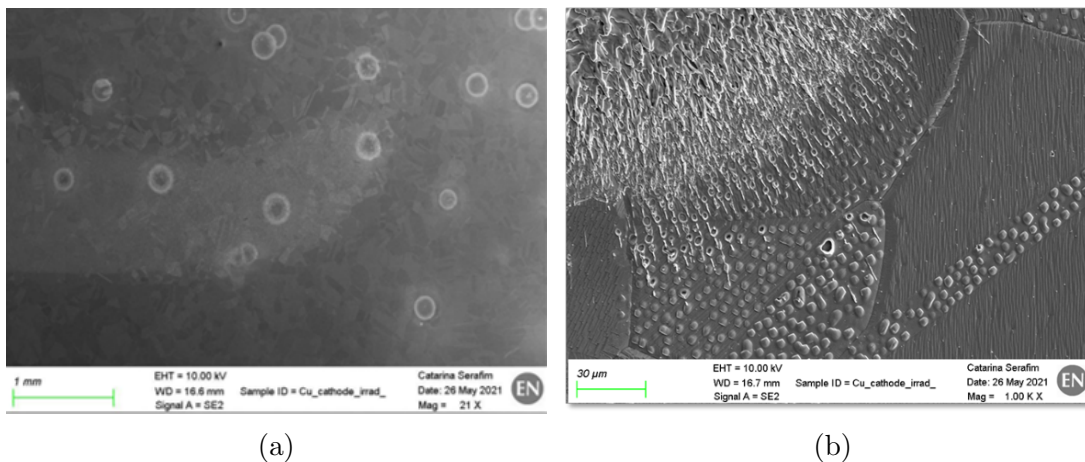


Figure 4.13: SEM images of the breakdowns over the blistered area from irradiation and the splash and melting of blisters surrounding a crater [104]

Figure 4.12b displays the breakdown locations on the irradiated electrode where clusters occurred in different areas of the halo and not all of the beam centre area. SEM images of part of the 'C' shape and surrounding area of a crater can be seen in Figure 4.13 [104]. From this evidence it can be seen that there are many densely blistered areas that have not experienced any breakdowns. This suggests that blisters are remarkably not more susceptible to breakdown than non-blistered areas. Currently it is not known why the blisters do not cause breakdowns given

they should produce a electric field enhancement.

There were several clusters within the halo area that were not the case with the non-irradiated electrodes, suggesting there was some features causing breakdowns from this area also. As mentioned this increase in the number of breakdowns may be explained by the irradiation-induced carbon layer. However, this does not explain why the effect produced clusters, rather than breakdowns over the whole surface.

4.5.3 Copper Chromium Zirconium (CuCr_1Zr)

As mentioned during the first irradiation of CuCr_1Zr the material in the centre of the beam spot melted, most likely due to the high current intensity. Due to the melting in the centre it was decided that this was not suitable for testing and therefore the same electrode was re-machined and re-irradiated using the same sample.

The following irradiation of CuCr_1Zr went as planned, the areas of the electrode in this case looked very similar to Cu OFE. Visual observation showed the hollow beam spot with a diameter of 2 cm and collimator halo of 3 cm. SEM observation of the beam spot displayed blisters similar to that seen from the Cu OFE pair [104].

During conditioning CuCr_1Zr was not able to condition up to the first step of 35 MV/m in electric field and was limited in electric field by the breakdown rate of $1\text{E-}5$ specified within the code. Due to large clusters in breakdowns a lower electric field target was set to find a stable electric field. After a number of pulses at a 20 MV/m with very few breakdowns the target was increased to 25 MV/m. Several breakdowns occurred during the step but it appeared stable at this electric field. With the following target set as 30 MV/m the number of breakdowns reduced the

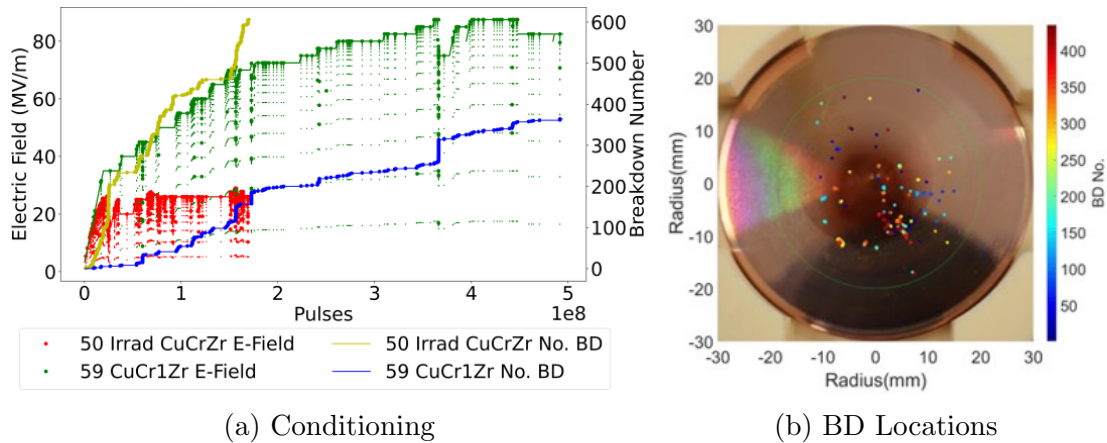


Figure 4.14: CuCr_1Zr (a) conditioning of the irradiated and non-irradiated pairs and (b) the breakdown locations of the irradiated cathode with the breakdown number given from dark blue being the first to dark red being the last.

achievable electric field. The highest maintainable electric field from the irradiated CuCr_1Zr was 26 MV/m which was far below the electric field of 85MV/m from the non-irradiated pair. This suggests the cause of this decrease in electric field is a result of the irradiation.



Figure 4.15: Large cluster of breakdowns around 2mm in length, and located within the irradiation halo area. This image was taken with a digital camera meaning an accurate scale cannot be provided.

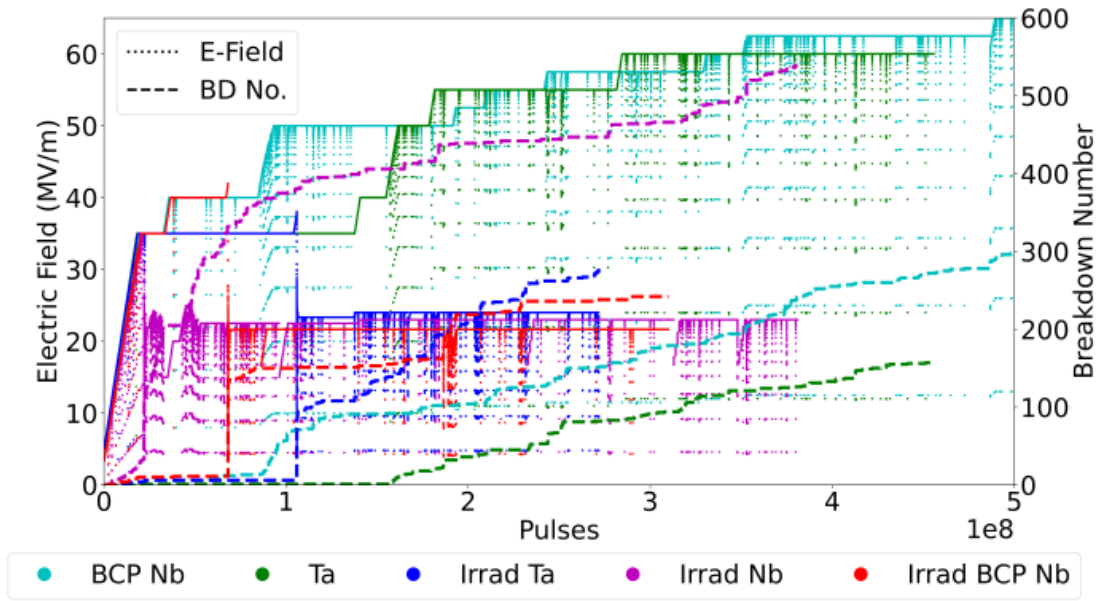
One of the concerns throughout testing the materials was the effect of

machining, but this is generally the worst in the centre of the electrodes. From analysis of the breakdown locations they appear to be concentrated in clusters within the beam and halo areas and not the centre, suggesting that it was limited by the irradiation. There was one relatively concentrated cluster of breakdowns that can be seen in Figure 4.15, during testing due to the image given in Figure 4.14b it was not possible to determine whether it correlated with irradiation. From analysis after the removal it could be seen that it was within the darker area of the beam pipe output halo of carbon. Similarly to the Cu OFE, the majority of the blistered area of the CuCr_1Zr did not create a field enhancement to induce breakdowns.

4.5.4 Tantalum (Ta) and Niobium (Nb)

Ta and both Nb samples displayed similar results to TiAl_6V_4 with respect to no physical defects in appearance after irradiation [104]. As two different Nb samples will be discussed these are referred to as "Nb" which was tested as machined using diamond turning and "Nb BCP" that was polished using buffer chemical polishing (BCP) after machining. The first Nb cathode (Nb) was irradiated 2 times in overlapping areas, as seen in Figure 4.16c. This was due to an issue with no current being measured in the first attempt, the sample was taken out and put back in with the issue corrected and a full dosage supplied during the second attempt. The beam centre spot area and halo for Ta can be seen in 4.16b, with a half circle collimator shape used due to a change in electrode size.

Figure 4.16 displays the conditioning plot of both the irradiated and non-irradiated Ta and Nb BCP and the irradiated Nb (without polishing). The non-irradiated Nb results are not included as the reduced electric field achieved are believed to be a result of machining, whereas this does not appear to be the case



(a) Ta and Nb conditioning

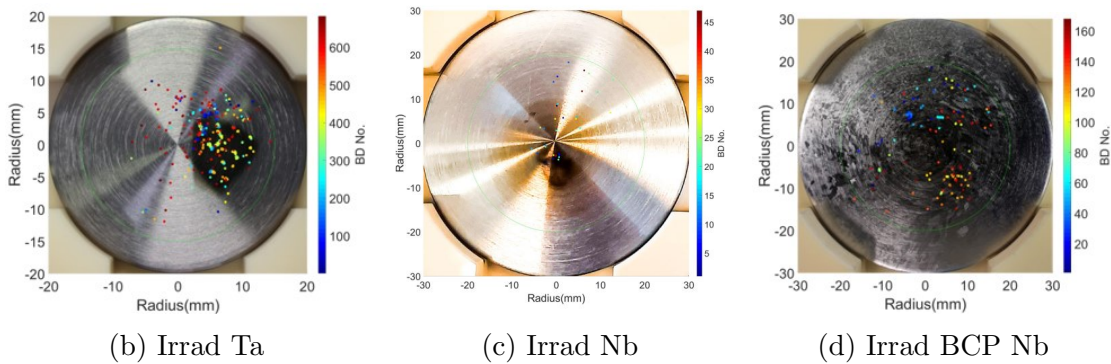


Figure 4.16: Ta, Nb and Nb BCP (a) conditioning of the irradiated and non-irradiated pairs and (b) the breakdown locations of the irradiated cathode with the breakdown number given from dark blue being the first to dark red being the last.

for the irradiated. From the plot it can be seen that both the non-irradiated Ta and Nb BCP conditioned to relatively high electric field as discussed in the previous chapter. Where as each irradiated pair had a large cluster of breakdowns with respect to pulses at 38 MV/m, 35 MV/m and 42 MV/m for Ta, Nb and Nb BCP respectively. This reduced the electric field and the pairs were unable to recover with a stable electric field achieved of around 23 MV/m for each. The larger difference compared to the non-irradiated pairs suggests this is an effect of

irradiation. But as discussed there is a possibility it is an effect of machining errors or defects. If it was a result of irradiation, both Ta and Nb would be unsuitable choices for an RFQ.

Ta and Nb BCP pairs have very few breakdowns before the large clusters occurred, this meant operation was very unpredictable. Whereas, Nb had breakdowns throughout the initial ramp to 35 MV/m before experiencing a larger cluster. This may have been a result of the difference in the surfaces between the different samples, with the Nb pair having defects that attracted breakdowns during the initial stages of conditioning.

Due to the low electric fields a number of breakdown locations were not detected as there is a dependence seen as discussed in Chapter 2.6. Breakdowns for the irradiated Ta were mostly clustered spatially on the side of the irradiation halo with a relatively large concentration to one side of the beam centre area. It is possible that the beam intensity was uneven, meaning one area receives a higher dose, which may explain this effect. Unlike other materials, breakdowns were concentrated in the irradiated area of the Ta sample, with 85 % of breakdowns detected being within the irradiated area. The fact of this high concentration within the irradiation area with very few breakdowns externally to this is good evidence of the reduced electric field being related to the irradiation. It may also suggest that something additional happened with this material causing the large reduction in achievable field.

The reason for including the initial test of irradiated Nb was that is performed in a very similar manner to the Ta and Nb BCP in terms of conditioning. Also seen from Figure 4.4b, there was an area within the double irradiated zone that had experienced several breakdowns, removing the discolouration caused by the carbon layer. This is strong evidence that the cause of the reduction in electric field was the irradiation rather than machining defects as seen for the non-irradiated

electrodes. Breakdowns for the second Nb having received BCP, appeared to be spread over the beam halo area and not just the beam centre. As it performed similar to the others discussed it would suggest that this also had reacted differently to irradiation causing the significant reduction in electric field.

4.5.5 Summary and Comparison

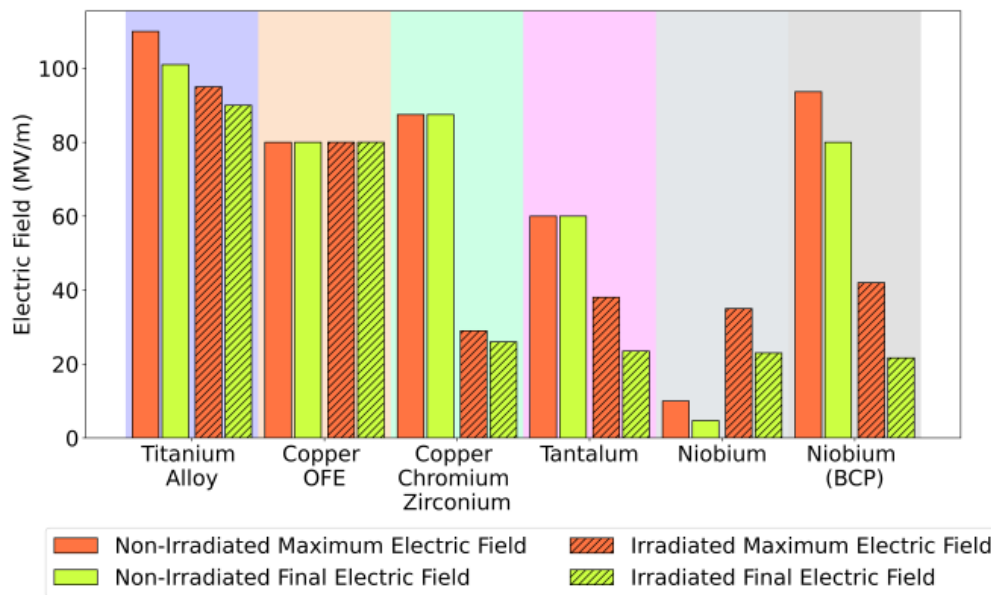


Figure 4.17: Summary bar chart of the maximum and stable fields of both the irradiated and non-irradiated materials tested using the same conditioning parameters.

Figure 4.17 displays a bar chart showing the maximum and final stable electric fields for the irradiated and non-irradiated pairs of each material. The materials are ordered by descending stable electric-field for the irradiated samples. From this it can be seen that only the TiAl_6V_4 and Cu OFE pairs performed well after irradiation. All of the other materials had a significant reduction in electric field, most likely as a result of the irradiation.

The roughness of the machined surfaces varied significantly, mostly due to the inherent difference in the difficulty of machining the different materials. The

difficulty to machine some of the materials could also influence the feasibility of making an RFQ [86]. Additionally, making a whole RFQ out of a material with low conductivity would result in an inefficient RF structure, requiring higher input power compared to a structure built from copper. The low conductivity can be compensated by including the material only in the vane tips, where the electric field is highest [105]. But this would also result in a significantly more complicated construction. As TiAl_6V_4 achieved the highest electric field this may be the best material for resistance to the affects of irradiation and conditioning higher than Cu. The issue with using TiAl_6V_4 is that this would need to be only for the vane tips and bonded to a more conductive material [105]. Joining copper to Ti is very complicated, and an RFQ using this method currently does not exist and would require research and prototyping before a working RFQ would be produced. Whereas Cu OFE RFQs are already common and used for Linac4.

	Max E-Field (MV/m)	Stable E-Field (MV/m)	No. BDs	No. Pulses
TiAl6V4	110	100	444	1.24E+09
	95	90	924	1.10E+09
Cu OFE	83	83	785	7.19E+08
	80	80	214	6.90E+08
	80	80	1020	7.31E+08
CuCr1Zr	85	85	254	3.60E+08
	29	26	606	1.70E+08
Ta	60	60	248	7.10E+08
	38.1	24	470	3.32E+08
Nb	10	4.7	273	5.94E+08
	35	23	539	3.81E+08
Nb BCP	94	80	2305	1.45E+09
	42	21.7	293	3.26E+08

Non-Irrad

Irrad

Table 4.2: Summary table of Irradiated and non irradiated conditioning

Table 4.2 displays a summary of the main test results including, the maximum

and stable electric field reached, number of breakdowns over conditioning and the total number of pulses, where highlighted rows indicate irradiation before testing. For the majority of the materials excluding Nb BCP the number of breakdowns was greater for the irradiated materials despite having conditioned for few pulses. This is strong evidence that the irradiation has an impact on the number of breakdowns during conditioning.

		TiAl6V4	Cu OFE	CuCr1Zr	Ta	Nb	Nb BCP
Breakdown Number	Inside	626	916	417	398	5	62
	Outside	166	0	9	15	1	11
	All	915	1025	606	470	284	293
	No Location	123	109	180	57	278	220
Breakdown Number/mm ²	Inside	0.88668	1.2960	0.5906	0.5637	0.0070	0.0878
	Outside	0.3023	0	0.0163	0.0273	0.0018	0.0200
	All	0.7290	0.8167	0.4828	0.3745	0.2262	0.2334
	No Location	0.0980	0.0868	0.1434	0.0454	0.2215	0.1752

Table 4.3: Absolute and normalised number of breakdowns inside and outside of the irradiated beam pipe halo area, compared with the total number and breakdowns not detected by the cameras.

Analysis of the breakdowns detected by the cameras with relation to their location inside or outside of the irradiated halo area of each material can be seen in Table 4.3. Plots showing these results over the number of pulses with relation to the conditioning can be seen in Appendix M. In the cases where the breakdowns were detected by the cameras it can be seen that there was a significantly more breakdowns within the irradiated area compared to the surrounding areas also after being normalised by square mm. The results for Cu OFE are included to show the number of breakdowns that occurred and were detected but in this case there was no high field area outside of the halo. For the 'Nb' pair very few breakdowns were detected but it was observed after removal that there was a cluster within the double irradiated area.

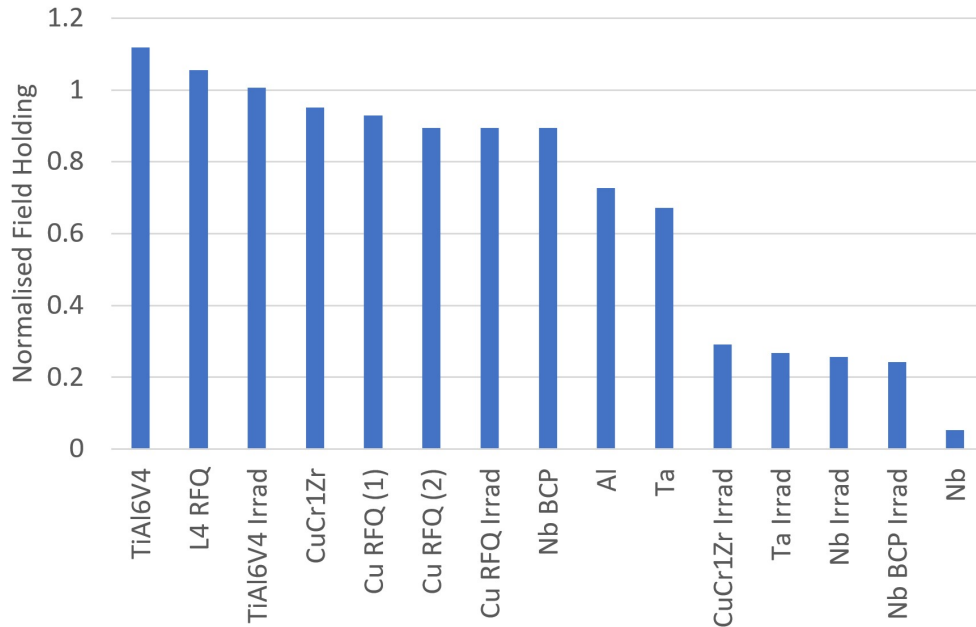


Figure 4.18: Bar chart of the calculated normalised field holding values for the L4 RFQ and all pairs of electrodes tested and the L4 RFQ, using the stable electric field values and Equation [4.1].

The final stable electric fields of all electrode pairs tested were used to calculate the gap dependence normalised field holding, using Equation [4.1]. Figure 4.18 shows the normalised electric fields of Cu OFE L4 RFQ and all materials tested in order from the highest to lowest normalised electric fields. From this it can be seen that the only material that exceeded the normalised electric field of the RFQ was the non-irradiated TiAl_6V_4 . This could mean that the other materials and irradiation are not able to achieve the electric fields required for the RFQ. Alternatively it could mean that the use of the normalised field holding equation is not directly applicable to the RFQ and that both TiAl_6V_4 would be suitable even with the effects of irradiation.

4.6 Effects of Irradiation Conclusions

The best choices of material for an RFQ, based on the irradiated field holding results shown are TiAl_6V_4 and Cu OFE. Both TiAl_6V_4 pairs reached the highest stable electric field. However, TiAl_6V_4 may display unpredictable instabilities causing a decrease in obtainable electric field if run close to the limit. It also has a lower conductivity so careful design would be required if used for an RFQ. Copper gave the second best results and appears to reach the same electric field with an initial increase in the number of breakdowns that conditions away irradiated defects. Whilst blisters were produced during irradiation they did not prove to be a critical cause of breakdowns as many blisters were unaffected during conditioning. Copper is the current material used for the L4 RFQ, and well established within the electric field, it would not require any changes.

Ni and Ta both had a significant reaction to the irradiation causing a large and unpredictable cluster in break-downs that it was not possible to recover from. CuCr_1Zr was not discussed but can be seen in the summary plot of Figure 4.17. The achievable electric field was greatly reduced by the irradiation and therefore it would also not be a suitable material.

Breakdown locations for TiAl_6V_4 , Cu OFE, CuCr_1Zr , and Nb were distributed over the irradiated area and did not show preference to the beam centre area for irradiated electrodes. For the irradiated Ta electrodes, the break-downs were mostly clustered in the beam centre area. For the non-irradiated electrodes breakdowns were distributed over the whole high electric field area. Analysis of the areas of the irradiated electrodes suggests a possible higher carbon content in the beam and halo areas from the head of bunch focused differently.

It is important to note that in this experimental study the electrodes were irradiated before, this process differs from the RFQ due to the RFQ receiving

constant irradiation throughout running. Re-irradiating or constant irradiation may affect the performance or the achievable electric field. In the cases of the TiAl_6V_4 and Cu OFE pairs where the conditioning seems to reduce the effects of irradiation may suggest an ability to run stably. This would be the case if the RFQ conditioned away impurities faster than they are produced.

It can be seen that all materials reached relatively high electric fields with only irradiated pairs being restricted suggesting it is an effect of irradiation. Cu OFE was tested non-irradiated twice whilst the other materials were only tested once. This makes the results shown less reliable as it may change between tests and parameters in a way that is currently not understood.

Chapter 5

Field Emission Measurements

5.1 Introduction

As a result of tests of different materials shown in Chapter 3.6, after the conditioning of each, field emission current measurements were conducted. As discussed in chapter one for breakdown in a vacuum environment, an electrical connection need to be formed between the anode and cathode. One of the likely initial stages for this to occur is field emission and measurements of this have been done previously in the same system [106]. By measuring the field emission current, this gives a value for an amount of current emitted for a given voltage. This chapter discusses the setup, method, measurements and analysis for each of the materials tested within the system.

For each material tested, measurements of the field emission current were done. For this, controlled steps of the supply voltage are set, then for each step the field emission current is measured and the gap voltage can be calculated. Using the method to be shown with a resistance in series with the means the gap voltage is limited by the about on field emission current for each supply voltage step. The gap voltages achieved and field emission currents measured for each material can

be compared with the field holding capabilities from the pulsed conditioning. A description of the calculations of the field enhancement factors using the Murphy-Good equation [23], which corrected the previous equations known as the Fowler-Nordheim equation [30]. Calculation of the field enhancement factor are then shown for analysis looking at how they correlate with conditioning results.

Measurements were previously conducted with a reverse polarity to that of conditioning with Cu electrodes [60]. To expand on those results, measurement have also been done with the normal and reverse polarities for the different materials. This is done to observe the difference in field emission current in the reverse polarity as there is strong evidence of breakdowns being cathode dependent suggesting the anode from the normal polarity will not experience the same conditioning effect throughout and therefore should have a higher field enhancement factor.

Additionally, as measurements were also taken of the field emission for irradiated and non-irradiated pairs, results of the effects of irradiation on field emission are given. As mentioned, the field emission current gives an indication of the field enhancement factor, an increase in field emission at lower supply voltages was observed, which correlated with the reduced electric field holding capabilities observed during conditioning of the irradiated samples.

5.2 Electrical Setup

Figure 5.1 displays the schematic of the setups used for field emission measurements, during which spectrometer measurements are taken. Figure 5.1a shows a cross section of the LES with the upper and lower feedthroughs highlighted. Due to the different systems tested, the bottom feedthrough is only a property with one of the two chambers, with the other using the chamber to ground the bottom

electrode.

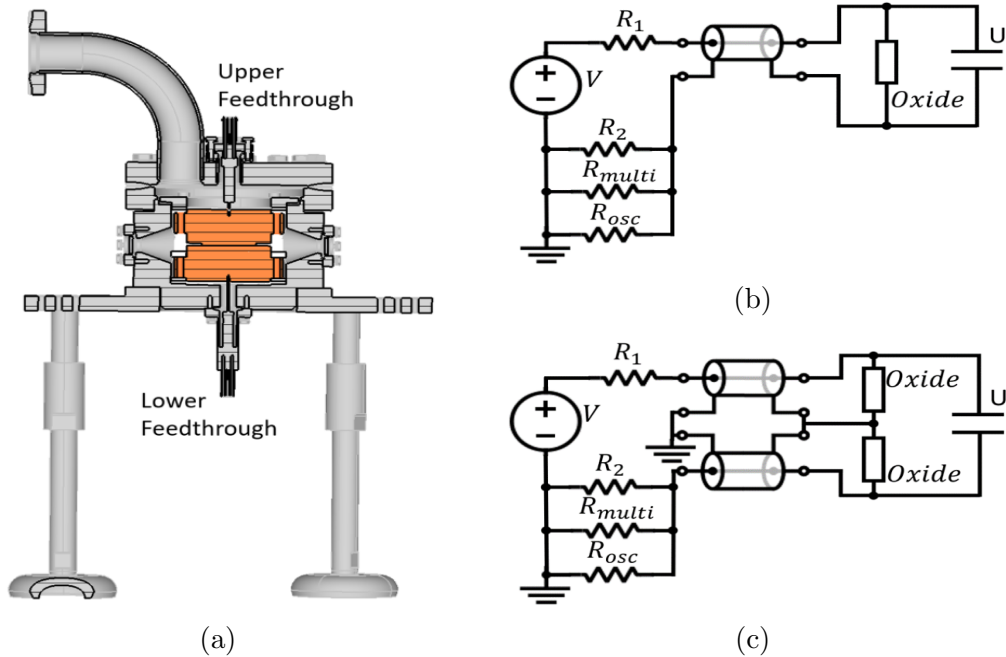


Figure 5.1: (a) Upper and Lower feedthrough to LES 3. (b) Schematic representation of connecting to only one feedthrough with possible oxide contamination. (c) Schematic representation of connecting to two feedthroughs with possible oxide contamination.

The schematic for when one feedthrough is connected and the bottom electrode is grounded to the chamber is displayed in Figure 5.1b and when two feedthroughs are used can be seen in Figure 5.1c. The two configurations give different measurement values if there is an electrical connection from high voltage to ground due to contamination on the feedthroughs. In the case where only one connector is used and there is leakage through the connector to the chamber, the leakage current cannot be distinguished from field emission current, and the sum of the two is inadvertently measured. Previous results made with this configuration could have systematic errors due to this effect.

When two connectors are used, the leakage from the top connector goes to ground without passing through R_2 , the multimeter, or the oscilloscope, and thus does not influence the measurement. The leakage current still contributes

to the load on the high-voltage power supply, and can be measured by the supply's internal current measurement. A discrepancy in the current measured by the multimeter and the power supply therefore indicates the presence of leakage current, and also corresponds to current drawn from the supply at low voltages where no field emission current can be reasonably expected. Whenever significant leakage current was observed, the connector was cleaned before measurements were continued. The two-connector configuration is still susceptible to leakage on the lower feedthrough. However, physical signs of contamination were not seen on the lower feedthrough. Also, as the voltage on the lower feedthrough was much lower than on the upper feedthrough (tens of volts as opposed to kilovolts), the leakage current would also be proportionally smaller given the same leakage resistance.

Providing that the connectors are clean and there is no leakage then the tests should work as intended. For the following tests a constant voltage supply was used without the pulsed generator. These tests were limited to a maximum of 1 mA by the power supply and 8 kV by the cables used. From the power supply there is 6.39 M Ω resistor (R1) in series with the system where the system acts electrically as a capacitor. R1 and R2 reduce the probability of a breakdown from occurring as they reduce the gap voltage as the field emission current increases.

There is a spark gap from the floating cathode to ground where R2 is measured. This is rated at around 70 V and therefore past this voltage will start conducting, this is to protect the oscilloscope from high voltages. This means measurements from the multi-meter should not exceed 70 V, as past this point the measurement would be false.

During measurements the supply voltage is increased in steps, with voltage measurements across R2 recorded on an oscilloscope once per second, for a set number of seconds specified by the user. For each measurement, the supply voltage is reduced if the breakdowns occur in an unstable temporal cluster, this is decided

by the user. For these measurements this can be described as several breakdowns consecutively within a few seconds. This is decided by the user, if it appears that breakdowns will continue to occur. The other reason for reductions in the supply voltage is if the supply voltage reaches 8 kV or when the voltage measured across the multi-meter reaches 70 V as mentioned. If field emission measurements do not show a significant increase during measurements, R2 can be decreased to increase the field across the gap for a given supply voltage. To counter this, if there is a significant increase in field emission current and many breakdowns occurring, R2 can be increased for the opposite effect.

Calculations of the field emission current can be done using the voltage measured across the second resistor (R2), with relation to the supplied voltage. An oscilloscope and a multi-meter were placed in parallel to R2 to measure the voltage. For this, the resistance of both of these devices also needs to be included in the calculation. Equations for these calculations are given as:

$$U = V - V^* - I \times R_1 \quad (5.1)$$

$$I = V^*/R_1^* \quad (5.2)$$

$$1/R^* = 1/R_{osc} + 1/R_{multi} + 1/R_2 \quad (5.3)$$

Where U = gap voltage, V = supplied voltage, I = field emission current, V* = multi-meter voltage, R* = gap resistance, R₁ = series resistance = 6.36 MΩ, R₂ = 100 kΩ, 1 MΩ, or 10 MΩ, therefore R_{osc} = 1 MΩ = oscilloscope resistance, R_{multi} = 10 MΩ = multi-meter resistance.

Use of these equations allowed for the field emitted current and voltage in the electrode gap to be calculated. This was then used to analyse the relationship between these values and to generate current vs. voltage plot.

5.3 Field Emission Measurements and Analysis

5.3.1 Normal Field Emission Measurements

As a result of having several different materials to condition a study of the field emission of each material after conditioning was conducted. Field emission measurements were done after all other tests were completed, as it can be damaging to the surface and could influence following tests. Although the resistors as part of the electronics of the setup reduce the likelihood of breakdowns and absorb the power, breakdowns do still occur and can cause significant damage. When a breakdown does occur, unlike with the pulsed setup when the power is stopped, for these measurement there are no controls to stop the power. Therefore, it is still applied and this can lead to maintaining an arc that damages the surface of the electrodes.

The different reasons for no longer increasing the supply voltage are associated with a gap voltage. Whether it was because breakdowns occurred at that voltage or there was a significant amount of field emission causing the gap voltage to saturate. This means that for each of the field emission tests the field achieved by the electrodes was different and these values can be compared to the field emission measured and electric field achieved from conditioning.

Figure 5.2 shows the field emission curves for each of the materials and a vertical line showing the fields achieved during conditioning for the materials. Other than an additional hard Cu OFE example, all materials shown are the same non-irradiated electrode pairs described previously. It can be seen that there is a correlation between the stable electric-fields reached during conditioning and the gap voltages achieved during the field emission tests. This suggests that the conditioned field holding capability of a specific material, as measured by the maximum stable field after conditioning influences the voltage at which the

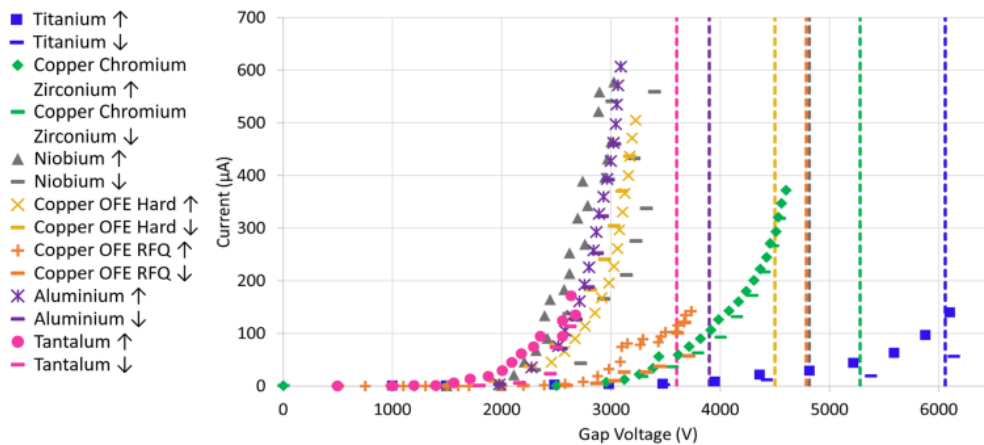


Figure 5.2: Field emission current measurements with the increase given using different symbols for each materials and the decrease given as a dash of the same colour. Voltages achieved during pulsed conditioning are given as dashed vertical lines with corresponding colours.

electrodes start field emitting. Additionally, the materials with higher electric field holding capability show less field emission current. The relationship between the gap voltage and both the stable and maximum electric fields during pulsed tests is plotted in Figure 5.3. Fitting a linear trend line to this data shows a relatively close correlation between the field emission measure gap voltage and pulsed stable fields and a weaker correlation when compared to the pulsed maximum fields.

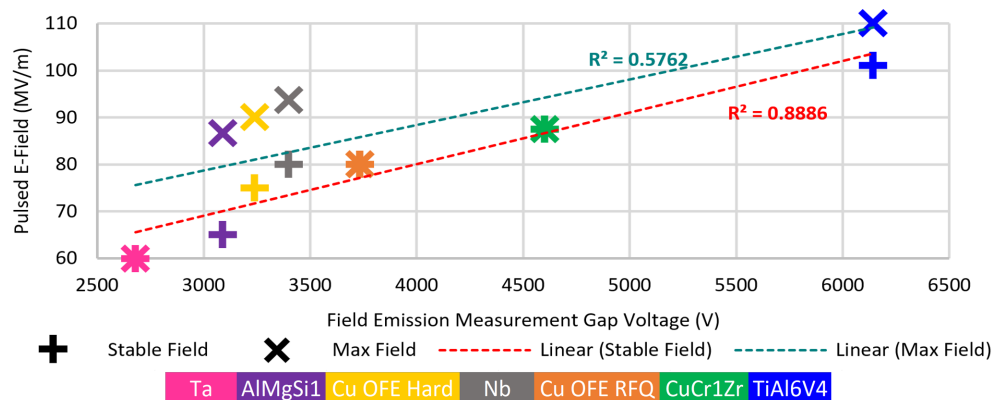


Figure 5.3: Gap voltage during field emission measurements as described in Equation 5.1, compared to the final stable and maximum electric fields achieved during pulsed conditioning.

The Ti alloy electrodes reached a similar gap voltage during field emission

measurements as achieved during pulsed conditioning, with a relatively low field emission current of $140 \mu\text{A}$ measured. At the peak of the field emission testing of the Ti alloy, a number of breakdowns occurred despite the low amount of field emission current, which may suggest something else had an effect to cause breakdowns that meant a high field emission current was not needed. Breakdowns with low amounts of field emission current were also observed for the Cu OFE RFQ and Ta electrodes, all measurements with a field emission current between $140 \mu\text{A}$ and $170 \mu\text{A}$. CuCr_1Zr achieved the second highest voltage with a relatively high current compared to the Ti alloy. It appeared to have a relatively stable field emission producing a smooth curve which was also the case for Cu OFE Hard and the Al alloy.

There are two Cu OFE results shown, the difference between the two is that "Cu OFE RFQ" tested was heat treated the same as the RFQ and the other was not heat treated and is as received from machining, named "Cu OFE Hard" in these plots. The Cu OFE Hard were conditioned using the X-band CLIC structures algorithm and achieved a final field of 75 MV/m with a relatively high breakdown rate.

Cu OFE Hard, Nb, Al Alloy and Ta follow a similar trajectory with an increase in field emission current starting around the same voltage. For Nb, the decrease in supply voltage shows a small hysteresis of the voltage increasing, this may have been a result of conditioning effects during the increase allowing it to reach higher field when decreasing the supply voltage. This can be seen as the grey arrows of the increasing field emission current in Figure 5.2 reaching a gap voltage just below 3000 V and when the supply voltage decreases the gap voltage increases to over 3000 V due to a decrease in field emission current. The Ta electrodes whilst following this had experienced breakdowns and therefore the supply voltage was not increased further limiting the field emission current.

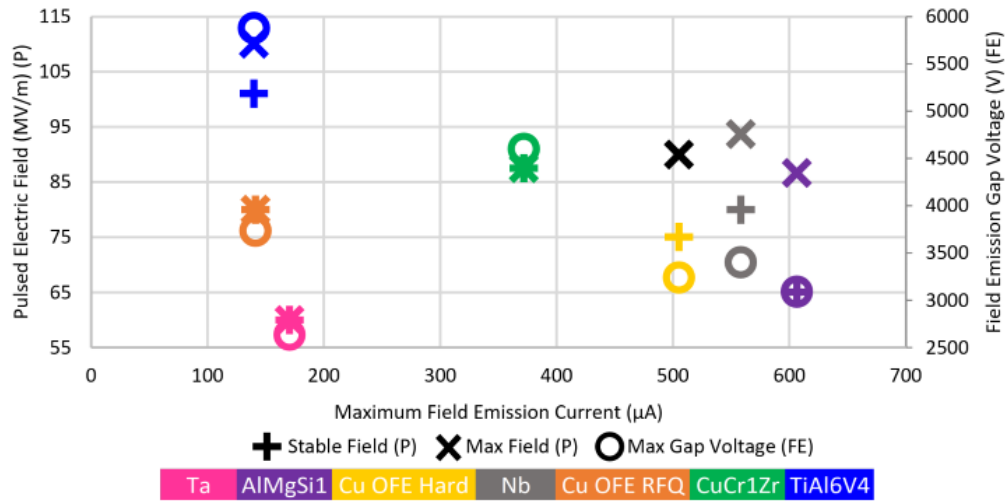


Figure 5.4: Maximum field emission currents versus the gap voltage during the field emission measurements and the maximum and stable fields during pulsed conditioning.

Figure 5.4 shows the correlation between the maximum field emission current with the maximum gap voltage during field emission measurements as well as the stable and maximum field during pulsed measurements. The following discussion excludes ‘Cu OFE RFQ’ and ‘Ta’ that did not reach high fields and currents due to breakdowns occurring, leading to the field being reduced. There appears to be a linear inverse correlation between voltage holding capabilities and the maximum field emission current for the different materials. This relation between the reduced field emission may influence the capabilities of the electrode pair to reach higher electric fields. The maximum electric fields during conditioning that are different to the final stable electric fields, do not correlate with the voltage holding capabilities during the field emission measurements. This suggests the electrode pairs reaching higher electric fields at some point during conditioning did not affect the field holding capabilities during the field emission measurement.

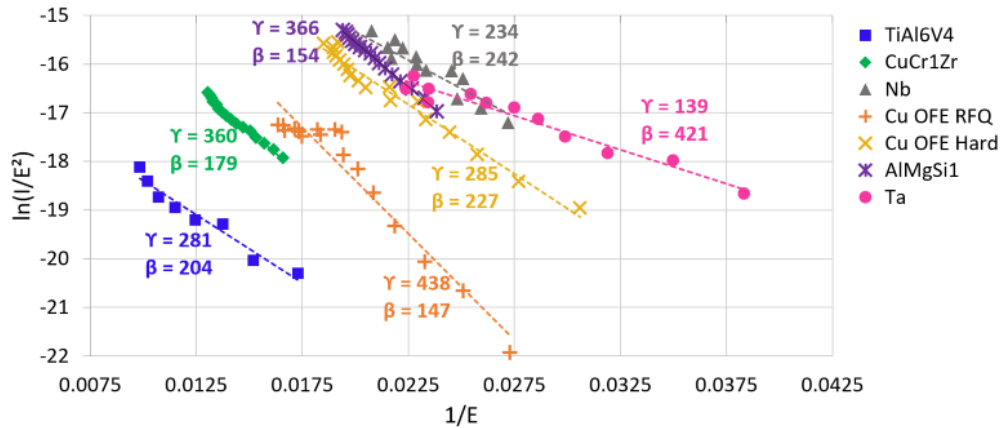


Figure 5.5: FN plots for each of the materials, with γ determined as the gradient of the slope and the calculated β indicating the field enhancement factor, with E denoting electric field in MV/m and I denoting current in A.

5.3.2 Field Enhancement Factor Calculations

Fowler-Nordheim plots for each of the materials tested can be seen in Figure 5.5. For each materials the individual measurements are shown and a line of best fit given in the same colour. Substituting the gradient of each line into the equations as described, the β for each measurement is also given. Most of the plots are not perfectly linear, but have an upwards curvature. This corresponds to the β value decreasing at high electric fields. Possible explanations for this are space-charge effects beginning to play a role as the field-emitted current becomes large [107], or the gas discharge tube (present in the measurement setup in order to protect the measurement electronics from possible overvoltages) beginning to conduct a small current.

To analyse the values of β calculated, Figure 5.6 includes 2 plots with beta on one axis and the field emission measurement maximum gap voltage and field emission current for each material. This could indicate whether the field enhancement calculated has an impact on the field holding capabilities of a material or the field emission current observed. Error bars can be seen for AlMgSi₁ and CuCr₁Zr to indicate the possible variation in the beta as a result of the unknown

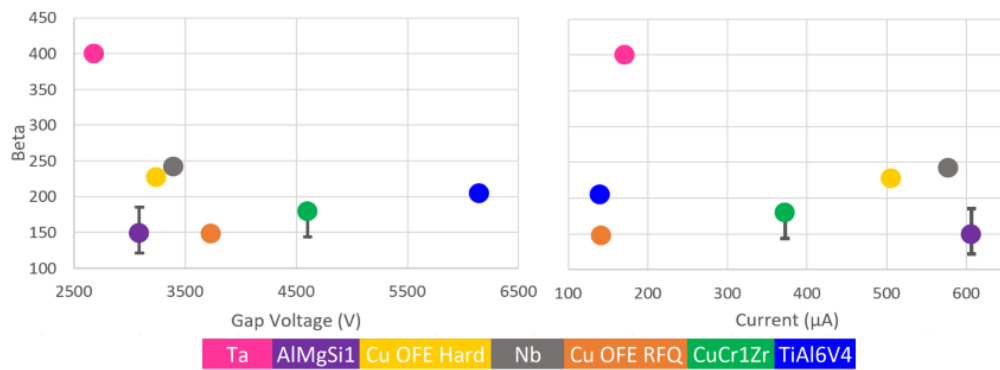


Figure 5.6: Maximum gap voltage and field emission current with respect to β during the field emission measurements for the different materials.

work function for the alloy. The dots in these cases represent that main materials of Al and Cu respectively and the largest variation for the alloyed materials, the work functions for different materials can be found in Appendix P. This was also done for the Ti Alloy but the error bars are within the size of the marker and therefore has little variation on the work function. These results are not very compelling evidence of correlations between the beta, gap voltage and current for each of the materials tested. Whilst there are linear correlations within the data to count these would require excluding around half of the data suggesting these are not statistically relevant. More pairs of materials would need to be tested to verify whether there is a correlation or if these are not related.

5.3.3 Normal and Reverse Polarity

Studies have been conducted previously of the field emission in the normal polarity of conditioning and the reverse polarity [60]. As well as conditioning in one polarity and then switching the polarity to see the effect this had on the conditioning curves and breakdown location. The previous studies shown in Figure 5.7 had electrodes of the same diameter which differs to the current measurements shown in Figure 5.8 in which a small anode to large cathode was used. Figure 5.7 displays the results

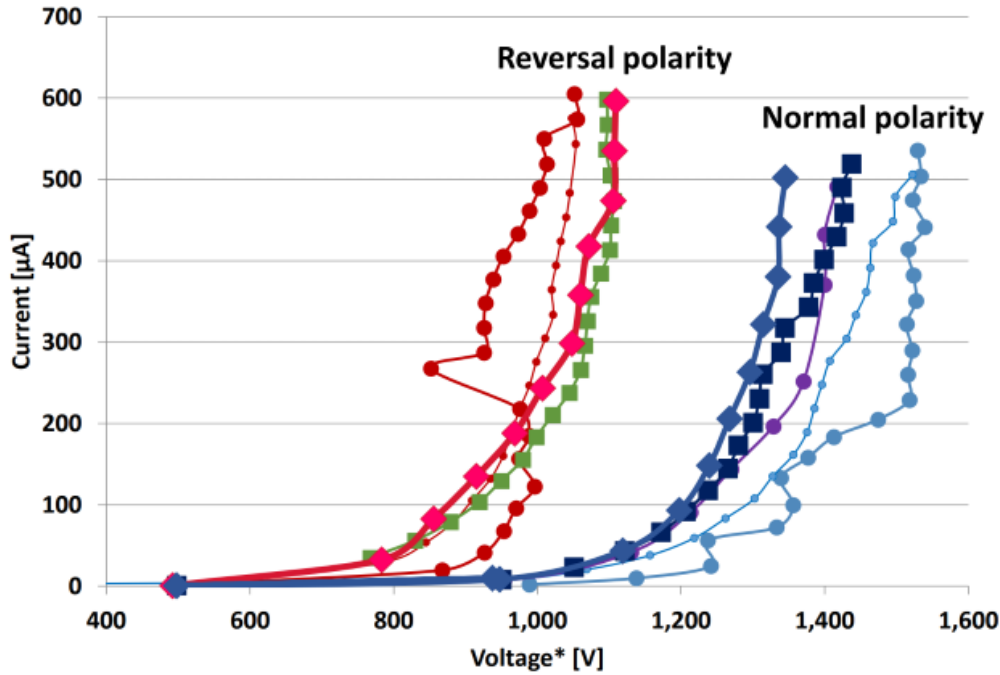


Figure 5.7: Measurements of field emission current with respect to the gap voltage made in the normal and reverse polarity from a previous study using Cu OFE electrodes [60].

shown for Cu electrodes with a 20 μm gap. From these plots it is consistently observed that the field emission occurs at lower voltages for the reverse polarity with similar levels of current measured at the peak of these curves.

During field emission measurements of each of the materials after conditioning, several scans of the normal polarity were made before the final field emission measurements made with the reverse polarity. The results of both normal and reverse polarity tests are displayed in Figure 5.8. It was also observed consistently with the different materials except Nb that the field emission occurred at a lower field in the reverse polarity. The difference in the achieved field varies for the different materials with the Ti alloy showing the largest variation, then CuCr_1Zr , then the Ta electrodes. Each of the results shown are of consecutive measurements with a normal polarity test and then a reverse with the possibility of occurring on different days meaning they may have experienced some conditioning effect

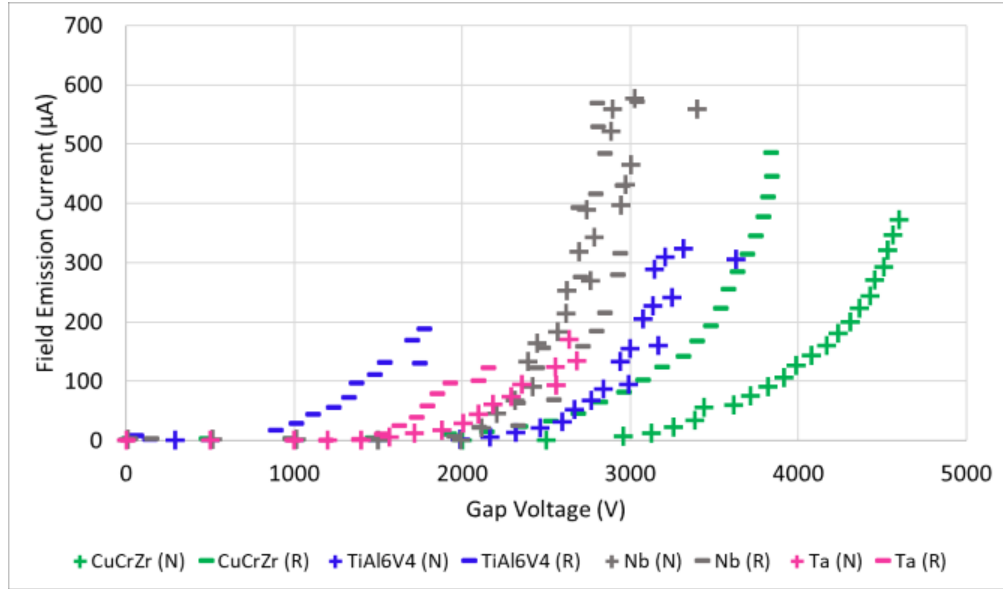


Figure 5.8: Normal (N) and reverse (R) polarity field emission current measurements of different materials tested.

during the initial ramp. Breakdowns are also more prone in the reverse polarity and can be catastrophic. During some field emission tests, the current fluctuated significantly with time, causing the curves to appear jagged rather than smooth as expected from field emission. Also to note is that for these tests, a small anode and large cathode was used which when in the reverse polarity would introduce an additional field enhancement from the electrode edge that could contribute to the increase in field emission currents at lower gap voltages.

	Normal Polarity		Reverse Polarity		Difference (Reverse/Normal)	
	Gap Voltage (V)	FE Current (μA)	Gap Voltage (V)	FE Current (μA)	Gap Voltage	FE Current
CuCr1Zr	4602.09	372.089	3842.48	485.15	0.834942	1.303855
TiAl6V4	3631.84	323.051	1772.21	187.891	0.487965	0.581614
Nb	3399.17	577.472	3036.15	570.618	0.893203	0.988131
Ta	2679.58	170.582	2152.61	121.627	0.803339	0.713012

Table 5.1: Maximum gap voltage and field emission current for both normal and reverse polarity of the different materials as seen in Figure 5.8, and the difference between them.

Table 5.1 summarises the results shown in Figure 5.8 giving the maximum gap voltage and current in the different polarities for each of the materials. Additionally the difference between the two is given as the reverse value divided by the normal value for the voltage and current. From this it can be seen that for CuCr_1Zr , TiAl_6V_4 , and Nb, the difference between the current is higher proportionally compared to the change in voltage. Meaning that whilst the voltage for field emission was reduced the amount of current for the specific voltage was increased. Ta is an exception from this with a smaller change in current compared to voltage, this was most likely a result of being unable to increase the supply voltage further due to breakdowns.

5.3.4 Irradiation Effects on Field Emission

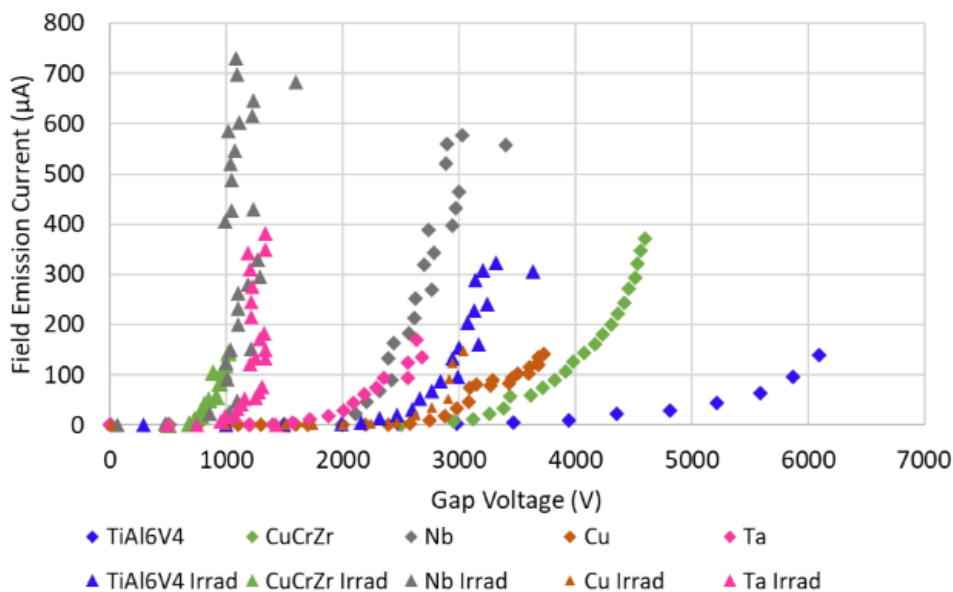


Figure 5.9: Field emission current measurements for the non-irradiated and irradiated pairs of the different materials tested.

Another comparison is the effect of irradiation on field emission for each of the materials tested, can be seen in Figure 5.9. This displays the field emission

measurements for the irradiated and non-irradiated pairs of each material tested. For all of the materials the non-irradiated pairs reached higher voltages. Each of the irradiated materials that had a very low stable field after testing can be seen to start field emitting around 1250 V. For the Cu electrodes that reached the same field with similar breakdown rates, they also had similar voltages and amount of field emission. The difference in voltage for the Ti alloy electrodes was relatively larger around 2.5 kV, with higher field for the irradiated pair before experiencing breakdowns.

	Non-Irradiated		Irradiated		Difference (Irrad/Non-Irrad)	
	Gap Voltage (V)	FE Current (μ A)	Gap Voltage (V)	FE Current (μ A)	Gap Voltage	FE Current
TiAl6V4	6099.12	140.031	3631.84	323.051	0.59547	2.306996
Cu OFE	3734.33	141.617	3040.32	149.144	0.814154	1.05315
CuCr1Zr	4602.09	372.089	1018.62	143.891	0.221339	0.386711
Ta	2679.58	170.582	1431.98	382.309	0.534405	2.241204
Nb	3399.17	577.472	1597.29	731.51	0.469906	1.266745

Table 5.2: Maximum gap voltage and field emission current for both irradiated and non-irradiated pairs of the different materials as seen in Figure 5.9, and the difference between them.

Table 5.2 shows a similar analysis to that of Table 5.1, except with the values for the non-irradiated and irradiated measurements given in Figure 5.9. From this table it can be seen that in all cases the gap voltage is reduced for the irradiated samples, with some have a greater decrease than others. In terms of the field emitted current measured, in all cases except CuCr₁Zr there was a higher field emission current for the irradiated pairs. For the Ti alloy and Ta pairs the amount was more than double for the irradiated pairs of each material.

5.4 Field Emission Conclusions

A good correlation between the stable fields achieved during conditioning and the fields during the field emission measurements can be seen for the different materials tested. There were different levels of field emission with relation to voltage with some experiencing several breakdowns at low levels of current. Field enhancement factors were calculated for each of the field emission measurements shown, with possible correlations between the gap voltage and current measurements with some outliers making this less convincing. Due to there only being one of each material tested this was not the most reliable result and more studies may provide more insight.

Additional tests of the field emission for the different materials, looked at the normal polarity being the same as conditioned and the reverse polarity. This was previously looked at for Cu OFE and showed that field emission rose at a smaller voltage in the reverse polarity compared to the normal polarity. When the same test was conducted for the different materials Nb did not show this phenomenon but the others did with different amounts of change between the positive and negative voltages achieved.

Field emission tests were conducted for the non-irradiated and irradiated electrodes and a comparison of these shows a reduction in the field during field emission tests in all cases. With these pairs the difference in field for each material also varies. As 3 of the pairs of irradiated electrodes did not reach significant fields and this can also be seen in the field emission results as they show similar curves with different levels of field emission. The difference between the irradiated and non-irradiated Cu OFE electrodes was relatively small in terms of voltage with the same amount of field emission when breakdowns became unstable.

Chapter 6

Optical Emission Spectra

6.1 Introduction

Additional to the interest in field emission current, is the light emitted during field emission and understanding the relationship between these two phenomena. For this reason, correlated measurements of field emission and the optical spectra related to this have been conducted. For field emission measurements, a constant DC supply was used, this was as part of the setup to be described. A constant DC supply also has an effect on the light emission, to be discussed in the next chapter. The most likely reason for this is that the source of light is related to the supplied voltage and a constant supply means light is being emitted the whole time increasing the total amount of light collected with respect to time.

There are several possible causes of light during field emission; some of the ones considered include thermal radiation from heated emitter sites [108], optical transition radiation produced when the field emitted electrons strike the anode [109], plasmon oscillation [110] and recombination radiation from electrons captured in an excited state due to electron bombardment which subsequently decay to the ground state, producing photons [111]. It is expected that the

dependencies on time, voltage, current and material will give experimental results for addressing important high-field questions such as the origin of the field enhancement factor, the nature of breakdown nucleation, the nature of the conditioning process and the evolution of high-field surfaces with pulses and time.

Light has been measured during field emission experiments in a tip-to-plate DC system at CERN (See Section 1.6). Due to the difference between geometry of that system and the LES, there was no certainty that the light during breakdowns or field emission would be measurable. The different design of system introduced several optical restrictions that make it more difficult to observe the high field area directly.

Measurements of spectra within the current setup were first achieved using ridged electrodes producing a small high-field surface area allowing for better optical conditions. These highlighted a difference in the field for different alignments of the ridged electrodes. Studies measuring the light from the perpendicular windows and with different polarities displayed a difference in light intensity for the windows and an additional peak at the wavelength of 700 nm when the reverse polarity to conditioning was applied. Variations in the light intensity over times were observed during measurements, therefore a measurement of this phenomenon was made to correlate the fluctuations in the spectra with the changes in the field emitted current. The studies of the variation with times showed that wavelengths with the least variation in time followed the current more closely, suggesting the variation were a results of something additional occurring. Analysis of the light emission showed a good correlation with the field emission current for all results suggesting they were related.

As there were several different materials that where used for measuring the field emission as discussed in Chapter 5.4, spectra measurement were done in parallel. For Cu and CuCr₁Zr the spectra was consistently measured, with the

spectra produced corresponding closely to the reflectance curve of Cu suggesting a filtering affect. During the field emission tests of Nb and Ta, spectra was only measured on one occasion and was extinguished after a breakdown in both cases. When light reflected off Cu OFE electrodes, a colour filtering was observed giving only copper colours. Therefore, tests of Al alloy electrodes were conducted due the materials ability to reflect colours relatively evenly over the visible spectrum. Despite reaching gap voltages and currents on a similar level as Cu there was no light measured, which may suggest that this is more prone in Cu based materials.

6.2 Optical Setup

For optical purposes, initially, a different design of electrodes to normal were used whilst measuring the spectrum. Figure 6.1, shows the ridged electrodes with a crossed and parallel alignment respectively, giving in both cases a smaller high-field area compared to normal. This meant that the high field area and therefore the area in which the light could be coming from was reduced. As this system was not designed for the purpose of optical measurements it is difficult to have a good alignment. Due to the configuration of the crossed electrodes, there was possibility that the gap between the electrodes was higher or lower with respect to the alignment with the collimator for measuring the light. Therefore, observations from perpendicular angles would play a role in seeing into the gap between the electrodes, this will be discussed in more detail.

When using large electrodes, light can come from anywhere on the surface, and if it is emitted from a point far away from a camera it is less likely to be detected or to be more distorted. If the light source was not on the edge where the collimator is located, then the light would not have a direct exit to the collimator and would most likely reach the collimator via reflections off the surface of the material. The

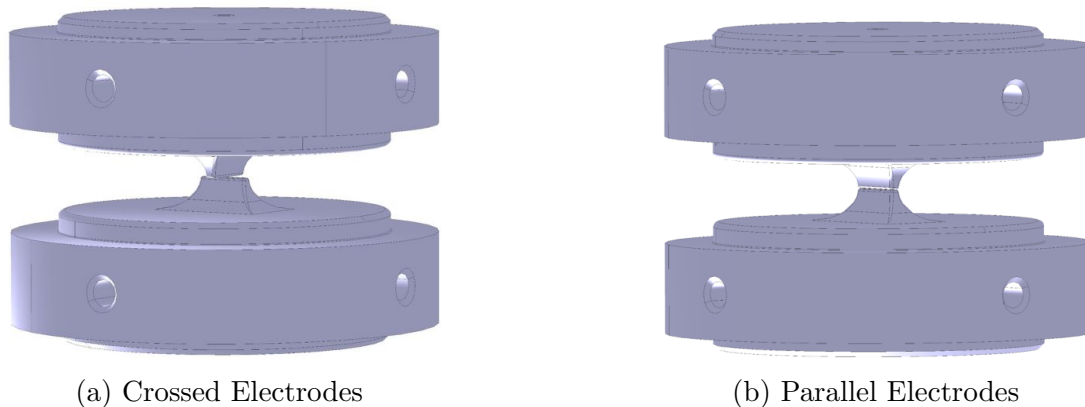


Figure 6.1: Images of the (a) crossed and (b) parallel alignments of the ridged electrodes

electrodes tested on this system are most frequently made of copper, therefore any light reflected off this will be filtered by the reflectance spectrum of copper.

The surface of these electrodes is 1.039 mm by 9.039 mm, therefore the area of high field is approximately 9 mm^2 for parallel electrode and 1 mm^2 for crossed electrodes, drawing can be found in Appendix E. Having this small area should allow for the light emitted to be transmitted directly to the output collimator. As there is the possibility to change the gap distance between the electrodes by changing the ceramic between the electrodes to one of a different height, gaps of $60 \mu\text{m}$ and $100 \mu\text{m}$ have been tested.

As mentioned in Chapter 2.6, due to either the design or manufacture of an electrode edge there is an inevitable field enhancement at the electrode edge. Having a field enhancement on the edge of the electrodes leads to more current being released for a given gap voltage. The design of the ridged electrodes was not optimised to remove the field enhancement. A simulation of electric field close to the surface of one of the electrodes was done for both alignments, with a gap of $60 \mu\text{m}$. Figure 6.2 shows a 3D image of the electric field across the surface, with the noise seen as a result of the mesh. The simulated maximum electric field for a gap voltage of 5 kV for the parallel alignment was 86.8 MV/m (a field enhancement

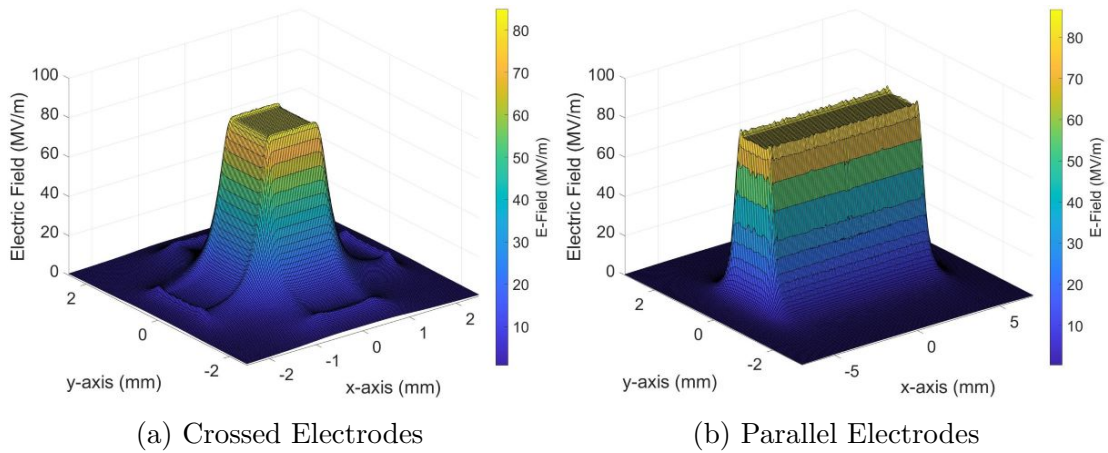


Figure 6.2: Plots of the electric field on the surface of the electrodes for the (a) crossed and (b) parallel alignments. Where the x and y labelled axis give the surface dimensions and the electric field is given from the other axis and the colour representation.

factor of 1.04 with respect to infinite parallel plates) and for the crossed alignment was 85.0 MV/m (a field enhancement factor of 1.02). This could lead to an increase in the amount of field emission proportional to the field enhancement.

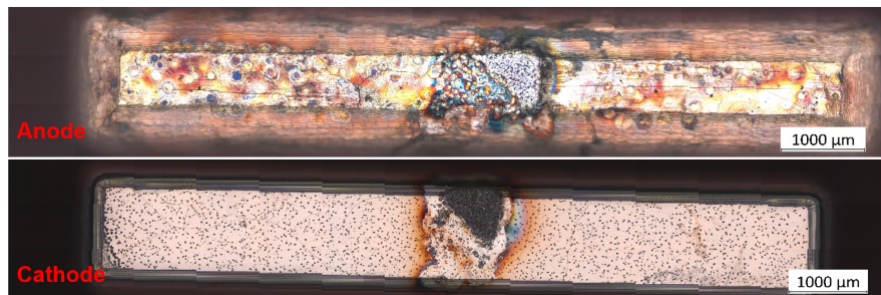


Figure 6.3: Microscopy images of the anode and cathode high-electric-field surfaces respectively after testing in both alignments.

One limitation to the use of electrodes with small surface areas is that breakdowns on the area of high field can cause significant amounts of damage as all breakdowns are concentrated in the small area. The electrodes shown in Figure 6.3, show the electrodes after testing in the LES. Within the system the electrodes are held 60 μm apart. It can be seen that there is more damage in the centre that would have occurred when the electrodes were tested in the crossed

configuration. From the scale it is shown that this damage was 1 mm wide, which verifies this. It is important to note that the damage seen would have affected the gap distance, and therefore electric field and the field enhancements on the surface. During tests, this could not be measured to know the gap distance throughout the measurements.

6.2.1 Spectrometer

Throughout the following measurements the two perpendicular cameras were in place to detect light. The cameras are used to determine the location of each breakdown or any other intense light emission using the configuration shown in Chapter 2.6. Additionally a collimator was attached to one of the 4 windows as seen in Figure 6.4, with the aim to capture as much light as possible from within the system. The collimator lens placed at close to the window into the system, as is the light input to the spectrometer, and can be focused by adjusting a screw system on the output of the collimator, that is attached to the optical fibre. All light external to the system was blocked using various shields due to the low light intensity that occurs during field emission. Light was measured before the voltage was applied to make a record of the counts in the spectra from any sources whilst field emission was not present, this was then removed by the software for the following measurements.

An optical fibre was screwed onto the output of the collimator and transmitted the light to the spectrograph. There were two types of optical fibre used due to attenuation at different wavelengths, these were Ultra-Violet (UV) and Near Infra-Red (NIR), with details given in Figure 6.5. For the majority of the measurements the fibre used was the UV, due to the wavelengths measured being within this range. The NIR fibre was used in some cases to verify that there was not light in

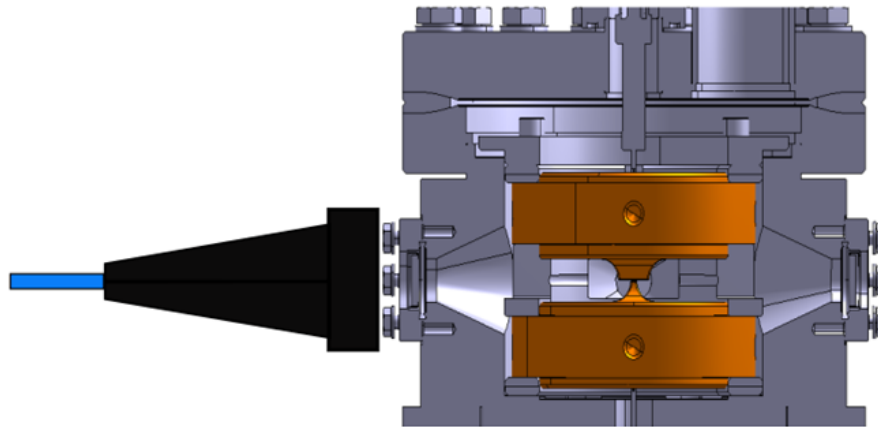


Figure 6.4: Diagram of the collimator aligned with one of the chamber windows, to view the electrode high electric field gap, without the light shielding applied.

the NIR range of wavelengths.

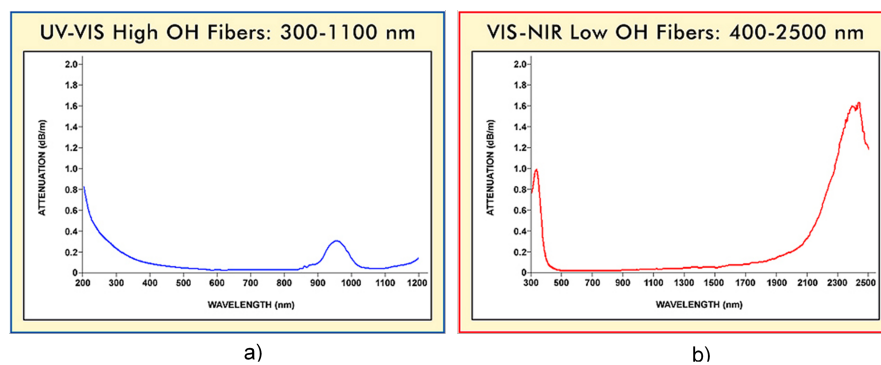


Figure 6.5: Plots of wavelength attenuation for the a) UV-VIS [112] and b) VIS-NIR [113] optical fibres

The spectrograph used was a Andor Shamrock 303i, which has a number of settings for the elements of the spectrometer that were optimised based on the requirements of the measurement. Figure 6.6 shows the layout internally of the spectrograph. On the input there is an adjustable slit, the width of which determined the spectral resolution (the smaller the slit width the higher the spectral resolution). Light was then defocused using mirrors and directed towards the diffraction grating. A diffraction grating is used to decompose the light into its spectral component at different wavelengths. Different gratings sample different

ranges of wavelengths providing a higher resolution at a point of interest, due to the broad band spectra expected the grating with the largest range was chosen. Changing the angle of the grating allows the user to sweep across the wavelengths of interest for individual measurements. The separated light was then focused using further mirrors before passing through the output.

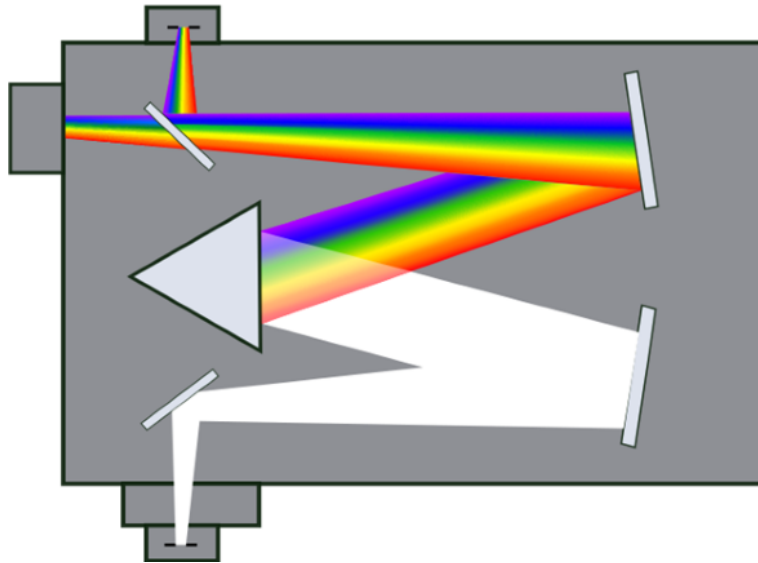


Figure 6.6: Layout inside of the spectrograph with white light entering at the input and diffracted by the one of the three grating represented by the triangle, with mirrors to change the direction of the light.

An iDus CCD camera is a spatially resolved light intensity sensor that is connected to the direct output of the spectrograph, and was used to capture the spectrum. As seen in Figure 6.7, diffracted light was measured horizontally on each row of pixels and the intensity of that light was measured. The camera pixels were integrated vertically, with each row of pixels providing a spectra point, used to form a graph. The grating used for the following measurements had a range of 570 nm in wavelength with 1024 values across this range. The frame rate of the camera used is relatively slow in the millisecond range and for a sufficient amount of light to be measured of the light during field emission, a large exposure time of 5 s was used for the following measurement. Therefore it is not possible to take

high speed captures using this setup.

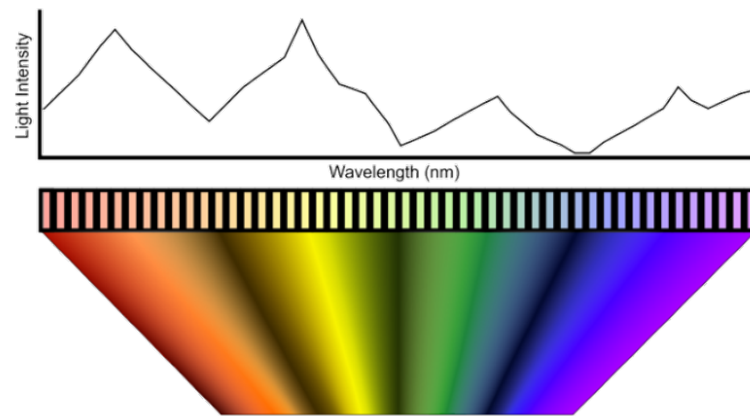


Figure 6.7: Diffracted light is captured by the different pixels of the CCD camera corresponding to a wavelength and is used to generate a corresponding graph of the light intensity are different wavelengths.

Control of the different aspects of the spectrometer was done from the computer using the Andor Solis software. The software contained the settings for the spectrometer to change the different parameters for capturing spectra. A background measurement was taken with no applied voltage and this was removed from subsequent measurements, labelled 'background corrected'. This removed the light measured as a result of dark current in the CCD camera. Results were also saved to short term memory on the software after each capture and could be saved to the computer in the desired format.

6.3 Copper OFE Ridged Electrode Tests

6.3.1 Spectra Dependence on Alignment of Electrodes

The following measurements look at the difference in the light spectra with increasing voltage for the different alignments of the ridged electrodes. These include crossed and parallel with a gap of $60 \mu\text{m}$. Several measurements were taken at each voltage, with the number of measurements ranging from 1-10 depending

on the voltage and the visible variation in results between measurements. All the measurements for each voltage were averaged together to give the values used in the following plots. Parameters for the measurement were set to measure a sufficient amount of light, including an exposure time of 5 seconds and input slit width of $2500 \mu\text{m}$. Wavelengths observed are between 300 nm and 900 nm, to view the majority of different wavelengths generated by copper, therefore a UV fibre was used.

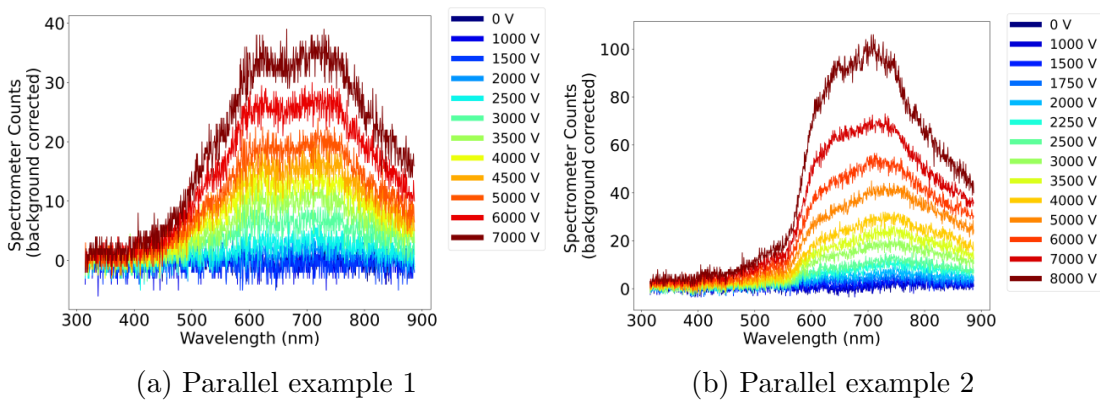


Figure 6.8: Field emission spectroscopy measurements at different supply voltages during 2 individual tests with the parallel electrode alignment. From this a broad band light between 550 nm and 750 nm can be seen with an increase with supply voltage.

Figure 6.8 displays two of the measured spectra with the electrodes aligned parallel to one another. The voltage values given in this case are the supply voltage at each step, this is the voltage from the power supply and not the gap voltage. Details of the relationship between the supply voltage and gap voltage can be found in Chapter 5.4. A significant result was that the spectra were seen to increase in light intensity with respect to the supply voltage. At low voltages there was no light detected but the intensity began to increase quickly with voltage. Measurements displayed relatively broad band spectra between 600 nm and 800 nm with a drop off on either side.

Figure 6.9 shows the spectra at different voltages from consecutive tests with

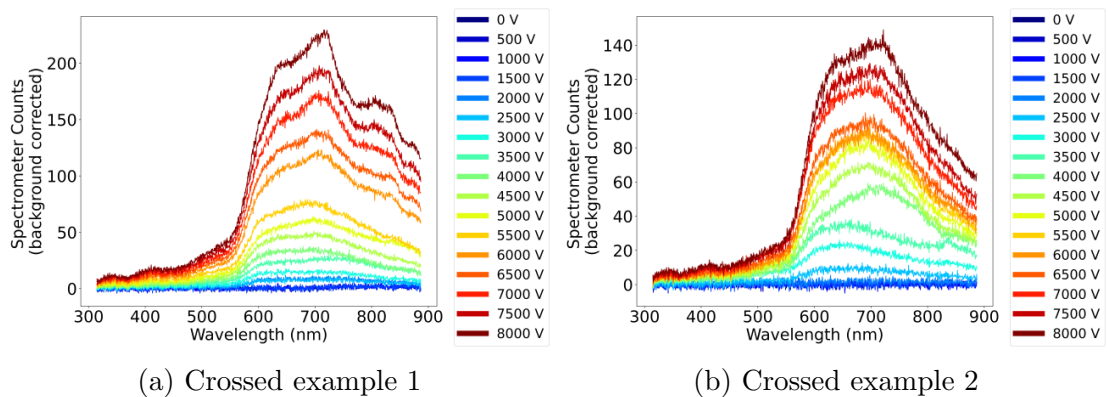


Figure 6.9: Field emission spectrum measurement at different supply voltages during 2 individual tests with the crossed electrode alignment with observations of a variation in the spectrum between 700 nm and 850 nm.

the electrode in the crossed alignment. The parameters for these measurements were kept as similar to the parallel measurement as possible in order to compare the results more effectively. From the figure it can be seen that the general shape was similar but with a higher light intensity than the parallel measurements.

It is important to note that these tests were done consecutively in the order shown, with up to 2 hours in between. One property was the increase in counts at the wavelength of 850 nm, this develops in the first test and could be seen at the beginning of second. Each voltage was held constant whilst measurements are taken, and at 3500 V the increase in counts decreased. The increase in counts shown was observed several times during the tests and fluctuated between measurements.

To compare the results from the parallel and crossed electrode alignments, Figure 6.10 shows a plot of the gap voltage versus the light intensity at 700 nm in wavelength and the current measured for each step in voltage. The results show a clear correlation between the current and light intensity as a function of the gap voltage for each measurement. The spike in the x-axis in the measurements for crossed ex.1, was the results of an increase in the current for the given supply

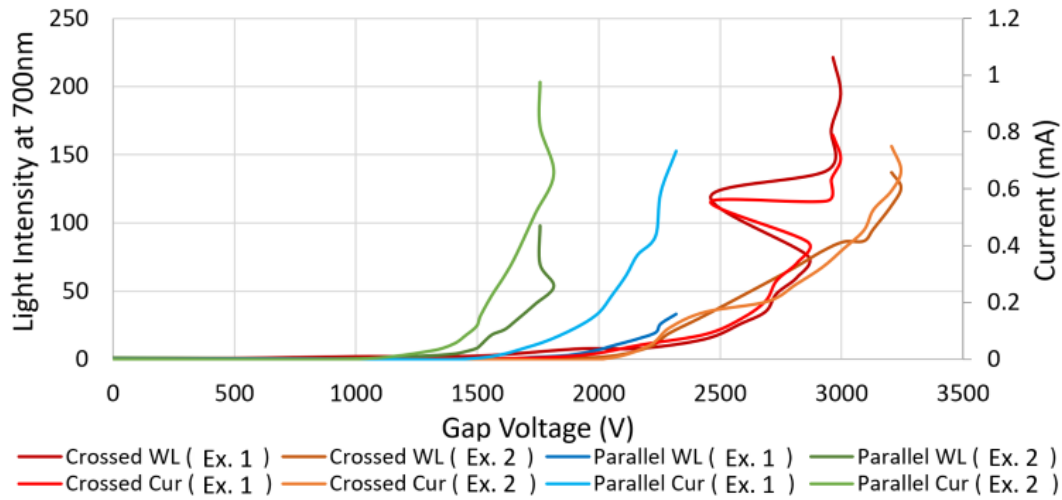


Figure 6.10: Counts at a single wavelength (WL) around the peak of each measurement from Figures 6.9 and 6.8 and the current (Cur) for different supply voltages for each of the crossed and parallel examples given

voltage causing the gap voltage to drop, this would have most likely been an breakdown but the electronics was preventing this but allowing an amount of current through the gap.

The main difference observed from the graph is the difference between the alignments. For both alignments the current reached a similar value, whereas there was a more significant difference in the light intensity. For the parallel electrodes the light intensity reached a much lower value and a lower gap voltage when the current limit of the supply was reached.

As discussed for the field enhancements of this design of electrodes in the different configurations, there is a field enhancement on the edge. It is also possible that the reduced light was the result of the optical alignment. For a gap voltage of 5 kV the highest field on the edge for the parallel alignment would be 86.8 MV/m and for the crossed alignment was 85.0 MV/m. As shown the electrodes experienced large amounts of damage when tested with the crossed alignment which would have influenced the gap distance and most likely would have had areas with field enhancement as a result of the craters.

6.3.2 Dependence on Observation Angle

The following measurements look at the spectra dependence on observation angle, to try and determine whether this was a result of the anode or cathode emitting light. For these tests a crossed alignment of the electrodes was used, with measurements made in both the normal and reverse polarities to change which electrode was the anode and cathode. As previous studies suggested the source of light to be OTR, this would most likely originate from the anode [44]. If the light emitting surface was the cathode then it would be expected that a more direct observation of the high field area of the cathode would provide a higher intensity of the light. Therefore, observing the cathode transversely should have given the higher light intensity. The expected resultant spectra for each perpendicular angle would be the same as the alternate angle for the different polarities. An image of the view through the window and the polarity are shown in the diagrams for each measurement. These measurements were done consecutively with no breaks between and in the order given from a-d in Figure 6.11.

Figure (a) and (c) show the same measurement configuration for the normal polarity, it is clear that the light intensity between 500 nm and 600 nm was more intense during these measurements and therefore more dominant. The dependence on angle still had a large impact on the amount of light measured. Figure (b) and (d) show the measurement with the polarity reversed to the polarity in which all previous tests and conditioning were done. Figure (d) had some residual noise when no voltage was applied, therefore the results shown (in purple) had the noise removed during analysis. The result of these measurements gave a prominent narrow peak at 700 nm that did not appear in any previous measurements of the normal polarity. There was still a visibly larger amount of light from the same angle as observed in (a) and (b), indicating this is not a result of alignment with

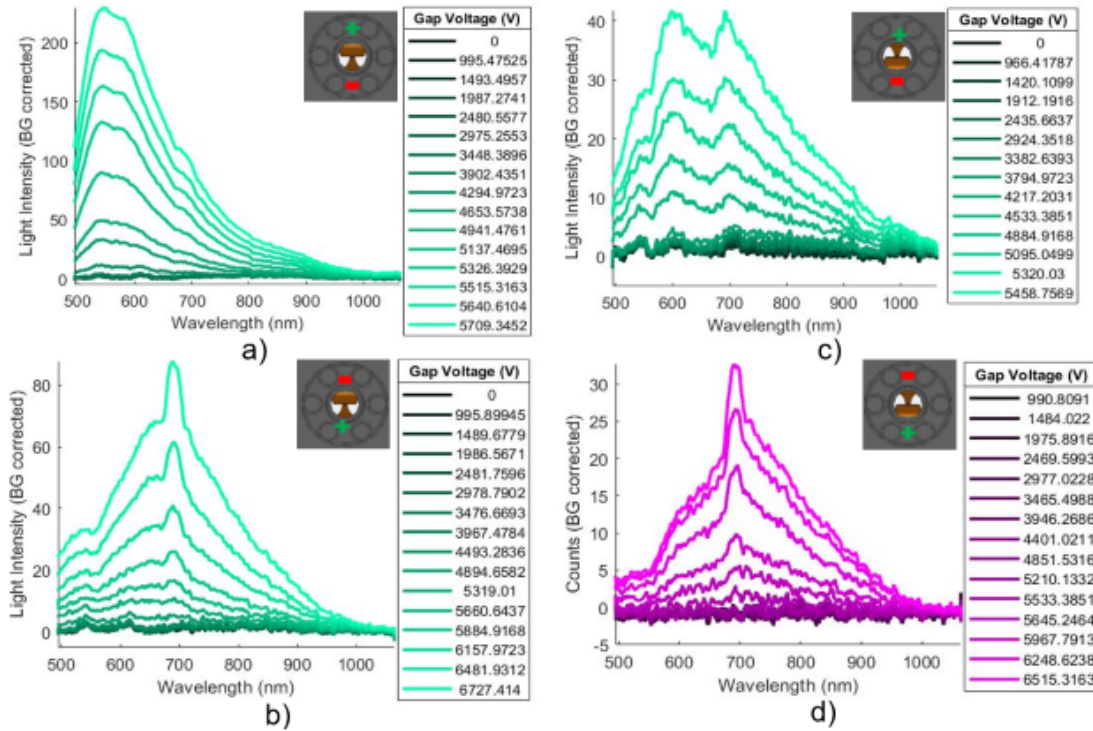


Figure 6.11: Spectra measurements from each perpendicular angle and both polarities. (a) Conditioning polarity transverse anode, (b) Reverse polarity longitudinal anode, (c) Conditioning polarity longitudinal anode, (d) Reverse polarity transverse anode with noise removed in post processing.

the emitting surface.

A significant result from these measurements can be seen when comparing the spectra taken with the same polarity as during conditioning with that of the reversed polarity. The difference in spectra suggests that the conditioning of the electrodes plays a role in the field emission and spectra. Currently it is unknown what is causing the peak in spectra or exactly why it is different in the reverse polarity, but it does lead to possible further tests to analyse this.

These results indicate that there may have been an alignment issue with the collimator and the gap limiting the light measured. As the system was not design for this purpose the windows to the system do not align exactly with the gap of the electrodes. Due to limited availability of equipment for more precise alignment, it

was not possible during this measurement, but the implementation of an optical table could improve future measurements.

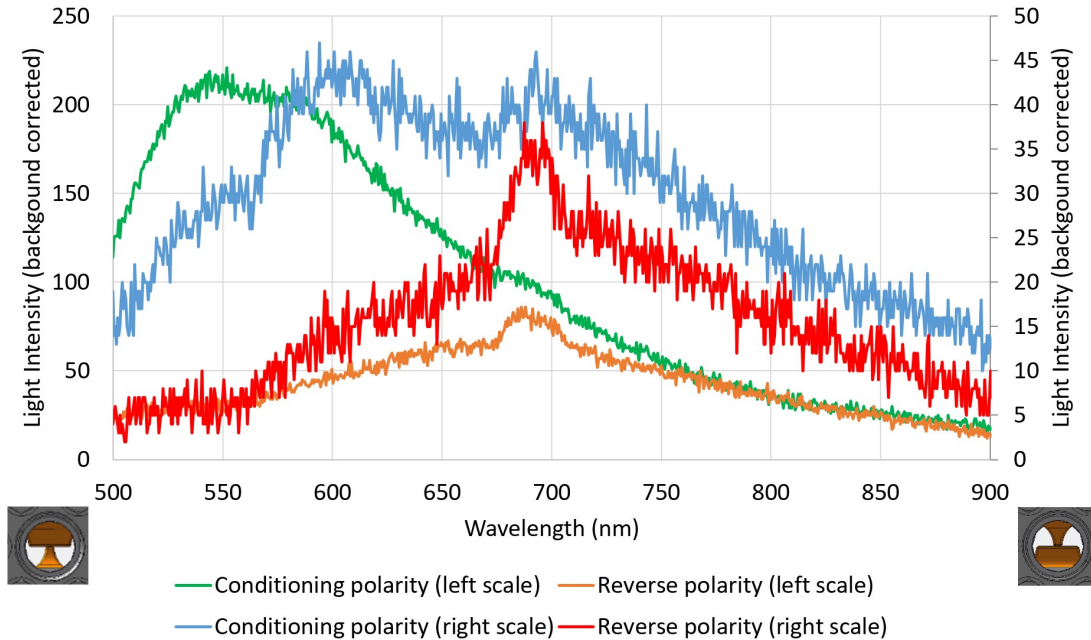


Figure 6.12: Spectra measurements from each perpendicular angle and both polarities at their maximum supplied voltages. This shows the correlation in the light intensity at the 700 nm wavelength for the different polarities, with the change in wavelengths being below 700 nm.

In Figure 6.12, it can be seen that a peak between 675 nm and 700 nm was consistently present, with a prominence of about 10 to 20 counts throughout the different tests shown. The additional features at wavelengths below 650 nm appear after a period of conditioning. A possible explanation for this would be that the conditioned surface has an influence of the light emitted, which could agree with theories of this being a result of a plasmon resonance due to grating-like features being formed on the surface.

6.3.3 Measurements of Spectra Variation with Time

The following measurements continue from the crossed electrode measurements where fluctuations in time were observed. All parameters for this test were the

same as described in spectra dependence on alignment of electrodes for the crossed electrodes. For this test the supply voltage was kept at 7kV and the current and spectra were measured every 30s.

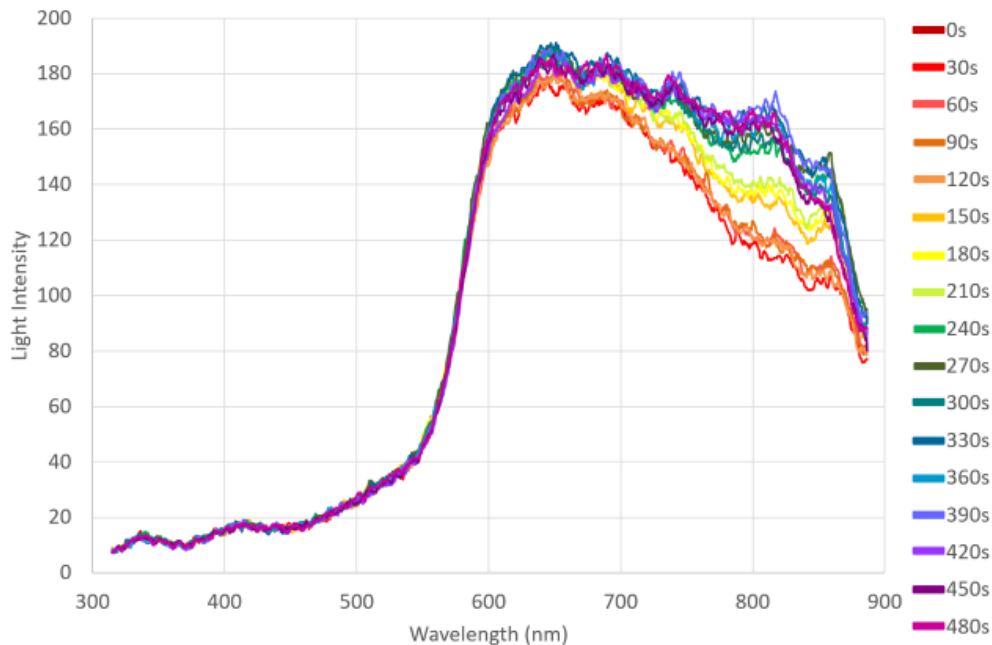


Figure 6.13: Spectrum taken every 30 s with a 7 kV supply voltage applied with the colours indicating the order of the measurements. It is observed that there are variations of the spectra with time between 700 nm and 850 nm.

Figure 6.13 displays measurements of spectra recorded every 30s; where gradient colour indicates measurement time from the lightest shade being the first measurement to the darkest shade being the last. It is clear from this plot that the fluctuations in spectra were between 650 nm and 850 nm, with the largest fluctuations between 800 nm and 850 nm. This verified that fluctuations were able to occur, but this was not always observed during measurements. The fluctuations were also more prominent at higher voltages and clearer due to the higher intensity of light. It was interesting that only part of the spectrum was fluctuating and not the whole thing, and looking at this in more detail could give more insight as to what causes field enhancements.

Figure 6.14 displays the results of the total light intensity of each spectra, the

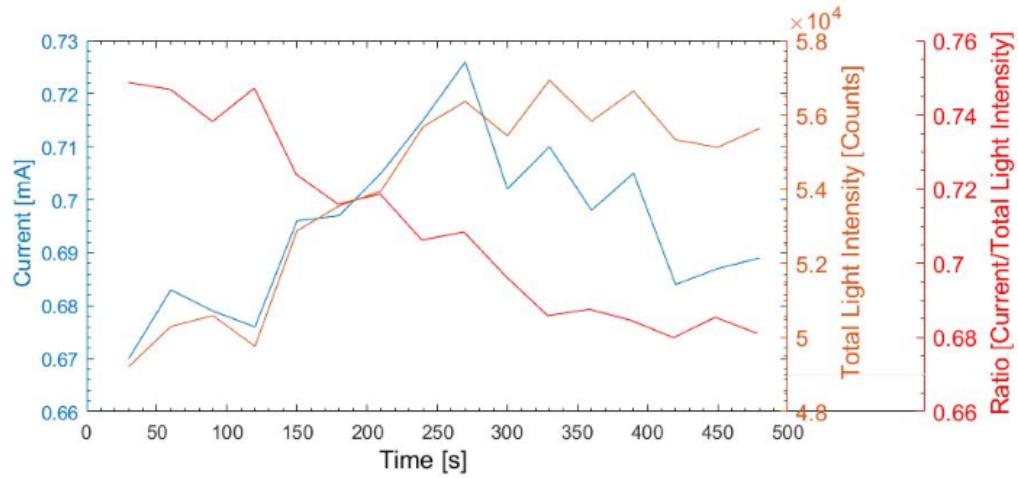


Figure 6.14: Value of total light intensity, current measured with respect to time where a measurement is taken every 30 s and the ratio (current/total light intensity). Total light intensity is the number of counts at each wavelength summed together for each spectrum.

current measured every 30s and the ratio between corresponding non-normalised values. Total light intensity is the light intensity at every measured wavelength summed together. The results appear to give a clear correlation between the light and current measured as a function of time. As the current fluctuated the light intensity appeared to follow the same changes in terms of increasing and decreasing by similar proportions. A point of interest also from this result was the deviation after a spike in current where the current decreases and the total light intensity remains high. From looking at the ratio of the original values it can be seen that the light emission mechanism changed with time.

To analyse this relationship further, Figure 6.15 displays the light intensity at individual wavelengths at intervals of 50 nm compared to the field emission current. The different results are all normalised to range between 0 to 1 to simplify the comparison. It can be seen that all the wavelengths shown follow the general fluctuations of the current. Some wavelengths appear to follow the current more closely, these include at 600 nm and 875 nm; from Figure 6.13 these

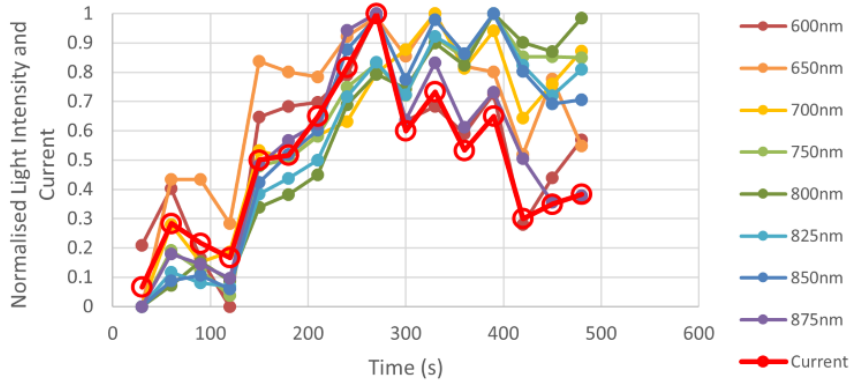


Figure 6.15: Normalised light intensity at different wavelengths and current with respect to time with measurement taken every 30 s. The values are normalised to the minimum and maximum values ranging between 0 and 1.

two wavelengths have the least fluctuations in light intensity. This may suggest that there is some additional factor that is causing these fluctuations at specific wavelengths, as wavelengths with the most variation have the least correlation with the current. Due to the variation after the spike in current providing an additional enhancement at some wavelengths this may be a results of the current that caused something else to start occurring. Currently it is not known what the current caused that would give enhanced optical emission at these wavelengths. The spectra given is a most likely a sum of the normal spectra that is a result of field emission current and the fluctuations between 700 nm and 850 nm that are influenced by a different phenomenon less correlated with the field emission current. Reasons for this should cause fluctuations in the light emission over time without directly influencing the current emission.

6.3.4 Correlation of Light with Measured Field Emission Current, Gap Voltage and Power

Figure 6.16 shows a plot of the gap voltage verses current and light intensity at a selection of wavelengths and the total light intensity measured from the

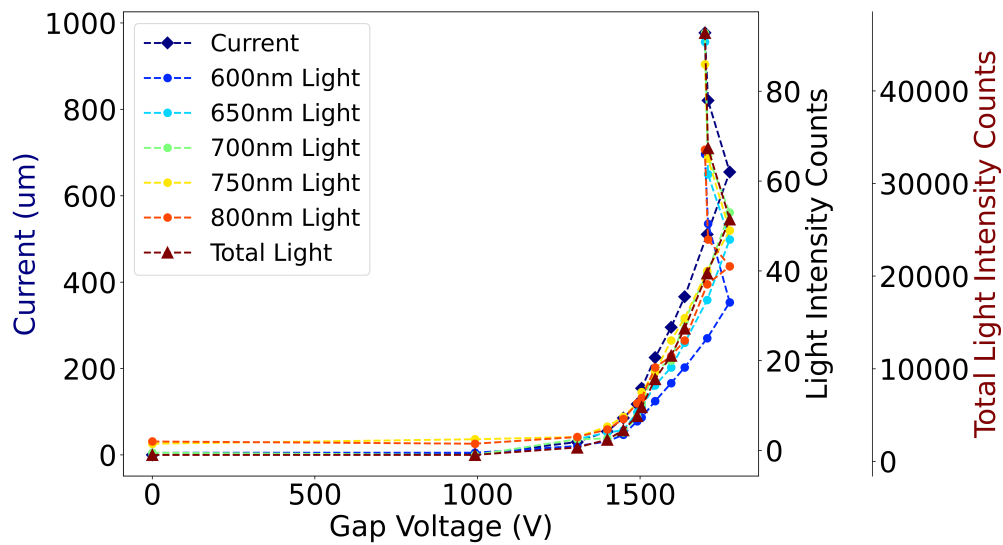


Figure 6.16: Field emission current, total light intensity counts, and counts of light intensity at different wavelengths with respect to the gap voltage.

spectrometer. These measurements were taken from the parallel electrode configuration given in Figure 6.8. All measurements of spectra displayed a similar correlation to other parameters. Both total light intensity and the light intensities at specific wavelengths are provided. This graph shows a similar relationship to a plot of voltage versus field current emission.

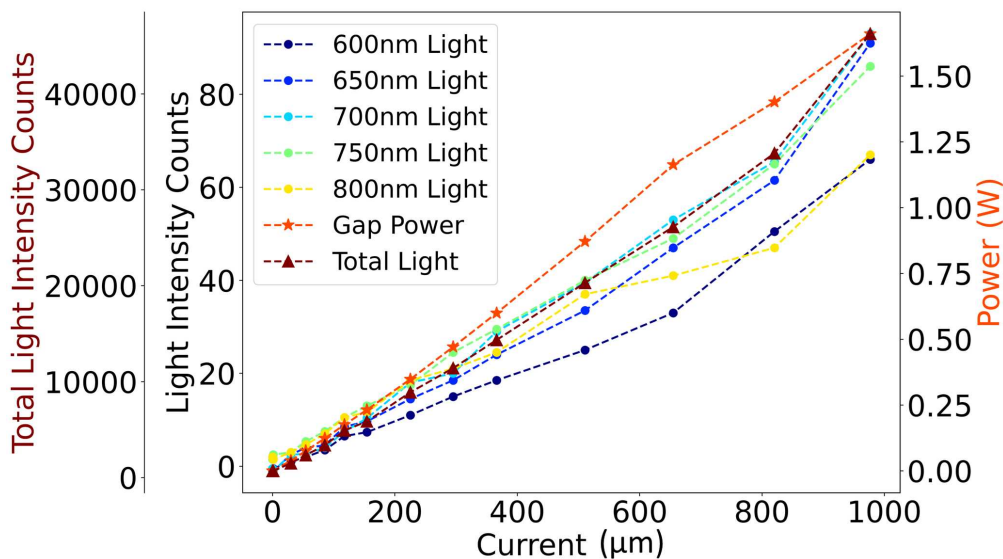


Figure 6.17: Total light intensity counts, counts of light intensity at different wavelengths and gap power with respect to the field emission current.

Following on from the previous plot, Figure 6.17 shows the correlation between the measured field emission current and the power and light intensity at different wavelengths, where the gap power is given as the gap voltage multiplied by the current measured. There is a clear linear correlation between the current, power and light intensity both at individual wavelengths and the total light over all wavelengths. As both the current and power have a linear correlation with the light intensity, it is not possible to specify which is directly related to the cause of the light.

6.4 Large Electrode Tests

The previous light emission plots given are from light measured with ridged electrodes installed in the system. As discussed this made the light easier to detect directly compared to measuring from large electrodes with a small gap. As there were several materials to be tested with the large electrode configuration and the field emission current was systematically measured for each, the spectrometer was set up for each measurement in case light emission was detected.

It is easiest to see light from a source near to the camera and becomes increasingly difficult the further away the light emitted is from the window that the collimator is located. Also, if the emission spot was within close proximity to the collimator, in the gap as small as $60\mu\text{m}$ it may still reflect off the surface multiple times filtering the colour. The materials to be discussed include Cu and CuCr_1Zr that are copper coloured and therefore are similar to the reflectance curve of copper. Other materials to be discuss include Ta, Nb and Al that are silver metallic colour and therefore have less of an affect of colours reflected through the gap.

Due to the increase in surface area of the electrodes compared to the ridged

electrodes previously discussed, for these cases it is not always possible to know locations of the source of the light. This leaves the possibility that field emission current may be dominated by one spot or in a more extreme cases distributed over the whole surface. The location and source of light would most likely play a role in the intensity and the filtering effects experienced by the light being emitted.

6.4.1 Copper Based Large Electrode Tests

Figures 6.18 to 6.20 display the results from the Cu and CuCr₁Zr electrodes tested. These are grouped together due to both being Cu based materials and the colour of Cu which was believed to influence the spectrum detected.

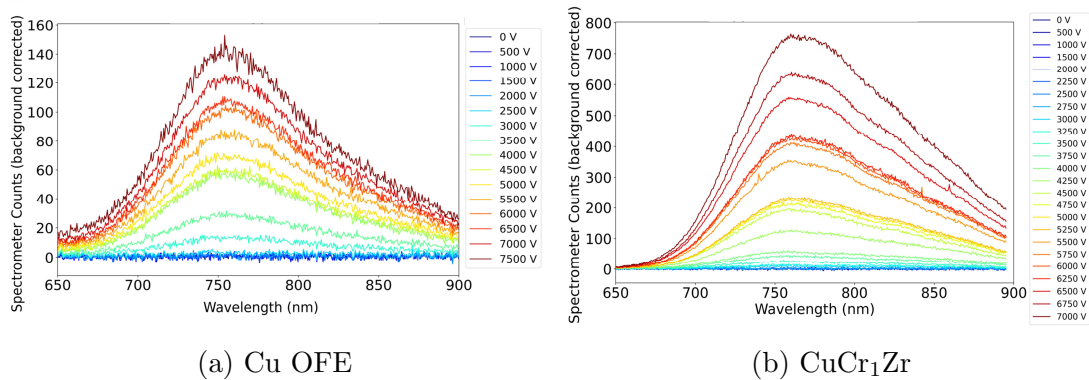


Figure 6.18: (a) Cu OFE and (b) CuCr₁Zr optical spectra during field emission current measurement, using large high-field area electrode tested and discussed in Chapter 3.6. Showing a similar broad band light measurement with a increase in light intensity with supply voltage.

Figure 6.18 shows the spectra of Cu OFE and CuCr₁Zr during field emission measurements. The x-axis is the wavelength and the y-axis the light intensity with the lowest supply voltage in blue and highest in dark red. It can be seen that as the supply voltage increases the light intensity also increases for both materials. There is a difference in the intensity between the two materials. This could be a result of the proximity of the light to the collimator, the optical alignment, the light intensity emitted or a mixture of these. From both it can be seen that the

spectra have a broad maximum between 700 nm and 850 nm, which corresponds to the reflectance on copper. This result of spectrum intensity with respect to supply voltage, and producing spectra at these specific wavelengths was consistent for the different Cu based materials. With similar results for each test, which was not the case for any other materials that were tested. This may suggest that it is a property of Cu that produces light consistently when there is a flow of field emission current between the electrodes.

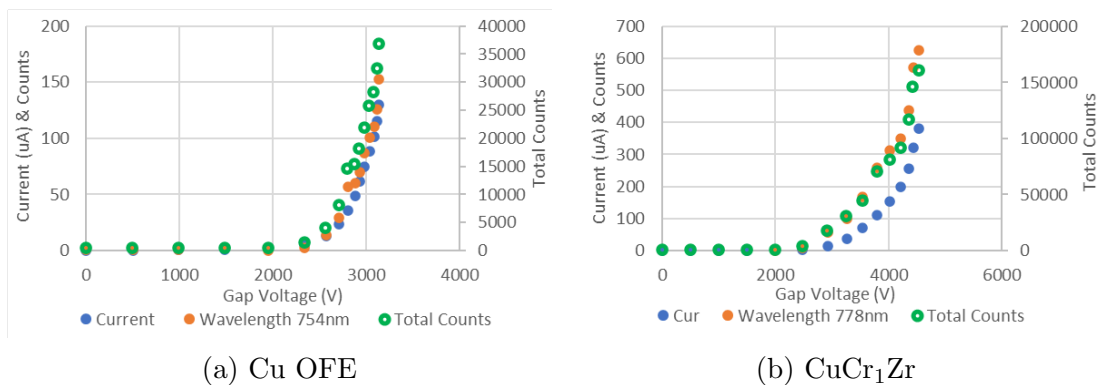


Figure 6.19: Plots of field emission current, light intensity at a specific wavelength and the total light intensity with respect to voltage for (a) Cu OFE and (b) CuCr₁Zr. Showing an exponential increase in the field emission current and light measured.

Figure 6.19 displays a plot of gap voltage with respect to field emission current and light intensity at specific wavelengths at the peak of the spectra and total light intensity. From the plots it can be seen that the current and light emission generally follow the same curve indicating they are related. In each of these plots the current in μA and the counts for a specific wavelengths are given on the same axis. The wavelength chosen is from around the maximum point of the curve, for these cases the values chosen were 754nm and 778nm for Cu and CuCr₁Zr respectively. From this it can be seen that the level of light detected is proportional to the field emission current. This would suggest that the difference in light intensity may be due to the difference in field emission current, as these

appear to be proportional between Figure 6.19a and 6.19b.

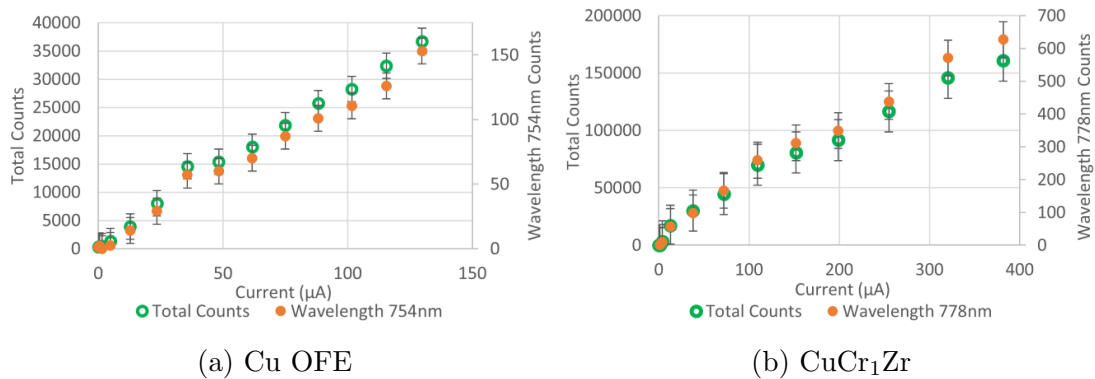


Figure 6.20: Light intensity at specific wavelengths and total light intensity at different supply voltages with respect to the field emission current. Showing a linear relationship between the light intensity detected and the field emission current measured. The spikes that can be seen are the result of cosmic-rays hitting the CCD.

When the field emission current and light emission are plotted against each other as seen in Figure 6.20, they have a linear correlation. It can be seen that for the lower intensities that there is some deviation, this point here match the number of values measurements of spectra with very low intensities in Figure 6.18. This suggests that the variation in the linearity is a result of a lower resolution with the light measurements at the low field emission range. With the exclusion of this data, this is good evidence that the source of the light being measured is related to the field emission current that has been measured.

6.4.2 Tantalum and Niobium

The following results shown were recorded at the same time as field emission measurements of the Ta and Nb BCP irradiated electrodes that each had a pulsed stable field of around 23 MV/m compared to other pairs with stable fields exceeding 70 MV/m. Conditioning plots for these pairs can be seen in Figure 4.16a. Measurements of the phenomenon to be discussed only occurred on the one

occasion for each material and was not seen during any other measurements. Due to the intensity of the light throughout this result, it was also detected by the cameras and therefore the location of the main light source can be determined, this is discussed in more detail below.

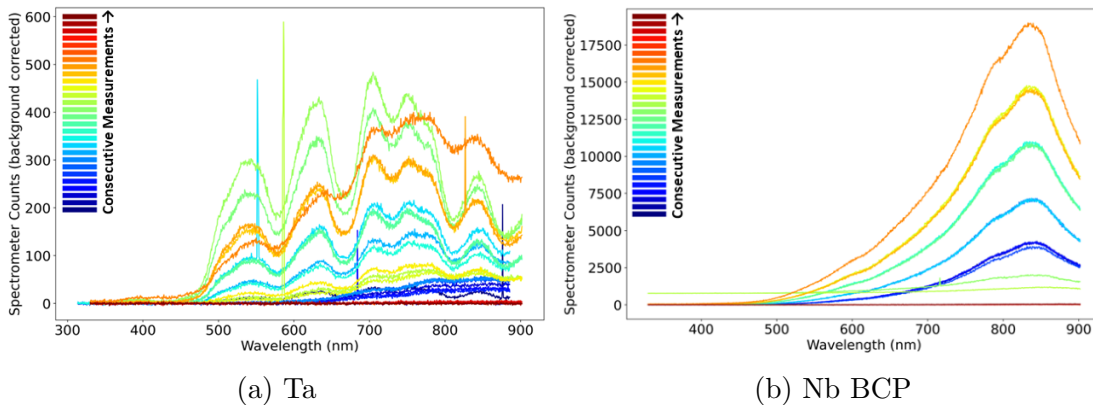


Figure 6.21: Optical spectra during field emission measurements for irradiated samples of (a) Ta and (b) Nb BCP as discussed in Chapter 4.6. Colours from dark blue to dark red show the measurements from the first to the last respectively with only increases in the supply voltage applied. The sharp peaks in (a) are believed to be caused by cosmic rays striking the sensor. Details of the measured field emission current can be found in Figure 6.23

The spectra shown in Figure 6.21 shows the intensity of the light as a function of each wavelength and given in order of measurements from dark blue being the first measurement to dark red being the last. In these cases, measurements only started to be saved when the light started to be produced. Throughout the measurements the spectra was taken between 2-7 times for each supply voltage step where the supply voltage for each step is held for a minimum of 100 seconds before increasing. It can be seen for the Ta spectra that the light peaks at the light green coloured plot and then decreases in light following the orange plot, whilst the voltage is still high. The last measurements shown in dark red have no light detected despite this being at the highest voltage. As for the Nb spectra the light suddenly goes from the highest point to no light detected, also with the high field still applied.

Spectra observed from the Ta electrodes had a large range of frequencies suggesting the light produced was possibly white with some filtering effects of the material. Determination of the cause of this light or the wavelengths produced is beyond the scope of this report, but further studies could produce some interesting insight. Unlike the broad Ta spectrum, the spectra seen from the Nb electrodes appeared to peak around 830nm looking similar to a black body radiation spectra [46].

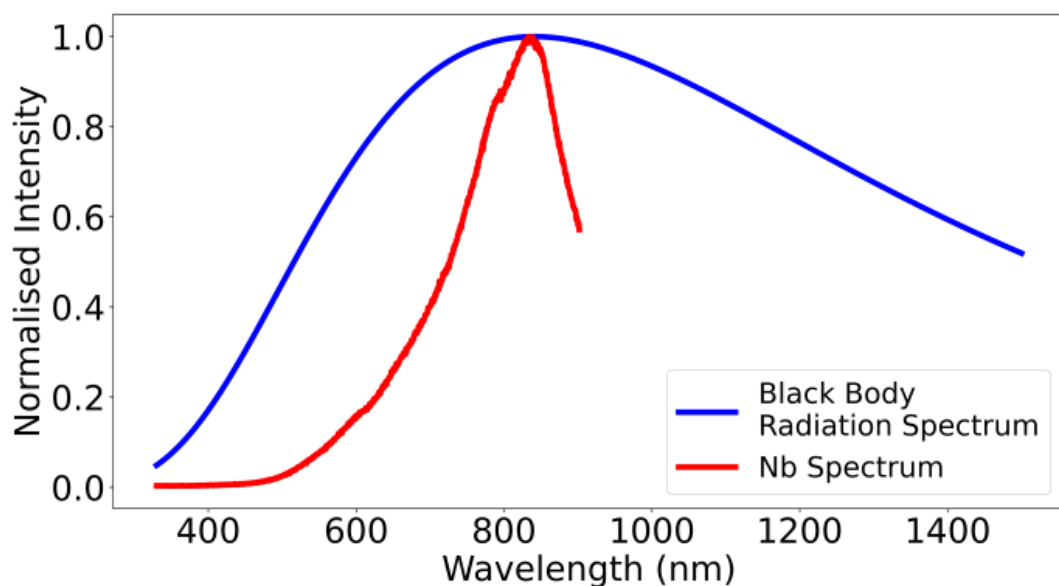
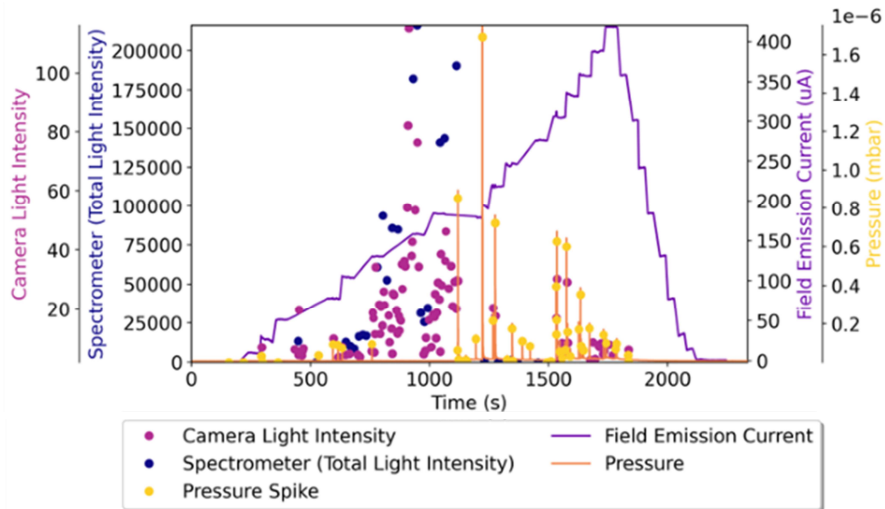


Figure 6.22: Normalised comparison of the black body radiation curve for a temperature of 3450K and a measured spectrum from the Nb electrodes. This shows a narrower spectrum from the Nb electrodes, suggesting the light detected is not the result of black body radiation.

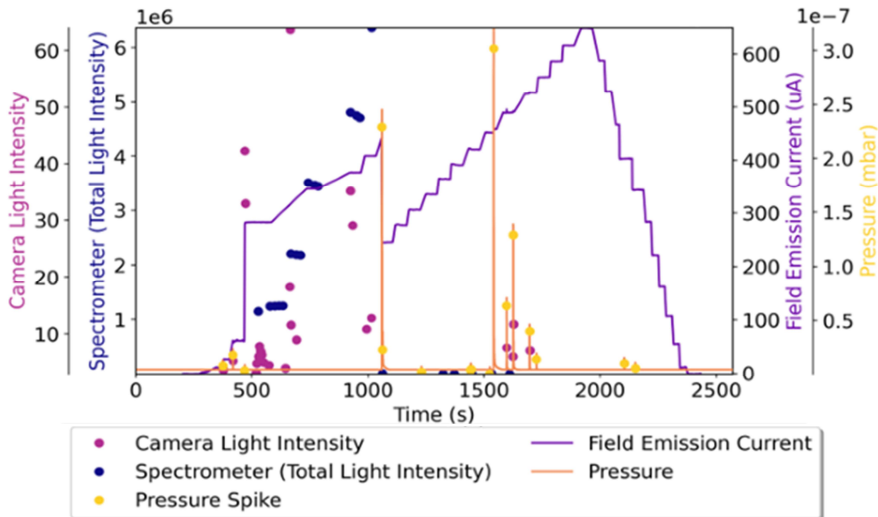
Figure 6.22 displays normalised results for the calculated spectrum for black body radiation using Planck's Law, at a temperature of 3450 K and a spectrum from the measured Nb. The reason for this choice of temperature is in order to have the peaks of the different plots are the same point. The shape of the spectrum calculated is determined by the temperature and as the temperature increases the peak of the curve increases in wavelength. From the data shown in Figure 6.21b the centre point of the spectrum only changes by a very small

amount suggesting if this was due to black body radiation then the temperature would have not changed significantly. Additionally this is above the melting point of Nb, which is further evidence that this result is not a measurement of black body radiation as it would be expected for the temperature to change as the field emission current increases and a lower temperature. Additionally, as seen in Figure 6.22, the observed spectrum is much narrower than black body for the same maximum intensity. It is possible that this means it is not a result of black body radiation or that this would be affected by filtering causing the light out at the surrounding wavelengths to be reduced.

In addition to field emission current and light spectra, breakdowns and vacuum were measured. Whilst the setup for field emission does reduce the likelihood of breakdowns occurring, they can occur and can be determined by the spikes in the pressure. Using this data, correlations amongst these can be seen in Figure 6.23. The light purple dots and blue dots give the light intensity at a specific time from the cameras and spectrometer respectively. There are two representations of the pressure, the dark yellow line gives the continuous measurements of the pressure and the light yellow dots display the spikes in pressure that are most likely representative of breakdowns. The purple line is the continuous measurements of field emission current recorded by the oscilloscope once per second. As mentioned the supply voltage is increased periodically which can be seen in the steps in field emitted current.



(a) Ta



(b) Nb BCP

Figure 6.23: Correlation between field emission current, light intensity measured from the perpendicular cameras and spectrometer, and pressure from breakdowns with respect to time. This shows the gradual increase and decrease of the field emission current with time due to step increases in the supply voltage, and a period in which light is detected and stops after a pressure spike as the result of a breakdown.

In both cases it can be seen that there were a number of small pressure spikes at the beginning indicative of breakdowns occurring but with relatively low impact in terms of crater or emission size. Then light begins to be detected on both the

cameras and spectrometer that appears to increase over time with the increase in the field emission current measured. There is a difference between Ta and Nb with regard to the field emission current measured when the light was detected, for the Ta the current appears to follow a fairly linear relation whereas for the Nb there is a step in the field emitted current. Then for both a large breakdown seen as the large spike in pressure is detected and all of the light stops emitting and for the Nb electrodes the current steps down to a point that lines up linearly with before the next normal step increase.

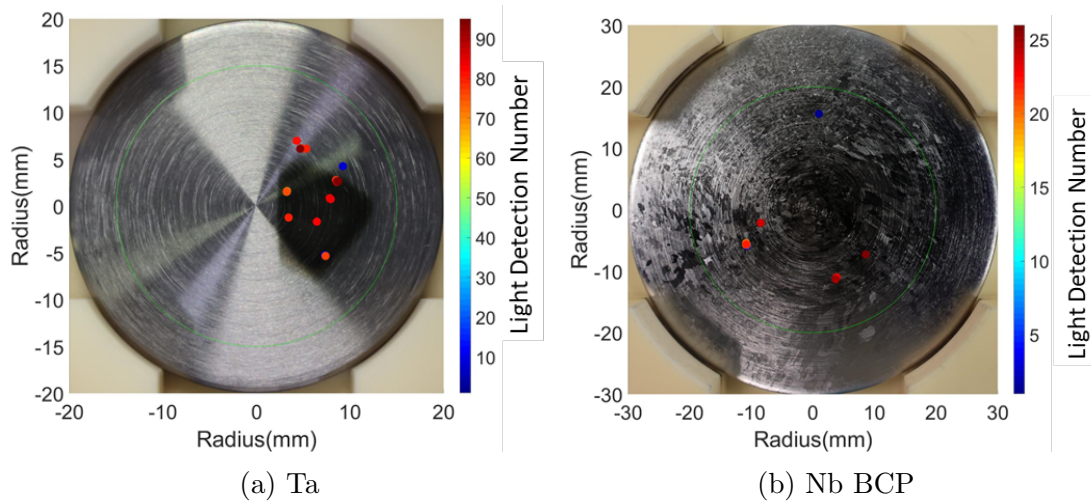


Figure 6.24: Light emission locations during the field emission measurements with the majority of locations being breakdowns, and one location being the source of the field emission light with no breakdown.

In both cases one or more breakdowns occurred in different locations before the light from field emission and then multiple breakdowns in different locations after the light stopped. The correlation between pressure spikes and breakdown locations suggest these are related with the appearance of light and its extinction. For the Ta the field emission light occurred where the orange spot ending in this location around light detection number 65 out of 93 and for the Nb is the spot furthest to the left ending around detection number 21 out of 26. This means that after the breakdown from the field emission site this location seemed to no longer

be the dominant field emitter.

6.4.3 Aluminium Alloy

Two pairs of Al alloy large electrodes have been tested, looking at the spectrum: The reason for this, is that it reflects relatively evenly the colours in the visible range. Therefore if there was light emitted in the gap, then this would be reflected with very little filtering from the material. In the case of the possible black body radiation seen in Figure 6.22 for Nb, possible filtering would have been known. As for Cu OFE large electrodes spectra results shown in Figure 6.18, this would not be filtered by the reflectance of the material.

During the initial tests no light was seen but due to the rough machining it was questioned whether this would attenuate the light stopping it from being able to escape from within the gap. The pair reached a field of around 65 MV/m and during field emission tested reached currents that would normally be sufficient for measuring light. No measurements of the roughness were made from this pair of electrodes but the machining is judged from physical appearance of machining lines and an inability to see a reflection on the surface of the electrodes. It was believed that the lack of light seen was due to the machining, therefore, a new pair of electrodes was ordered from a different company where a higher quality of machining was achieved.

The second pair of Al alloy electrodes had a mirror surface finish with a very good roughness with an average 3.9 nm [114]. These were installed in the system and conditioned with intermittent field emission measurements with the spectrometer attached. Despite the improved machining light was still not visible. As seen from the conditioning shown in Figure 3.7a, the electrodes reached around 90 MV/m before experiencing a crash in field with the majority of breakdowns

occurring in one area. One of the field emission measurements for this pair of electrodes can be seen in Figure 5.2 and shows that the voltage reached around 3 kV and just over 600 μA . With these fields and currents during a field emission measurement, light was expected to be seen if the source was OTR.

As a large number of the breakdowns where in an area close to one of the windows, the spectrometer was moved to the corresponding window but no light was seen. In other cases emission spots often were not known but for the Nb and Ta examples these emission spots were not as close to the spectrometer and light was visible. One query was as to whether there was something blocking the light from being measured but the light spectra from a breakdown was measured meaning that this was not the case. Currently it is not known why light was not visible with Al alloy electrodes and whether this result means the emission is not OTR in other cases. There are several unknown factors, including the size and temperature of the emission site for each material and also the effect of contamination on the surface. Al is a popular material for various products due its ability to form an oxide layer and this may also play a role in ways that are currently not understood.

6.5 Optical Spectroscopy Conclusions

During all field emission tests, an optical spectrometer was aligned to one of the windows to observe the light emitted during field emission. An increase in light intensity with supply voltage was seen and post analysis show a correlation between the field emission current and light intensity suggesting these are directly related. To compare the spectra properties seen throughout tests of different electrode shapes and materials with some of the possible causes for the different properties, Table 6.1 is given. This shows the possible correlations between the properties observed and the possible causes, where green means they should correlate, orange

		Cause						
		Plasmon Oscillations	OTR	Cathodoluminescence	Black Body Radiation	Contamination	Material Filtering	Surface Changes
Property	Correlates with field emission current	Green	Green	Green	Green	White	White	Green
	Doesn't correlate with field emission current	Orange	Red	White	Orange	Green	White	Orange
	Varies with time	White	White	White	Green	Green	White	Green
	Changes with polarity	White	White	White	White	Green	White	White
	Stop after a breakdown (still emission)	Orange	White	White	Orange	Green	White	White
	Temporary increase in current with light	Orange	White	White	Green	White	White	White
	Broad band (white light)	White	Green	White	White	White	White	White
	Narrow band (not white)	Green	Red	White	Green	Green	Green	White
	No light for some materials	Green	Red	White	White	White	White	White

Table 6.1: Table of the properties seen in the spectra throughout tests versus the possible causes. Squares are coloured based on whether the properties, align with (green), may align with (orange), rule out (red), or unknown (white) with respect to each of the possible causes.

is they might correlate, red means that they rule out this cause, and white is if it is not known and more research would be required.

As the ridged electrodes had a rectangular shape they were tested with both a parallel and crossed alignment configuration. With similar amounts of current at corresponding supply voltages, less light was detected with the parallel alignment. Field enhancement simulations suggest that for the parallel and crossed alignments should do not have a large difference. But from post testing observations the centre that would be the high field area during crossed alignment tests showed significant amounts of damage. This would have directly affected the fields during tests and the enhancements of the different areas. It was observed with the crossed alignment that the intensity of light detected by measuring from perpendicular windows varied. Measurements of both windows and polarities was conducted

with observation of a high light intensity in one window for both polarities. The measurements verified that the difference in light intensity was a result of optical alignment issues rather than an effect of observing the light emission surface. An additional observation during the test was a clear difference in the light intensity at different wavelengths when the polarity was changed, summarised in Figure 6.12. At first glance, the peak between 675 nm and 700 nm became less apparent, though a comparison of the light intensity for each case reveals that the prominence of the peak over the surrounding wavelengths is in fact very similar, with the main difference being an additional broad spectrum. This suggests that the peak and the broad spectrum are caused by two different phenomena. The broad spectra in Figure 6.12 for the conditioning polarity bear a resemblance to localised surface plasmon resonance spectra for copper shown in Figure 1.18, suggesting that this may be the mechanism responsible for this feature. Given the much narrower bandwidth of the 675 nm - 700 nm peak, it might be caused by another narrow-band mechanism such as cathodoluminescence of semiconducting impurities on the surface [44].

Also seen during the tests of the ridged electrodes was a variation in light intensity at some wavelengths. Correlations of different wavelengths and the current measured with respect to time indicated the wavelengths with the least variation matched the current more closely compared to wavelengths with the highest level of variation. This would suggest that something was changing on the surface that was not directly related to the current measured. A possible cause for changes in the field emission current could be changes to the surface and this could influence the 'grating' like features for plasmon oscillations or the shape of the area for black body radiation influencing the light seen by the spectrometer. In the case for OTR this most likely does not influence the light as it is the result of the electrons entering transitioning between the vacuum and material.

Tests for each of the material discussed in Chapter 3.6 were also conducted with light seen consistently with the Cu OFE and CuCr₁Zr pairs. The light observed was the colour of copper, most likely due to the filtering affect of Cu as the light travelled through the gap. During one section of a singular run with both Nb and Ta, light was seen for a period of time before a breakdown occurred and the light stopped. The spectra for the Nb electrodes looked similar to that of black body radiation but a comparison of the curves shows Nb to have a much narrower band of wavelengths, this may mean it was not the source or that some form of filtering occurred.

For the purpose of measuring the colour of the light being produced, Al alloy electrodes were tested due to there high reflectivity at different wavelengths. No light was detected throughout measurements even though other parameters of gap voltage and field emission current where on the same level as during measurements with Cu. Cu based materials have been the only ones to consistently emit light during field emission. The absence of light may suggest that the light produced is not from OTR as this should also be visible for Al alloy electrodes tested.

Another possibility that was not considered in detail within this thesis is cathodoluminescence, which may also be a source of light in the presence of field emission [111]. This is the energy emitted in the form of photons when an electron settles to the ground state after being captured in an excited state.

Chapter 7

Current Fluctuations During Conditioning

7.1 Introduction

The statistical properties of breakdowns are driven by the statistics of the trigger mechanism. There is a comprehensive theory of a possible breakdown trigger, in which the stress caused by the applied electric field causes movement of dislocations in the material [21], [22], [42]. Dislocations project on to the material surface, and cause surface features. These features can result in an enhanced field emission area and in some cases, breakdowns. Measuring the time behaviour of field emitted current is a way to probe the dynamics of the high-field surface. This chapter builds on previous work looking at small fluctuations in field emitted current with a constant DC field [21], [42]. Previously studies were done using the small ridged electrodes where a conditioning effect was observed from one test to the next, with pulsed conditioning in between tests. As there appeared to be a reduced number of fluctuations with increased conditioning, these tests were conducted during high-field pulsed operation throughout conditioning of large Cu

OFE electrodes. This was done to observe the effect of the step-wise conditioning, with ramped conditioning and running under constant field periodically as seen described in Chapter 2.6 for the step-wise conditioning method. This allows to observe the effects of pulses compared to a constant field as seen in previous studies [21]. Measuring during conditioning allowed for observations of fluctuation characteristics throughout the conditioning processes as electric field was increased.

The electronic setup is the same as previous studies with the exception of the constant supply being replaced with the pulsed power supply to be used for the following tests. Details of the high-frequency filter for measuring fast changes in the field emitted current and the recording of the measurements will be given. Additionally the appearance of current fluctuations and how these are counted for each of the high-voltage pulses, will be discussed. Also, explanations will be given of what the fluctuations could mean in terms of the behaviour of the field emission current.

The focus of this work has been to provide high-quality data on the time dependence, fluctuations of the current as benchmark data. Results are given without interpretations in terms of current fluctuations, with only explanations of characteristics seen for the different runs. Observations are made of how the field emission current fluctuations varied with respect to the conditioning, breakdowns, and constant field pulsing. As well the correlation with when there are many pulses between consecutive breakdowns, and during the degradation of the electrodes, when many breakdowns are occurring causing a reduction in the electric field. Also, a significantly large number of fluctuations during some individual pulses were observed, that may be the result of the pulse being temporally close to, or on the pulse of in which a breakdown occurs, causing a significant increase on current variations.

After the results are given an interpretation of what they could represent with

respect to dislocations is described, as this theory was the motivation for the following study [21], [22]. This includes some of the background theory of what happens within the material and what is expected when an electric field is applied to a material. The context of dislocations is then used to explain how each of the observed characteristics could be explained by dislocation movement within the electrodes changing the field enhancement factor.

7.2 Setup and Measurement Method

The electronic design and previous tests are shown in the thesis of Jan Paszkiewicz, where a constant DC supply and ridged electrodes were used [42]. An overview of the system is described below, for full details of the setup, choices of electrical components and the original measurements refer to the previous work. It was observed from the previous measurements, that there appeared to be a reduction in the current fluctuations associated with dislocation that was related to conditioning between tests. Therefore, the following measurements of current fluctuations were conducted during the conditioning of the electrodes. Additionally, large electrodes were used. Whilst large electrodes had been studied previously, they were conditioned which may have influenced the field emission current fluctuations.

The pulsed DC system with electrodes of a 40 mm high field area allow for studies of the field emitted current to be measured during high field pulsed testing with observations of fast changes in the current measured periodically throughout conditioning. A simplified diagram of the electric setup for measuring small changes in the field emission current can be seen in Figure 7.1 [42]. This uses a bias-tee that is capacitively coupled to the high-voltage line to the chamber to an oscilloscope. During pulsing this gives a large amount of transients current

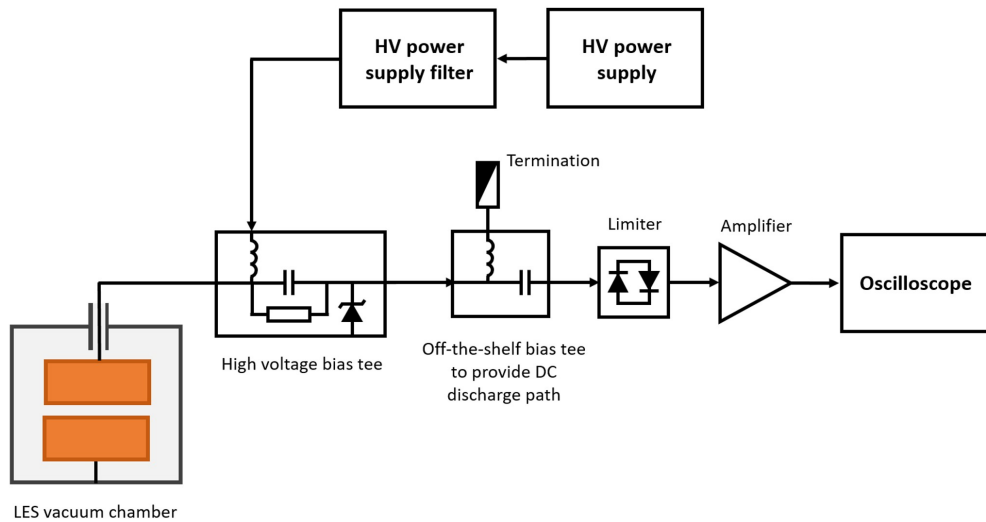


Figure 7.1: Block diagram of the setup for field emission current fluctuation during tests in the pulsed DC system [42].

during the charging and discharging, but also detects signals originating from the chamber during the pulse when the field emission current changes. Additionally within the box of the bias-tee are a series of diodes for protection of the oscilloscope, in case of failure of the capacitor of the bias-tee. Then external to the specialised box are off the shelf components, the first providing a DC discharge path and the second as an additional diode limiter to reduce the voltage output further to below the maximum rating of the oscilloscope of 5V peak when 50 Ω impedance is selected. Then a number of low-noise amplifiers can be used, in this case only one but more can be added if the signal is too small. This is then connected to the input of the oscilloscope to record to high frequency changes in current during measurements. The design of the setup shown was for broad bandwidth (>1.5 GHz) and low noise, for measuring a large range of signals.

Measurements previously done used a constant DC supply, observations were made of field emission current fluctuations over time, an example of one can be seen in Figure 7.2 for an example of an event. It was also observed that the number of spikes increased with an increase in the gap voltage. As the measurement was

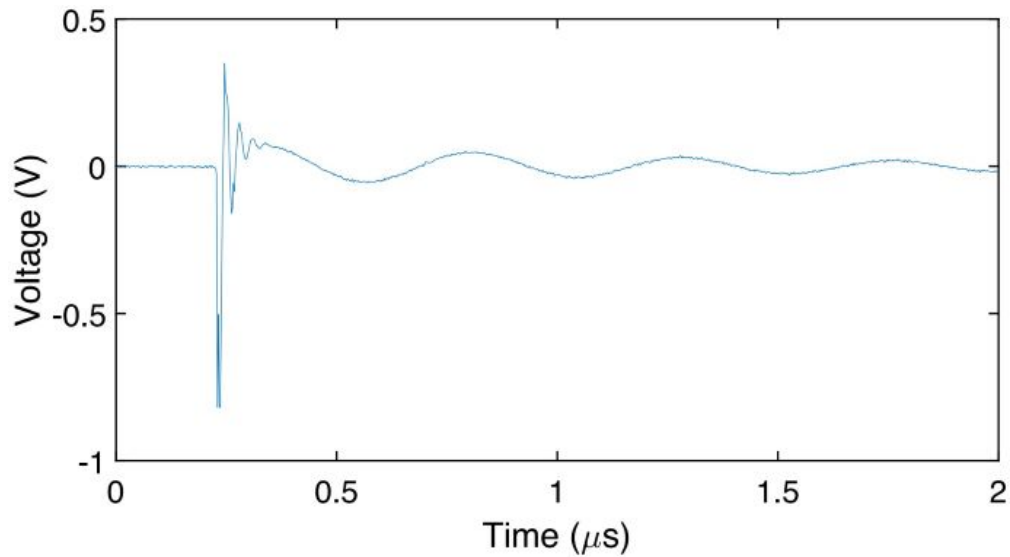
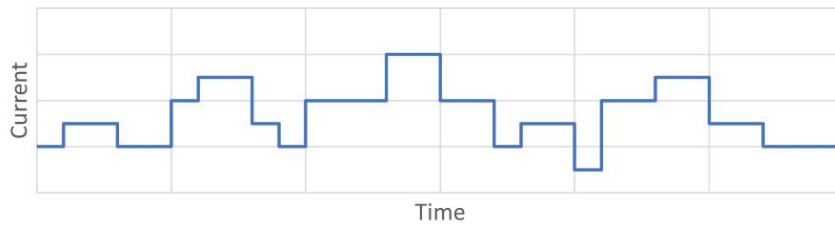


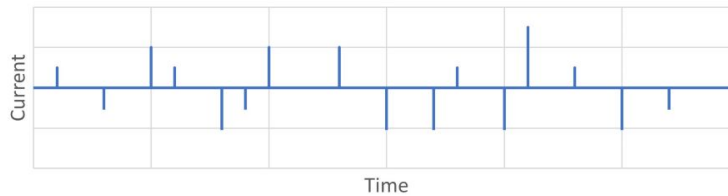
Figure 7.2: Oscilloscope measurement of a single current fluctuation from the output of the bias-tee using a sample rate of 500 MHz. This shows an oscillation after the initial spike in the voltage measured, which is proportional to the change in current [21].

AC-coupled, when a spike was observed it was unknown whether they are the results of a fast pulse or step changes in the current. A fast pulse would be an increase and decrease or vice versa in the field emitted current instantaneously and step changes would be a fast increase or decrease in the amount of field emitted current with a difference in the field emitted current after.

Figure 7.3, shows the hypothetical current going into the bias-tee filter and the filtered signal being measured on the oscilloscope. As mentioned it cannot be guaranteed that random walk is what is happening as there is no information about the DC level. Reasons why it is believed to be the case are discussed further during the interpretation of results section. To capture the spikes as seen in Figure 7.3, from the fluctuation detection electronics, the sample rate was varied to observe the resolution of the measurements taken. by varying the sample rate on the oscilloscope and observing the details of the wave form, a rate of 25 MS/s was chosen. This sample rate was sufficient to resolve the slower oscillations (e.g. after



(a)



(b)

Figure 7.3: Hypothetical example of (a) the random walk of current that occurs (b) and how this would be seen after filtering.

the $0.4 \mu\text{s}$ mark in Figure 7.4) caused by each event.

The measurement results to be shown were all taken during pulsed conditioning which differs from the previous measurements where measurements were taken whilst applying a constant DC supply [42]. Figure 7.4 shows the supplied voltage, current and measured bias-tee output signal over a $200 \mu\text{s}$ pulse. During the period of charging current whilst the voltage is ramping on the pulse, there are a significant number of transients in the current fluctuations for the initial $60 \mu\text{s}$ of the pulse. As a result of this and to be able to measure the small changes in current for the fluctuations, a long pulse is required. For these measurements from the oscilloscope the voltage is divided such that 1 V on the oscilloscope corresponds to 200 V supply voltage, and 2 A of current from the Marx generator. The second y-axis to the right is the voltage of a separate oscilloscope for the bias-tee where $1 \mu\text{A}$ current, which approximately corresponds to 1.75 mV measured on the oscilloscope. Due to the high-voltage pulse being $200 \mu\text{s}$ long, the window for each measurement was set to measure the whole pulse, leading to a total of 5000

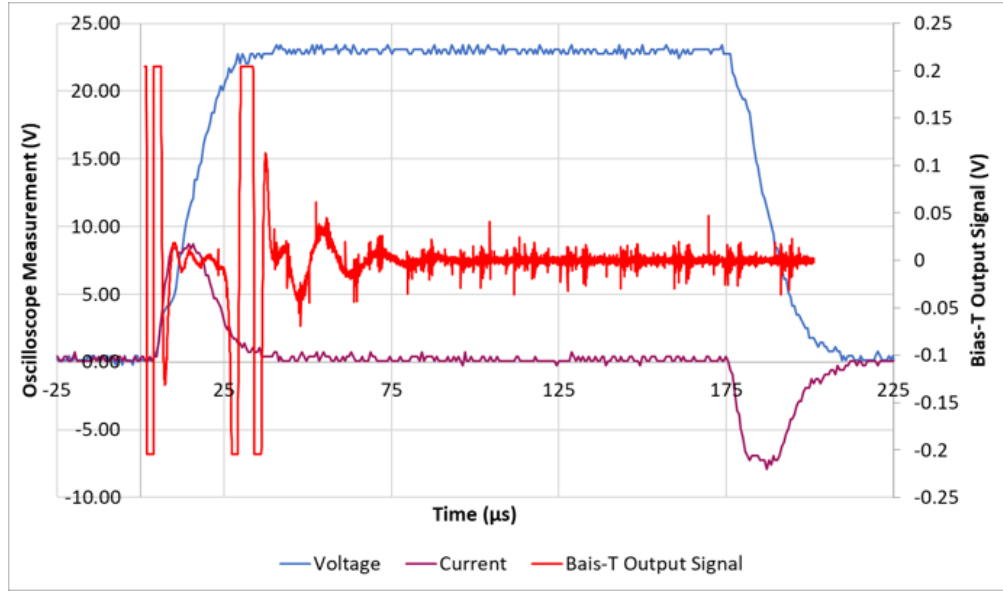


Figure 7.4: Oscilloscope measurement of a single pulse, showing the voltage, supply current and bias-tee output measuring current fluctuations with an amount of transients at the beginning of the pulse.

points per measurement being taken.

Measurements were taken during pulsing whilst conditioning and during ramping, where the electrical field is increased in accordance with the breakdown rate limiting conditioning algorithm and during flat runs with a constant electric field. The oscilloscope for the bias-tee was set to take a measurement every 10000 pulses using the synchronisation signal from the Marx generator. During conditioning the voltage steps by 10 V every 100000 pulses, meaning 10 measurements were taken for each step. Measurements from the bias-tee do not take into consideration the breakdowns and therefore the fluctuation measurements are not timed and can fall at any point with the likelihood of being measured just before or during a breakdown is relatively low.

To avoid counting fluctuations when there are transients during the ramping of the pulse when the gap is charging and the Marx generator was discharging, analysis was only done on the part of the waveform in a window that was specified

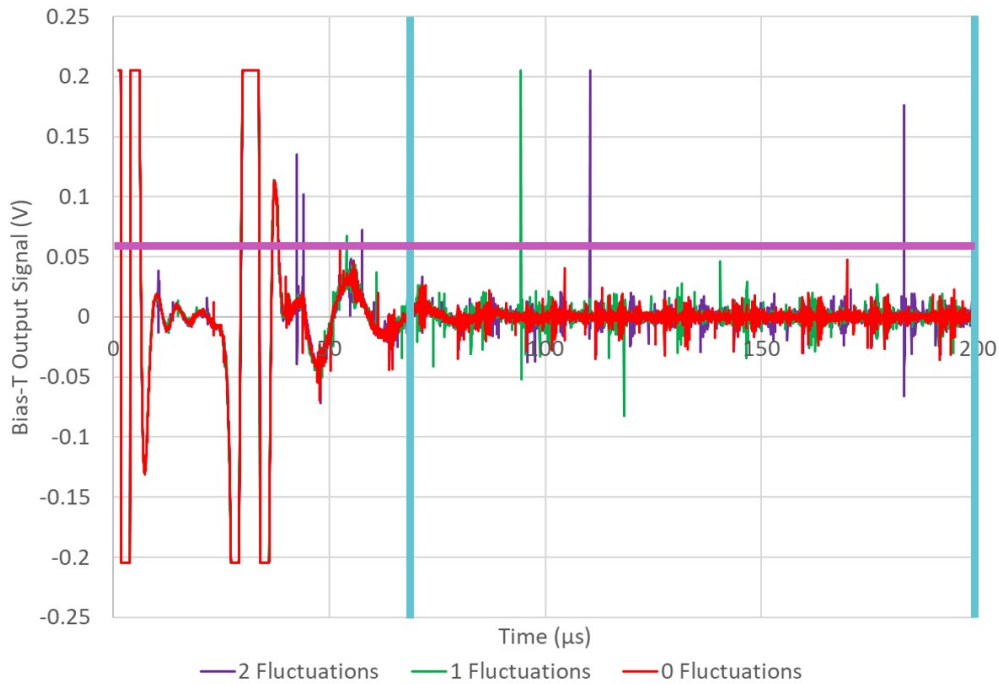


Figure 7.5: Three different fluctuation measurements for different pulses, counting between 0 and 2 fluctuations per pulse. Blue vertical lines indicate the window in which the results are analysed and a horizontal purple line indicating the threshold over the noise to count the fluctuations.

between the charging and discharging. This is given as the light blue lines as seen in Figure 7.5, where the measurements within this range are relatively low noise and periodic. Due to the noise during the pulse that occurs even with no voltage applied, a threshold was set, given by the light purple horizontal line in Figure 7.5. The noise is most likely a result of electromagnetic interference from switch-mode power supplies in other equipment lab or sub-components of the Marx generator. The threshold is used to determine the number of fluctuation in the current as the number of times the bias-tee output exceeds the threshold. From Figure 7.5, the measurement given in red has no fluctuations, the green has one fluctuation and the dark purple has two fluctuations.

7.3 Results and Discussion

The plots shown in Figures 7.6 to 7.10 show the pulsed conditioning electric field, accumulated number of breakdowns, and number of current fluctuations per pulse. In this section, only the salient features of the data in each figure will be highlighted. This will be to specify the correlations between the fluctuations during conditioning and flat electric field pulsing and the breakdowns and breakdown rates. The results shown are given in the order of testing of the system with different properties seen described. They are shown in pairs with (a) giving the positive fluctuations in current and (b) giving the negative fluctuation counts, with observations of the differences also given. A possible explanation that may explain the different observations from the results is given in the following section.

Figure 7.6 shows the ramp in the electric field followed by a number of pulses at a constant electric field due to the code being set to ramp up to 3000 V. A relatively regular occurrence of breakdowns is observed, in this case with a breakdown rate around 1×10^{-5} as specified within and controlled from the LabVIEW code. This leads into a number of pulses with a constant voltage of 3000 V, a reduction in the breakdown rate is observed, as determined by the slope of the plot of cumulative breakdown number. In terms of the current fluctuations this shows an increase in fluctuation rate when there was a decrease in breakdown rate. With respect to the number of positive current fluctuations per pulse, there appears to be a step type appearance giving an overall average increase. There were also fewer fluctuations related to a reduction in the field emission current suggesting a possible increase in field emission current in total.

Figure 7.7 shows two interesting events to be discussed with regard to the correlations between the occurrence of breakdowns and fluctuations. A large temporal cluster of breakdowns coincided with an increase in the number of

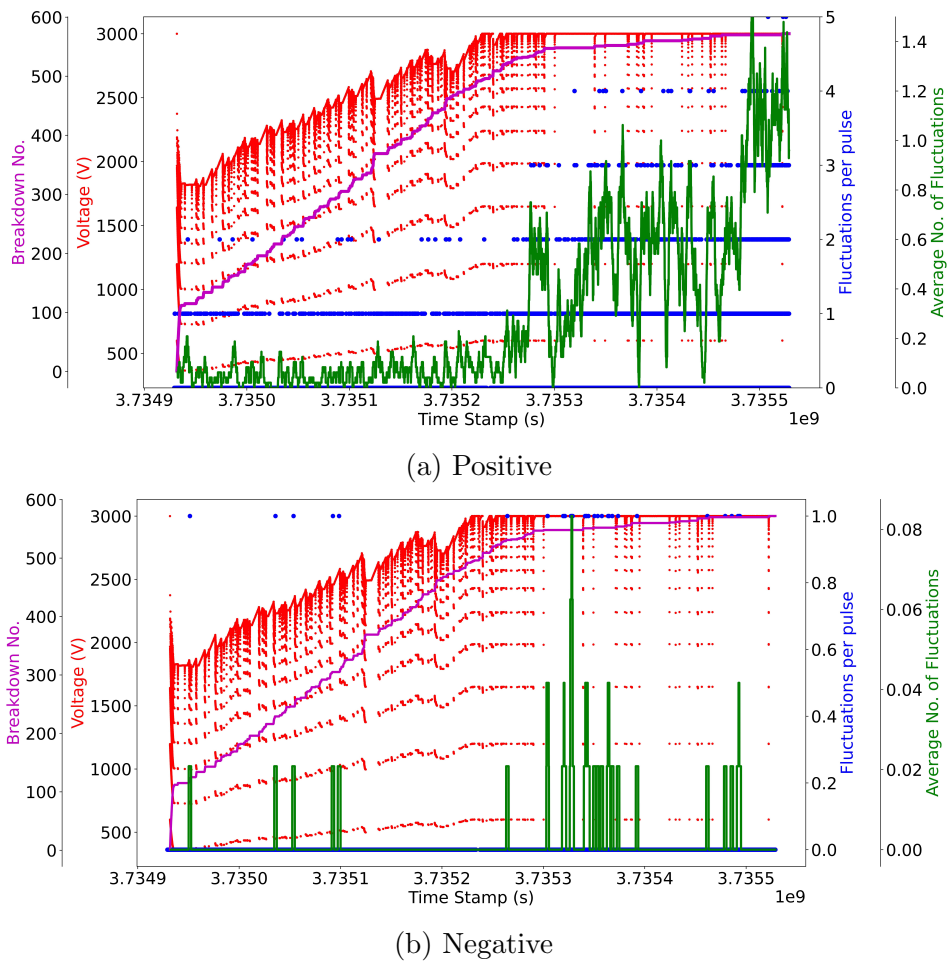


Figure 7.6: Plot showing the breakdown number, electric field, (a) positive and (b) negative fluctuation counts per pulse, and the average number positive and negative fluctuations per pulse. This shows a gradual increase in the number of fluctuations per pulse when the electric field stops increasing.

fluctuations, indicated by the green box. After the breakdowns stopped occurring, the number of positive fluctuations per pulse started to decrease, but in a relatively gradual way. The negative fluctuations also increases and decreases, but with a delay in time compared to the positive ones.

When voltage starts ramping again after a number of pulses without a breakdown allowing the breakdown rate to go below the threshold of 1×10^{-5} at around $770000 + 3.735e9$ s, there was an observed increase in the number of fluctuations to the point at which a breakdown occurred, indicated by the blue

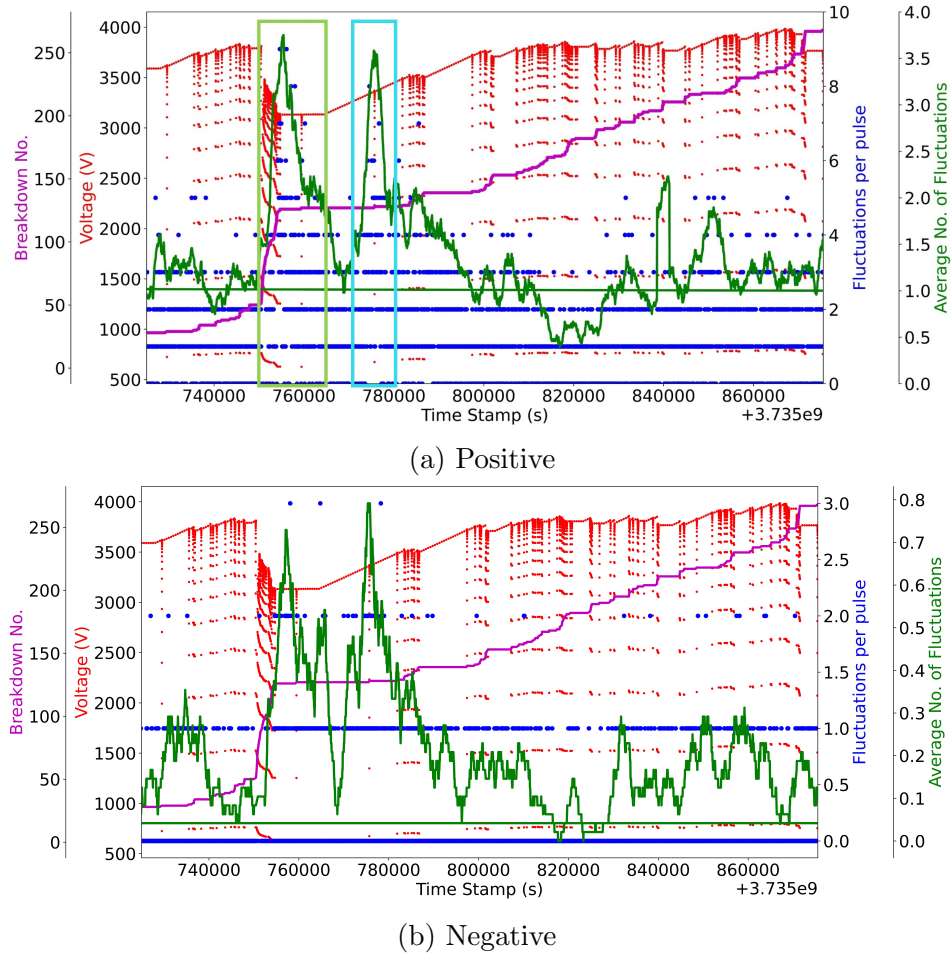


Figure 7.7: Plot showing the breakdown number, electric field, (a) positive and (b) negative fluctuation counts per pulse, and the average number positive and negative fluctuations per pulse. Showing an increase during a higher breakdown rate and decrease after (green box), and an increase before a breakdown and decrease after (blue box).

box. After the breakdown, similar to the cluster, the fluctuation rate per pulse started to decrease gradually. In the case of this observation both the positive and negative fluctuations appeared to occur simultaneously. For both of the cases given there are a smaller number of negative fluctuation counts, with a maximum of 3 counts for the negative and 9 counts of positive current fluctuations.

The main observation taken from Figure 7.8, are that some breakdowns coincided with a reduction in the fluctuation rate and in other cases it coincided

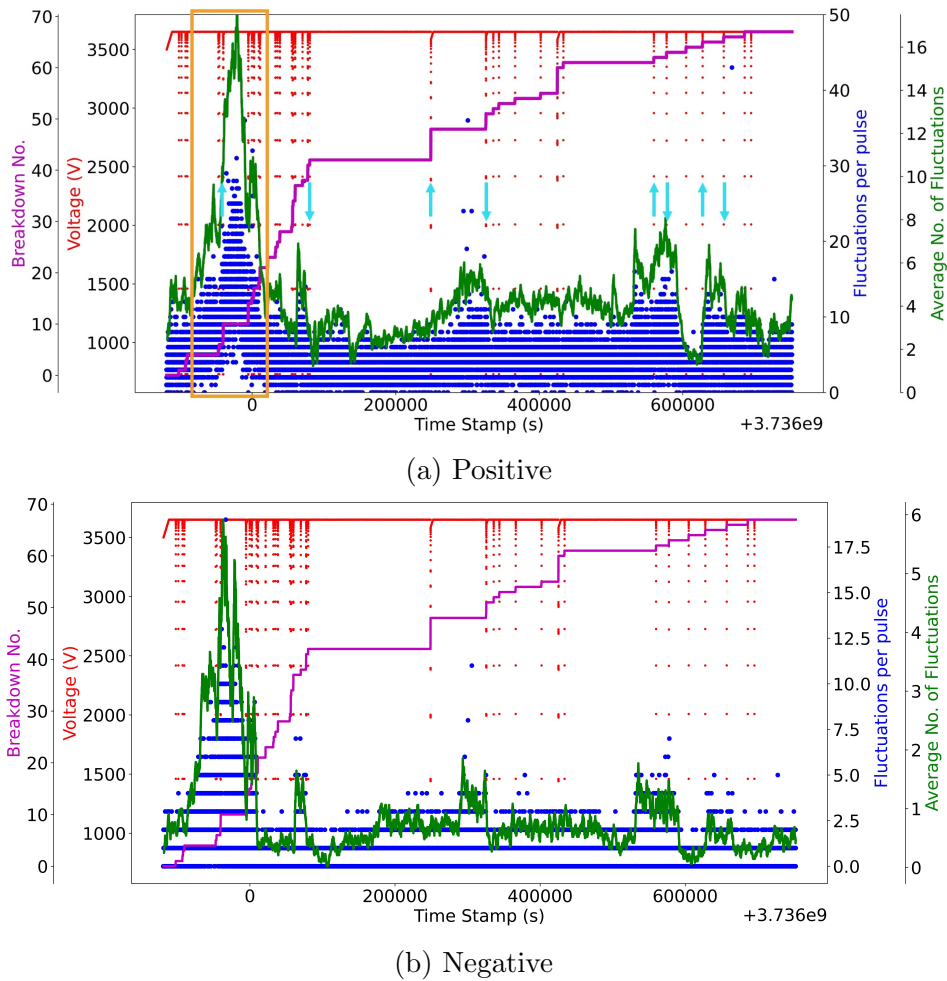
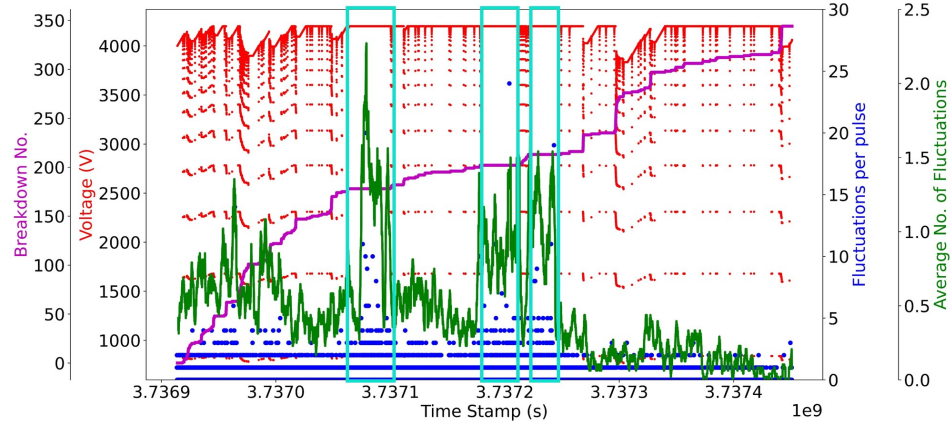


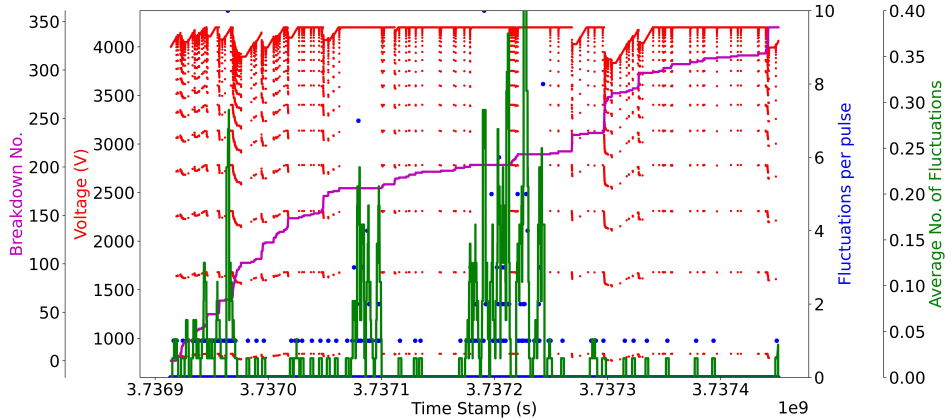
Figure 7.8: Plot showing the breakdown number, electric field, (a) positive and (b) negative fluctuation counts per pulse, and the average number positive and negative fluctuations per pulse. A relatively large increase and decrease in the fluctuations per pulse can be seen between consecutive breakdowns (orange box). Also seen are breakdowns that lead to an increase or decrease in the number of fluctuations per pulse, indicated by blue arrows.

with an increase. Additionally, the number of positive and negative current fluctuation appear to be correlated, again with a greater number of positive fluctuations. Several examples can be seen where, when a breakdown occurs there can be an increase in fluctuations and after different breakdowns the number of fluctuations decreases. This would suggest that the different breakdowns can lead to more instabilities in the field emission current with a possible general increase due to the larger number of positive fluctuations detected. This is

consistent with a breakdown creating collateral damage that is inherently unstable. Alternatively, some breakdowns make the field emission current more stable than before, suggesting a reduced number of changes to the surface, consistent with eliminating a large breakdown site.



(a) Positive



(b) Negative

Figure 7.9: Plot showing the breakdown number, electric field, (a) positive and (b) negative fluctuation counts per pulse, and the average number positive and negative fluctuations per pulse. Showing 3 time intervals with a relatively large amount of time between consecutive breakdowns where the number of fluctuations per pulse increases compared to the surrounding pulses (3 blue boxes).

Figure 7.9 shows an increase in the number of fluctuations from an average up to 0.5 fluctuations per pulse to up to 1.5 when there are a significant number of pulses between breakdowns. There are three long gaps between consecutive

breakdowns during which the number of fluctuations is increased. Following the increase, when breakdowns occurred the number of fluctuations per pulse decreased rapidly and increase rapidly during the following gap in breakdowns. Even without the breakdowns, the fact that there are changes in the current suggests that there were physical changes to the surface of the electrodes. Also, that these changes occur during each pulse, causing the field emission current to fluctuate.

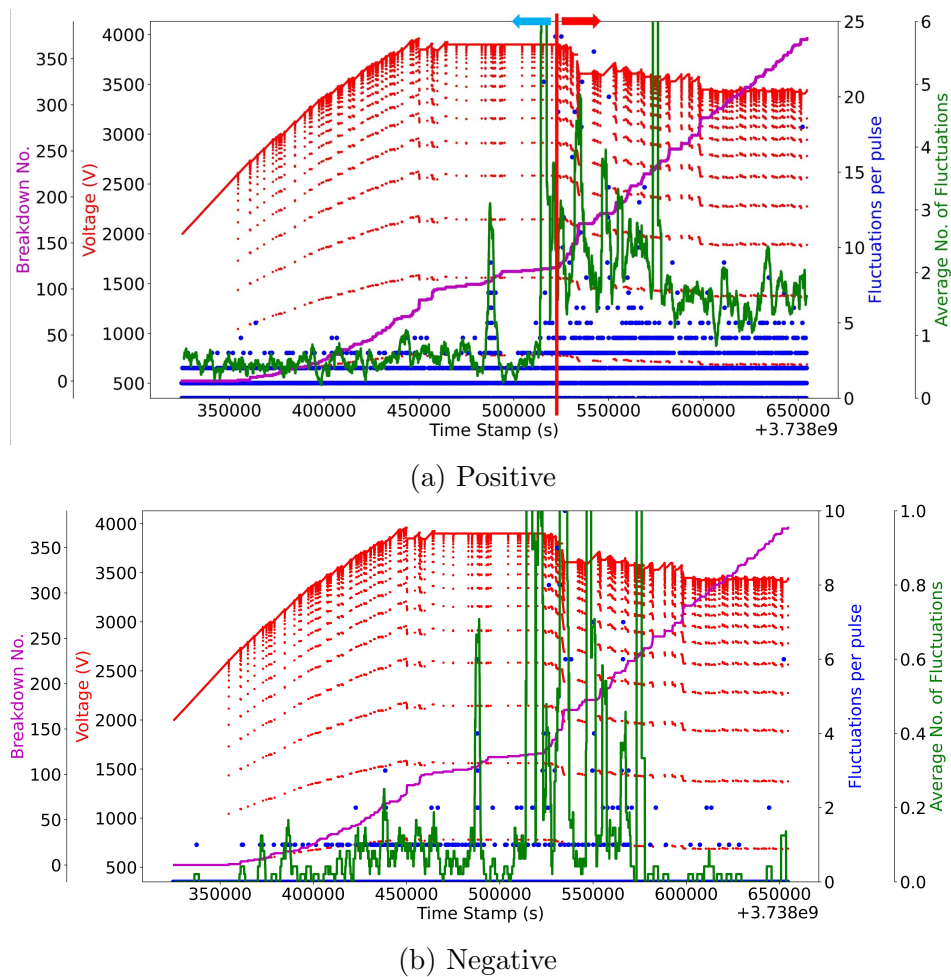


Figure 7.10: Plot showing the breakdown number, electric field, (a) positive and (b) negative fluctuation counts per pulse, and the average number positive and negative fluctuations per pulse. Showing relatively stable running and low fluctuation rate before the red line in the direction of the blue arrow and a deconditioning of the electrodes with an increased fluctuation rate in the direction of the red arrow.

Figure 7.10 shows the degradation of this pair of electrodes where the field

is reduced due to the increased breakdown rate. Initially there are a relatively large number of breakdowns with a low number of fluctuations per pulse which matches other results shown. A difference in number fluctuations per pulse with a high breakdown rate is observed, when the breakdown rate increases, which could suggest degradation of the material. During the degradation phase there was an observed increase in the number of current fluctuations per pulse. The increased number of fluctuations during each pulse suggests that even between the breakdowns, there is an additional effect causing an increase in the changes to the surface that are leading to the breakdowns.

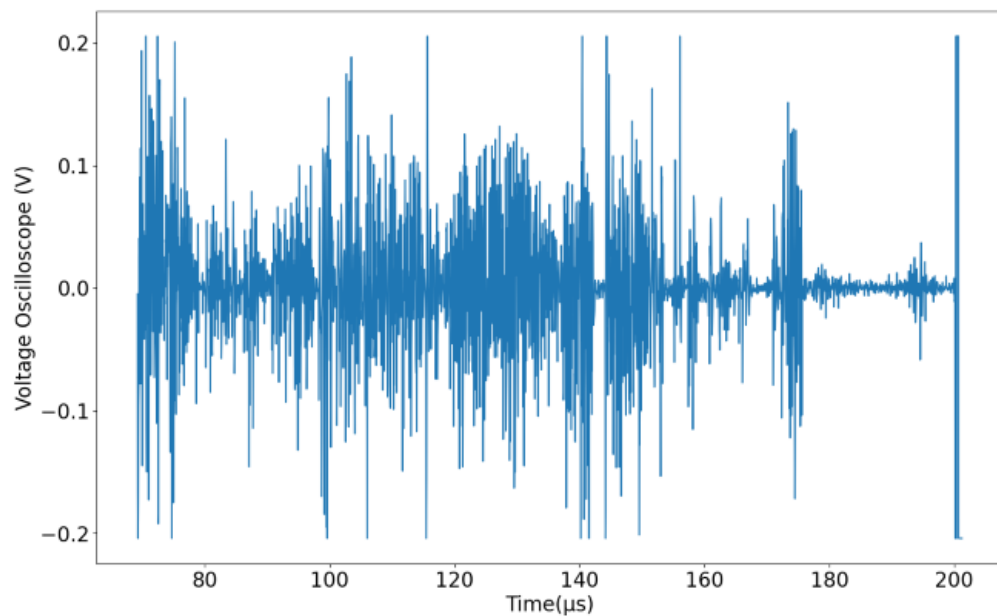


Figure 7.11: Oscilloscope measurement of many current fluctuation during a singular high voltage pulse.

In some cases an individual pulse was seen to have significantly more current fluctuations, one example of the bias-T output from one of these can be seen in Figure 7.11. In some cases the count of fluctuations exceeded 100 during a single pulse, compared to around 10 during the other pulses recorded. Measurements of this sort are very rare in the results and isolated with no consecutive measurements having a similar number. With a repetition rate of 200 Hz and fluctuation

measurements taken 10000 pulses apart, each fluctuation measurement would be around 50 seconds apart. One of possible causes of a single-pulse fluctuation trace measurement like this would be from noise from other equipment running within the lab but this would normally be ongoing and therefore would affect traces of other consecutive measured pulses. Another observed source of noise on some occasions seen during experiments, was due to the use of mobile phones in the lab, as this can be picked up by the electronics. This is possibly a result of the ground loop formed by the connections between the system, power supply, oscilloscope, etc, acting as an antenna.

Alternatively the reason for these fluctuations in current, may be that these measurements happened to be taken on a pulse in which a breakdown occurred or a pulse a few pulses before a breakdown. This occurrence was observed more consistently during the results from the time period shown in figure 7.10 and appeared to correlated well with the breakdown pulses, appearing to occur temporally close. Due to issues with timing between the two oscilloscopes the time correlation between the two could only be determined to the nearest minute. From what is seen and taking the reduced accuracy into account it is still reasonable to say that it is very possible that the fluctuations in current seen could be real and a result of either being close to a breakdown, or on the pulse of a breakdown.

In general throughout the different runs shown in Figures 7.6 - 7.10, it was seen that there were more positive fluctuations in field emission per pulse than negative fluctuations per pulse, that varied between measurements of around 2.5 to 5 times more. Whilst it may be the case that the field emission current was increasing in general in these cases, it may not actually be the case. Measurements of the field emission current were not measured in parallel with these results. Therefore, the effect of the rising and falling edge of the pulse are not known. Therefore, it is possible that each pulse would start at a given field emission current, increase

during the pulse seen as positive fluctuations and then return to the previous field emission current, lower or higher during the next pulse. To summarise, although it is possible that positive fluctuations could indicate a gradual increase in the field emitted current, without a direct measurement of the total field emitted current during each pulse, it is not possible to say for certain.

7.4 Mobile Dislocation Interpretation

The following section is on interpretation of what these results could mean in terms of mobile dislocation models that have been proposed to explain breakdown statistics. There have been theories of this developed previously with papers published of both the theoretical simulations and measurements made in the same test setup with the results shown to match the simulations [21], [22], [42]. This section describes how the field emission current fluctuation measurement results shown could relate to dislocation movement in the context given. With details to be given, of how the measured fluctuation rates may correspond to dislocations, and the properties experienced in terms of 'surface-hardening-like' effects of the electrodes during conditioning.

If the changes in field emission current are in steps and a result of dislocation movement then this is most likely only the case for the dominant emitter. Surface features caused by projected dislocation movement should occur over the whole surface all of the time, both reducing and increasing the field emitted current, as a result of this it is unlikely that individual steps would be resolved, instead producing an average that is measured as noise [115]. If a dislocation is on a dominant field emitter, being the prominent field enhancement on the electrode, a dislocation in this area will cause a more significant change to the field emission measured. As a result of this field enhanced area being generated the increase in

field also means an increase in the force applied and this should in turn lead to more dislocation movement, higher dislocation density and number of pinned slip planes.

In some cases in the results it was observed that there was a reduced number of fluctuations per pulse when the breakdown rate was high. This may be a result of the number of dislocations not being able to build up between breakdowns and the breakdowns would release the stress built up causing the dislocations. This seems to be the case during conditioning with increases in the field, therefore the force to cause specific dislocations may then be accelerated by the increasing field causing breakdowns at the initiation field enhancement rather than allowing it to develop and possibly settle on its own.

One other characteristic observed was that the intervals between breakdowns on occasion exhibit an increase and then a decrease in current fluctuations per pulse with no breakdowns occurring. Increases in the number of events per pulse suggests an increase in the amount of movements caused by dislocation and the decrease as the amount of movement during per pulse decreasing. A possible explanation for this is as the nature of dislocations, more dislocation should lead to a higher dislocation density close to the surface, that leads to more trapping of dislocations saturating the ability for dislocations to move as a result of being pinned. This observation of the number of dislocation increasing and decreasing is consistent with the MDDF theory and also agrees with observations of a 'surface-hardening-like' effect, agreeing with the conditioning conclusions made in Chapter 3.6. This suggests this movement does not occur as soon as the material experiences the field able to cause the dislocations and required a number of pulses to develop and saturate. The MDDF model considers dislocation movements during one pulse and does not consider the effect of pulsing and stress release from a breakdown. There has been some consideration of a 'memory effect', which is not fully understood

but may explain pulses leading to a breakdown [115]–[117]. Use of the words, ‘memory effect’, in this instance refers to if the dislocations do not return to the same state as before the pulse, and if in a state closer to a breakdown when the next pulse occurs. If some dislocations require a larger field to move than others, stopping at the different fields allows for the dislocations to settle, whereas a higher would induce an avalanche of dislocations causing a breakdown [118].

An observed result specifically seen in Figure 7.8 is that after some breakdowns there is an increase in fluctuations and other lead to a decrease in fluctuations. The observation that some breakdowns can improve the surface or worsen has been made previously and often described as primary and secondary or follow up breakdowns, where follow up breakdowns are the ones that occur as a result of its predecessors. The results from the fluctuations may also agree with this where one breakdowns may release the stress stored from dislocations locally hardening the surface. Where as in some cases the breakdown may increase the stress around the crater leading to an increase in dislocations. In more extreme cases of a build up of stress under the surface this may lead to a cluster of breakdowns [118].

7.5 Current Fluctuations Conclusions

To conclude changes in field emission current have been measured during pulsed conditioning and constant voltage runs with variations in the amount of fluctuations with respect to breakdowns and pulses. There was a general variability in the number of fluctuations per pulse and a poor correlation with breakdowns and conditioning between different measurement, meaning it is not possible to draw a solid conclusion of the characteristics. Different characteristics of the number of fluctuations per pulse observed include a variation in the number of fluctuations between breakdowns. Where some breakdowns lead to less fluctuations and other

more, meaning a reduced or increased field enhancement respectively. In some cases there was an increase in fluctuations leading up to a breakdown, and then decreasing after the breakdown occurs. The number of fluctuations appeared to be reduced when the breakdown rate was high with the exception of when there was degradation of the pair.

Additionally, some measurements contained a significant increase in the number of fluctuations in the current. Whilst this could be the result of noise in the lab, its isolated appearance and proximity to a breakdown suggests that they may correlated with breakdowns. This could be several pulses before or during a breakdown causing a lot of fluctuations in the field emission current.

Correlating the fluctuations measured with dislocation movements may provide some insight into the characteristics of dislocation movement and conditioning. It is most likely that measurements only give insight into the field emission characteristics of dominant field emitter due to this being the area that can make a significant enough difference in the field emission to be detected. The results shown could indicate that the dominant field emission area causes an increase in dislocations as a result of the increasing electric-field and that this can be reduced or increased as a result of a breakdown. Currently there is not a way to determine the location that the highest amount of field emission is occurring, meaning this cannot be guaranteed to cause a breakdown. Additionally the observations on increasing and decreasing number of fluctuations when no breakdowns occur could explain the conditioning effect with respect to the dislocation density reaching a saturation point with a 'surface-hardening-like' effect.

Further analysis is beyond the scope of this thesis. The data will be analysed in further detail by other institutions that analyse data in a more statistical manner. The current fluctuations observed may be the result of more than one mechanism causing changes to the surface.

Chapter 8

Conclusions

The final chapter will give an overall conclusion of the work outlined in this thesis to bring together the individual sections. Additionally the suggestions for future work based on the insight provided from the results to gain further understanding and improvements of the measurements discussed.

8.1 Relevance

In this thesis, results from the pulsed DC large electrode systems at CERN have been presented, looking at different aspects related to conditioning and vacuum electrical breakdown phenomena. This work was done in the context of particle accelerators in collaboration with various groups working towards understanding what causes vacuum breakdown. All accelerating structures use a conditioning process to reach the designed operating field. Ideally, breakdowns would not occur, as they can cause damage to the structure and disrupt the beam. Studies of vacuum breakdown are done to develop understanding of the cause and to reduce their likelihood whilst increasing the high-field capabilities and improve overall accelerator performance.

8.2 Summary of Results

The following bullet points highlight the main conclusions from this thesis:

- Removal of the cathode edge field enhancement by using a small anode to large cathode configuration appears to have remove the clusters around the edge of the electrodes throughout the tests shown.
- Changes to the conditioning method to use steps in the field with periods of constant field appears to be an effective way of conditioning for most of the materials tested.
- The electric fields achieved appear to correlate for the majority with previous material studies. Additionally, observations of pulse length dependence on the breakdown rate, for pulse length between 100 μs and 1 ms for different materials showed very little to no effect. Whereas, for Cu with pulse lengths of 1 μs and 250 μs , this shows a clear effect on the breakdown rate that requires more studies.
- Tests of irradiated and non-irradiated samples of different materials show a relatively high effect from irradiation, from no change in stable-electric field to being limited to around 23 MV/m. A carbon layer was observed after irradiation in the halo area, which could be a potential reason for the increased BDR, although further work is required to verify this. Also, there was no clear influence from the blisters formed on the Cu based materials, as there were many blisters remaining after testing.
- Field emission current measurements show a correlation between the stable electric fields during pulsed conditioning and gap electric field during field emission measurements. This indicated that the stable electric field

influences the amount field emission current at different electric fields during field emission measurements, and that this can also be observed with respect to when different materials starts to breakdown.

- Optical spectroscopy measurements conducted in parallel with field emission current measurements show a clear correlations between the current and light intensity measured for Cu based materials. However, light from other materials such as Ta and Nb was only detected for a short period before being extinguished and no light detected from TiAl_6V_4 and AlMgSi_1 . These results suggest that whilst the light is related to the field emitted current, the cause may not be a result of OTR due to only being consistent for Cu based materials and not black body due to the shape of the wave forms acquired. It is most likely that there are several factors that influence the light detected, but this requires further studies.
- Studies of current fluctuations during pulsed high-field operation during initial conditioning shows a number of different characteristic with respect to rate of fluctuation during different periods of the conditioning. It is possible that these different characteristics can be linked to breakdown phenomenon like follow up breakdowns and de-conditioning as well being related to theories of mobile dislocations causing surface enhancements.

Changes to the electrodes edge design were made as well as the use of a small anode to large cathode configuration to avoid cathode field enhancements, this appears to have removed breakdowns coinciding with the edge of the high-electric-field area. Additionally, changes to the conditioning method were made, conditioning through pulses at intermediate electric fields to avoid over conditioning to the point of de-conditioning. Materials tested in order of performance include, TiAl_6V_4 , CuCr_1Zr , Nb, Cu OFE, AlMgSi_1 , and Ta. Only 1

pair of each material was tested with some variation in the procedure and final breakdown rate. The majority of the materials performed well using the step-wise conditioning method with the exception of Nb and Ta, where Nb appeared to condition more efficiently using the breakdown rate limiting algorithm. The performance with respect to the step-wise conditioning algorithm may be explained by dislocation movement, this is providing the fluctuations in field emission current measured for Cu electrodes was the result of dislocation movement.

An additional pair of each material except the Al alloy was irradiated with 1×10^{19} H⁻p/cm² on a portion of cathode high-field area before testing in the pulsed DC system. This resulted in a significant reduction in the achievable electric field for all materials except the Ti alloy and Cu OFE pairs that reached similar or the same electric field respectively to the non-irradiated pairs, with an increase in the number of breakdowns at the beginning possibly conditioning away the imperfection introduced from irradiation. Whilst the irradiation did introduce blisters on the Cu based materials this did not appear to influence the breakdown locations, the most likely cause of the reduction in the electric field for the majority of the materials was the presence of a carbon layer on the surface due to contamination. This can be seen as there were many blisters still remaining on the Cu OFE in Figure 4.13, as well as cluster in the halo area and the fact that the irradiation caused a significant decrease in the electric field for Nb and Ta materials, as seen in Chapter 4.6. From these results the best option for an RFQ would be Cu due to this requiring no changes to the current design of many RFQs. Alternatively, research into the production and operation of a Ti alloy vane RFQ could increase the electric field capabilities and improve the overall performance and resistance to blistering of RFQs. Tests to determine the effects of pulse length dependence of the breakdown rate were done, this showed no clear dependence with pulse lengths between 100 μ s and 1 ms, suggesting decreasing the RFQ pulse

length within this range will not improve the performance. Additional tests with pulse lengths between 1 μs and 200 μs shows a clear dependence on the breakdown rate, suggesting decreasing to lower pulse lengths within this range could allow for higher fields to be used.

Measurements of field emission were done for each of the materials, with the maximum electric field during field emission measurements having a good correlation with the electric field achieved during conditioning. Calculations of the field enhancement factor did not correlate with the maximum current or maximum voltage during the measurements suggesting that this is influenced by something else or a combination of variables. This suggests that the purely field emission current models are do not have the same complexity as is measured from the pulsed DC systems. Comparisons field emission for the reverse polarity to conditioning and with irradiated pairs showed a decrease in the achievable voltage due to an increase in field emission.

During each field emission test, optical spectra measurements were made with only consistent light detected for Cu based materials suggesting that the light is not the result of OTR. For analysis of the spectra from Cu based electrodes a ridged pair of electrodes were tested that showed a good correlation between field emission current, gap power and the spectra light intensity. Additionally, observations were made of the variation in spectra over time that did not correlate with the field emission current, variations with respect to the observation angle, and a sharp peak at 700 nm when the reverse polarity to conditioning was applied.

During field emission measurements of Ta and Nb irradiated electrodes a temporary light emission was detected that increased with field emission current and shown to be in a singular location for each. In both cases the light emission stopped after a breakdown. For Ta the spectra was broadband, whereas for Nb the spectra looked similar to black body radiation. Post analysis of the Nb spectra

showed that it had a narrower band width than the calculated black body radiation spectrum, suggesting that the light was not the result of black body radiation. The measurements of spectra throughout the field emission tests suggest that the source is not OTR or black body radiation and would need to be something that would vary depending on the material and more prominent in Cu based materials.

8.3 Suggestions for Future Work

8.3.1 Proposed Conditioning Algorithm

For the conditioning done with each of materials shown, most of the conditioning was automatically controlled by the breakdown rate limiting algorithm with intermediate steps set, however some important changes of set-points and parameters were made by the operator. Based on the experience gained with the electrodes described in this thesis, an entirely automated step-wise conditioning code would be more beneficial for conditioning of future electrodes. This sections describes the different steps, giving a descriptive way as to how a computer could use the results to condition the different electrodes. Figure 8.1 shows the flow diagram of how this could be implemented with the already existing breakdown rate limiting conditioning algorithm program.

The first stage of the step-wise conditioning process was an initial step in voltage as specified by the user, with the aim that it will have no issues reaching the voltage. After pulsing flat a decision is made as to the next command by first comparing the current BDR to a higher BDR given as BDR3, if this BDR is exceeded then the voltage is no longer increased and the electrodes are considered as fully conditioned to their capabilities. If it is lower, then the code will look at the rate of clusters in breakdowns.

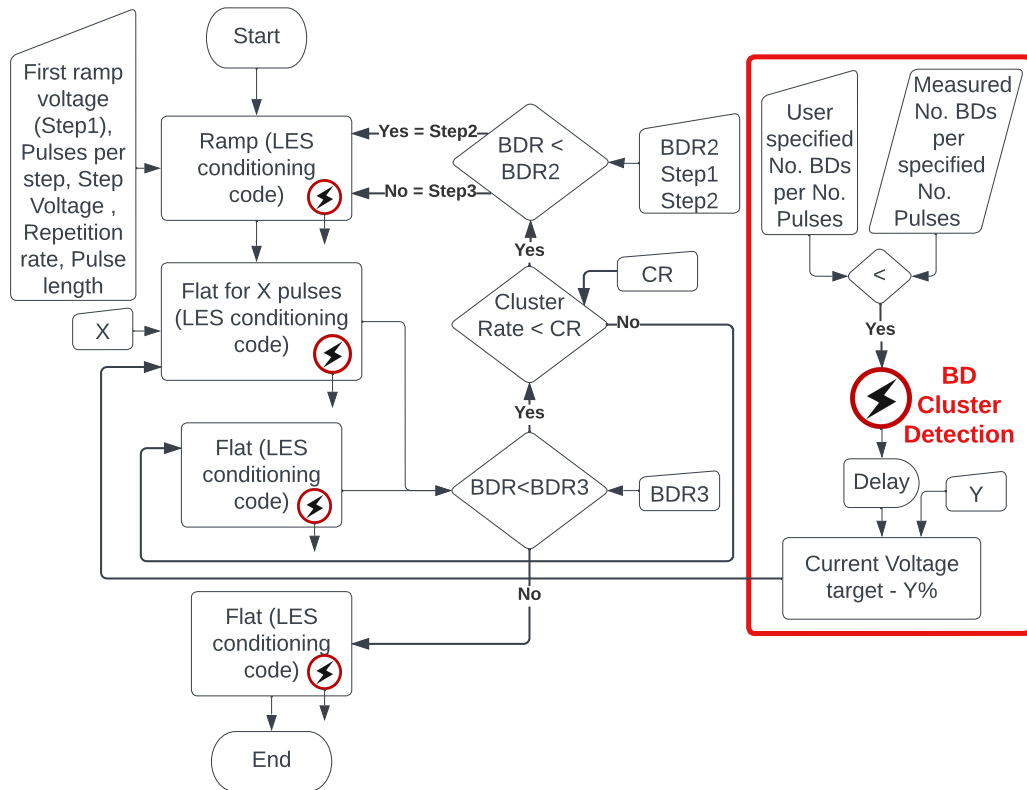


Figure 8.1: Flow diagram integrating the breakdown rate limiting conditioning algorithm with a higher level of control that more qualitatively makes the decisions of the user during the conditioning of the various materials shown.

Currently there is no part of the code that takes this into account, but small clusters in breakdowns appear to be a sign of instability whilst conditioning and an indication that you are approaching a achievable electric field limit of the electrode pair. Figure 8.2 is an example of results where a number of clusters occurred, this data is taken from the CuCr_1Zr electrode pair shown in Chapter 3.6. These clusters are generally not seen at lower electric fields and are seen as the electric field increases. To quantify this, a cluster could be defined as more than n number of breakdowns in m number of pulses, and the rate can be calculated from this and a limit specified within the code. Provided both of the previous rates are below the threshold specified, the BDR will be compared to an additional BDR (BDR2)

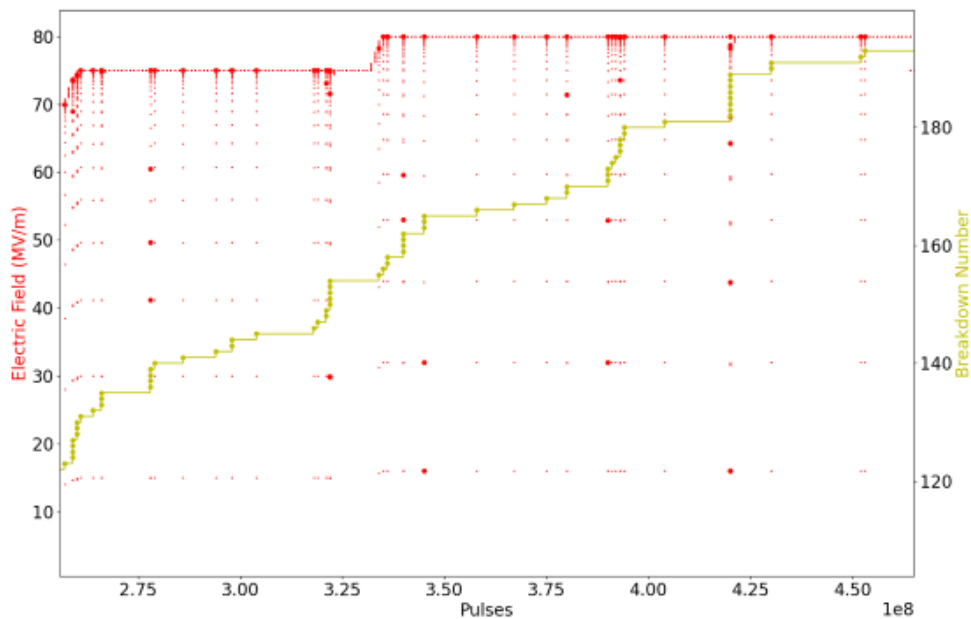


Figure 8.2: Small clusters in breakdowns taken from the CuCr_1Zr conditioning shown in Chapter 3.6.

to determine the size of the next step in voltage. If the BDR is lower than the threshold then a larger step in voltage will be applied in order to approach the limit with a reduced amount of BDs.

Another issue with the current code is that sometimes a large cluster breakdowns will occur and this can degrade the surface, and will need re-conditioning after, as seen in Chapter 3.6, for TiAl_6V_4 and AlMgSi_1 . When a large cluster in the breakdowns occurs it is most likely in one spot and will continue to breakdown with the possibility of making the area worse each time, this was most visible with the Al electrodes. If this is stopped earlier it is less likely to affect the achievable field as it will be less damaged and easier to condition back up. To implement this into the code there will need to be part inside the current code that triggers when a significant number of BDs occurs over a small number of pulses, with boundaries set by the user. When this is detected it escapes from the code

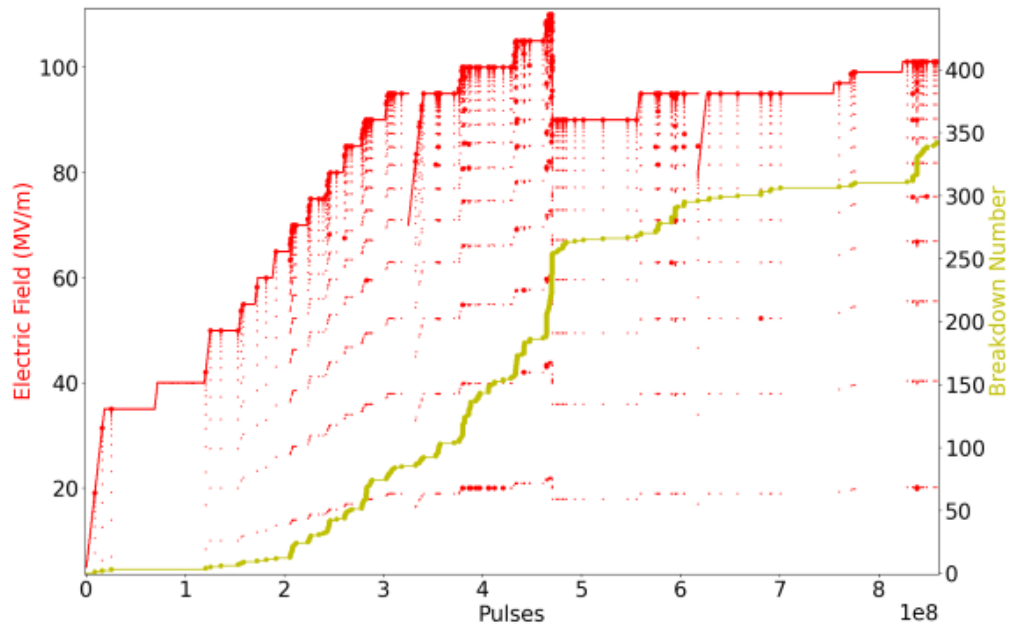


Figure 8.3: Large cluster in breakdown leading to a significant decrease in the electric field and the following reconditioning, taken from the TiAl_6V_4 conditioning shown in Chapter 3.6.

as seen by the lightning icons and will proceed as seen in the BD cluster detection box, as seen in Figure 8.1. This will include a small delay of no pulsing before reducing the field by a specified amount and setting it to pulse, if it continues to cluster it will trigger again and be reduced further.

8.3.2 Pulse Length Dependence

The pulse length dependence was only observed once for the majority of materials with only one scan from $100 \mu\text{s}$ to $1000 \mu\text{s}$. Over these pulse length no clear observation of breakdown rate of pulse length was observed suggesting that $100 \mu\text{s}$ is beyond the length that makes a difference to the breakdown rate. To improve the reliability of this result further studies could be conducted with increases and decreases in the pulse length to rule out the affect of conditioning throughout

pulsing.

An additional short test looking at the pulse lengths of 1 μs and 200 μs was conducted and shown that this difference in pulse length changes the achievable field. This would suggest that there is a pulse length dependence between of breakdown rate between these two pulse lengths that may saturate before reaching 100 μs suggested by the previous tests. Further tests in this range would most likely provide a dependence on pulse length between the previous results in the ns range and these results to bridge this gap. If possible to decrease the pulse length of this supply then a comparison of the pulse length in RF could be compared to the pulsed DC results.

8.3.3 Self Organising Plasma

It may be possible to replicate the results shown of the evidence of self organising plasma to study the phenomenon further, one way would be to generate tips on the surface. The issue is that this as a test on its own would generate the result relatively early and would need to be replaced to repeat again. Having multiple tips of different sizes may allow to stagnate the melting of the individual tips at different fields to analyse each individually. It could be part of a normal pair of electrodes to be tested with the aim of it being removed and the electrodes to be used as normal after providing it does not have an impact on the performance of the electrodes.

Another option that has not been proven to work in this system to date is to pump gas into the system and try to generate the plasma. This would require a constant through put of gas that can be ionised with the aim to form these shapes. Pumping gas into the whole gap may lead to a larger area of pattern formation. It may be possible that in the case of the pair shown that the machining lines also

aided in the organising of the plasma. In the system it is possible to pump gas in through the window and out through the normal output above the electrodes. Using this method would allow one to monitor the pressure, maintain a more consistent pressure, repeat multiple times, choose the gas present.

8.3.4 Linac4 RFQ

The amount of H^- irradiation on the electrode target for these tests was the equivalent of 10 days of the RFQ [119], [120]. A full year of operation of the RFQ is 100 days and therefore it may change the results for the materials that performed well. Also, the energies used for these tests were 45 keV which is the energy at the input of the RFQ, whereas the energy at the output is 3 MeV. Putting the electrode after the RFQ would give the highest energies the RFQ vanes would see which could impact the depth of the implantation and the operation of the electrodes during conditioning. Another difference to the RFQ is that the electrodes were irradiated once before conditioning. Ideally the irradiation would occur throughout but this would not be possible. One option being considered is re-irradiation of an electrode after conditioning in the system.

As only one of each material was irradiated and tested these results are not statistically significant. Whilst the evidence from the breakdown locations and the correlations between the different materials make a good argument for the effects of irradiation, tests with the same materials would help to verify these results.

8.3.5 Field Emission

Due to only having one non-irradiated pair of each material to test it would be more reliable if this was to be repeated for the different materials. Throughout the tests with the different materials, when the field emission results produced significantly

different amounts of field emission for a given supply voltage compared to Cu, it raised the question of whether there was an issue with the electronic components of electrical cables used or a property of the electrode materials. Tests were done to verify that it was not the electronics, but testing more of the same material would help to verify the results provided.

8.3.6 Spectroscopy

One of the questions raised when measuring the spectra for the Al alloy electrodes was whether the light was occurring but not being measured at the spectrometer. It was seen that the light from the ridged Cu electrodes was easier to detect and may also be the case for Al. This may also allow for the use of an optical fibre feedthrough to place the fibre closer to the emission site.

An additional test that could be conducted with the variety of materials tested it pairs of 2 different materials. These could be conditioned in both polarities and also field emission tests to observe how the difference in anode and cathode affects these results. It may also provide in site into the spectroscopy depending of the wavelengths of light emitted are different or if any light is emitted at all for each configuration.

There are a few possible explanation for light emitted during field emission but during these tests the speed at which the spectrum could be measured was relatively low. To measure the very fast elements of field emission and breakdowns would require the implementation of solid state spectroscopy. To measure light from field emission at these speed may require a close proximity to the emitter, therefore this would also require the ridged electrodes and fibre feedthrough.

8.3.7 Fluctuations

For the current fluctuation measurements shown a sample pulse was only taken every 10000 pulses with no synchronisation with the breakdowns. Part of the motivation behind this study is the hypothesis that there would be a large number of fluctuations in the pulses leading up to a breakdown as predicted by the MDDF. If this were the case then it would be possible to use current fluctuations to predict breakdowns. To gain insight into whether this happens within this system and setup measurements would need to be either taken for every pulse or an additional synchronisation of the measurements with breakdowns defections. By sampling both normal pulses as well as the pulses before and after a breakdown, it would be possible to compare these to determine whether they could predict breakdowns.

Measurements of the field emission current during the pulses would also be useful for determining whether the fluctuations seen are in fact a result of a random walk of steps in the current or are very fast oscillations with no last change in the current. Knowing this would help to understand whether the change to the surface maintains a higher field emission current emission or if there is just a brief current emission. Evidence of a step in current would indicate some form of field enhancement on the surface whereas a spike may indicate the movement of something on the surface that does not increase the field.

Currently there is not much physical evidence to support the theory of mobile dislocations having an effect on conditioning [39]. Observations of the slip planes have been made at the university of Jerusalem but these look very similar from areas subject to large and small peak electric field as well area with no electric field applied. More recent studies as seen in Figure 1.16 show a difference in the distance between the dislocation lines. A more comprehensive study of this could be conducted within the pulsed DC system using an anode with angles surface to

create a smoothly varying surface field vs location. This could be then used to relate different fields to the appearance and distance between the dislocation lines.

References

- [1] *Compact Linear Collider (CLIC)*, <https://clic.cern/>, Accessed: 2022-12-05.
- [2] M. Aicheler, P. Burrows, M. Draper, *et al.*, *A Multi-TeV Linear Collider Based on CLIC Technology: CLIC Conceptual Design Report* (CERN Yellow Reports: Monographs). Geneva: CERN, 2012. DOI: 10.5170/CERN-2012-007. [Online]. Available: <https://cds.cern.ch/record/1500095>.
- [3] *CERN Accelerator Complex*, <https://www.home.cern/science/accelerators>, Accessed: 2022-12-05.
- [4] A. Grudiev and W. Wuensch, “Design of the CLIC main Linac accelerating structure for CLIC conceptual design report,” 2010. [Online]. Available: <https://cds.cern.ch/record/1346987>.
- [5] A. Palaia, M. Jacewicz, R. Ruber, V. Ziemann, and W. Farabolini, “Effects of rf breakdown on the beam in the Compact Linear Collider prototype accelerator structure,” *Phys. Rev. ST Accel. Beams*, vol. 16, p. 081004, 8 2013. DOI: 10.1103/PhysRevSTAB.16.081004. [Online]. Available: <https://link.aps.org/doi/10.1103/PhysRevSTAB.16.081004>.
- [6] S. Doebert, C. Adolphsen, G. Bowden, *et al.*, “High gradient performance of NLC/GLC X-band accelerating structures,” 2005, pp. 372–374, ISBN: 0-7803-8859-3. DOI: 10.1109/PAC.2005.1590438.

- [7] *The PS Booster*, <https://cerncourier.com/a/the-ps-booster-hits-40/?fbclid=IwAR3fATgf65KMmFVwqPIY2mNLn79fVACxWl8b7-06TDU7Q1XEzK28f8cfY7I>, Accessed: 2022-12-05.
- [8] A. M. Lombardi, “The radio frequency quadrupole (RFQ),” 2006. DOI: 10.5170/CERN-2006-012.201. [Online]. Available: <https://cds.cern.ch/record/1005049>.
- [9] S. Calatroni, “Low-energy H- irradiation of accelerators components: influence of material and material properties on the breakdown resistance at high electric fields,” in *MeVArc meeting*, Tartu, Estonia, 2021. [Online]. Available: <https://indico.cern.ch/event/966437/contributions/4245468/attachments/2203398/3727533/RFQ3%202021.03.08%20-%20final.pdf>.
- [10] S. Ramberger, “Linac4 RFQ issue,” in *RF Development Meeting*, CERN, Switzerland, 2020. [Online]. Available: <https://indico.cern.ch/event/918452/contributions/3860214/attachments/2054608/3448854/Linac4-RFQ-Issues.pdf>.
- [11] K.-C. Kao, *Dielectric phenomena in solids : with emphasis on physical concepts of electronic processes*. San Diego: Elsevier Academic Press, 2004.
- [12] E. Hantzsche, “G. A. Mesyats, D. I. Proskurovsky: “Pulsed Electrical Discharge in Vacuum” Springer-Verlag Berlin, Heidelberg 1989,” *Contributions to Plasma Physics*, vol. 30, no. 5, pp. 586–586, Jan. 1990. DOI: 10.1002/ctpp.2150300505.
- [13] D. Faircloth, “Technological Aspects: High Voltage,” pp. 381–419, 2013, Comments: 39 pages, contribution to the CAS-CERN Accelerator School: Ion Sources, Senec, Slovakia, 29 May - 8 June 2012, edited by R. Bailey,

- CERN-2013-007. DOI: 10.5170/CERN-2013-007.381. arXiv: 1404.0952. [Online]. Available: <https://cds.cern.ch/record/1693330>.
- [14] H. Timko, “Modelling vacuum arcs : from plasma initiation to surface interactions,” 2011. [Online]. Available: <https://helda.helsinki.fi/items/b10462f2-a7dd-4501-b9e6-4157b512d98d>.
- [15] F. Djurabekova, S. Parviainen, A. Pohjonen, and K. Nordlund, “Atomistic modeling of metal surfaces under electric fields: Direct coupling of electric fields to a molecular dynamics algorithm,” *Physical review. E, Statistical, nonlinear, and soft matter physics*, vol. 83, p. 026 704, 2011. DOI: 10.1103/PhysRevE.83.026704.
- [16] A. S. Pohjonen, F. Djurabekova, K. Nordlund, A. Kuronen, and S. P. Fitzgerald, “Dislocation nucleation from near surface void under static tensile stress in cu,” *Journal of Applied Physics*, vol. 110, no. 2, p. 023 509, 2011. DOI: 10.1063/1.3606582. eprint: <https://doi.org/10.1063/1.3606582>. [Online]. Available: <https://doi.org/10.1063/1.3606582>.
- [17] A. Descoedres, F. Djurabekova, and K. Nordlund, “DC breakdown experiments with cobalt electrodes,” CERN, Geneva, Tech. Rep., 2009. DOI: 10.17181/CLIC-Note-875. [Online]. Available: <https://cds.cern.ch/record/1355401>.
- [18] A. Descoedres, T. Ramsvik, S. Calatroni, M. Taborelli, and W. Wuensch, “Dc breakdown conditioning and breakdown rate of metals and metallic alloys under ultrahigh vacuum,” *Phys. Rev. ST Accel. Beams*, vol. 12, p. 032 001, 3 2009. DOI: 10.1103/PhysRevSTAB.12.032001. [Online]. Available: <https://link.aps.org/doi/10.1103/PhysRevSTAB.12.032001>.

- [19] H. Timko, M. Aicheler, P. Alknes, *et al.*, “Energy dependence of processing and breakdown properties of cu and mo,” *Phys. Rev. ST Accel. Beams*, vol. 14, p. 101003, 10 2011. DOI: 10.1103/PhysRevSTAB.14.101003. [Online]. Available: <https://link.aps.org/doi/10.1103/PhysRevSTAB.14.101003>.
- [20] W. Wuensch, A. Degiovanni, S. Calatroni, *et al.*, “Statistics of vacuum breakdown in the high-gradient and low rate regime,” English, *Physical Review Special Topics - Accelerators and Beams*, vol. 20, no. 1, 2017, ISSN: 1098-4402. DOI: 10.1103/PhysRevAccelBeams.20.011007.
- [21] E. Engelberg, J. Paszkiewicz, R. Peacock, S. Lachmann, Y. Ashkenazy, and W. Wuensch, “Dark current spikes as an indicator of mobile dislocation dynamics under intense dc electric fields,” *Physical Review Accelerators and Beams*, vol. 23, 2020. DOI: 10.1103/PhysRevAccelBeams.23.123501.
- [22] E. Z. Engelberg, Y. Ashkenazy, and M. Assaf, “Stochastic model of breakdown nucleation under intense electric fields,” *Physical Review Letters*, vol. 120, no. 12, p. 124801, 2018. DOI: 10.1103/PhysRevLett.120.124801.
- [23] E. L. Murphy and R. H. Good, “Thermionic emission, field emission, and the transition region,” *Phys. Rev.*, vol. 102, pp. 1464–1473, 6 1956. DOI: 10.1103/PhysRev.102.1464. [Online]. Available: <https://link.aps.org/doi/10.1103/PhysRev.102.1464>.
- [24] J. Holzl and F. K. Schulte, “Work function of metals,” in *Solid Surface Physics*, J. Holzl, F. K. Schulte, and H. Wagner, Eds. Berlin, Heidelberg: Springer Berlin Heidelberg, 1979, pp. 1–150, ISBN: 978-3-540-35253-2. DOI: 10.1007/BFb0048919. [Online]. Available: <https://doi.org/10.1007/BFb0048919>.

- [25] M. Green, *Solid State Surface Science* (Solid State Surface Science v. 1). M. Dekker, 1969. [Online]. Available: <https://books.google.ch/books?id=yRS2AAAAIAAJ>.
- [26] H. B. Michaelson, “The work function of the elements and its periodicity,” *Journal of Applied Physics*, vol. 48, no. 11, pp. 4729–4733, 1977. DOI: 10.1063/1.323539. eprint: <https://doi.org/10.1063/1.323539>. [Online]. Available: <https://doi.org/10.1063/1.323539>.
- [27] R. H. Fowler and L. Nordheim, “Electron emission in intense electric fields,” *Proceedings of the Royal Society of London. Series A, Containing Papers of a Mathematical and Physical Character*, vol. 119, no. 781, pp. 173–181, 1928, ISSN: 09501207. [Online]. Available: <http://www.jstor.org/stable/95023> (visited on 12/07/2022).
- [28] H. Padamsee, T. Hays, and J. Knobloch, *RF superconductivity for accelerators* (Wiley series in beam physics and accelerator technology). New York, NY: Wiley, 1998. [Online]. Available: <https://cds.cern.ch/record/366783>.
- [29] R. G. Forbes, “Comments on the continuing widespread and unnecessary use of a defective emission equation in field emission related literature,” *Journal of Applied Physics*, vol. 126, no. 21, p. 210901, 2019. DOI: 10.1063/1.5117289. eprint: <https://doi.org/10.1063/1.5117289>. [Online]. Available: <https://doi.org/10.1063/1.5117289>.
- [30] R. H. Fowler and L. Nordheim, “Electron emission in intense electric fields,” *Proceedings of the Royal Society of London. Series A, Containing Papers of a Mathematical and Physical Character*, vol. 119, no. 781, pp. 173–181, 1928, ISSN: 09501207. [Online]. Available: <http://www.jstor.org/stable/95023> (visited on 12/06/2022).

- [31] J. W. Wang and G. A. Loew, “Field emission and RF breakdown in high gradient room temperature linac structures,” in *Joint CERN-US-Japan Accelerator School: Course on Frontiers of Accelerator Technology: RF Engineering for Particle Accelerators*, 1997, pp. 768–794.
- [32] A. Kyritsakis, M. Veske, K. Eimre, V. Zadin, and F. Djurabekova, “Thermal runaway of metal nano-tips during intense electron emission,” *Journal of Physics D: Applied Physics*, vol. 51, no. 22, p. 225 203, 2018. DOI: 10.1088/1361-6463/aac03b. [Online]. Available: <https://dx.doi.org/10.1088/1361-6463/aac03b>.
- [33] C. D. Child, “Discharge from hot cao,” *Phys. Rev. (Series I)*, vol. 32, pp. 492–511, 5 May 1911. DOI: 10.1103/PhysRevSeriesI.32.492. [Online]. Available: <https://link.aps.org/doi/10.1103/PhysRevSeriesI.32.492>.
- [34] Y. Y. Lau, “Simple theory for the two-dimensional child-langmuir law.,” *Physical review letters*, vol. 87 27 Pt 1, p. 278 301, 2001.
- [35] V. Jansson, E. Baibuz, A. Kyritsakis, *et al.*, “Growth mechanism for nanotips in high electric fields,” *Nanotechnology*, vol. 31, no. 35, p. 355 301, Jun. 2020. DOI: 10.1088/1361-6528/ab9327. [Online]. Available: <https://dx.doi.org/10.1088/1361-6528/ab9327>.
- [36] W. Wuensch, “Advances in the Understanding of the Physical Processes of Vacuum Breakdown,” 2014. DOI: 10.1142/9789814602105_0003. [Online]. Available: <https://cds.cern.ch/record/1694664>.
- [37] E. M. Bringa, S. Traiviratana, and M. A. Meyers, “Void initiation in fcc metals: Effect of loading orientation and nanocrystalline effects,” *Acta Materialia*, vol. 58, pp. 4458–4477, 2010.

- [38] G. Schneider, G. Denbeaux, E. H. Anderson, *et al.*, “Dynamical x-ray microscopy investigation of electromigration in passivated inlaid cu interconnect structures,” *Applied Physics Letters*, vol. 81, no. 14, pp. 2535–2537, 2002. DOI: 10.1063/1.1509465. eprint: <https://doi.org/10.1063/1.1509465>. [Online]. Available: <https://doi.org/10.1063/1.1509465>.
- [39] Y. Ashkenazy, A. Yasha, O. Cohen, and I. Popov, “Observations of dislocations in Soft Cu samples exposed to high fields,” in *MeVArc2022*, Chania, Crete, 2022. [Online]. Available: https://indico.cern.ch/event/1099613/contributions/4969676/attachments/2510462/4316091/ashkenazy_mevarc2022v4.pdf.
- [40] J. Polák, V. Mazánová, M. Heczko, I. Kuběna, and J. Man, “Profiles of persistent slip markings and internal structure of underlying persistent slip bands,” *Fatigue & Fracture of Engineering Materials & Structures*, vol. 40, no. 7, pp. 1101–1116, 2017. DOI: <https://doi.org/10.1111/ffe.12567>. eprint: <https://onlinelibrary.wiley.com/doi/pdf/10.1111/ffe.12567>. [Online]. Available: <https://onlinelibrary.wiley.com/doi/abs/10.1111/ffe.12567>.
- [41] J. D. Jackson, *Classical Electrodynamics*. Wiley, 1998, ISBN: 978-0-471-30932-1.
- [42] J. Paszkiewicz, “Studies of Breakdown and Pre-Breakdown Phenomena in High Gradient Accelerating Structures,” Presented 27 Aug 2020, 2020. [Online]. Available: <https://cds.cern.ch/record/2749494>.
- [43] E. Z. Engelberg, A. B. Yashar, Y. Ashkenazy, M. Assaf, and I. Popov, “Theory of electric field breakdown nucleation due to mobile dislocations,” *Phys. Rev. Accel. Beams*, vol. 22, p. 083501, 8 Aug. 2019. DOI: 10.1103/

- PhysRevAccelBeams.22.083501. [Online]. Available: <https://link.aps.org/doi/10.1103/PhysRevAccelBeams.22.083501>.
- [44] J. Kovermann, “Comparative studies of high-gradient RF and DC breakdowns,” Ph.D. dissertation, 2010.
- [45] V. L. Ginzburg and I. M. Frank, “Radiation of a uniformly moving electron due to its transition from one medium into another,” *J. Phys. (USSR)*, vol. 9, pp. 353–362, 1945.
- [46] P. Jain, “On blackbody radiation,” *Physics Education (IoP, UK)*, vol. 26, pp. 190–194, May 1991. DOI: 10.1088/0031-9120/26/3/011.
- [47] T. Abe, T. Kageyama, H. Sakai, Y. Takeuchi, and K. Yoshino, “Direct observation of breakdown trigger seeds in a normal-conducting rf accelerating cavity,” *Phys. Rev. Accel. Beams*, vol. 21, p. 122002, 12 Dec. 2018. DOI: 10.1103/PhysRevAccelBeams.21.122002. [Online]. Available: <https://link.aps.org/doi/10.1103/PhysRevAccelBeams.21.122002>.
- [48] J. I. Goldstein, D. E. Newbury, J. R. Michael, N. W. M. Ritchie, J. H. J. Scott, and D. C. Joy, “Cathodoluminescence,” in *Scanning Electron Microscopy and X-Ray Microanalysis*. New York, NY: Springer New York, 2018, pp. 481–489, ISBN: 978-1-4939-6676-9. DOI: 10.1007/978-1-4939-6676-9_28. [Online]. Available: https://doi.org/10.1007/978-1-4939-6676-9_28.
- [49] S. Kaya, “Photo-thermal control of surface plasmon mode propagation at telecom wavelengths,” Ph.D. dissertation, Oct. 2016.
- [50] E. J. Vesseur, J. Aizpurua, T. Coenen, A. Reyes-Coronado, P. Batson, and A. Polman, “Plasmonic excitation and manipulation with an electron beam,” *MRS Bulletin*, vol. 37, Aug. 2012. DOI: 10.1557/mrs.2012.174.

- [51] M. Gonçalves, H. Minassian, and A. Melikyan, “Plasmonic resonators: Fundamental properties and applications,” *Journal of Physics D: Applied Physics*, vol. 53, May 2020. DOI: 10.1088/1361-6463/ab96e9.
- [52] J. Scaiano, K. Stampelcoskie, and G. Hallett-Tapley, “Photochemical norrish type i reaction as a tool for metal nanoparticle synthesis: Importance of proton coupled electron transfer,” *Chemical communications (Cambridge, England)*, vol. 48, pp. 4798–808, Apr. 2012. DOI: 10.1039/c2cc30615h.
- [53] N. Catalán Lasheras, T. Argyropoulos, D. Esperante Pereira, *et al.*, “Commissioning of XBox-3: A very high capacity X-band test stand,” TUPLR047, 2017. DOI: 10.18429/JACoW-LINAC2016-TUPLR047. [Online]. Available: <http://cds.cern.ch/record/2304526>.
- [54] V. A. Dolgashev, L. Faillace, B. Spataro, S. Tantawi, and R. Bonifazi, “High-gradient rf tests of welded X-band accelerating cavities,” *Phys. Rev. Accel. Beams*, vol. 24, p. 081002, 8 Aug. 2021. DOI: 10.1103/PhysRevAccelBeams.24.081002. [Online]. Available: <https://link.aps.org/doi/10.1103/PhysRevAccelBeams.24.081002>.
- [55] S. Matsumoto, M. Akemoto, S. Fukuda, *et al.*, “Nextef: The 100MW X-band Test Facility in KEK,” *Conf. Proc. C*, vol. 0806233, I. Andrian and C. Petit-Jean-Genaz, Eds., WEPP096, 2008.
- [56] A. Saressalo, I. Profatilova, A. Kyritsakis, *et al.*, “Classification of vacuum arc breakdowns in a pulsed DC system,” *Phys. Rev. Accel. Beams*, vol. 23, no. 2, p. 023101, 2020. DOI: 10.1103/PhysRevAccelBeams.23.023101. arXiv: 1911.05192 [physics.ins-det].
- [57] M. Jacewicz, J. Eriksson, R. Ruber, S. Calatroni, I. Profatilova, and W. Wuensch, “Temperature-dependent field emission and breakdown measurements using a pulsed high-voltage cryosystem,” *Phys. Rev. Appl.*,

- vol. 14, p. 061002, 6 Dec. 2020. DOI: 10.1103/PhysRevApplied.14.061002. [Online]. Available: <https://link.aps.org/doi/10.1103/PhysRevApplied.14.061002>.
- [58] K. Nordlund and F. Djurabekova, “Defect model for the dependence of breakdown rate on external electric fields,” *Phys. Rev. ST Accel. Beams*, vol. 15, p. 071002, 7 Jul. 2012. DOI: 10.1103/PhysRevSTAB.15.071002. [Online]. Available: <https://link.aps.org/doi/10.1103/PhysRevSTAB.15.071002>.
- [59] M. Veske, A. Kyritsakis, F. Djurabekova, K. N. Sjobak, A. Aabloo, and V. Zadin, “Dynamic coupling between particle-in-cell and atomistic simulations,” *Phys. Rev. E*, vol. 101, p. 053307, 5 May 2020. DOI: 10.1103/PhysRevE.101.053307. [Online]. Available: <https://link.aps.org/doi/10.1103/PhysRevE.101.053307>.
- [60] I. Profatilova, “Recent progress at pulsed DC systems,” in *8th International Workshop on Mechanisms of Vacuum Arcs (MeVArc 2019)*, Padova, Italy, 2019.
- [61] A. Saressalo, I. Profatilova, W. L. Millar, *et al.*, “Effect of dc voltage pulsing on high-vacuum electrical breakdowns near cu surfaces,” *Phys. Rev. Accel. Beams*, vol. 23, p. 113101, 11 Nov. 2020. DOI: 10.1103/PhysRevAccelBeams.23.113101. [Online]. Available: <https://link.aps.org/doi/10.1103/PhysRevAccelBeams.23.113101>.
- [62] A. Lopez-Cazalilla, F. Djurabekova, F. Granberg, *et al.*, “Punching of arbitrary face prismatic loops from hydrogen nanobubbles in copper,” *Acta Mater.*, vol. 225, p. 117554, 2022. DOI: 10.1016/j.actamat.2021.117554. [Online]. Available: <http://cds.cern.ch/record/2852709>.

- [63] A. Grudiev, S. Calatroni, and W. Wuensch, “New local field quantity describing the high gradient limit of accelerating structures,” *Physical Review Special Topics - Accelerators and Beams*, vol. 12, no. 102001, 2009. DOI: 10.1103/PhysRevSTAB.12.102001.
- [64] S. Doebert, C. Adolphsen, G. Bowden, *et al.*, “High gradient performance of nlc/glc x-band accelerating structures,” Jun. 2005, pp. 372–374, ISBN: 0-7803-8859-3. DOI: 10.1109/PAC.2005.1590438.
- [65] W. L. Millar *et al.*, “High-Power Test of Two Prototype X-Band Accelerating Structures Based on SwissFEL Fabrication Technology,” *IEEE Trans. Nucl. Sci.*, vol. 70, no. 1, pp. 1–19, 2023. DOI: 10.1109/TNS.2022.3230567.
- [66] I. Profatilova, N.-M. Pienimaki, X. Stragier, *et al.*, “News from Pulsed DC System at CERN,” in *MeVArc2017*, Jerusalem, Israel, 2017. [Online]. Available: https://indico.cern.ch/event/521667/contributions/2409294/attachments/1430075/2488849/2017_03_20_Profatilova_MEVARC2017.pdf.
- [67] A. Vnuchenko, D. Esperante Pereira, B. Gimeno Martinez, *et al.*, “High-gradient testing of an S-band, normal-conducting low phase velocity accelerating structure,” *Phys. Rev. Accel. Beams*, vol. 23, p. 084801, 8 Aug. 2020. DOI: 10.1103/PhysRevAccelBeams.23.084801. [Online]. Available: <https://link.aps.org/doi/10.1103/PhysRevAccelBeams.23.084801>.
- [68] N. Shipman, “Experimental Study of DC Vacuum Breakdown and Application to High-Gradient Accelerating Structures for CLIC,” Ph.D. dissertation, 2014.
- [69] I. Profatilova, X. Stragier, S. Calatroni, A. Kandratsyev, E. R. Castro, and W. Wuensch, “Breakdown localisation in a pulsed dc electrode system,” *Nuclear Instruments and Methods in Physics Research Section A*:

- Accelerators, Spectrometers, Detectors and Associated Equipment*, vol. 953, p. 163 079, 2020, ISSN: 0168-9002. DOI: <https://doi.org/10.1016/j.nima.2019.163079>. [Online]. Available: <https://www.sciencedirect.com/science/article/pii/S0168900219314238>.
- [70] M. Barnes, L. Redondo, A. Kandratsyev, and T. Fowler, “Marx prototype pulse generator design and initial results,” in *FCC Week 2018*, Amsterdam, Netherlands, 2018. [Online]. Available: https://indico.cern.ch/event/656491/contributions/2947267/attachments/1628338/2600446/Barnes_FCC_Marx_generators_InjectionKickers.pdf.
- [71] *Pfeiffer Vacuum: HiCube 80 Classic*, <https://www.pfeiffer-vacuum.com/en/products/vacuum-generation/pumping-stations/turbo-pumping-stations/hicube-classic/16385/hicube-80-classic>, Accessed: 2023-01-15.
- [72] B. Woolley, “High power x-band rf test stand development and high power testing of the clic crab cavity,” English, Ph.D. dissertation, Lancaster University, 2015.
- [73] *National Instruments LabVIEW*, <https://www.ni.com/en-us/shop/labview.html>, Accessed: 2022-11-21.
- [74] A. V. Edwards, “X-Band LLRF Developments for High Power CLIC Test Stands and Waveguide Interferometry for Phase Stabilisation,” Presented 10 Jun 2022, 2022. [Online]. Available: <https://cds.cern.ch/record/2843363>.
- [75] A. Degiovanni, W. Wuensch, and J. Giner Navarro, “Comparison of the conditioning of high gradient accelerating structures,” *Phys. Rev. Accel. Beams*, vol. 19, p. 032 001, 3 2016. DOI: [10.1103/PhysRevAccelBeams.19.032001](https://doi.org/10.1103/PhysRevAccelBeams.19.032001).

- 19.032001. [Online]. Available: <https://link.aps.org/doi/10.1103/PhysRevAccelBeams.19.032001>.
- [76] W. Wuensch, A. Degiovanni, S. Calatroni, *et al.*, “Statistics of vacuum breakdown in the high-gradient and low-rate regime,” *Phys. Rev. Accel. Beams*, vol. 20, p. 011007, 1 2017. DOI: 10.1103/PhysRevAccelBeams.20.011007. [Online]. Available: <https://link.aps.org/doi/10.1103/PhysRevAccelBeams.20.011007>.
- [77] R. R. Anders Korsback Jorge Giner Navaro and W. Wuensch, “Statistics of breakdown and conditioning in pulsed dc and rf systems,” in *Mini MeVArc meeting*, 2016. [Online]. Available: https://indico.cern.ch/event/464716/contributions/1983092/attachments/1246167/1835392/breakdown_statistics_and_conditioning.pdf.
- [78] V. Zadin, private communication.
- [79] R. Levien, “The euler spiral: A mathematical history,” 2012.
- [80] S. Calatroni, private communication.
- [81] E. R. Castro, private communication.
- [82] I. Profatilova, private communication.
- [83] E. R. Castro and I. Profatilova, “Observation Report of electrodes nr 17 and nr 19 from DC system,” in *Pulsed-dc electrode SEM analysis, TD26 conditioning progress*, 2017. [Online]. Available: https://indico.cern.ch/event/527311/contributions/2383899/attachments/1401438/2139033/EDMS-1724346_Observation_report_of_LES_nr_17_and_nr_19_ERC.pdf.

- [84] G. V. Samsonov, *Handbook of the Physicochemical Properties of the Elements*, G. V. Samsonov, Ed. Boston, MA: Springer US, 1968, ISBN: 978-1-4684-6066-7. DOI: 10.1007/978-1-4684-6066-7_1. [Online]. Available: https://doi.org/10.1007/978-1-4684-6066-7_1.
- [85] L. P. Jeurgens, W. G. Sloof, F. Tichelaar, and E. Mittemeijer, “Structure and morphology of aluminium-oxide films formed by thermal oxidation of aluminium,” *Thin Solid Films*, vol. 418, pp. 89–101, Aug. 2002.
- [86] K. Scibor, “Machining of electrodes for L4-RFQ3 DC tests,” in *56th meeting: RF design and fabrication of RFQ3*, 2022. [Online]. Available: <https://indico.cern.ch/event/1119220/>.
- [87] C. Serafim, private communication.
- [88] A. Grudiev, S. Calatroni, and W. Wuensch, “New local field quantity describing the high gradient limit of accelerating structures,” *Phys. Rev. ST Accel. Beams*, vol. 12, p. 102001, 10 2009. DOI: 10.1103/PhysRevSTAB.12.102001. [Online]. Available: <https://link.aps.org/doi/10.1103/PhysRevSTAB.12.102001>.
- [89] C. Serafim *et al.*, “Microscopy investigation on different materials after pulsed high field conditioning and low energy H- irradiation,” Chania, Greece, 2022. [Online]. Available: <https://indico.cern.ch/event/1099613/contributions/4969667/attachments/2511662/>.
- [90] M. S. Bieniek and M. I. Hasan, “Modeling of dc micro-glow discharges in atmospheric pressure helium self-organizing on cathodes,” *Physics of Plasmas*, vol. 29, no. 3, p. 034503, 2022. DOI: 10.1063/5.0078236. eprint: <https://doi.org/10.1063/5.0078236>. [Online]. Available: <https://doi.org/10.1063/5.0078236>.

- [91] C. Rossi *et al.*, “LINAC 4 RFQ DESIGN, CONSTRUCTION, COMMISSIONING, AND OPERATION,” in *Linac 4 Spare RFQ Working Group Meeting*, Geneva, Switzerland, 2018. [Online]. Available: https://indico.cern.ch/event/754020/contributions/3123638/attachments/1713693/2763818/L4SpareRFQ_C_Rossi_11092018.pdf.
- [92] V. Bencini, G. Bellodi, and A. Lombardi, *Simulations of beam losses in Linac4 RFQ*, EDMS, Geneva, Switzerland, 2021. [Online]. Available: [https://edms.cern.ch/ui/file/2616165/0.1/Linac4_RFQ_losses_analysis_\(2\).pdf](https://edms.cern.ch/ui/file/2616165/0.1/Linac4_RFQ_losses_analysis_(2).pdf).
- [93] A. Lombardi, private communication.
- [94] C. S. Ana Teresa Pérez Fontenla, “FIB analysis,” Geneva, Switzerland, 2022. [Online]. Available: <https://indico.cern.ch/event/1173622/contributions/4929225/attachments/2468055/4233107/fib-cu-sample.pdf>.
- [95] A. T. P. Fontenla, “CuCr1Zr cathode inspection after irradiation at CERN,” Geneva, Switzerland, 2021. [Online]. Available: <https://indico.cern.ch/event/1005592/contributions/4221667/attachments/2188671>.
- [96] A. T. P. Fontenla, “Microscopy investigation of the surface behaviour of different materials after H- irradiation in different conditions,” in *MeV Arc meeting*, Tartu, Estonia, 2021.
- [97] W. D. Newhauser and R. Zhang, “The physics of proton therapy,” *Physics in Medicine & Biology*, vol. 60, no. 8, R155, 2015. DOI: 10.1088/0031-9155/60/8/R155. [Online]. Available: <https://dx.doi.org/10.1088/0031-9155/60/8/R155>.

- [98] *Stopping Power and Range Tables for Electrons*, https://physics.nist.gov/cgi-bin/Star/e_table.pl, Accessed: 2023-01-21.
- [99] P. Hammond, *Electromagnetism for Engineers: An Introductory Course* (Applied electricity and electronics). Elsevier Science, 2013, ISBN: 9781483149783. [Online]. Available: <https://books.google.ch/books?id=-8QgBQAAQBAJ>.
- [100] A. Maitland, “New derivation of the vacuum breakdown equation relating breakdown voltage and electrode separation,” *Journal of Applied Physics*, vol. 32, no. 11, pp. 2399–2407, 1961. DOI: 10.1063/1.1777081. eprint: <https://doi.org/10.1063/1.1777081>. [Online]. Available: <https://doi.org/10.1063/1.1777081>.
- [101] A. Kojima, “Development of the design technique with empirical scaling of vacuum insulation for electrostatic accelerators with large surface area and locally concentrated electric field for fusion application,” in *8th International Workshop on Mechanisms of Vacuum Arcs (MeVArc 2019)*, Padova, Italy, 2019. [Online]. Available: https://indico.cern.ch/event/774138/contributions/3570712/attachments/1911934/3159570/6.5_MeVArc2019_Oral_Kojima_r0.pdf.
- [102] A. Grudiev, “WP 10: RFQ3 design Introduction,” in *1st WP10 - RFQ3 Design Meeting*, 2020. [Online]. Available: https://indico.cern.ch/event/925403/contributions/3889048/attachments/2050505/3436872/20200604_WP_RFQ3_design_Introduction.pdf.
- [103] L. Millar, “Operation of Multiple Accelerating Structures in an X-Band High-Gradient Test Stand,” Presented 22 Jul 2021, 2021. [Online]. Available: <https://cds.cern.ch/record/2798232>.
- [104] C. D. P. Serafim, G. Bellodi, S. Calatroni, *et al.*, “Microscopy Investigation on Different Materials After Pulsed High Field Conditioning and Low En-

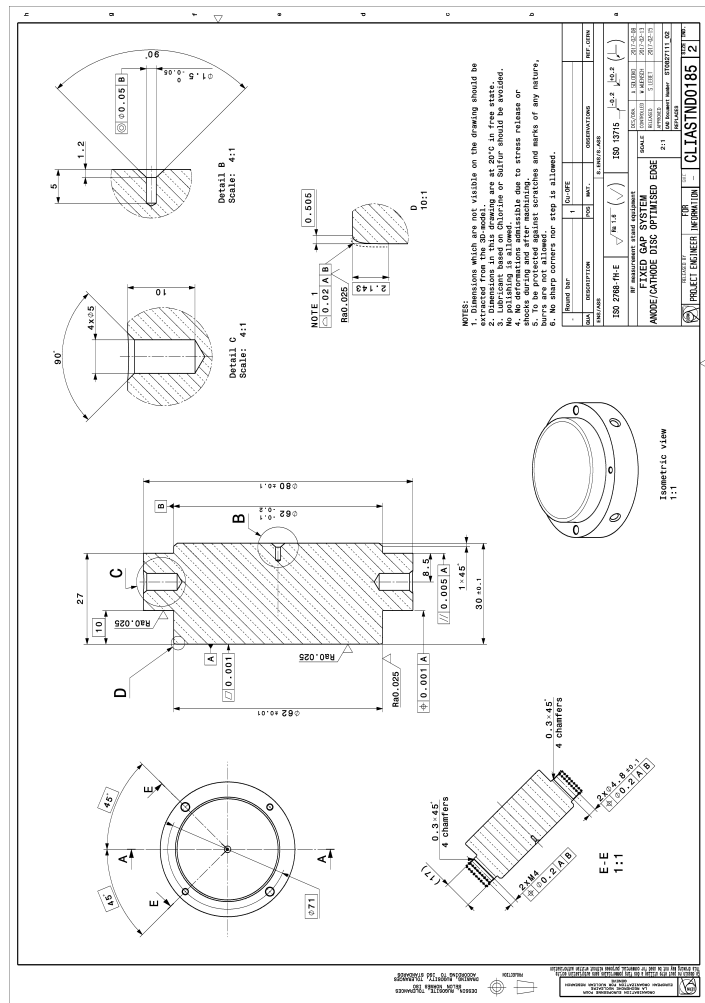
- ergy H-Irradiation,” in *Proc. LINAC'22*, (Liverpool, UK), ser. International Linear Accelerator Conference, JACoW Publishing, Geneva, Switzerland, 2022, TUPOPA06, pp. 422–425, ISBN: 978-3-95450-215-8. DOI: 10.18429/JACoW-LINAC2022-TUPOPA06. [Online]. Available: <https://jacow.org/linac2022/papers/tupopa06.pdf>.
- [105] A. Grudiev, “RFQ3 R&D,” in *RFQ3 Review*, 2022. [Online]. Available: <https://indico.cern.ch/event/1140512%7D>.
- [106] S. Lachmann, M. Jacewicz, I. Profatilova, J. Paszkiewicz, W. Wuensch, and Y. Ashkenazy, “Statistical analysis of field-emission currents,” *Phys. Rev. Applied*, vol. 16, p. 024007, 2 2021. DOI: 10.1103/PhysRevApplied.16.024007. [Online]. Available: <https://link.aps.org/doi/10.1103/PhysRevApplied.16.024007>.
- [107] W. P. Dyke, J. K. Trolan, E. E. Martin, and J. P. Barbour, “The field emission initiated vacuum arc. i. experiments on arc initiation,” *Phys. Rev.*, vol. 91, pp. 1043–1054, 5 Sep. 1953. DOI: 10.1103/PhysRev.91.1043. [Online]. Available: <https://link.aps.org/doi/10.1103/PhysRev.91.1043>.
- [108] R. Loudon, *The Quantum Theory of Light*. OUP Oxford, 2000, ISBN: 9780191589782. [Online]. Available: <https://books.google.ch/books?id=AEkfajgqldoC>.
- [109] A. Aleinik, O. Chefonov, B. Kalinin, *et al.*, “Low-energy electron-beam diagnostics based on the optical transition radiation,” *Nuclear Instruments and Methods in Physics Research Section B: Beam Interactions with Materials and Atoms*, vol. 201, no. 1, pp. 34–43, 2003. DOI: 10.1016/S0168-583x(02)01745-7.

- [110] W. Wuensch, “A possible mechanism for enhanced field emission,” in *8th International Workshop on Mechanisms of Vacuum Arcs (MeVArc 2019)*, Padova, Italy, 2019. [Online]. Available: https://indico.cern.ch/event/774138/contributions/3507919/attachments/1907968/3151683/field_emission_2019_final.pdf.
- [111] M. Klyan, V. Kritskii, Y. Kulyupin, Y. Kucherenko, K. Pilipchak, and S. Pop, “Electron bombardment induced photon emission from copper,” *Nuclear Instruments and Methods in Physics Research Section B: Beam Interactions with Materials and Atoms*, vol. 59, no. 3, pp. 653–657, 1984. [Online]. Available: http://inis.iaea.org/search/search.aspx?orig_q=RN:16055523.
- [112] *UV-Visible Optical Fiber*, <https://www.oceaninsight.com/products/fibers-and-probes/fibers/patch-cords/uv-vis-fibers/>, Accessed: 2020-07-09.
- [113] *Visible-NIR Optical Fiber*, <https://www.oceaninsight.com/products/fibers-and-probes/fibers/patch-cords/vis-nir-fibers/>, Accessed: 2020-07-09.
- [114] M. Burkowski, private communication.
- [115] J. Paszkiewicz, private communication.
- [116] E. Engelberg, Y. Ashkenazy, I. Popov, A. Yashar, and M. Assaf, “Theory of Electric Field Breakdown Nucleation: Mobile Dislocation Population Dynamics and Atomic Simulations,” in *8th International Workshop on Mechanisms of Vacuum Arcs (MeVArc 2019)*, 2019. [Online]. Available: <https://indico.cern.ch/event/774138/contributions/3507896/attachments/1911925/3159556/main.pdf>.
- [117] E. Z. Engelberg, private communication.

- [118] Y. Ashkenazy, private communication.
- [119] G. Bellodi, “Linac4 RFQ loss simulations,” in *14th meeting: Status of testing, materials and fabrication, news from WP11*, 2020. [Online]. Available: https://indico.cern.ch/event/969561/contributions/4080703/attachments/2133205/3592593/irradiation_test1.pdf.
- [120] A. Grudiev, “Irradiation dose summary,” in *16th meeting: DC testing, electrode fabrication, irradiation news*, 2020. [Online]. Available: <https://indico.cern.ch/event/978225/contributions/4120331/attachments/2150771/>.

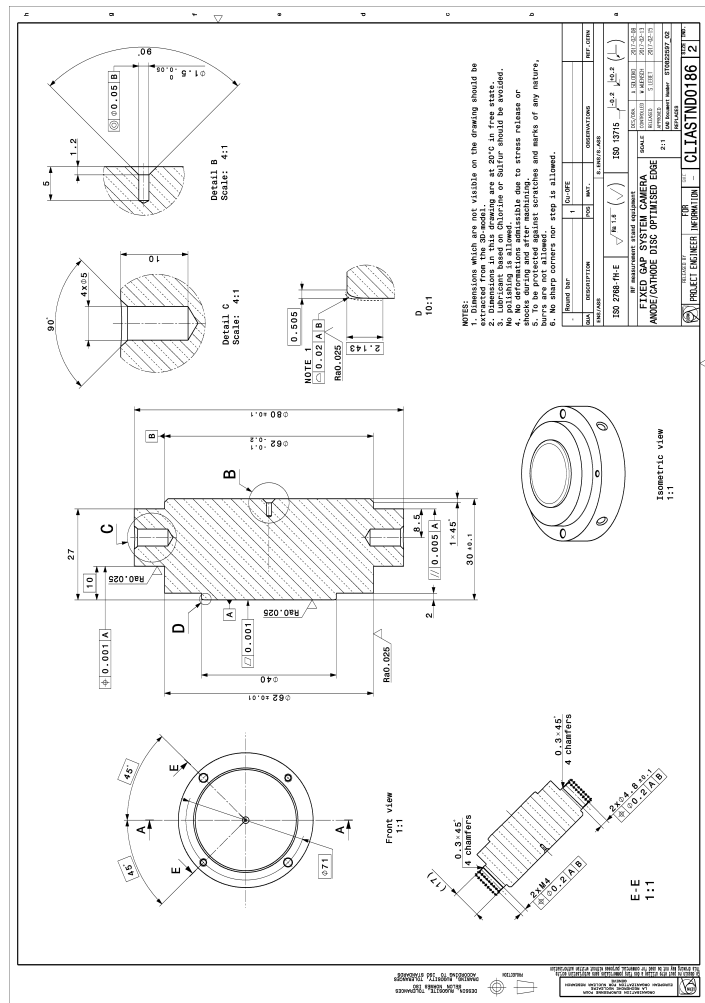
Appendix A

CLIASTND0185



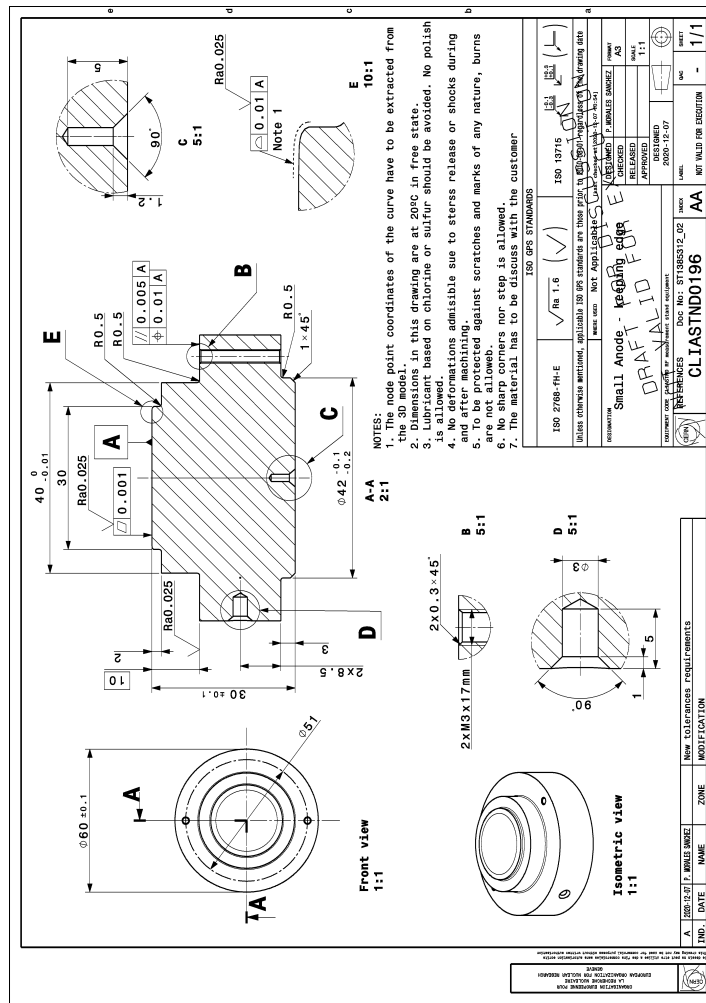
Appendix B

CLIASTND0186



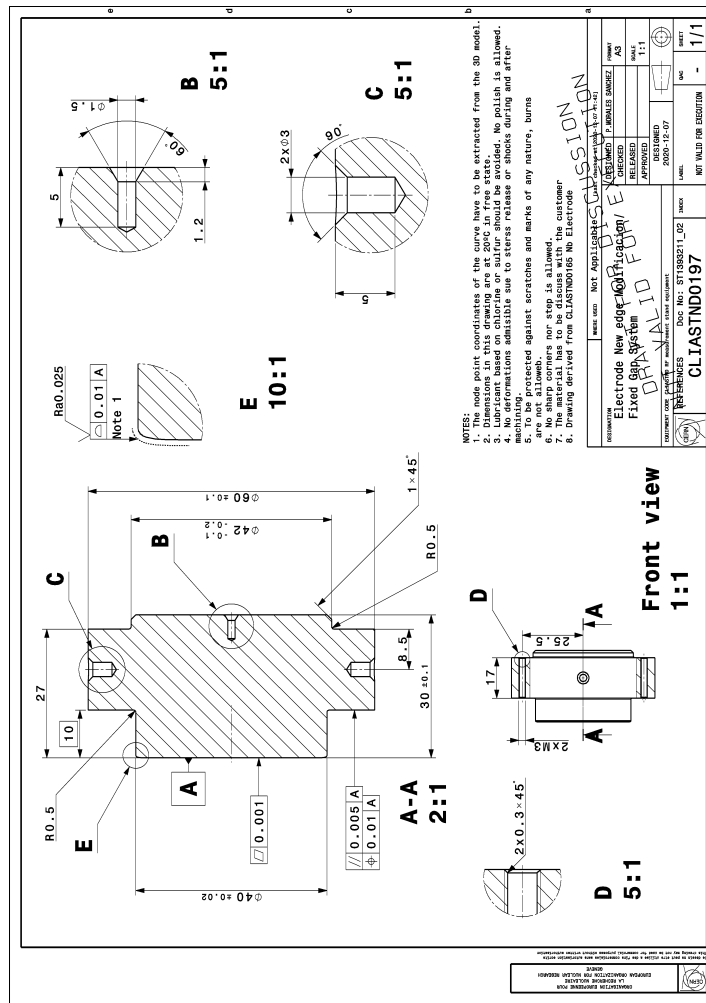
Appendix C

CLIASTND0196



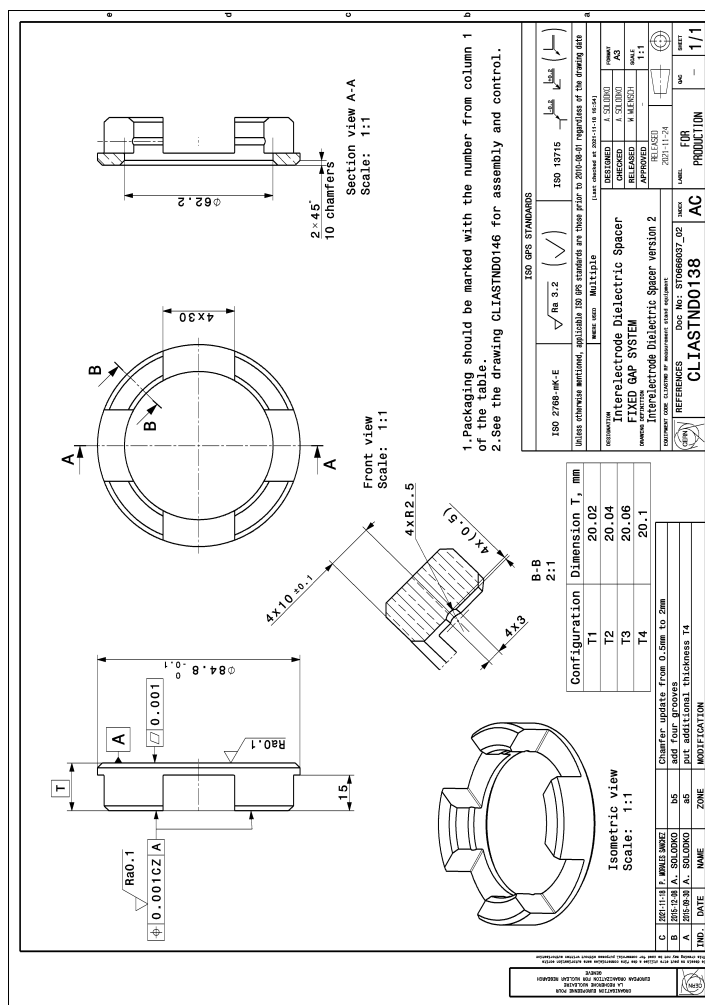
Appendix D

CLIASTND097



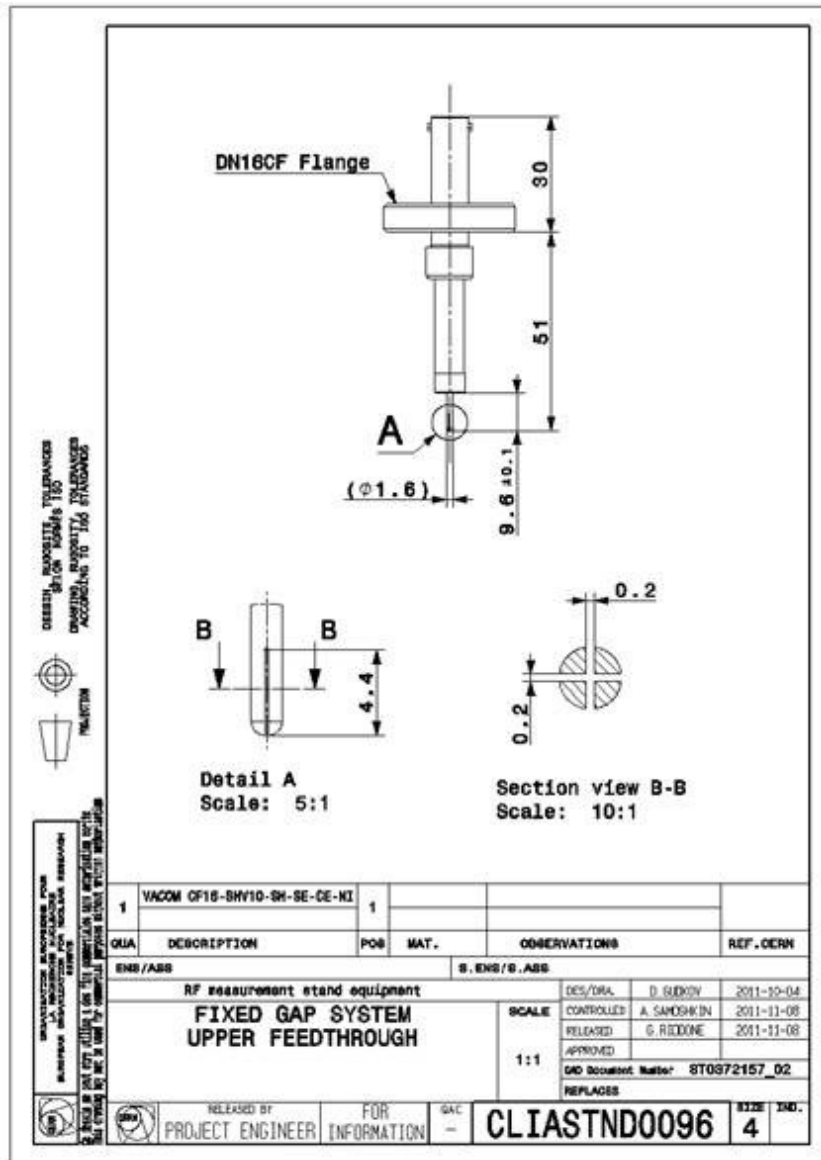
Appendix F

CLIASTND0138



Appendix G

Upper feed-through



Appendix H

Copper OFE Tests

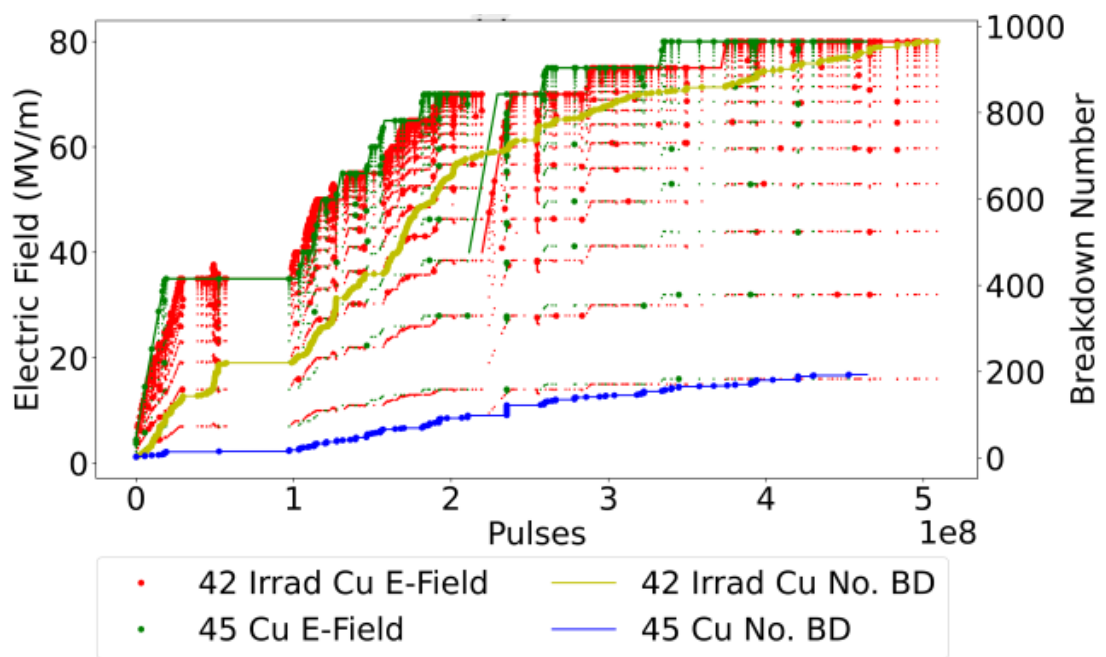


Figure H.1: Conditioning plots of both Irradiated and non-irradiated Copper OFE, showing the electric field and number of breakdowns on the respective axes.

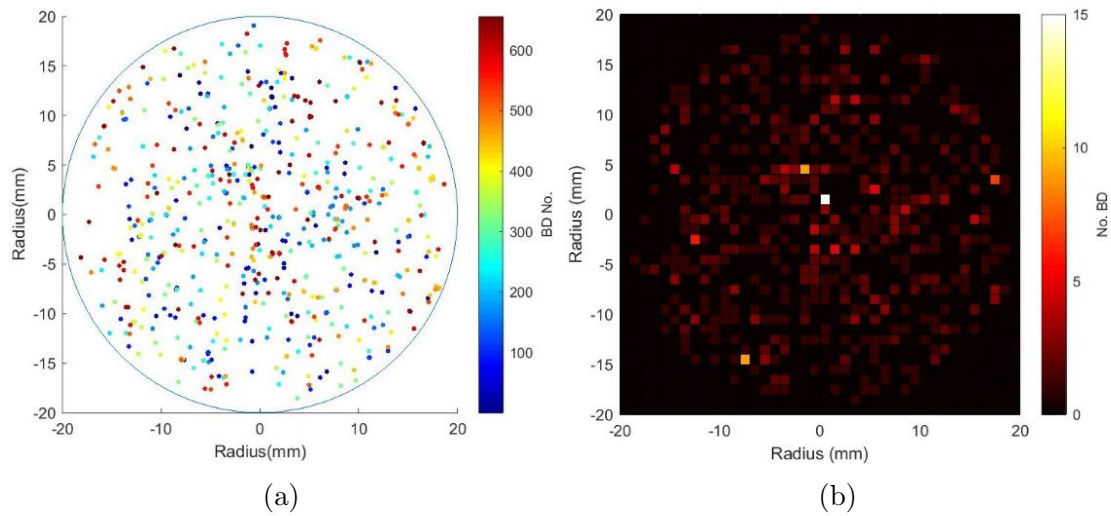


Figure H.2: Breakdown locations measured during testing of electrode pair 40. a) shows the breakdown locations over time relative to the scale to the right of the image, b) shows the number of breakdowns per square mm

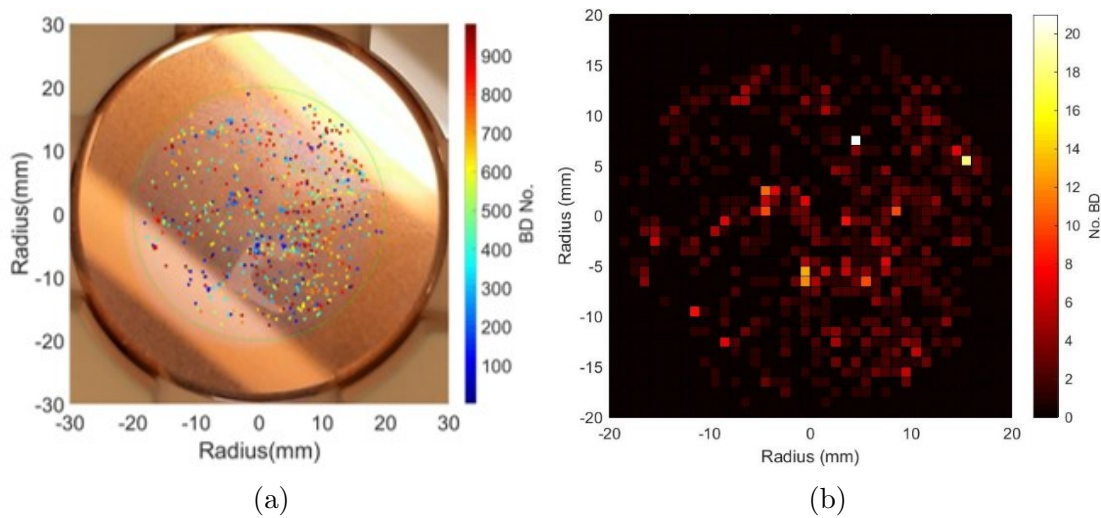


Figure H.3: Breakdown locations measured during testing of electrode pair 42. a) shows the breakdown locations over time relative to the scale to the right of the image, b) shows the number of breakdowns per square mm

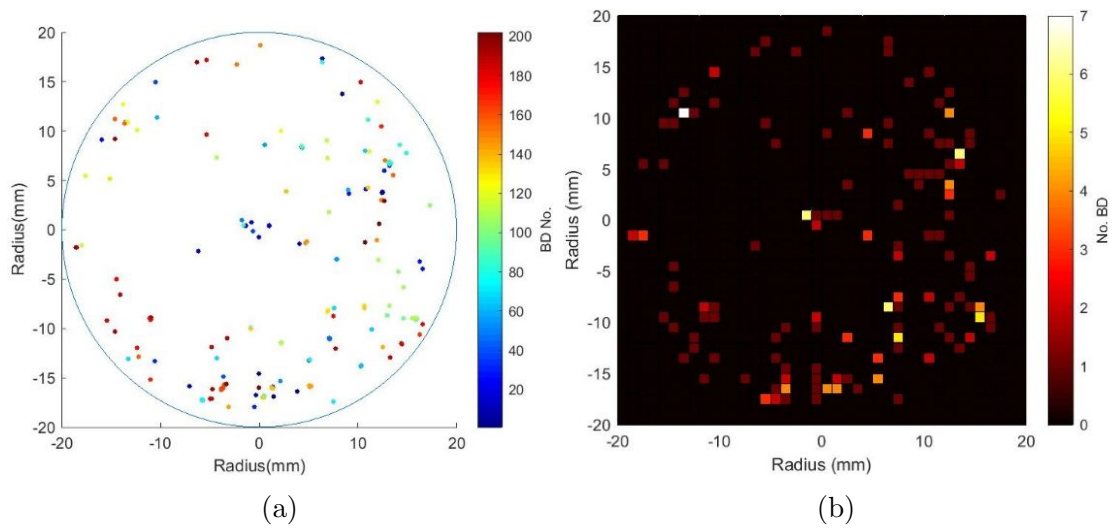


Figure H.4: Breakdown locations measured during testing of electrode pair 45. a) shows the breakdown locations over time relative to the scale to the right of the image, b) shows the number of breakdowns per square mm

Appendix I

Copper Chromium Zirconium

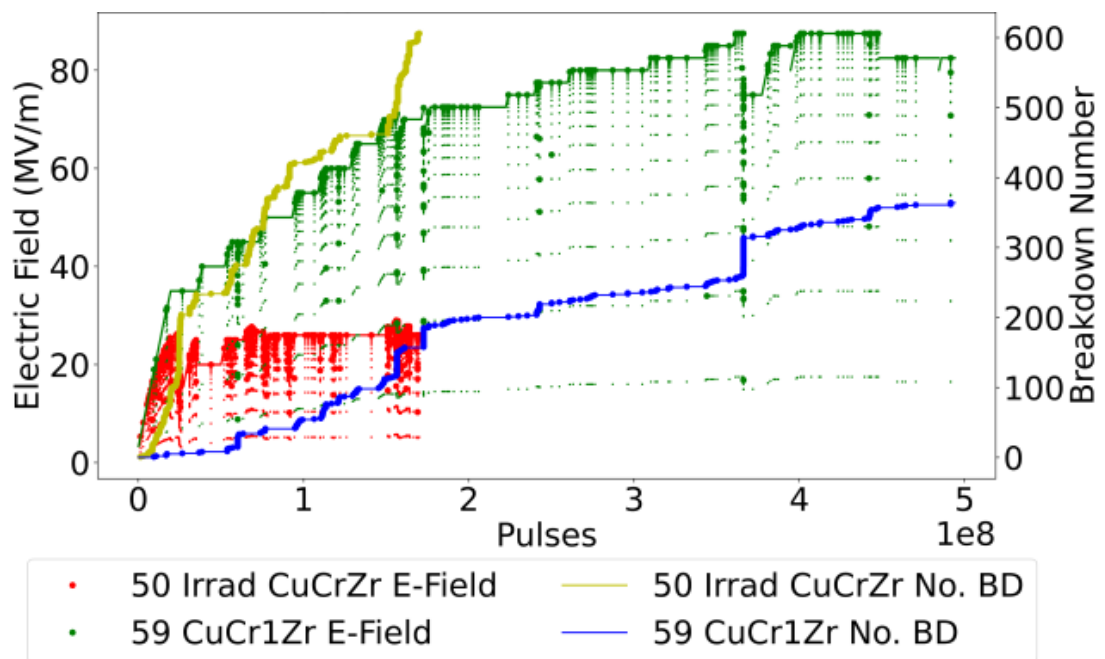


Figure I.1: Conditioning plots of both Irradiated and non-irradiated Copper Chromium Zirconium, showing the electric field and number of breakdowns on the respective axes.

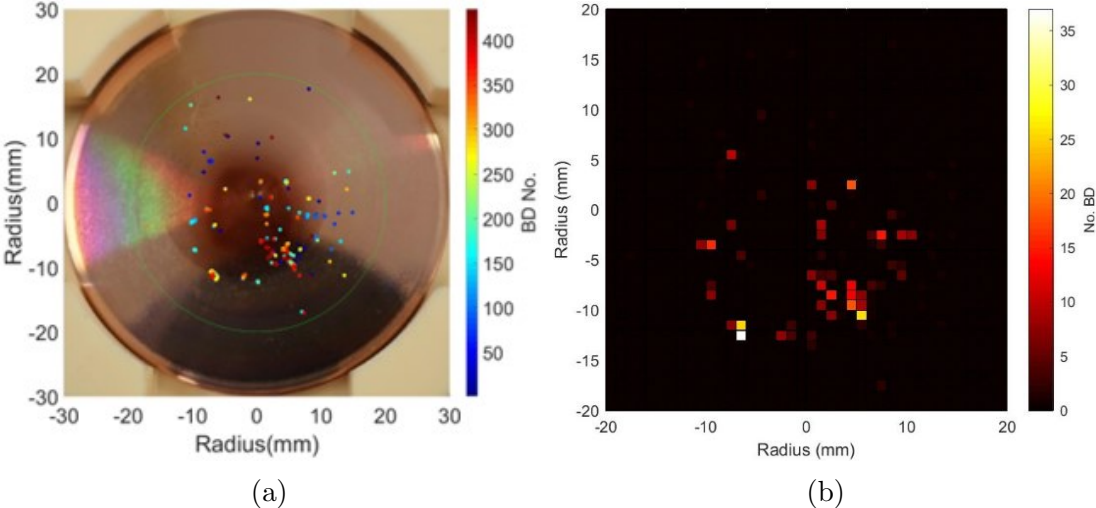


Figure I.2: Breakdown locations measured during testing of electrode pair 50. a) shows the breakdown locations over time relative to the scale to the right of the image, b) shows the number of breakdowns per square mm

Appendix J

Titanium Alloy Tests

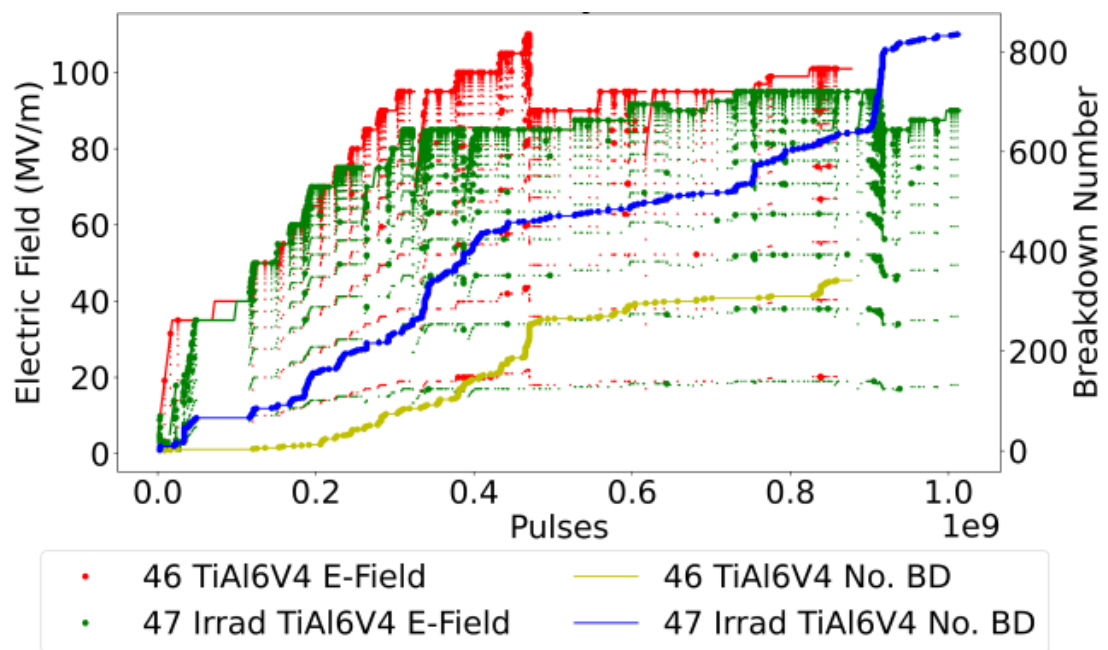


Figure J.1: Conditioning plots of both Irradiated and non-irradiated Titanium Alloy (TiAl6V4), showing the electric field and number of breakdowns on the respective axes.

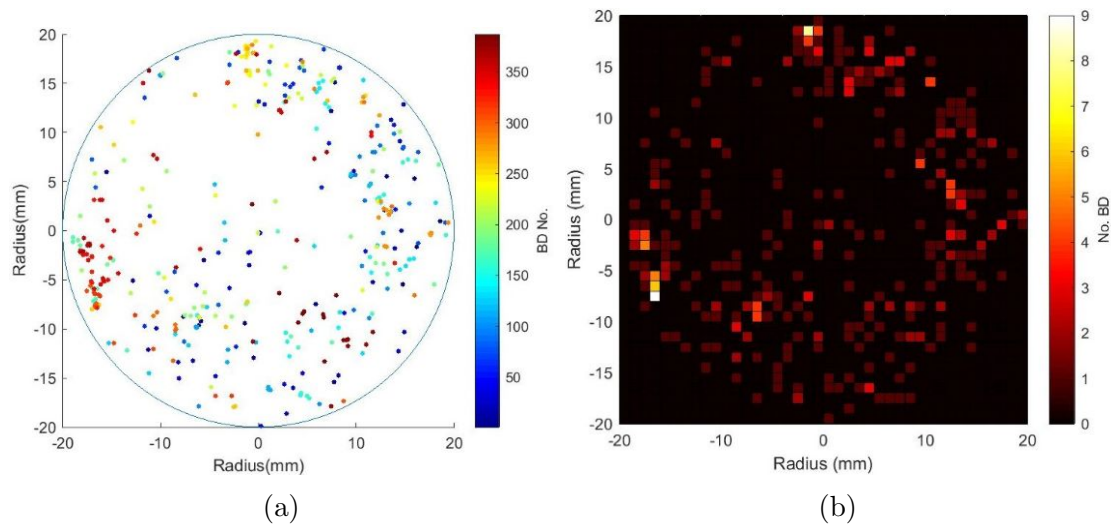


Figure J.2: Breakdown locations measured during testing of electrode pair 46. a) shows the breakdown locations over time relative to the scale to the right of the image, b) shows the number of breakdowns per square mm

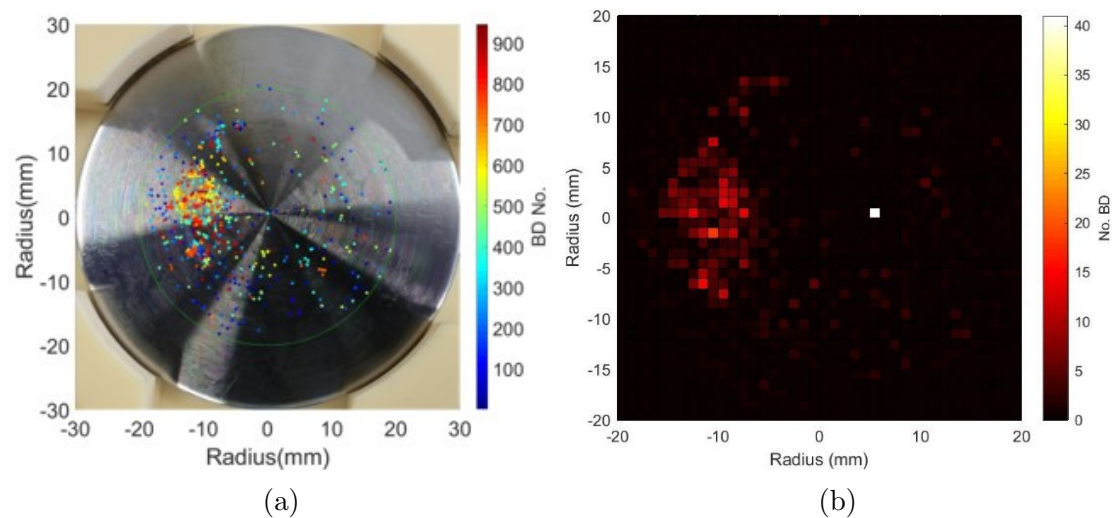


Figure J.3: Breakdown locations measured during testing of electrode pair 47. a) shows the breakdown locations over time relative to the scale to the right of the image, b) shows the number of breakdowns per square mm

Appendix K

Tantalum Tests

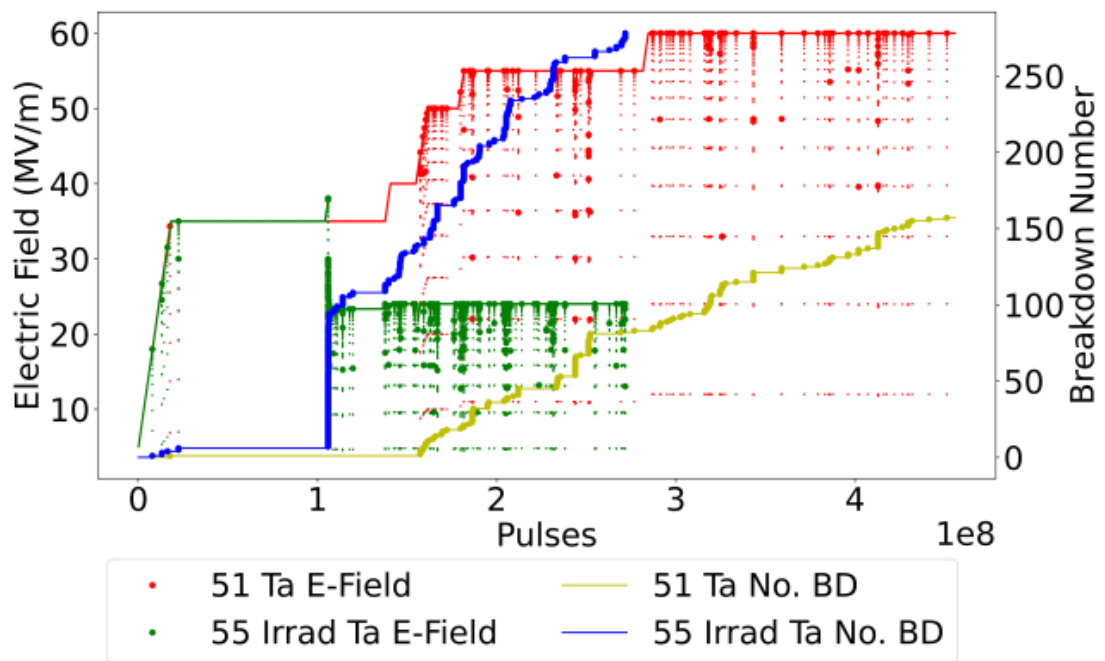


Figure K.1: Conditioning plots of both Irradiated and non-irradiated Tantalum, showing the electric field and number of breakdowns on the respective axes.

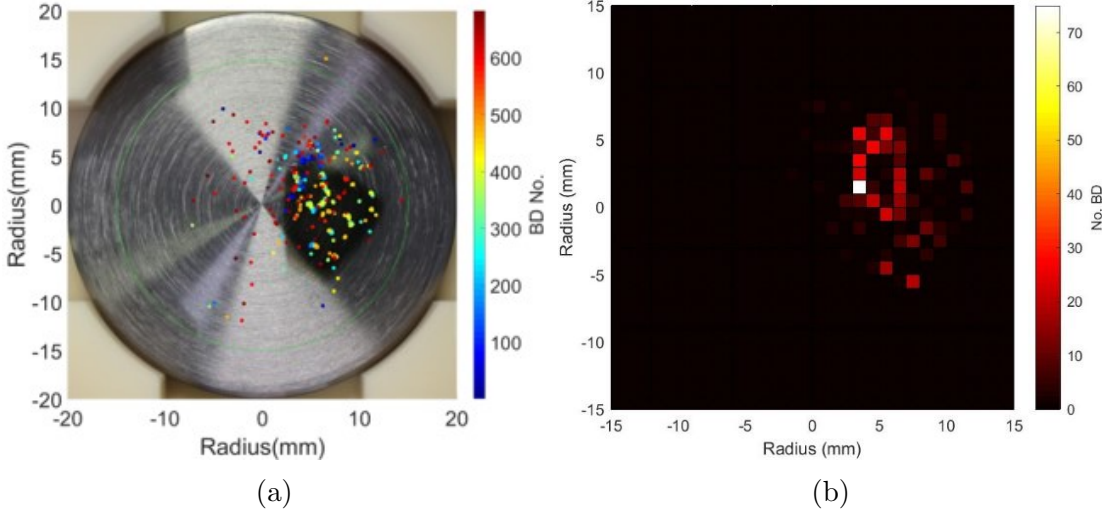


Figure K.2: Breakdown locations measured during testing of electrode pair 55. a) shows the breakdown locations over time relative to the scale to the right of the image, b) shows the number of breakdowns per square mm

Appendix L

Niobium Tests

L.1 No BCP

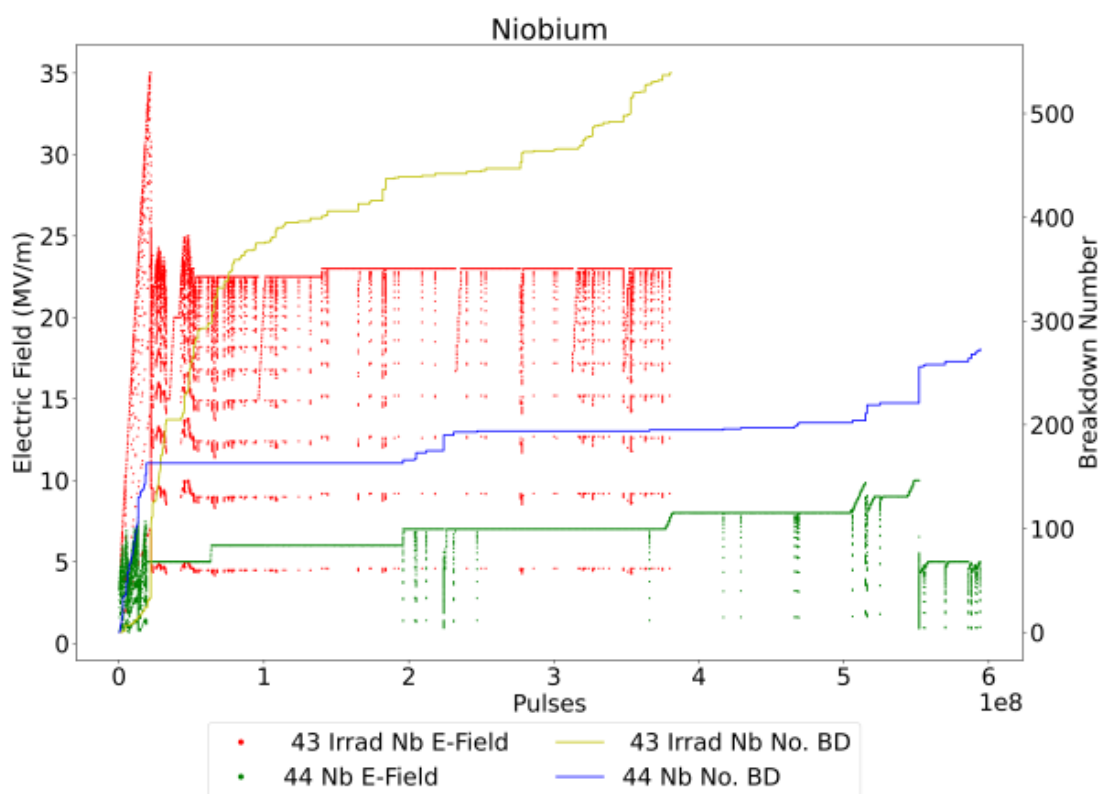


Figure L.1: Conditioning plots of both Irradiated and non-irradiated Niobium, showing the electric field and number of breakdowns on the respective axes.

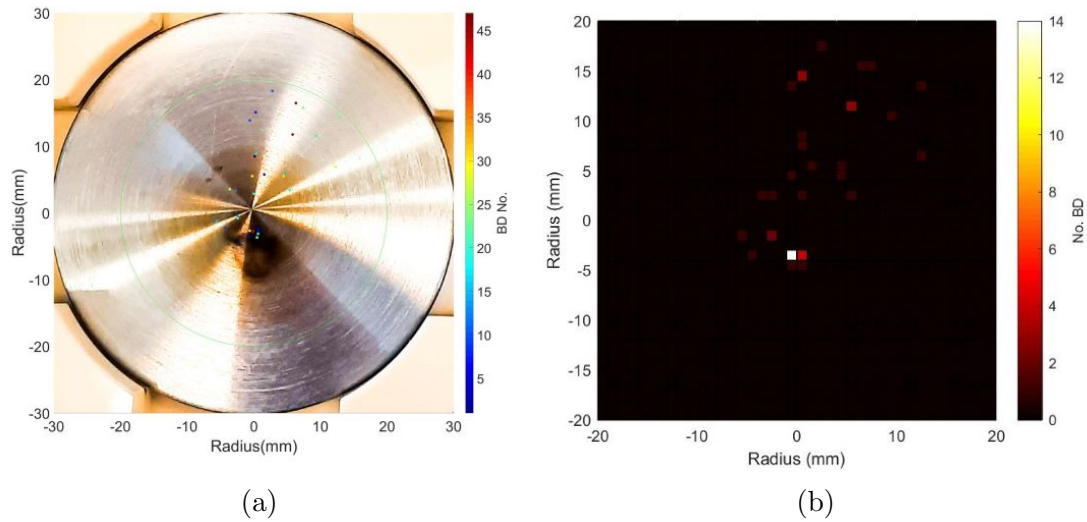


Figure L.2: Breakdown locations measured during testing of electrode pair 43. a) shows the breakdown locations over time relative to the scale to the right of the image, b) shows the number of breakdowns per square mm

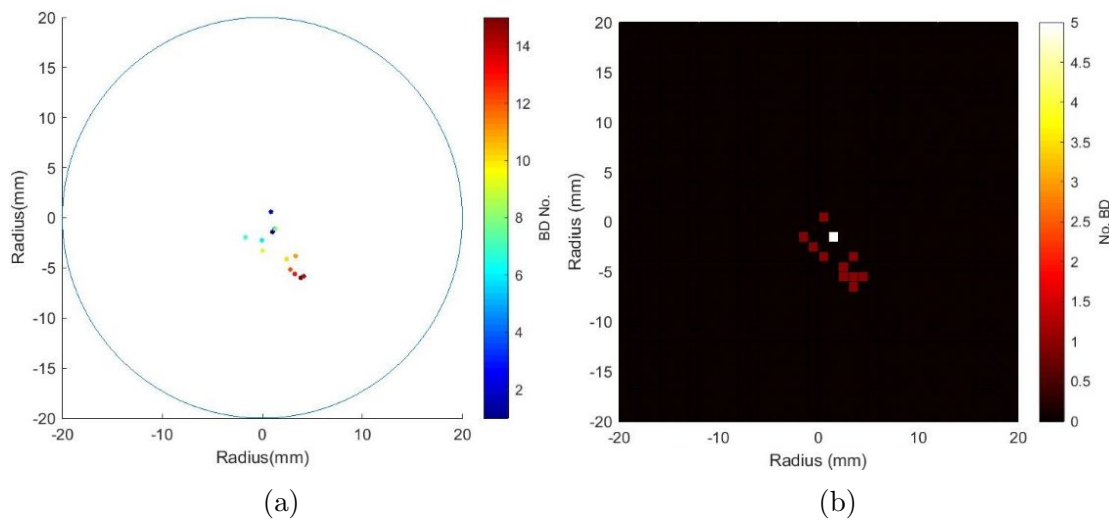


Figure L.3: Breakdown locations measured during testing of electrode pair 44. a) shows the breakdown locations over time relative to the scale to the right of the image, b) shows the number of breakdowns per square mm

L.2 After BCP

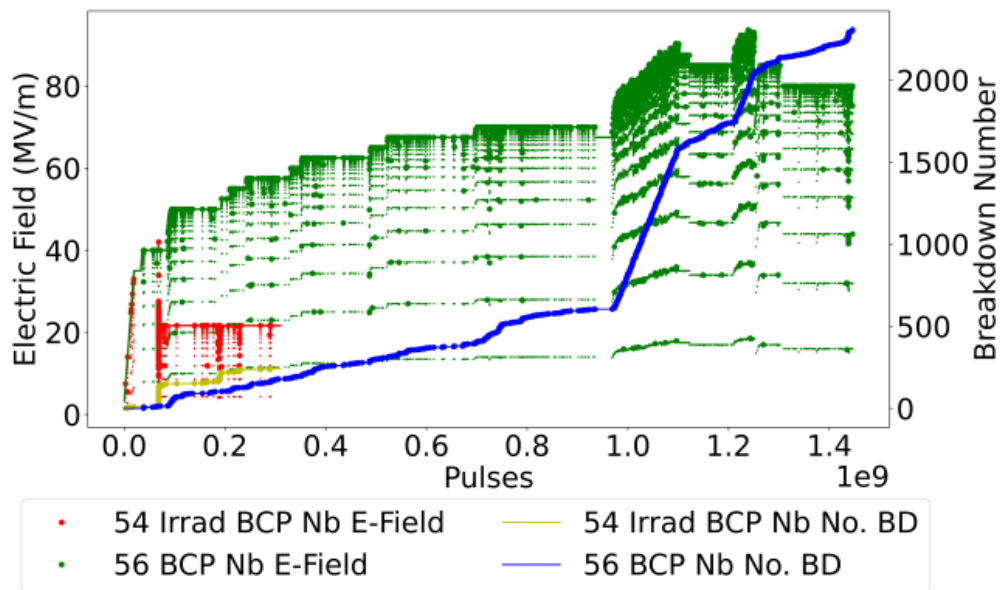


Figure L.4: Conditioning plots of both Irradiated and non-irradiated BCP Niobium, showing the electric field and number of breakdowns on the respective axes.

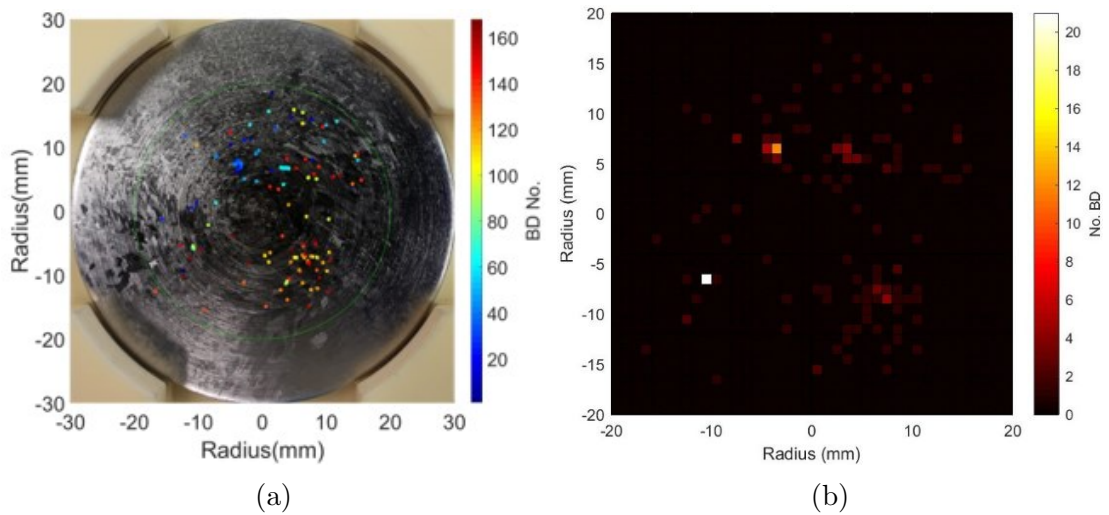


Figure L.5: Breakdown locations measured during testing of electrode pair 54. a) shows the breakdown locations over time relative to the scale to the right of the image, b) shows the number of breakdowns per square mm

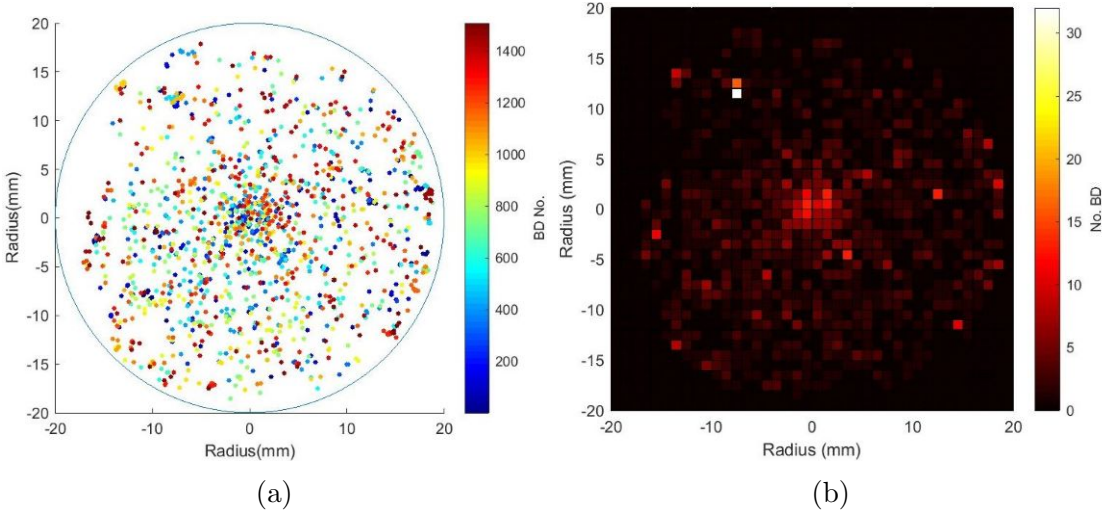


Figure L.6: Breakdown locations measured during testing of electrode pair 56. a) shows the breakdown locations over time relative to the scale to the right of the image, b) shows the number of breakdowns per square mm

Appendix M

Breakdowns within the irradiated area

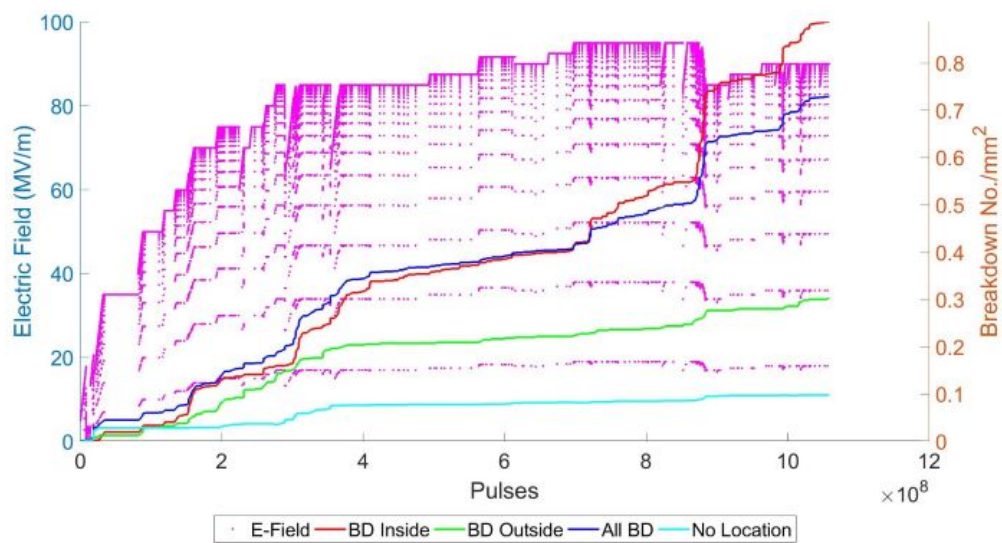


Figure M.1: Shows the normalised number breakdown per square mm, inside and outside the irradiated, over all the surface, and not detected by the cameras, for the TiAl_6V_4 electrodes.

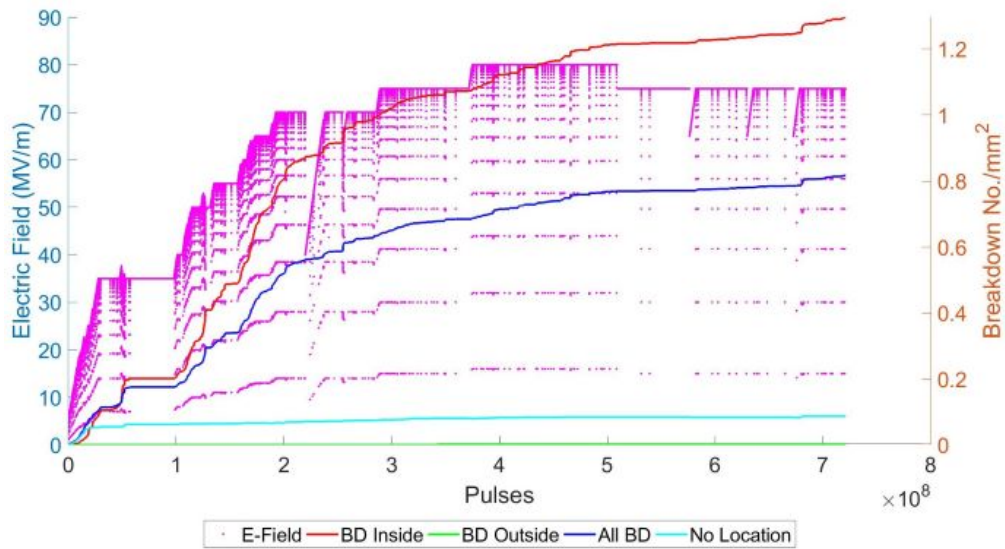


Figure M.2: Shows the normalised number breakdown per square mm, inside and outside the irradiated, over all the surface, and not detected by the cameras, for the Cu OFE electrodes.

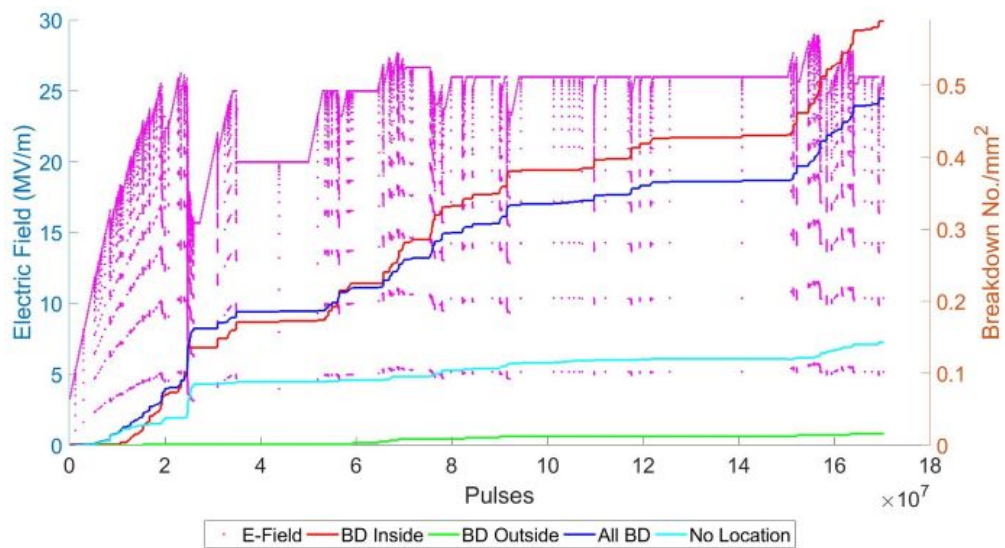


Figure M.3: Shows the normalised number breakdown per square mm, inside and outside the irradiated, over all the surface, and not detected by the cameras, for the CuCr₁Zr electrodes.

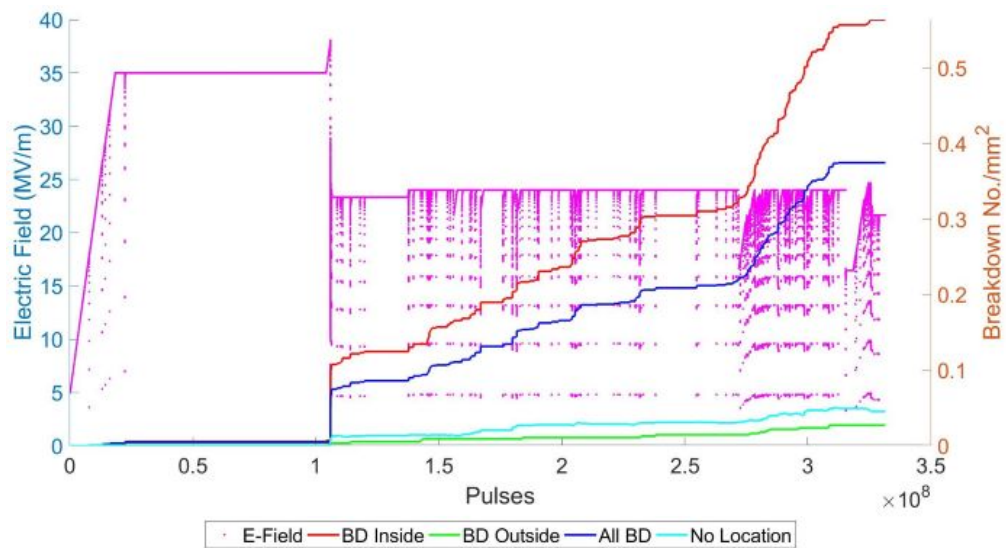


Figure M.4: Shows the normalised number breakdown per square mm, inside and outside the irradiated, over all the surface, and not detected by the cameras, for the Ta electrodes.

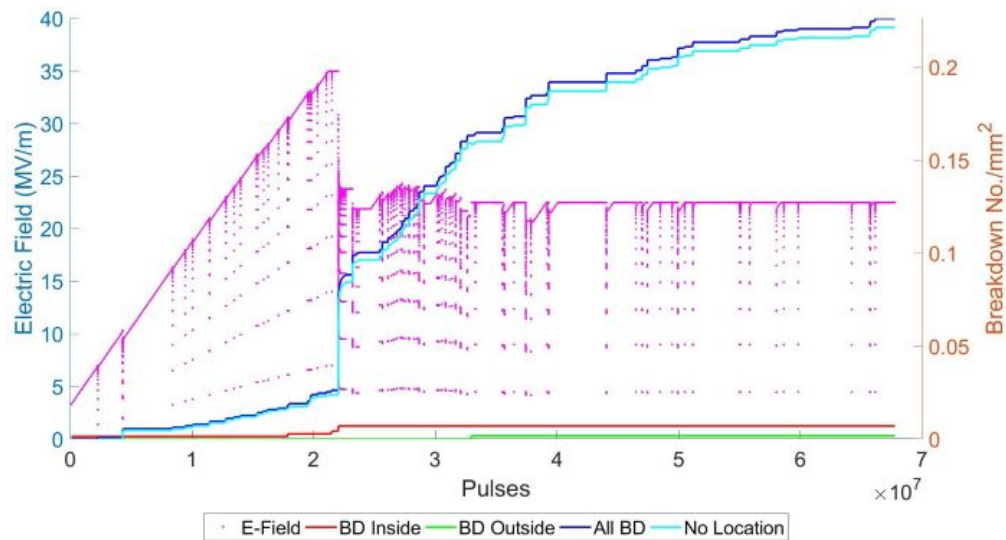


Figure M.5: Shows the normalised number breakdown per square mm, inside and outside the irradiated, over all the surface, and not detected by the cameras, for the Nb electrodes.

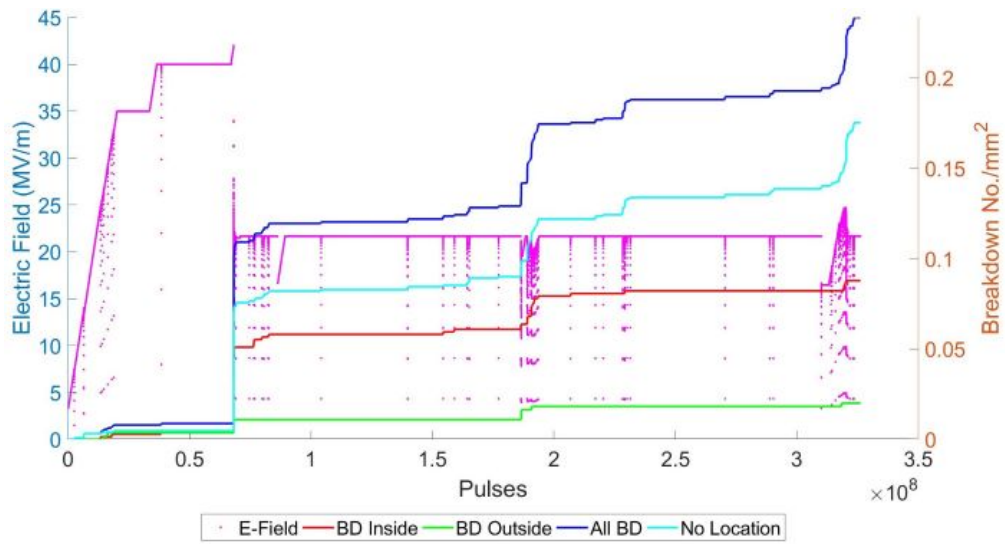


Figure M.6: Shows the normalised number breakdown per square mm, inside and outside the irradiated, over all the surface, and not detected by the cameras, for the Nb BCP electrodes.

Appendix N

Pulse Length Dependence Table

Material	Pulse Length (μ s)	Number of Pulses	Number of Breakdowns	Breakdown Rate	Standard Error
TiAl ₆	100	54938267	1	1.82E-08	1.82E-07
	250	48909972	8	1.64E-07	5.78E-08
	500	86372400	11	1.27E-07	3.84E-08
	1000	96851946	21	2.17E-07	4.73E-08
CuCr ₁ Zr	100	36306486	4	1.10E-07	5.51E-08
	250	29131636	3	1.03E-07	5.95E-08
	500	52378947	6	1.15E-07	4.68E-08
	1000	67873794	22	3.24E-07	6.91E-08
Nb	100	34466392	14	4.06E-07	1.09E-07
	250	35723903	29	8.12E-07	1.51E-07
	500	52185535	49	9.39E-07	1.34E-07
	1000	20893965	76	3.64E-06	4.17E-07
Cu OFE	100	64831617	4	6.17E-08	3.08E-08
	250	51529457	7	1.36E-07	5.13E-08
	500	47866073	2	4.18E-08	2.95E-08
	1000	61147006	8	1.31E-07	4.63E-08
Ta	100	1.74E+08	74	4.25E-07	4.94E-08
	250	65394388	25	3.82E-07	7.65E-08
	500	51874613	22	4.24E-07	9.04E-08
	1000	37770626	26	6.88E-07	1.35E-07

Table N.1: Table showing the number of pulses and breakdowns used for each pulse length for each material used to determine the breakdown rate and standard error for the value given in Figure 3.14.

Appendix O

Material Hardness Table

Symbol	Name	Mohs Hardness	Vickers Hardness (MPa)	Brinell Hardness (MPa)
Al	Aluminium	2.75	160–350	160–550
Cr	Chromium	8.5	1060	687–6500
Cu	Copper	3	343–369	235–878
Mg	Magnesium	2.5		260
Nb	Niobium	6	870–1320	735–2450
Si	Silicon	6.5		
Ta	Tantalum	6.5	873–1200	441–3430
Ti	Titanium	6	830–3420	716–2770
V	Vanadium	7	628–640	600–628
Zr	Zirconium	5	820–1800	638–1880

Table O.1: Table of the hardness values using different methods for the materials tested, where hardness is given for individual materials and not the alloys as tested. [84]

Appendix P

Work Function Values Table

Element	Plane	φ /eV	Method
Al	100	4.2	PE
	110	4.06	PE
	111	4.26	PE
Be	Polycr	4.98	PE
Cr	polycr	4.5	PE
Cu	100	5.1	PE
	110	4.48	PE
	111	4.94	PE
Mg	polycr	3.66	PE
Nb	001	4.02	TH
	110	4.87	TH
	111	4.36	TH
Si	n	4.85	CPD
Ta	polycr	4.25	TH
	100	4.15	TH
	110	4.8	TH
	111	4	TH
Ti	polycr	4.33	PE
V	polycr	4.3	PE
Zr	polycr	4.05	PE

Table P.1: Table of the work function values for different elements, given for individual materials and not the alloys as tested. [24]–[26]

Where,

TE - Thermionic emission

PE - Photoelectric effect

CPD - Contact potential difference

polycr - Polycrystalline sample

Appendix Q

Irradiation Setup

Q.1 Changing disk only

- Keep the end plate on throughout
- Undo the screw connecting the steel plate to the ceramic holding the disk in place
- Remove disk and place in silk paper to avoid contamination and scratched
- Replace with the next disk and fix in place the same as previously
- Check that the current wire is still in place
- Check the electrical connection
 - You should have an electrical connection to the inside of the output connector and the disk and not the ground
- Cover with foil and rubber cap

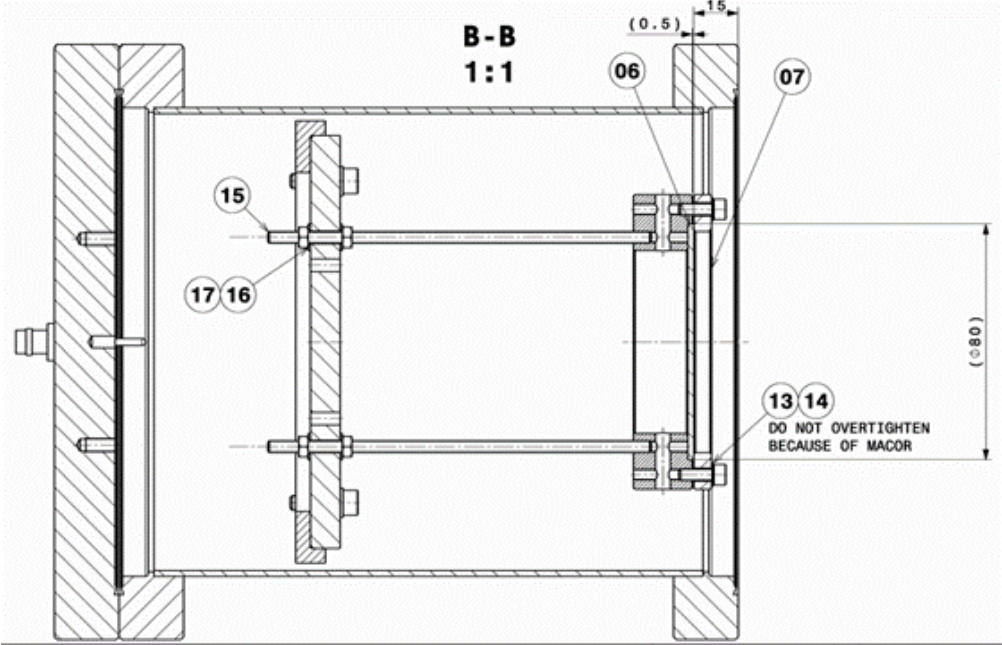
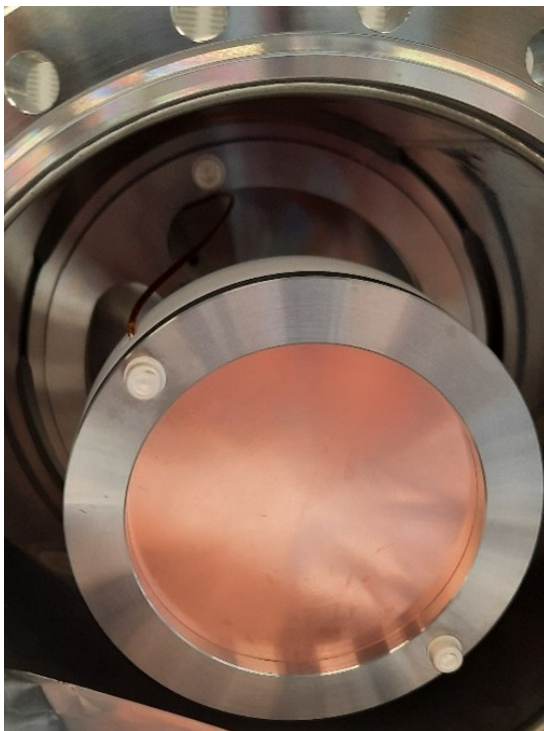
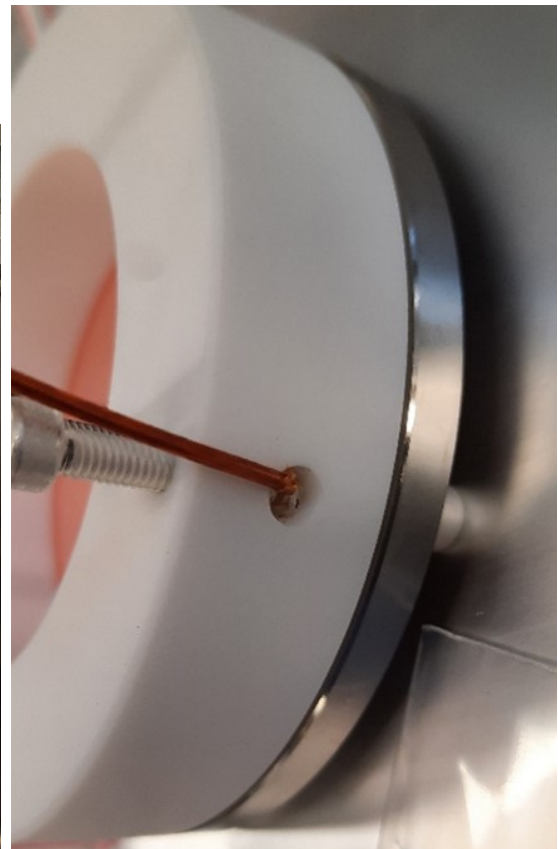


Figure Q.1: Sample disk irradiation setup assembly drawing.



(a)



(b)

Figure Q.2: Images of disk attached with the irradiated chamber from (a) above and (b) the side to highlight the wire to ground.

Q.2 Remove Plate

- Remove end plate by taking out all screws with 13mm spanner
- Cover this end with foil and rubber cap and place face down
- Open the end to access the disk
- Undo the screw connecting the steel plate to the ceramic holding the disk in place.
- Remove disk and place irradiated store in silk paper to avoid contamination and scratched
- Use a cleaned Allen key to undo the screw steel plate to the chamber
- Pull out the ceramic, rods and plate together. It is a bit tight so you needs some force.
- Remove the steel plate using a cleaned 7mm spanner but leave on the second pair of bolts because they will help with positioning for re-installation. Place bolts and washers in a clean plastic bag.
- Remove rods from the ceramic and place into a clean plastic bag. Place ceramic in silk paper in a plastic bag.

Q.3 Installation of Electrode

- Put the electrode face down on the ceramic to make sure the critical surface is not in contact with the table (different ceramics for different size electrodes, spacer for small electrodes). Be careful not to scratch the electrode whilst placing onto the ceramic.

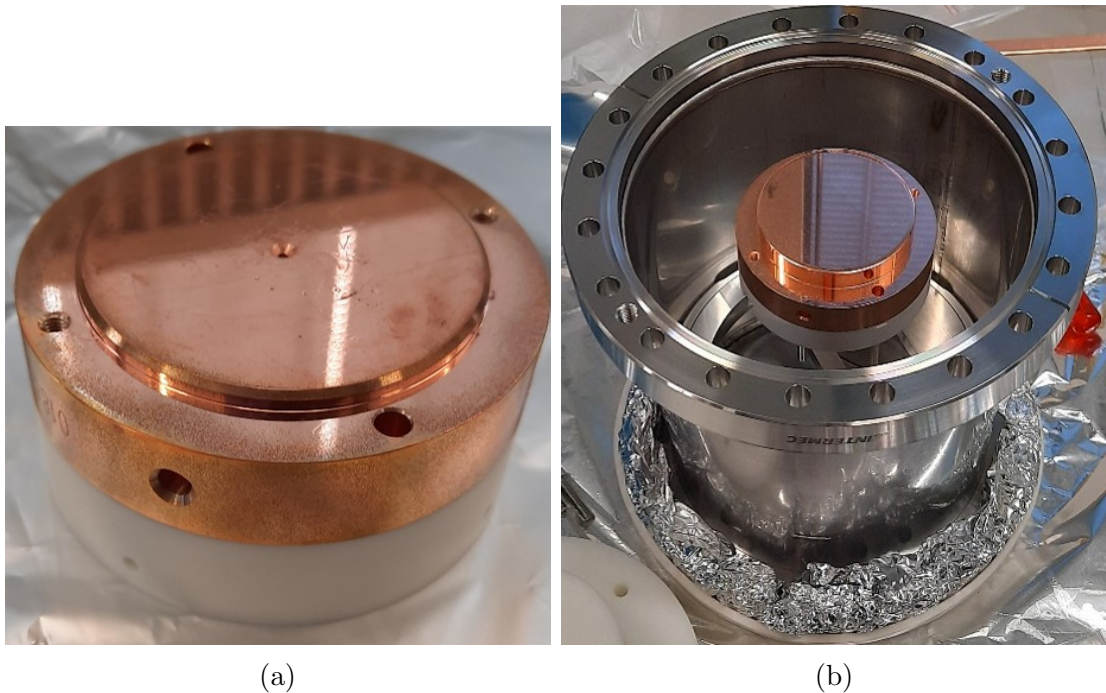


Figure Q.3: (a) Image of an electrode upside down on a ceramic to avoid damaging the surface during assembly, and (b) showing the electrode installed in the irradiation assembly.

- Place the irradiation setup ceramic on the bottom of the electrode and secure with screws, one side should have the 2 washers and the current wire in between
- Attach the threaded rods to the bottom of the ceramic
- Put the same metal plate as previously on the rods using the bolts for support, the critical surface should be 20mm from the flange (shoulder 30mm). Tighten bolts using a cleaned 7mm spanner
- Place the setup in the chamber with the electrode facing up
- Fasten the screws whilst moving round as it will move down due to being slightly too large.
- Check the distance from the flange to the shoulder is 30mm approximately

- Clean the ruler and micrometre with alcohol
- Place ruler over the flange and use the micrometre to measure the distance to the shoulder of the electrode, be careful not to scratch the critical surface.
- Cover the end with foil and the rubber cap and put face down
- Place the copper gasket on the flange
- Connect the wire for measuring the current to the connector with positive sign on end plate
- Put in 2 bolts and secure loosely
- Place horizontally and remove cap and use to stop the setup from rolling to access the disk
- Check the electrical connection
 - You should have an electrical connection to the inside of the output connector and the disk
 - You should not have a connection between the walls of the chamber (ground) and the disk
- Cover with foil and rubber cap and place face down
- Put the remaining screws in, to secure the end plate, tighten opposite sides whilst moving around to secure evenly

Appendix R

Nominal vs. Metrology Gap

Pair	Metrology Calculated Gap						60 μm Gap		Stable Field Difference (%)
	Ceramic (μm)	Cathode Shoulder (mm)	Anode Shoulder (mm)	Gap (μm)	Max Field (MV/m)	Stable Field (MV/m)	Max Field (MV/m)	Stable Field (MV/m)	
TiAl6V4	59	10.001	10.0014	61.4	107.5	97.7	110	100	97.7
TiAl6V4	59	10	10.0016	60.6	94.1	89.1	95	90	99.0
Cu (1)	59	9.9998	9.9998	58.6	84.9	84.9	83	83	102.3
Cu (2)	59	10.0003	10.0004	59.7	80.4	80.4	80	80	100.5
Cu RFQ	59	9.9998	10.0002	59.0	81.4	81.4	80	80	101.7
CuCr1Zr	59	10.0005	10.0022	61.7	82.7	82.7	85	85	97.3
CuCr1Zr	59	9.9975	10.0013	57.8	30.2	27.0	29	26	104.0
Ta	60	9.9998	10.0011	60.9	59.1	59.1	60	60	98.5
Ta	60	9.9999	10.0022	62.1	36.8	22.7	38.1	24	94.7
Nb	59	10.0002	10.001	60.2	10.0	4.7	10	4.7	99.7
Nb	59	10.001	10	60.0	35.0	23.0	35	23	100.0
Nb BCP	59	9.9998	10.0022	61.0	92.1	78.7	94	80	98.4
Nb BCP	59	10.001	10.0022	62.2	40.5	20.9	42	21.7	96.3
Al	59	9.9992	9.9992	57.4	90.6	67.9	86.7	65	104.5
Non-Irrad									
Irrad									

Table R.1: Electric fields for the calculated gap using the metrology reports for each electrode and the given results using the 60 μm nominal gap